DISSERTATION

Titel der Dissertation

Entanglement Swapping and Quantum Interference with Independent Sources

Verfasserin / Verfasser
Mag. Rainer Kaltenbaek

angestrebter akademischer Grad
Doktor der Naturwissenschaften

Wien, im Februar 2008

Introduction

There are two purposes to the experiments presented in this thesis. One, a purely fundamental purpose, is to demonstrate, for the first time, interference of single photons originating from independent sources. The other, a mostly application-oriented purpose, is to utilize this effect to realize a central ingredient of quantum repeaters [25, 42], namely entanglement swapping [141] (see 1.6.2) with pairs emitted from independent nodes.

Interference, as it is understood in classical electromagnetism, is an effect due to the superposition of field amplitudes. A stable interference patterns can only occur when there is a stable phase relation between the interfering fields. If an interference pattern is washed out in the average over time, it is denoted as *transient interference* (see e.g. [83]).

Fields from independent sources in general have, per definition, no stable phase relation relative to each other. They are incoherent, and only transient interference patterns can be observed. This interference can lead to stable higher-order correlations between multiple detectors [83, 94], see 2.1, but their visibility cannot exceed a limit of 50 % [94].

In quantum physics the particle nature of light allows for the possibility of interference of light from independent sources with a visibility up to 100 %. As stressed by Mandel "this prediction has no classical analogue, and its confirmation would represent an interesting test of the quantum theory of the electromagnetic field" [82]. A well known example is Hong-Ou-Mandel (HOM) interference [60]. By utilizing this effect we have demonstrated interference of single photons from independent photons with a visibility clearly exceeding the classical limit of 50 %. Although several experiments have analyzed or employed interference of this kind, ours is the first rigorous, i.e. where the interfering photons can be called independent without restraints (see chapter 3).

Quantum interference combined with post selection [71] has become an important tool in optical quantum communication and quantum computation [23, 90]. One example, which is of specific interest for us, is the realization of a partial Bell-state measurement (BSM) using HOM-type interference, see 2.3 and 6.5.2. It plays a central role in quantum state teleportation [12, 24] and entanglement swapping [141, 92, 64].

Many quantum communication and quantum computation schemes are based on the utilization of entanglement [108, 109, 110, 111, 112] as a resource. In implementations of these techniques entanglement will have to be distributed between, possibly very distant, communication parties or nodes of a quantum network. Photon loss [127] and decoherence limit the distribution of entanglement to distances on the order of a hundred kilometers [117, 84, 120]. Quantum repeaters [25, 42] allow to overcome this limitation. Their realization is essential for any future implementations of large scale quantum networks. Although a full-scale implementation might still be in the far future, our experiments provide an essential cornerstone in the development of quantum repeaters.

Rainer Kaltenbaek, May 26th, 2007

Outline of the thesis

I divided the thesis into two parts to separate the main part of the thesis from the appendices. The appendices contain information that is also centered around the topic of the main part of the thesis but is not necessary for its immediate understanding.

In chapter 1 of the main part I will introduce and discuss a number of concepts, which our work is based on. Where such discussions can also be found in other works or even text books, I have tried to present them from a new angle and/or to keep our discussion as short as possible. These points have been included for the sake of completeness and as a reference within the thesis.

Interference itself is a such important part of this thesis that I am going to present its principles separately in chapter 2. Apart from a short overview over the basics I will present a detailed discussion of the interference of independent sources in general, and of HOM-type interference in particular.

Naturally, many of the concepts, which this thesis is based upon, are no novelties but have been employed frequently in earlier experiments. In chapter 3 I will present a short review of a selection of prior works, which stand in direct relation to this thesis. On the one hand, this should provide a clear picture of the difference between these efforts and ours and, on the other hand, it is intended to further the understanding of the nature of the effects, which we are going to demonstrate.

The single-photon sources used in our experiment consist and make use of various components. In chapter 4 I will give a short review about their nature and working principles. Prominent aspects are the theoretical background for the correction of general astigmatism of two-dimensional Gaussian beams and novel results on the heralding efficiencies in spontaneous parametric down-conversion.

Because we used pulsed lasers, our sources emitted single photons at well defined times. When a photon from one of the sources is detected, the time of detection in relation to the emission times of the sources allows, in principle, to determine where the detected photon originated from. The photons will be distinguishable, and no interference will occur. To render the photons indistinguishable in order to allow for high-visibility interference with pulsed sources it was necessary to synchronize the emission times of the sources. This is one of the most central parts of our work. The principles of synchronization and how its performance influenced the results of our experiments will be described in chapter 5.

A detailed description of our experimental setup is given in chapter 6. This encompasses the implementation of the synchronization mechanism, the single-photon sources and the setup for HOM-type interference. I will also discuss which changes had to be made to the experimental setup for the realization of entanglement swapping, our second experiment.

Chapter 7 will present our scan routines, the measurements, and their results. I will discuss the details of the scanning procedures and how the measurement results are interpreted.

Conclusion, outlook and ideas for possible future experiments and applications related to the presented work are given in chapter 8. It is the end of the main part of the thesis.

In chapter A of the appendix I present a slight modification to our theoretical results on

HOM-type interference, such that the description encompasses the occurrence of distinct fringes in the interference pattern.

Chapter B contains a discussion of the alignment of the lasers in order to document aspects of it that are not common knowledge. Moreover, I will present a short discussion of a specific part of the alignment of spontaneous parametric down-conversion sources.

In chapter C I will give a detailed account on my calculations on the determination and optimization of the beam profiles of the pump beam before and after second-harmonic generation.

A novel method to numerically simulate the emission pattern of photons emerging from type-II down conversion will be introduced in chapter D.

Finally, in chapter E, I will list and roughly describe the contents of the CD-ROM that accompanies this thesis

Contents

Part I.

Entanglement Swapping and Quantum Interference with Independent Sources

1. Principles

It is not the purpose of this thesis to explain all notations and technical terms employed. On the other hand, a short overview of the relevant principles creates a basic terminology and provides a point of reference within the thesis. I will give a not very extensive but consistent overview of the most important concepts and principles related to the work that I will present in the chapters succeeding this one.

1.1. Superposition

The principle of superposition of quantum states is one of the most elementary characteristics of quantum theory. I will first explain superposition formally for the most simple quantum systems. These carry at the most one bit of information [138]. Partly due to this maximal information content these systems are referred to as *qubits* [113]. The Hilbert space used to describe the state of a qubit can be spanned by any set of two non-collinear states.

Let us denote two orthogonal states by $|0\rangle$ and $|1\rangle$ in analogy to the possible values of a classical bit. Any qubit state $|\psi\rangle$ can be written as a linear combination or *superposition* of these states:

$$|\psi\rangle = \alpha|0\rangle + \beta|1\rangle, \tag{1.1}$$

where $\alpha, \beta \in \mathbb{C}$ and

$$|\alpha|^2 + |\beta|^2 = 1. \tag{1.2}$$

Superposition allows for infinitely many qubit states but only orthogonal states can be distinguished with certainty (see e.g. [90]). This stands in direct relation to the no-cloning theorem [134], which states that it is impossible to produce a perfect copy of an unknown quantum state. The no-cloning theorem is what makes quantum cryptography secure [132, 11, 44, 51]. It follows directly from quantum theory, and it can be shown that if this theorem was violated, it would be possible to realize "impossible machines" like a super-luminal telephone (see e.g. [1]).

In addition to its relevance for quantum computation and communication superposition lies at the heart of all interference phenomena. The superposition of two or more probability amplitudes for different but indistinguishable processes, which result in the same detection event, leads to the well known phenomenon of interference fringes.
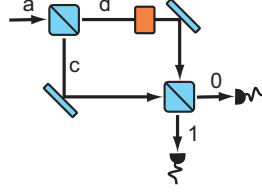
Figure 1.1.: A Mach-Zehnder interferometer. Light is split at the first beam splitter. The two parts are directed along two separate paths and are recombined at a second beam splitter. There they will interfere. A phase shift χ is introduced along one of the paths. If χ is a multiple of π, all light will exit via one and the same output port.

A common example is the interference in a Mach-Zehnder interferometer as illustrated in figure 1.1. Suppose a photon enters along mode a, and that we can write it as:

$$|\psi\rangle = \hat{a}_a^\dagger|\Omega\rangle, \tag{1.3}$$

where $|\Omega\rangle$ is the vacuum state, and I used $\hat{a}_a^\dagger$ to denote the creation operator for mode a [1]. Behind the first beam splitter and after a phase shift d, which is introduced in mode d, the state becomes:

$$|\psi\rangle = \frac{1}{2}\left(-\imath\hat{a}_c^\dagger + e^{\imath\chi}\hat{a}_d^\dagger\right)|\Omega\rangle. \tag{1.4}$$

The additional shift of $-\imath$ results from the reflection at the beam splitter. I am going to neglect the additional global phase factor that results from the reflections at the mirrors in modes c and d.

The probability amplitude to detect a photon in mode 0 after the second beam splitter is given by $\langle\Omega|\hat{a}_0|\psi\rangle$. Interference will occur if and only if a detection event in mode 0 (or 1) does not allow to distinguish whether the excitation came from mode c or d. In our simple example we can put this in simpler words: interference will occur only if we can express $\hat{a}_0^\dagger|\Omega\rangle$ and $\hat{a}_1^\dagger|\Omega\rangle$ as **superpositions** of $\hat{a}_c^\dagger|\Omega\rangle$ and $\hat{a}_d^\dagger|\Omega\rangle$. Then we can write the probability amplitude for detecting a photon in mode 0 as:

$$\langle\Omega|\hat{a}_0|\psi\rangle = \frac{1}{\sqrt{2}}\langle\Omega|\left(\hat{a}_c + \imath\hat{a}_d\right)|\psi\rangle. \tag{1.5}$$

If we use equ. 1.4, we will get:

$$\langle\Omega|\hat{a}_0|\psi\rangle = \frac{\imath}{2}(e^{\imath\chi} - 1), \tag{1.6}$$

---

[1]For the sake of simplicity I will neither state wavelengths nor polarizations throughout this short discussion.

and a similar calculation leads to:

$$\langle\Omega|\hat{a}_1|\psi\rangle = \frac{\iota}{2}(e^{\iota\chi}+1).\tag{1.7}$$

By taking the modulus square of these expressions we finally arrive at the probabilities for detecting a photon in mode 0 and 1, respectively:

$$|\langle\Omega|\hat{a}_0|\psi\rangle|^2 = \frac{1}{2}(1+\cos\chi) = \cos^2\frac{\chi}{2}\tag{1.8}$$

and

$$|\langle\Omega|\hat{a}_1|\psi\rangle|^2 = \frac{1}{2}(1-\cos\chi) = \sin^2\frac{\chi}{2}.\tag{1.9}$$

We see that these probabilities depend strongly on the value of the relative phase χ. Always when χ is a multiple of π, we will be able to predict with certainty, in which output mode we will find the photons.

Once more I want to stress the origin of the occurrence of interference in this case. It is because excitations in modes c and d lead to indistinguishable detection events. Excitations in the detector modes can be written as superpositions of excitations in modes c and d.

1.2. Density matrices

If a system is in a pure state, $|\psi\rangle$, this state describes the system completely. There is no more information, which can be gained about it. For such systems we can always find a measurement, the outcome of which will be certain. This measurement is defined by the projectors:

$$\begin{aligned}P_1 &= |\psi\rangle\langle\psi|\\ P_2 &= 1 - P_1.\end{aligned}\tag{1.10}$$

On the other hand, if we do not know the state of a system, we have to deal with the probabilities for the system to be in one out of a set of states $|\phi_i\rangle$. In this case we can describe the system by its *density matrix*, which is given by

$$\rho = \sum_i p_i|\phi_i\rangle\langle\phi_i|.\tag{1.11}$$

For every density matrix p_i and ϕ_i can be chosen such that the states ϕ_i form an orthonormal set. In this case the quantities p_i are probabilities and fulfill the relations $0 \leq p_i \leq 1$ and $\sum_i p_i = 1$. This is equivalent to the statement that every density matrix ρ must be Hermitian, and that its trace must be unity:

$$\mathrm{Tr}(\rho) = 1.\tag{1.12}$$

Every system that is in a pure state can be assigned a state vector $|\psi\rangle$ and we can write its density matrix as:

$$\rho_{pure} = |\psi\rangle\langle\psi|. \tag{1.13}$$

It fulfills the relation:

$$\mathrm{Tr}\left(\rho_{pure}^2\right) = 1. \tag{1.14}$$

Let us investigate the density matrix of a qubit. Because it is a Hermitian 2×2 matrix, it can be written as a linear combination of Pauli matrices:

$$\rho = \sum_{\mu=0}^{3} c_\mu \sigma_\mu, \tag{1.15}$$

where σ_0 is the 2×2 identity matrix, c_μ are constants, and

$$\sigma_1 = \begin{pmatrix} 0 & 1 \\ 1 & 0 \end{pmatrix}, \quad \sigma_2 = \begin{pmatrix} 0 & -\imath \\ \imath & 0 \end{pmatrix}, \quad \sigma_3 = \begin{pmatrix} 1 & 0 \\ 0 & -1 \end{pmatrix}. \tag{1.16}$$

Because of equ. 1.12 the trace of the density matrix must be 1 and equ. 1.15 can be simplified to:

$$\rho = \frac{1}{2}(1 + \mathfrak{a} \cdot \vec{\sigma}), \tag{1.17}$$

where $\vec{\sigma}$ denotes a three-component vector of the Pauli matrices and $\mathfrak{a}$ is the *Bloch vector* assigned to the qubit. Because of equ. 1.13 $\mathfrak{a}$ must be a unit vector for pure states. For mixed states $|\mathfrak{a}|$ will be less than unity.

It is convenient to denote $\mathfrak{a}$ in spherical coordinates [2]:

$$\mathfrak{a} = a \begin{pmatrix} \sin(2\theta)\cos(\phi) \\ \sin(2\theta)\sin(\phi) \\ \cos(2\theta) \end{pmatrix}. \tag{1.18}$$

When it is written in this form, a can be used as a measure of the purity of the qubit state. If it is a pure state, we will have $a = 1$, and the qubit state can be written as:

$$|\psi\rangle = \cos\theta|0\rangle + e^{-\imath\phi}\sin\theta|1\rangle, \tag{1.19}$$

where $|0\rangle$ and $|1\rangle$ are the eigenstates of σ_3 for the eigenvalues $+1$ and -1, respectively. The unit sphere defined by all pure states is called *Bloch sphere*.

---

[2]Because of the factor of 2 in the arguments of the functions of θ orthogonal pure states are represented by collinear vectors pointing in opposite directions.

1.3. Quantum information theory

Over the last decades a large number of quantum communication schemes have been developed, which utilize the principles of superposition and entanglement. Part of them are more efficient versions of already existing classical analogues, others do not even have such analogues.

Usually, the resources used for quantum communication and quantum computation are qubits [3]. These systems have the same elementary role in quantum computers as bits have in classical computation.

In these communication schemes as well as in quantum computation we often come across the situation, where qubits are processed that are part of larger quantum systems but do not carry any classical information on their own. Nevertheless, if we destroyed their state, information would be lost in the larger system.

A good example is super-dense coding [14, 86], where two bits of classical information are transmitted by sending one qubit, which is entangled (see below) to a second qubit that is already present at the receiver side. By manipulating the qubit that is going to be sent two classical bits can be stored in the two-qubit state, while one qubit on its own does not carry any information. It is a baffling concept that information can instantaneously and without communication be stored in possibly very distant qubits by manipulating only one of them. Maybe even more baffling is that we have to send this one qubit, which carries no information, in order to complete the transfer of two bits of information.

In this and similar contexts one often comes across the term "quantum information", to denote information present in a quantum system but kind of not available to be read out. This notion is nonsense. All information in quantum communication and quantum computation schemes is, of course, classical. Information is always classical. There is no superposition between knowing and not knowing. Even if there was, it could not be communicated by any language we know.

1.4. Entanglement

Entanglement [108, 109, 110, 111, 112] is a unique feature of multipartite quantum systems. Its most astonishing property is surely that it allows to experimentally distinguish quantum physics from a large class of realistic physical theories [7, 8, 79] (see 1.5).

Another intriguing aspect of entanglement is that it has proved to be a rather useful resource for communication. Prominent examples are quantum cryptography [132, 11, 44, 51], super dense coding [14, 86], quantum teleportation [12, 24] and entanglement swapping [141, 92, 63, 64]. It has been shown, that entangled states can be used as quantum computing resource [102], and recent works have demonstrated the influence of entanglement up to even macroscopic levels [91, 49, 121, 122, 133, 33].

---

[3]Larger systems could also be used but this is, at least at the moment, not common.

Up to now, entanglement is still not fully understood. For systems consisting of many subsystems even the case of pure states still poses riddles. For bipartite systems only low dimensional systems are well understood for both pure and mixed states.

Speaking in general terms entanglement manifests itself in possibly very strong correlations between the outcomes of measurements performed on the entangled subsystems. Essentially, the problem in understanding general entangled density matrices is to discern between correlations due to entanglement and classical correlations. The latter exist only for mixed states.

For a more formal description let us investigate a bipartite composite system C of subsystems A and B. A density matrix ρ on the Hilbert space $\mathfrak{H}_C = \mathfrak{H}_A \otimes \mathfrak{H}_B$ will be called entangled if and only if it cannot be written as a mixture of separable states, i.e.:

$$\nexists\, p_i \in [0,1], \rho_i^A \in \mathfrak{H}_A, \rho_i^B \in \mathfrak{H}_B : \rho = \sum_{i=1} p_i \rho_i^A \otimes \rho_i^B, \qquad (1.20)$$

where $[0,1]$ denotes the closed interval of real numbers from 0 to 1 and $\sum_{i=1} p_i = 1$. From this definition it follows that the set of separable states is convex because every mixture of two separable states is again separable.

While the definition of separability is clear and unambiguous, it is in general a non-trivial task to determine if a given density matrix ρ is separable or not. To find an operational criterion for it would with certainty deepen our understanding of entanglement.

1.5. (Local) Realism and why it cannot be

Up to this day the controversy continues (see e.g. [79] and [58]) whether the predictions of quantum theory can be explained by realistic theories. These are theories, which assume that the outcomes of measurements are predetermined by elements of reality like the classical concepts of position and momentum. I will provide an overview about the discussion as far as it concerns *local* realistic theories.

1.5.1. Einstein-Podolsky-Rosen

In their 1935 paper [43] Einstein, Podolsky and Rosen (EPR) attempted to show that the quantum-theoretical description of physical reality is incomplete [4]. Although Bohr shortly afterwards showed the flaw in EPR's argumentation [22] there are several reasons for giving a short review of the EPR argument.

First, EPR define in very clear words criteria that can be used to define a whole class of physical theories. This class of theories plays as central role in Bell's theorem, which I will discuss later on. Today it is known as the class of *Local-Hidden-Variable (LHV) theories*. Second, in EPR's gedankenexperiment the concept of entanglement and its intriguing

---

[4]Their use of the term "description of physical reality" shows already in the beginning that they assume the objective existence of a physical reality and that any physical theory should try to describe it.

implications made their first appearance. Third, in discussions with colleagues the author often noted that it does not seem clear to everybody that EPR did *not* succeed with their argument. They did *not* prove that quantum theory is incomplete.

EPR argument

The EPR argument starts with the following assumptions:

- **realism**: if the outcome of a measurement can be predicted with a probability equal to unity, there must exist a corresponding element of reality.

- **locality**: there can be no influence between events in space-like separated regions of space time (locality assumption).

They argue that for a physical theory to be satisfactory it should (1) be correct and (2) be complete. That it should be correct means that it should be consistent and in agreement with experimental results. According to EPR a physical theory is *complete* when it fulfills the following requirement: "*every element of physical reality must have a counterpart in the physical theory*". Starting from here, the course of the EPR argument is straight forward: they attempt to show that there are elements of reality that have no counterpart in quantum theory.

To this end they consider an entangled two-particle state of the form

$$\Psi(x_1, x_2) = \int_{-\infty}^{\infty} dp\, e^{\left(\frac{2\pi\iota}{h}\right)(x_1 - x_2 + x_0)p}, \tag{1.21}$$

where x_1 and x_2 are variables to describe the positions of the two particles, and x_0 is some constant.

If the experimenter chose to measure the *momentum* of particle 1 and if the result was p, one can show [43] that the state of particle 2 would be projected into a momentum eigenstate corresponding to a momentum of $-p$. That means, from the result of the momentum measurement on particle 1 we could with certainty predict the outcome of a momentum measurement performed on particle 2. The momentum $-p$ of particle 2 must be an element of reality.

On the other hand, the experimenter could choose to measure the *position* of particle 1. If the outcome were x, the state of particle 2 would be projected onto a position eigenstate corresponding to the eigenvalue $x + x_0$. That means we could with certainty predict a position measurement on particle 2 to yield the result $x + x_0$. Its position is an element of reality.

Depending on the choice of the experimenter either the momentum or the position of particle 2 would be an element of reality. Due to the locality assumption the outcomes of measurements on particle 2 cannot depend on the outcomes of measurements or even the choice of measurements on particle 1. Therefore, so EPR, both position and momentum must be elements of reality. According to quantum mechanics these are non-commuting observables and cannot simultaneously be known to arbitrary precision. There cannot be
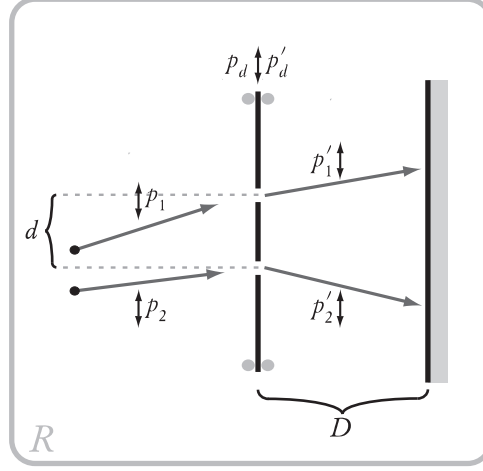
Figure 1.2.: Bohr's Gedankenexperiment to refute the EPR argument. Two particles with well known transverse momenta p_1 and p_2 with respect to the frame of reference, R, impinge on a diaphragm with two slits, which are separated by a distance d. In order for us to be able to measure its momentum the diaphragm can move relative to the reference frame R. Its momentum before the particles pass through it is p_d, after the particles pass through it is p_d'. For Bohr's argument to work the distance D between diaphragm and detection screen has to be small, while d can be large.

counterparts for both of these elements of reality in quantum theory. Quantum theory must be incomplete.

Bohr's answer

Bohr's answer [22] does not only discuss EPR's gedankenexperiment but engages in a more general discussion on the complementarity of non-commuting observables. For the purposes of this thesis it is enough to concentrate on the points, which demonstrate where EPR's argumentation fails [5].

To refute EPR's argumentation Bohr comes up with a simple (hypothetical) experimental arrangement to prepare particles in a state similar to the one used by EPR. Figure 1.2 gives an outline of this gedankenexperiment. The whole experiment happens in a frame of reference R, which could e.g. be an optical table. That means also that every measurement of position or momentum is performed relative to R.

Suppose we have two particles in momentum eigenstates [6] corresponding to momenta p_1

---

[5]To distill this information out of Bohr's paper is not a trivial task. The difficulty is to understand what he is actually talking about. As soon as that is accomplished, the line of his argumentation becomes clear.

[6]Throughout the argument, if I talk about momenta, I will mean the components of the momenta of the

and p_2. Each of them passes through one of the two slits of a diaphragm. These two slits should be separated by a distance d much larger than their width a [7]. The state in EPR's argumentation is reproduced in the limit $a \to 0$ and $D \to 0$.

Before the two particles pass the diaphragm we know their momenta and also their sum $P = p_1 + p_2$. Assume that we measure the momentum of the diaphragm before the passing of the particles and afterwards, and that the results are p_d and p_d', respectively. In order for us to be able to measure the momentum of the diaphragm means that it must not be rigidly connected with R.

According to the argumentation of EPR we can choose to measure either the position or the momentum of particle 1 without in any way "disturbing" particle 2 [8]. Let us first explain the gedankenexperiment according to the argumentation of EPR. Later I shall point out, based on Bohr's argumentation, where EPR's argumentation fails.

Suppose we measure the momentum p_1' of particle 1. In this case we can directly conclude, without *mechanically* disturbing particle 2, that its momentum p_2' must be given by:

$$p_2' = P - \left(p_d' - p_d \right) - p_1'. \tag{1.22}$$

That means, in EPR's terminology that p_2' will be an element of reality.

Now, let us suppose we choose to measure the position x_1 of particle 1 [9]. From this measurement we can, with certainty, calculate the position of particle 2 to be:

$$x_2 = x_1 - d. \tag{1.23}$$

That means it will be an element of reality. Because of the locality assumption the choice of the measurement, which is performed on particle 1, as well as its outcome cannot "disturb" particle 2. The position x_2 and p_2' must both be elements of reality.

Let us point out where the argument fails. If we measure p_1', there will be a corresponding uncertainty in the position of particle 1. That means at the same time that there will be an uncertainty in the position of the diaphragm. This is due to the fact that the position of particle 1 corresponds to the position of one of the slits of the diaphragm. Not knowing the position of particle 1 is equivalent to not knowing the position of the slit and the position of the diaphragm. In a similar way the position of particle 2 is equivalent to the position of the second slit of the diaphragm. It will be uncertain as well.

---

particles parallel to the diaphragm.

[7] Bohr does not take into account the limited velocity, with which the impuls transfer from a particle to the diaphragm travels within the diaphragm. Because this effect does not influence the validity of the argument, I am also going to neglect it.

[8] Here, "disturbance" is to be understood as *mechanical disturbance*, as Bohr puts it. It is a terminology resulting from the notion that a measurement of the position (or momentum) of a particle introduces an unknown change or disturbance in the momentum or (position) of the observed particle. This idea of disturbing a particle is a wide spread misconception used to "explain" the uncertainty relation.

[9] For the argument to work in case of the position measurement the measurement must be performed directly after the slits of the diaphragm. Otherwise, to infer the position of particle 2 from the position of particle 1 we would have to take into account the momentum of both particles.

On the other hand, if we measure the position of particle 1, the corresponding uncertainty of its momentum will be passed to the frame of reference, R. If the momentum of R is uncertain, so will be the momentum of the diaphragm and the same uncertainty will enter into any prediction of the momentum of particle 2.

Apart from the fact that this argumentation invalidates the argument of EPR the course of argumentation is the first of its kind in the history of quantum theory. Before Bohr's paper the uncertainty principle had always been related to a mechanical disturbance of the measured particle. Even in this paper Bohr often refers to an "uncontrollable displacement" or an "uncontrollable momentum" but these are not directly connected to a particle but rather to the frame of reference.

In accordance with EPR's locality assumption particle 2 is not influenced (or "disturbed") by the measurements on particle 1. But the information, which we have about particle 2, is directly dependent on our frame of reference and on the position and the momentum of the diaphragm. A measurement of particle 1 introduces uncertainty in the conclusions we can draw about the position and momentum of particle 2. This is essentially different from the concept of "mechanically disturbing" the particle because *the information, which we base our conclusions on, can change instantaneously*.

A simplified version of the EPR argument

We can repeat the EPR argument in a simpler form by using a polarization entangled state instead of the state in equation 1.21. In this form the EPR argument itself as well as the explanation of its failure becomes clearer.

Suppose we have two photons in the state

$$|\psi^-\rangle = \frac{1}{\sqrt{2}}(|HV\rangle - |VH\rangle) = \frac{1}{\sqrt{2}}(|+-\rangle - |-+\rangle),\tag{1.24}$$

where $|\pm\rangle = \frac{1}{2}(|H\rangle \pm |V\rangle)$. If the experimenter chooses to measure particle 1 in the HV basis, the state of particle 2 will be projected onto $|H\rangle$ or $|V\rangle$ accordingly. On the other hand, if the experimenter chooses to measure particle 1 in the $\pm$ basis, particle 2 will be projected onto $|\pm\rangle$.

Because of Einstein locality the choice of the measurement performed on particle 1 cannot influence particle 2. But, depending on the choice of measurement of the experimenter, either a state of the HV basis or of the complementary $\pm$ basis could be predicted with certainty for particle 2 once particle 1 has been measured. Both of these complementary states must, according to EPR, correspond to elements of reality.

To refute this argument is simple. It is true that the state of particle 2 is projected on either H, V or $\pm$ - but only for somebody who knows the outcome of the measurement for particle 1. The state describes our knowledge about the particle and *not* a physical entity.

For somebody who does not know the outcome of the measurement on particle 1 particle

2 will be in a completely mixed state:

$$\rho = \frac{1}{2}\left(|H\rangle\langle H| + |V\rangle\langle V|\right) = \frac{1}{2}\left(|+\rangle\langle +| + |-\rangle\langle -|\right), \tag{1.25}$$

where I wrote ρ in two equivalent representations to signify that it does not matter, which basis particle 1 is measured in.

As soon as we know the choice of the measurement on particle 1 as well as its outcome, we can use this knowledge to adjust our measurement basis for particle 2 and only then we will be certain, what the measurement outcome will be.

When the EPR argument is presented in this form it becomes much clearer that the whole point of entangled states is that by measuring one subsystem we gain knowledge about the other subsystem. Only for someone who knows the measurement result for particle 1 the state of particle 2 will change. As long as we do not know the result [96], the measurement of particle 1 has no influence whatsoever on particle 2. This should make it clear that the resolution of the EPR "paradox" does neither require a "spooky interaction at a distance" [10] nor "quantum non-locality" [11].

1.5.2. Realistic and local-realistic hidden-variable models

Especially during the early years of quantum theory many physicists tried to hold on to their classical view of reality, which physics should describe. It was ascribed to Nils Bohr [97] to have said that

> *"It is wrong to think that the task of physics is to find out how nature is. Physics concerns what we can say about nature."*

Although the EPR argument had been refuted by Bohr (see above) the possibility of a realistic theory, which could reproduce quantum predictions, had not been ruled out.

In such a theory measurement outcomes would be determined by elements of reality. Because the variables in the theory, which correspond to these elements of reality, could, in principle, be inaccessible for measurements, they are called *hidden* variables (HV) [12].

Suppose a given measurement is described by projectors $P_b(a)$, where a is a parameter defining the measurement, and b denotes the measurement outcome. If the system, which we want to measure, was in the state $|\psi\rangle$, quantum theory would predict the expectation value:

$$E_{QM}(a) = \sum_{b=1}^{N} C_b \langle \psi | P_b(a) | \psi \rangle, \tag{1.26}$$

---

[10]This expression is part of a remark by A. Einstein, which he seems to have made in his correspondence with M. Born. I cite it based on [88].

[11]Especially the term "quantum non-locality" often occurs even in scientific works about entanglement. If one does not try to uphold classical principles of naive realism, it is unnecessary to speak of non-locality.

[12]I will often use the abbreviation for a polarization measurement basis. The meaning of the abbreviation should be obvious from the context, in which it occurs.

where N is the number of possible measurement outcomes and C_b is the value assigned to measurement outcome b [13].

An HV model ascribes a set λ of hidden variables to the system, which determine the measurement outcome. According to quantum theory the outcome of a particular measurement will only be deterministic if the system measured is in an eigenstate of the observable. Otherwise it will be objectively random. In an HV model this randomness is due to the fact that we do not know the hidden variables associated with the system measured. Over many measurements the hidden variables of the measured systems will be distributed according to some probability distribution $\rho(\lambda)$ over the space Γ of hidden variables, where

$$\int_\Gamma d\lambda \rho(\lambda) = 1. \tag{1.27}$$

The expectation value according to HV models will be an average over the results for the various hidden variables weighted by the probability density:

$$E_{HV}(a) = \int_\Gamma d\lambda \, \rho(\lambda) C(a, \lambda), \tag{1.28}$$

where C is a function that yields the measurement outcome depending on the experimental parameter a and λ.

Because we want the HV model to reproduce quantum predictions, the expectation values resulting from quantum theory and the HV model must be the same for all measurements we could perform. Von Neumann [126] claimed to have proved that such an HV model of quantum theory is impossible in general. Unfortunately, his conclusion was based on the unphysical assumption that the expectation values for any two observables must be additive. Non-commuting observables cannot be measured simultaneously, and it does not make sense to talk about the expectation value with respect to a linear combination of such operators (see [8]). Apart from this argument von Neumann's statement was disproved by a direct counter example given by Bohm [19, 20]. He came up with an inherently non-local hidden-variable model, which seems, up to now, to be able to reproduce all predictions of non-relativistic quantum mechanics.

The non-locality in Bohm's theory manifests itself clearly when it is applied to entangled particles. For instance, if we consider the state used by EPR (see equ. 1.21), a measurement on particle 1 and also the outcome of that measurement directly and instantaneously influence the trajectory of particle 2. As Bell states it [8]:

> *"In fact the Einstein-Podolsky-Rosen paradox is resolved in the way which Einstein would have liked least."*

---

[13] For $N = 2$ we could, for instance, choose $C_1 = +1$ and $C_2 = -1$.

1.5.3. Bell's theorem

From this point Bell set out to see if there could be any further impossibility proofs against hidden-variable theories. Because it is a central element in our second experiment, I will reproduce his line of argumentation.

To this end he investigated an important subclass of hidden-variable theories, which fulfill Einstein's locality condition. They are called *local hidden-variable theories* (LHV). In his 1964 paper [7] he examines two spin one-half particles, which are in the spin singlet state

$$|\psi^-\rangle = \frac{1}{2}(|\uparrow\downarrow\rangle - |\downarrow\uparrow\rangle), \tag{1.29}$$

where $|\uparrow\rangle$ ($|\downarrow\rangle$) denotes the eigenstate of σ_z with eigenvalue $+1$ (-1).

Suppose we measure the spin of particle 1 along the direction given by a unit vector $\mathbf{a}$ and particle 2 along the direction given by a unit vector $\mathbf{b}$. On both sides the measurements will give results ± 1 but what we are interested in is the product of the two results. For this product quantum theory predicts the expectation value

$$E_{QM}(\mathbf{a}, \mathbf{b}) = \langle \psi^- | \vec{\sigma}_1 \cdot \mathbf{a} \otimes \vec{\sigma}_2 \cdot \mathbf{b} | \psi^- \rangle = -\mathbf{a} \cdot \mathbf{b}, \tag{1.30}$$

where $\vec{\sigma} = \left(\sigma_x, \sigma_y, \sigma_z \right)^T$ denotes the vector of Pauli matrices (see equ. 1.16) and the indices $1, 2$ denote the subsystems they apply to.

If we suppose that the Bloch angle ϕ is zero for $\mathbf{a}$ and $\mathbf{b}$ (see equ. 1.18), the expectation value will simplify to

$$E_{QM}(\mathbf{a}, \mathbf{b}) = -\cos\left[2(\theta_\mathbf{a} - \theta_\mathbf{b})\right]. \tag{1.31}$$

On the other hand, an LHV theory will predict the expectation value

$$E_{LHV}(\mathbf{a}, \mathbf{b}) = \int_\Gamma d\lambda \, \rho(\lambda) A(\lambda, \mathbf{a}) B(\lambda, \mathbf{b}). \tag{1.32}$$

Here, I introduced

$$A(\lambda, \mathbf{a}) = \pm 1, \; B(\lambda, \mathbf{b}) = \pm 1, \tag{1.33}$$

where A (B) is the result of the spin measurement on particle 1 (2). These functions can only depend on the hidden variables λ and on the experimental parameters $\mathbf{a}$ and $\mathbf{b}$. Due to Einstein locality the outcome for particle 1 can neither depend on the measurement setting $\mathbf{b}$ for particle 2 nor on the outcome of that measurement. The same is true the other way round.

For the HV model to reproduce quantum predictions it must first of all reproduce following perfect correlations:

$$\begin{aligned} E_{LHV}(\mathbf{a}, \mathbf{a}) &= E_{QM}(\mathbf{a}, \mathbf{a}) = -1 \\ E_{LHV}(\mathbf{a}, -\mathbf{a}) &= E_{QM}(\mathbf{a}, -\mathbf{a}) = +1 \\ E_{LHV}(\mathbf{a}, \mathbf{a}^\perp) &= E_{QM}(\mathbf{a}, \mathbf{a}^\perp) = 0. \end{aligned} \tag{1.34}$$

Because $\rho(\lambda)$ is positive and normalized (see equation (1.27)) the first of these perfect correlations can only be fulfilled if $A(\lambda, \mathfrak{a}) = -B(\lambda, \mathfrak{a})$. It follows that

$$E_{LHV}(\mathfrak{a}, \mathfrak{b}) = -\int_\Gamma d\lambda \, A(\lambda, \mathfrak{a}) A(\lambda, \mathfrak{b}). \qquad (1.35)$$

Now Bell performs the step that will lead to the contradiction between LHV models and quantum theory. In the case of LHV models λ holds all the information needed to predict various measurement results, i.e. A allows us to predict what the measurement outcome *would have been* if we had measured something else. For instance we could have measured the spin of particle 2 along the direction defined by a unit vector c different from b. The difference between the expectation values for these two cases is given by

$$
\begin{aligned}
E_{LHV}(\mathfrak{a}, \mathfrak{b}) - E_{LHV}(\mathfrak{a}, \mathfrak{c}) &= -\int_\Gamma d\lambda \, \rho(\lambda) \left[A(\lambda, \mathfrak{a}) A(\lambda, \mathfrak{b}) - A(\lambda, \mathfrak{a}) A(\lambda, \mathfrak{c}) \right] \\
&= \int_\Gamma d\lambda \, \rho(\lambda) A(\lambda, \mathfrak{a}) A(\lambda, \mathfrak{b}) \left[A(\lambda, \mathfrak{b}) A(\lambda, \mathfrak{c}) - 1 \right], \quad (1.36)
\end{aligned}
$$

where I used the fact that $A^2(\lambda, \mathfrak{a}) = 1$ and $B^2(\lambda, \mathfrak{b}) = 1$ (see equation 1.33).

Using the triangle inequality [14] it follows that

$$|E_{LHV}(\mathfrak{a}, \mathfrak{b}) - E_{LHV}(\mathfrak{a}, \mathfrak{c})| \leq \int_\Gamma d\lambda \, \rho(\lambda) |A(\lambda, \mathfrak{b}) A(\lambda, \mathfrak{c}) - 1| = 1 + E_{LHV}(\mathfrak{b}, \mathfrak{c}). \qquad (1.37)$$

Because $A(\lambda, \mathfrak{b}) A(\lambda, \mathfrak{c}) - 1 \leq 0$ we have $|A(\lambda, \mathfrak{b}) A(\lambda, \mathfrak{c}) - 1| = 1 - A(\lambda, \mathfrak{b}) A(\lambda, \mathfrak{c})$ and:

$$|E_{LHV}(\mathfrak{a}, \mathfrak{b}) - E_{LHV}(\mathfrak{a}, \mathfrak{c})| \leq \int_\Gamma d\lambda \, \rho(\lambda) \left[1 - A(\lambda, \mathfrak{b}) A(\lambda, \mathfrak{c}) \right] = 1 + E_{LHV}(\mathfrak{b}, \mathfrak{c}). \qquad (1.38)$$

This inequality holds for *all* local hidden-variable models independent of the choice of $\mathfrak{a}$, $\mathfrak{b}$ and $\mathfrak{c}$. Quantum theory violates this inequality for the right choice of measurement settings. Suppose, for example, that we choose the unit vectors such that $\mathfrak{a} \cdot \mathfrak{c} = 0$ and $\mathfrak{a} \cdot \mathfrak{b} = \mathfrak{b} \cdot \mathfrak{c} = \frac{1}{\sqrt{2}}$, which is easily fulfilled. With these vectors and equ. 1.30 we get:

$$\left| E_{QM}(\mathfrak{a}, \mathfrak{b}) - E_{QM}(\mathfrak{a}, \mathfrak{c}) \right| = \frac{1}{\sqrt{2}} \nleq 1 - \frac{1}{\sqrt{2}} = 1 + E_{QM}(\mathfrak{b}, \mathfrak{c}), \qquad (1.39)$$

which is a clear violation of the inequality.

Unfortunately, the derivation of the inequality depends on the perfect correlations given in equ. 1.34. These require perfect measurement devices and a perfectly pure ψ^- state, both of them luxuries unavailable in experiments. How this problem can be resolved will be described in subsection 1.5.4.

---

[14]I.e. $|x + y| \leq |x| + |y|$.

Nevertheless, Bell's work was a break through. Before his theorem it was considered possible that an LHV model for quantum theory could be found. To discuss it seemed futile because it was seen as a question of interpretation, which could not possibly be decided by experiment.

While Bell's theorem did not, initially, present the possibility for experimental tests it proved that there was an essential difference in the predictions of LHV models and quantum theory. LHV models could no longer be seen as just another possible interpretation of quantum theory - they had become discernible theories. To decide whether such theories could exist it was important to devise a method to perform an experimentum crucis.

1.5.4. The CHSH inequality

In 1969 Clauser, Horne, Shimony and Holt [36] (CHSH) derived the first inequality based on Bell's theorem, which was applicable for experimental tests. The original derivation of the inequality is very similar to the derivation of Bell's inequality. The essential difference is that it does not depend on perfect correlations.

Deriving the inequality

CHSH show that from the definition of $E_{LHV}(\mathfrak{a}, \mathfrak{b})$ and the triangle inequality it follows that:

$$
\begin{aligned}
|E_{LHV}(\mathfrak{a}_1, \mathfrak{b}_1) - E_{LHV}(\mathfrak{a}_1, \mathfrak{b}_2)| &\leq \int_\Gamma d\lambda\, \rho(\lambda) |A(\lambda, \mathfrak{a}_1) B(\lambda, \mathfrak{b}_1) - A(\lambda, \mathfrak{a}_1) B(\lambda, \mathfrak{b}_2)| \\
&= \int_\Gamma d\lambda\, \rho(\lambda) |A(\lambda, \mathfrak{a}_1) B(\lambda, \mathfrak{b}_1) [1 - B(\lambda, \mathfrak{b}_1) B(\lambda, \mathfrak{b}_2)]| \\
&= \int_\Gamma d\lambda\, \rho(\lambda) [1 - B(\lambda, \mathfrak{b}_1) B(\lambda, \mathfrak{b}_2)] \\
&= 1 - \int_\Gamma d\lambda\, \rho(\lambda) B(\lambda, \mathfrak{b}_1) B(\lambda, \mathfrak{b}_2). \tag{1.40}
\end{aligned}
$$

Then they introduce an additional measurement setting $\mathfrak{a}_2$ and divide Γ into two subspaces $\Gamma_\pm$, which are defined as

$$
\Gamma_\pm \equiv \{\lambda \,|\, A(\lambda, \mathfrak{a}_2) = \pm B(\lambda, \mathfrak{b}_1)\}. \tag{1.41}
$$

It follows that

$$
\begin{aligned}
E(\mathfrak{a}_2, \mathfrak{b}_1) &= \int_\Gamma d\lambda\, \rho(\lambda) A(\lambda, \mathfrak{a}_2) B(\lambda, \mathfrak{b}_1) = \int_{\Gamma_+} d\lambda\, \rho(\lambda) - \int_{\Gamma_-} d\lambda\, \rho(\lambda) = \\
&= \int_\Gamma d\lambda\, \rho(\lambda) - 2 \int_{\Gamma_-} d\lambda\, \rho(\lambda) = 1 - \delta, \tag{1.42}
\end{aligned}
$$

where I defined $\delta \equiv 2 \int_{\Gamma_-} d\lambda\, \rho(\lambda)$.

With these definitions we get:

$$\int_{\Gamma} d\lambda \, \rho(\lambda) B(\lambda, \mathbf{b}_1) B(\lambda, \mathbf{b}_2) = \int_{\Gamma_+} d\lambda \, \rho(\lambda) A(\lambda, \mathbf{a}_2) B(\lambda, \mathbf{b}_2) - \int_{\Gamma_-} d\lambda \, \rho(\lambda) A(\lambda, \mathbf{a}_2) B(\lambda, \mathbf{b}_2)$$
$$= \int_{\Gamma} d\lambda \, \rho(\lambda) A(\lambda, \mathbf{a}_2) B(\lambda, \mathbf{b}_2) - 2 \int_{\Gamma_-} d\lambda \, \rho(\lambda) A(\lambda, \mathbf{a}_2) B(\lambda, \mathbf{b}_2)$$
$$\geq E_{LHV}(\mathbf{a}_2, \mathbf{b}_2) - 2 \int_{\Gamma_-} d\lambda \, \rho(\lambda) |A(\lambda, \mathbf{a}_2) B(\lambda, \mathbf{b}_2)| = E_{LHV}(\mathbf{a}_2, \mathbf{b}_2) - \delta,$$

(1.43)

where I used the simple inequality $x - y \geq x - |y|$.

By inserting 1.43 in 1.40 and by using the relation 1.42, we get:

$$|E_{LHV}(\mathbf{a}_1, \mathbf{b}_1) - E_{LHV}(\mathbf{a}_1, \mathbf{b}_2)| \leq 1 - \int_{\Gamma} d\lambda \, \rho(\lambda) B(\lambda, \mathbf{b}_1) B(\lambda, \mathbf{b}_2)$$
$$\leq 1 + \delta - E_{LHV}(\mathbf{a}_2, \mathbf{b}_2) = 2 - E_{LHV}(\mathbf{a}_2, \mathbf{b}_1) - E_{LHV}(\mathbf{a}_2, \mathbf{b}_2).$$

(1.44)

This is the original form of the CHSH inequality:

$$|E_{LHV}(\mathbf{a}_1, \mathbf{b}_1) - E_{LHV}(\mathbf{a}_1, \mathbf{b}_2)| \leq 2 - E_{LHV}(\mathbf{a}_2, \mathbf{b}_1) - E_{LHV}(\mathbf{a}_2, \mathbf{b}_2).$$

(1.45)

It is possible [140] to derive this inequality in a much simpler way [15]. From equ. 1.33 it follows that:

$$A(\lambda, \mathbf{a}_1) [B(\lambda, \mathbf{b}_1) + B(\lambda, \mathbf{b}_2)] + A(\lambda, \mathbf{a}_2) [B(\lambda, \mathbf{b}_1) - B(\lambda, \mathbf{b}_2)] = \pm 2.$$

(1.46)

By averaging this equation over many measurements we get

$$-2 \leq E(\mathbf{a}_1, \mathbf{b}_1) + E(\mathbf{a}_1, \mathbf{b}_2) + E(\mathbf{a}_2, \mathbf{b}_1) - E(\mathbf{a}_2, \mathbf{b}_2) \leq +2,$$

(1.47)

or, by taking the modulus:

$$|E_{LHV}(\mathbf{a}_1, \mathbf{b}_1) + E_{LHV}(\mathbf{a}_1, \mathbf{b}_2) + E_{LHV}(\mathbf{a}_2, \mathbf{b}_1) - E_{LHV}(\mathbf{a}_2, \mathbf{b}_2)| \leq 2.$$

(1.48)

It is important to note that equation 1.46 is only one possibility how we could combine the various measurement outcomes. If we chose other signs in a way that fulfilled the equation, we would have arrived at a slightly different inequality. Which inequality is suited best depends on the entangled state and on the measurement settings.

Suppose we choose our measurement settings such that $\mathbf{a}_1 \cdot \mathbf{a}_2 = \mathbf{b}_1 \cdot \mathbf{b}_2 = 0$ and $\mathbf{a}_1 \cdot \mathbf{b}_1 = \mathbf{a}_2 \cdot \mathbf{b}_2 = \mathbf{a}_2 \cdot \mathbf{b}_1 = \frac{1}{\sqrt{2}}, \mathbf{a}_1 \cdot \mathbf{b}_2 = -\frac{1}{\sqrt{2}}$. This is usually achieved with the following Bloch angles (see equ. 1.18):

$$\phi_{\mathbf{a}_1} = \phi_{\mathbf{a}_2} = \phi_{\mathbf{b}_1} = \phi_{\mathbf{b}_2} = 0$$
$$\theta_{\mathbf{a}_1} = 0, \theta_{\mathbf{a}_2} = \frac{\pi}{4}$$
$$\theta_{\mathbf{b}_1} = \frac{\pi}{8}, \theta \theta_{\mathbf{b}_2} = \frac{3\pi}{8}.$$

(1.49)

---

[15]This simplified version of the derivations for two qubits was presented to me in a lecture by Marek Żukowski.

Let us assume that our state is ψ^-, i.e. $E_{QM}(\mathbf{a}, \mathbf{b}) = -\mathbf{a} \cdot \mathbf{b}$. With this state and the settings given above we will maximally violate the CHSH inequality by combining the expectation values in the following way:

$$\left| E_{QM}(\mathbf{a}_1, \mathbf{b}_1) - E_{QM}(\mathbf{a}_1, \mathbf{b}_2) + E_{QM}(\mathbf{a}_2, \mathbf{b}_1) + E_{QM}(\mathbf{a}_2, \mathbf{b}_2) \right| = 2\sqrt{2}. \tag{1.50}$$

As an alternative let us suppose that the state of our two particles is

$$|\psi^+\rangle = \frac{1}{\sqrt{2}} (|\uparrow\downarrow\rangle + |\downarrow\uparrow\rangle). \tag{1.51}$$

The expectation becomes $E_{QM}(\mathbf{a}, \mathbf{b}) = a_1 b_1 + a_2 b_2 - a_3 b_3$. Because the Bloch angle ϕ is zero for all our measurement settings, the expectation value will simplify to

$$E_{QM}(\mathbf{a}, \mathbf{b}) = -\cos\left[2(\theta_\mathbf{a} + \theta_\mathbf{b})\right]. \tag{1.52}$$

We will maximally violate the CHSH inequality by combining the expectation values in the following way:

$$\left| -E_{QM}(\mathbf{a}_1, \mathbf{b}_1) + E_{QM}(\mathbf{a}_1, \mathbf{b}_2) + E_{QM}(\mathbf{a}_2, \mathbf{b}_1) + E_{QM}(\mathbf{a}_2, \mathbf{b}_2) \right| = 2\sqrt{2}. \tag{1.53}$$

The minimum entanglement visibility for violation of the CHSH inequality

In an experiment the states, which are used to violate CHSH inequality are in general imperfect. If the entanglement of the states is low enough, they will not even violate the inequality. Let us assume having a source, which is intended to produce ψ^- states, and that they are mixed with white noise due to experimental imperfections. The two-particle states can then be described by Werner states [131], which I write in the form:

$$\rho_W = \frac{(1-V)}{4} \mathfrak{I}^{(4)} + V|\psi^-\rangle\langle\psi^-|, \tag{1.54}$$

where we use $\mathfrak{I}^{(N)}$ to denote the $N \times N$ identity matrix. In an experiment, which employs SPDC to generate the entangled states, the noise will in general not be white [30]. Nevertheless, Werner states are often used as a convenient approximation, where V is defined by the visibility of the correlations of polarization measurements in the 45° basis. This technique allows a rough estimation of the entanglement of a state if the noise is not too far from being white.

A Werner state is non-separable for $V > \frac{1}{3}$ [13] but V must be higher in order to violate the CHSH inequality. The expectation value for a Werner state of the product of the outcomes of polarization measurements $\mathbf{a}$ and $\mathbf{b}$ on the two particles is

$$E_{QM}(\mathbf{a}, \mathbf{b}; V) = -V\mathbf{a}.\mathbf{b}. \tag{1.55}$$

For $V = 1$ this corresponds to the expectation value for a ψ^- state, i.e. $E_{QM}(\mathfrak{a}, \mathfrak{b}; 1) = E_{QM}(\mathfrak{a}, \mathfrak{b})$. If we employ this in the CHSH inequality for the optimal setting, which I defined above, we get:

$$
\begin{aligned}
S &= \left| E_{QM}(\mathfrak{a}_1, \mathfrak{b}_1, V) - E_{QM}(\mathfrak{a}_1, \mathfrak{b}_2, V) + E_{QM}(\mathfrak{a}_2, \mathfrak{b}_1, V) + E_{QM}(\mathfrak{a}_2, \mathfrak{b}_2, V) \right| = \\
&\quad V \left| E_{QM}(\mathfrak{a}_1, \mathfrak{b}_1) - E_{QM}(\mathfrak{a}_1, \mathfrak{b}_2) + E_{QM}(\mathfrak{a}_2, \mathfrak{b}_1) + E_{QM}(\mathfrak{a}_2, \mathfrak{b}_2) \right| = 2\sqrt{2}V. \quad (1.56)
\end{aligned}
$$

To violate CHSH inequality this has to be greater than 2, i.e. the correlation visibility V in the 45° basis must fulfill $V > \frac{1}{\sqrt{2}}$.

1.5.5. Loopholes in experiments testing Bell's theorem

In the works, which I reviewed in the last subsections, a clear discrepancy between the theoretical predictions of quantum theory and LHV models has been shown. The CHSH inequality [16] in principle allows for an experimental test to decide between quantum theoretical predictions and those of LHV models. Because of experimental imperfections it is difficult to perform such a test without any additional assumptions. These are usually assumptions, which should be fulfilled by any sensible physical theory. But still, they do not necessarily have to be fulfilled by every LHV model. That means some of them might slip through these *loopholes* in experimental tests of the Bell theorem. Because the aim of such tests in general is to rule out *all* possible LHV models, it is important to consider possibilities to close those loopholes.

The locality loophole

In the derivation of the Bell theorem and the CHSH inequality it is assumed that A depends only on the measurement setting $\mathfrak{a}$ and that B depends only on the measurement setting $\mathfrak{b}$. For the violation of the CHSH inequality we have two settings for the measurements on each of the particles. Suppose now that the event of choosing and implementing either setting $\mathfrak{a}_1$ or $\mathfrak{a}_2$ was *not* space-like separated from the event of measuring particle 2. In this case the hidden variables λ, which determine the outcome of that measurement, might in principle depend on the chosen setting $\mathfrak{a}_1$ or $\mathfrak{a}_2$. Although we do not know of any interaction, which would allow that dependence, we cannot rule it out in principle. If we performed an experiment violating a Bell-type inequality without assuring the space-like separation of these events, we would have to assume that there cannot be any such dependence. The possibility that this assumption is wrong is called the *locality loophole*.

A first step to close this loophole was an experiment by Aspect et al. [4] where the measurement settings were changed over time. All previous experiments had used static settings [47, 34, 48, 5, 6]. The switching process in [4] between the measurement setting

---

[16]After the CHSH inequality had been derived other Bell-type inequalities were derived, which are also apt for experimental tests. In the present work I only use the CHSH inequality, and I am not going into details about other inequalities.

was periodic. Because of the specific periodicity in this experiment a dependence of a measurement result on the predictable measurement setting on the distant other side cannot be ruled out [137]. The experiment by Weihs et al. [130] ruled out even that possibility by switching the measurement settings unpredictably random and under strict Einstein locality conditions. That means the whole measurement processes including the choices of the measurement settings at the sites of the two observers involved were space-like separated.

There remains a (very remote) possibility to circumvent the conclusion that the experiment of Weihs et al. closed the locality loophole. The choice of the measurement setting in [130] was determined via a quantum random-number generator. This device produces an output of 0 or 1 depending on which output port of a 50:50 beam splitter, a single photon is detected in. The remaining loophole is that the outcomes of the measurements of these single photons might depend on the same λ as the measurements for the violation of the Bell-type inequality. In other words some unknown mechanism would allow the source of photon pairs to influence the outcome of the measurement processes in the random-number generator, which determine the measurement setting for the Bell experiment.

To rule out this possibility, which would come uncomfortably close to some conspiracy of nature against experiments (see also [9]), it has been proposed (see e.g. [130, 66]) that the measurement settings are chosen by humans, who are separated far enough (by at least some light seconds) to satisfy Einstein locality conditions. There, the randomness would be guaranteed by the free will of the experimenters.

The detection loophole

In experiments we usually have to cope with finite detection efficiencies. Not all of the entangled photons produced will be detected. In some cases, none of the two will be detected, in other cases only one of them. If we perform an experiment to violate a Bell-type inequality, the violation might, in principle, be due to a dependence of the detection efficiency on the measurement settings and/or on the hidden variables. In most experimental tests of the CHSH inequality only coincidence detection events are taken into account. It is assumed that the detection probability is independent of the measurement settings and that the measured sub ensemble is also representative for those particles, which have not been detected. This is called the *fair-sampling assumption* [17]. If this assumption were wrong, it would be possible to construct LHV models [95]., for which the detected sub ensemble would violate the CHSH inequality although the overall ensemble would fulfill it. Such models would be consistent with the results of many experimental tests of the CHSH inequality. This possibility is known as the *detection loophole*.

In 2001 the detection loophole was closed by an experiment violating the CHSH inequality with entangled ions [103]. They did not need to assume fair sampling because their results included the entire and not only a sub ensemble of events. But their experiment did

---

[17]Clauser and Horne derived an inequality [35], which does not rely on the fair-sampling hypothesis. To violate it experimentally it is necessary to use highly efficient detectors.

not close the locality loophole. An "ultimate Bell" experiment would simultaneously close all loopholes to finally rule out every possible LHV model.

1.5.6. Possible advantages for independent sources

Recently, there have been attempts to use independent sources in order to impose further restrictions on LHV models [55, 56]. These arguments were based on the fact that the sets of local hidden variables of two independently generated entangled pairs must also be independent. This additional restriction to LHV models seemed to allow closing the detection loophole even with inefficient detectors.

Unfortunately, the derivation of the contradiction for LHV models is not yet conclusive. The idea of the independence of the hidden variable sets is intriguing nonetheless, and it could prove useful in the future to derive even stronger contradictions between quantum theory and (local) realistic theories.

1.6. Quantum communication schemes

Quantum communication by now encompasses a large range of different communication schemes, which provide various advantages over comparable classical schemes of communication. Well known examples are quantum cryptography [132, 11, 44, 51], dense coding [14, 86], quantum teleportation [12, 24] and entanglement swapping [141, 92, 63, 64]. For the purpose of the presented work only the last two of them are of interest. Entanglement swapping because we want to demonstrate it in our experiment and quantum teleportation because it is the principle behind entanglement swapping.

1.6.1. Quantum state teleportation

The essence of communication is the reliable transmission of information from one communication party to another. For classically encoded information this can be achieved even over noisy channels via signal amplification and/or appropriate encoding.

In the case of quantum states the possibility of amplification is not applicable due to the no-cloning theorem. Only if the information is actually encoded classically (i.e. a classical mixture of known orthogonal states), it will be possible to amplify it. In all other cases, i.e. if the states to be transmitted are unknown or if they are a mixture of non-orthogonal states, amplification will lead to noisy or even illegible results.

As the qubit is a fundamental ingredient for all quantum communication and computation processes, it is essential to faithfully transmit qubits between separate communication parties. Solutions to this problem are the encoding of the qubit in decoherence-free subspaces [136, 80] or quantum error correction [115, 116, 31, 76]. Another possibility is the teleportation [12] of the qubit, because this way the qubit does not have to pass through a possibly noisy channel. The only prerequisite is the presence of a maximally entangled pair

shared between the two communication parties, which shall be called Alice (the sender) and Bob (the receiver).

Let us assume that Alice wants to teleport the state

$$|\chi\rangle_1 = \alpha|0\rangle_1 + \beta|1\rangle_1 \qquad (1.57)$$

of particle 1 to Bob. Both of them share a pair of particles 2 and 3, which are in the maximally entangled state $|\psi^-\rangle_{23}$. We encountered this state and also $|\psi^+\rangle$ before. They are two of the four *Bell states*:

$$\begin{aligned} |\psi^\pm\rangle &= \tfrac{1}{\sqrt{2}}(|01\rangle \pm |10\rangle) \\ |\phi^\pm\rangle &= \tfrac{1}{\sqrt{2}}(|00\rangle \pm |11\rangle). \end{aligned} \qquad (1.58)$$

The Bell states form a basis of the 4×4 Hilbert space. They fulfill the completeness relation:

$$\mathfrak{I}^{(4)} = \left(|\psi^-\rangle\langle\psi^-| + |\psi^+\rangle\langle\psi^+| + |\phi^-\rangle\langle\phi^-| + |\phi^+\rangle\langle\phi^+|\right), \qquad (1.59)$$

where $\mathfrak{I}^{(m)}$ denotes the $m \times m$ identity matrix. By using this relation we can write the overall state of the three particles involved as [12]:

$$\begin{aligned} |\Psi\rangle &= |\chi\rangle_1 \otimes |\psi^-\rangle_{23} \\ &= \frac{1}{\sqrt{2}} \mathfrak{I}^{(4)}_{12} \left[\alpha|001\rangle - \alpha|010\rangle + \beta|101\rangle - \beta|110\rangle\right] \\ &= \frac{1}{2} \big[\alpha|\phi^+\rangle_{12}|1\rangle_3 + \alpha|\phi^-\rangle_{12}|1\rangle_3 - \alpha|\psi^+\rangle_{12}|0\rangle_3 - \alpha|\psi^-\rangle_{12}|0\rangle_3 \\ &\quad + \beta|\psi^+\rangle_{12}|1\rangle_3 - \beta|\psi^-\rangle_{12}|1\rangle_3 - \beta|\phi^+\rangle_{12}|0\rangle_3 + \beta|\phi^-\rangle_{12}|0\rangle_3\big] \\ &= \frac{1}{2}\big[|\phi^+\rangle_{12}(-\beta|0\rangle_3 + \alpha|1\rangle_3) + |\phi^-\rangle_{12}(\beta|0\rangle_3 + \alpha|1\rangle_3) \\ &\quad + |\psi^+\rangle_{12}(-\alpha|0\rangle_3 + \beta|1\rangle_3) + |\psi^-\rangle_{12}(-\alpha|0\rangle_3 - \beta|1\rangle_3)\big]. \qquad (1.60) \end{aligned}$$

Now let Alice project particles 1 and 2 on the Bell-state basis. This two-particle measurement is called *Bell-state measurement* (BSM). In this case she will get any of the four Bell states with equal probability $\frac{1}{4}$. Depending on which outcome she gets, particle 3 will be in one of the following states according to the equation above (I neglect global phases):

$$\begin{aligned} \psi^- &\Rightarrow \alpha|0\rangle_3 + \beta|1\rangle_3 = U_3^{(1)}|\chi\rangle_3 \\ \psi^+ &\Rightarrow \alpha|0\rangle_3 - \beta|1\rangle_3 = U_3^{(2)}|\chi\rangle_3 \\ \phi^- &\Rightarrow \beta|0\rangle_3 + \alpha|1\rangle_3 = U_3^{(3)}|\chi\rangle_3 \\ \phi^+ &\Rightarrow \beta|0\rangle_3 - \alpha|1\rangle_3 = U_3^{(4)}|\chi\rangle_3, \end{aligned} \qquad (1.61)$$

where I introduced the unitary transformations

$$U^{(1)} = \begin{pmatrix} 1 & 0 \\ 0 & 1 \end{pmatrix} \quad U^{(2)} = \begin{pmatrix} 1 & 0 \\ 0 & -1 \end{pmatrix} \quad U^{(3)} = \begin{pmatrix} 0 & 1 \\ 1 & 0 \end{pmatrix} \quad U^{(4)} = \begin{pmatrix} 0 & -1 \\ 1 & 0 \end{pmatrix}. \qquad (1.62)$$

As long as Bob does not know the outcome of Alice's BSM, for him the state of particle 3 will be in a complete mixture:

$$\rho_B = \mathrm{Tr}\left(P_{12}^{BSM}|\psi\rangle\langle\psi|\right) = \sum_i \frac{1}{4} U_3^{(i)}|\chi\rangle_3\langle\chi|_3\left(U_3^{(i)}\right)^\dagger = \frac{1}{2}\mathfrak{I}_3^{(2)}, \tag{1.63}$$

where we used P_{12}^{BSM} to denote the projection operator on the Bell-state basis. Once Alice sends the BSM result, k, to Bob via a classical channel, he will be able to perform the correct inverse unitary transformation to transform the state of particle 3 into the original state:

$$|\chi\rangle_3 = \left(U_3^{(k)}\right)^{-1}\left(U_3^{(k)}|\chi\rangle_3\right). \tag{1.64}$$

It is important to realize that neither Alice nor Bob have to know anything about the state $|\chi\rangle$ to faithfully teleport it [12]. Note, that the state of the original qubit is destroyed during the BSM and that the outcome of the BSM is completely random. That means Alice gains no information about $|\chi\rangle$ during the teleportation process.

1.6.2. Entanglement swapping

A remarkable feature of quantum state teleportation is that the teleported qubit does not have to be in a well defined state. For instance particle 1 can be part of an arbitrarily large quantum system, which can even be entangled. If we perform teleportation on particle 1, essentially particle 3 will replace particle 1. The state of the larger quantum system will remain unchanged.

The most simple application is entanglement swapping. Suppose we have two pairs of maximally entangled qubits. One pair consists of particles 1 and 2, the other consists of particles 3 and 4. Now let us teleport the particle 2, such that particle 2 contains the qubit to be teleported and the BSM is performed on particles 2 and 3. If the teleportation succeeds (including the necessary unitary transformation), the states of particles 2 and 3 will be destroyed while particles 1 and 4 will be in the same state as particles 1 and 2 were before.

In our experiment we did not perform the inverse unitary transformation, which is necessary to restore the original state on Bob's side. Our aim was not to teleport a specific entangled state but we wanted to create entanglement between the independent particles 1 and 4. Which state they would be in, was secondary.

Our BSM was based on linear optics and could discern between ψ^+ and ψ^- (see 6.5.2). Depending on the outcome of the BSM the swapped state was given by (see equ. 1.61):

$$\begin{array}{lll} \text{outcome } \psi^- & \Rightarrow & U_4^{(1)}|\psi^-\rangle_{14} = |\psi^-\rangle_{14} \\ \text{outcome } \psi^+ & \Rightarrow & U_4^{(2)}|\psi^-\rangle_{14} = |\psi^+\rangle_{14} \end{array} \tag{1.65}$$

1.6.3. Quantum repeaters

If entanglement is to be used as a resource between distant nodes, it has to be faithfully distributed over that distance. This is a prerequisite for long distance quantum communication and large-scale quantum networks. Entanglement is very susceptible to noise and cannot be increased by classical communication and local operations acting only on parts of the entangled system [10, 123].

The absorption of the carriers of entanglement is another limiting factor. It results in a loss of the number of successfully transmitted pairs of entangled particles, which grows exponentially with the distance to be covered. This does not only result in a need for resources, which grow exponential with distance, but is also exponentially reduces the usefulness of the transmitted entanglement for quantum communication schemes [127].

Entanglement concentration [50, 10] and entanglement distillation (or purification) [13, 38] are methods to overcome the problem of deterioration of entanglement over long distances.

Entanglement distillation

Entanglement distillation is an integral part of quantum repeaters (see below). I will give a short description of the principles of this method, which allows to share highly entangled states over noisy channels.

Suppose that n pairs of entangled states with a density matrix ρ are distributed between two possibly distant parties, and that the entangled pairs initially were prepared in the singlet state ψ^-. The fidelity [113]

$$F = \langle \psi^- | \rho | \psi^- \rangle \tag{1.66}$$

of ρ with the initial state is a measure for the quality of the transmission. In [13] and [38] methods are presented to gain a number $m < n$ of states ρ' from the n original states ρ such that $F' = \langle \psi^- | \rho' | \psi^- \rangle > F$.

Both of these methods only need local operations and classical communication. Their central element is a bilateral controlled-NOT (CNOT) operation. A CNOT gate is a unitary two-qubit operation, which is defined by (see e.g. [90]):

$$\mathfrak{U}_{CNOT} = \begin{pmatrix} 1 & 0 & 0 & 0 \\ 0 & 1 & 0 & 0 \\ 0 & 0 & 0 & 1 \\ 0 & 0 & 1 & 0 \end{pmatrix}. \tag{1.67}$$

A bilateral CNOT means two CNOT operations, where the particles of one entangled pair are used as the control qubits, and the particles of a second entangled pair provide the target qubits (see fig. 1.3). After the bilateral CNOT operation the polarization of the target qubits is measured in the HV basis. The control qubits are kept if the outcomes of the polarization measurements are parallel. Otherwise they are discarded.
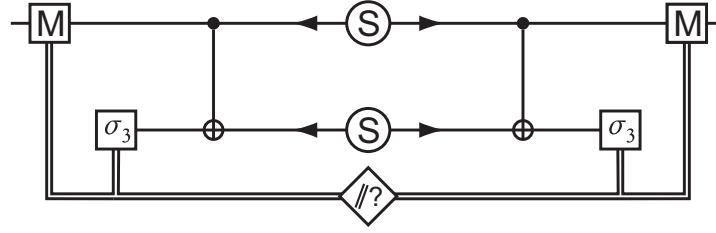
Figure 1.3.: A bilateral CNOT operation. Sources (S) emit two entangled pairs. Each of the members of one pair is employed as the control qubit in a CNOT operation. The members of the second pair provide the target qubits. After the operation, the states of the target qubits are measured in the HV basis (σ_3). If the outcomes are parallel, the control qubits are stored for further processing (M), otherwise they are discarded. Classical communication is denoted by double lines and the propagation of qubits by single lines.

The protocol introduced in [13] requires the states ρ either to be or to be made rotationally symmetric. The latter can be achieved by simultaneously applying rotations on both qubits of each pair. These rotations are chosen randomly for each pair. Then ρ can be written in the form of a Werner state (see subsection 1.5.4) with

$$V = \frac{4F-1}{3}. \tag{1.68}$$

These states are entangled if $V > \frac{1}{3}$ or, equivalently, if the fidelity F is greater than $\frac{1}{2}$. The distillation procedure itself is always performed on two entangled pairs and consists of the following three steps (see [13]):

1. a σ_2 rotation is performed on one particle of each pair. It exchanges ψ^- with ϕ^+.

2. the two pairs are passed through a bilateral CNOT (see fig. 1.3)

3. if the control pair is kept, a σ_2 rotation is performed on one of its particles to exchange ψ^- with ϕ^+ once more

If the initial states are entangled and have fidelity F, the fidelity F' of the distilled state will be greater than F. Depending on the initial fidelity and the fidelity desired this procedure might have to be reiterated several times. In this case, step 1 has to be performed once in the beginning and step 3 once in the end.

In [38] a similar protocol is introduced, which is not restricted to rotationally symmetric density matrices. Instead, the density matrix must be of the form:

$$\rho = A|\phi^+\rangle\langle\phi^+| + B|\psi^-\rangle\langle\psi^-| + C|\psi^+\rangle\langle\psi^+| + |\phi^-\rangle\langle\phi^-|. \tag{1.69}$$

The initial states are ϕ^+, the fidelity of ρ with these states is simply given by A. If $A > \frac{1}{2}$, repeated application of a bilateral CNOT will, in the limit, result in a maximally entangled state ϕ^+. This procedure converges faster [42] than the protocol of Bennett et al. [13].

In both of these distillation schemes the CNOT operations were assumed to operate without errors. If imperfect gate operations are allowed [42], the minimum fidelity F_{min} for successful entanglement distillation will be greater than $\frac{1}{2}$, and the maximum achievable fidelity F_{max} will be smaller than 1. As the error of the gates is increased, F_{min} will approach F_{max}, and they will become equal at some point. This point defines the upper limit for the gate errors where distillation is still possible. Above this threshold the errors introduced by the distillation procedure will reduce the entanglement rather than increasing it.

The repeater protocol

Because the fidelity of entanglement decreases with distance in the transmission over noisy channels, there is a limit to the distance, after which entanglement distillation can be successfully implemented. Losses, which grow exponentially with the distance, pose an additional problem. The quantum repeater protocol [25, 42] allows to overcome these limitations. It produces an overhead in time, which depends polynomially on the distance, and an overhead in resources, which grows only logarithmically with the distance.

Suppose we want to cover a distance L. We start by dividing it into smaller segments of length D such that the fidelity F_w of the pairs, which are distributed over each of these segments, fulfills $F_{min} < F_w < F_{max}$. Entanglement swapping [141] is employed to connect adjoining segments. Because $F_w < 1$, and because of imperfect gate operations, the fidelity of the swapped pairs will be even smaller. This limits the distance, which can be covered by entanglement swapping alone, such that the fidelity of the resulting pairs F_1 is still larger than F_{min}. At this point the pairs are stored for subsequent entanglement distillation. The distillation protocol is repeated until the fidelity of the distilled pairs becomes greater or equal to F_w. This fidelity, F_w, is called the *working fidelity* of the quantum repeater (see fig. 1.4). From this point on the repeater protocol can be reiterated.

The distillation protocols, which were introduced in [13] and [38], in each step perform a bilateral CNOT on the pairs resulting from the preceding step (see fig. 1.5). The advantage of this method is that a fidelity arbitrarily close to 1 can be reached if the CNOT gates work without errors. The disadvantage is that this method needs a high number of resources. In each step a large part of the entanglement resources is lost because at least the target pair is always destroyed during the measurement. But this pair is a result of all preceding distillation steps. That means by discarding a target pair, one also throws away all the pairs, which were needed to distill it in the first place.

Duer et al. [42] proposed a method, where only the control pairs are distilled, while the target pair is taken from a reservoir of ancilla pairs of some constant fidelity F_a (see fig. 1.6). With this method F_{max} is smaller than 1 even if the gates work without errors. For imperfect gates this limitation is not so important because the other methods are also limited to a maximal fidelity smaller than 1. In fact, if the gate operations are imperfect,

F_{max} can be even higher with this method than with the others. The huge advantage is that it significantly reduces the overhead in the resources needed for entanglement distillation. On the other hand, though, the time required for distillation is higher with this method than with the others [42].

We have seen that entanglement swapping and distillation are the central elements of a quantum repeater. For a practical implementation it is also necessary to store quantum states for further processing. Huge experimental progress has been made in the realization of quantum memories [85, 65, 18, 124, 29] and entanglement distillation [93, 128]. Proof of principle experiments were performed on entanglement swapping [92, 64, 135]. Any practical implementation of a quantum repeater necessitates entanglement swapping with pairs originating from independent nodes (one for each of the segments of length D). None of the experiments mentioned demonstrated the effect under these conditions. That demonstration was the aim of the present thesis [18].

---

[18]While the author wrote this thesis, a related work with independent sources was reported [59]. Although they could not violate a Bell-type inequality, the visibility of the correlations between measurements on the two particles showed the non-separability of the swapped states.
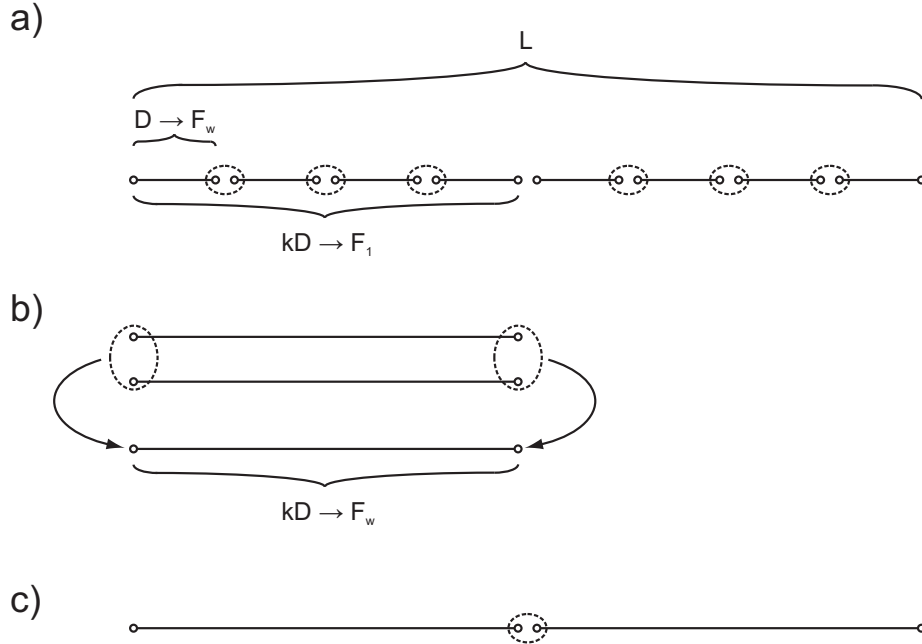
Figure 1.4.: Quantum repeater protocol. **(a)** We want to distribute entanglement over a distance L. To this end we divide that distance into smaller segments D, which entanglement can be distributed over with a *working fidelity F_w*. Entanglement swapping is employed to connect k adjoining segments. The parameters k and F_w have to be chosen such that the fidelity of the resulting states F_1 is greater than the minimum fidelity F_{min} needed for entanglement distillation. **(b)** Entanglement distillation is utilized to create states, which are once more of working fidelity F_w. **(c)** These states are swapped again between adjoining segments. The protocol can be iterated until the desired distance L is reached.
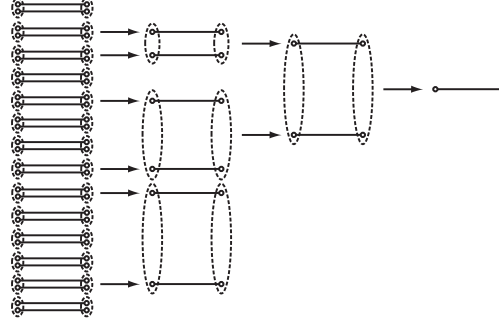
Figure 1.5.: Schematic of entanglement distillation as it was introduced in [13] and [38]. Starting with a number of entangled pairs, bilateral CNOTs are applied in parallel on pairs of entangled states. If the operation was successful, again bilateral CNOTs are applied on pairs of the resulting states and so on until at last a state results with a fidelity higher than or equal to the working fidelity F_w.
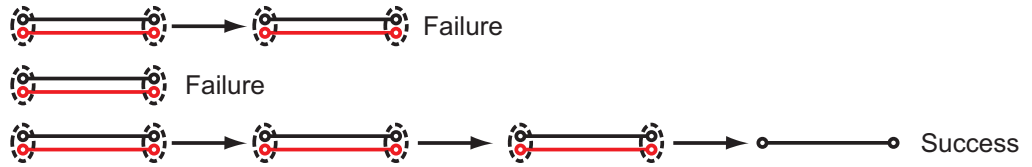
Figure 1.6.: Schematic of sequential entanglement distillation with ancilla pairs (see [42]). Instead of a second distilled state, an ancilla pair (drawn in red) is used for each of the distillation steps. Each step is performed sequentially. If an operation fails, the process is started again from the beginning until it succeeds. Here, I illustrated two subsequent failures, before a successful sequence occurs.

2. Classical and Quantum Interference

We will begin this chapter by giving a short introduction into the principles of classical and quantum interference. In contrast to classical electrodynamics interference in quantum electrodynamics is not due to the superposition of field amplitudes but due to the superposition of probability amplitudes for indistinguishable detection events. This essential difference will be demonstrated on the example of the interference of the radiation from two independent dipoles.

The main part of this chapter will deal with Hong-Ou-Mandel interference, which is the corner stone of our experiments. We will give a detailed theoretical treatment of the effect under the conditions, which we will encounter in the experiments. The theoretical results we obtain will later be compared to the experimental results in order to demonstrate the validity of the quantum theoretical concepts and the various assumptions, which we are going to make in order to simplify the analytical treatment.

Finally, we will demonstrate how HOM-type interference in combination with coincidence detection can be used to project arbitrary two-photon states on the Bell state ψ^-.

2.1. Classical interference

Quantum electrodynamics predicts the possibility of perfect two-photon interference visibility even when the photons originate from independent sources. The visibility of the interference of independent classical electromagnetic fields, on the other hand, cannot surpass 50 %. We are going to present the derivation of this limit in the context of a short review of the principles of classical interference.

2.1.1. Interference of plane waves with constant relative phase

The most simple case of interference occurs when we overlap two plane-wave electromagnetic fields. Their field amplitudes, $E_a(\mathbf{r}, t)$ $(a = 1, 2)$, are given by:

$$E_a(\mathbf{r}, t) = E_{a0} e^{i\left(-\omega_a t + \mathbf{k}_a \cdot \mathbf{r} + \varphi_a\right)}, \tag{2.1}$$

where φ_a denotes a (constant) phase shift, ω_a the angular frequencies and $\mathbf{k}_a$ the wave vectors of the fields. The overall field amplitude is the superposition of these two fields:

$$E(\mathbf{r}, t) = E_1(\mathbf{r}, t) + E_2(\mathbf{r}, t). \tag{2.2}$$

Let us assume the amplitudes and the frequencies of the two fields to be equal, i.e. $E_0 \equiv E_{10} = E_{20}$ and $\omega \equiv \omega_1 = \omega_2$. Then the superposition of the fields at position $\mathbf{r}$ and time t will yield the intensity:

$$
\begin{aligned}
I(\mathbf{r}, t) &= |E(\mathbf{r}, t)|^2 \\
&= 2E_0^2 \{1 + \cos\left[(\mathbf{\ell}_2 - \mathbf{\ell}_1) \cdot \mathbf{r} + \Delta\Phi\right]\} .
\end{aligned}
\tag{2.3}
$$

Here, we introduced the phase difference $\Delta\Phi \equiv \varphi_2 - \varphi_1$. For varying $\mathbf{r}$ at constant time t the interference part leads to spatial interference fringes of perfect visibility. This is only true if $\Delta\Phi$ is constant as we will see below. The visibility will tend to zero even for interfering fields originating from the same source if the optical delay between the interfering fields is larger than the coherence length of the field. This consideration does not enter our simple example with plane waves because their coherence time is infinite.

2.1.2. Stationarity and ergodicity

If the interfering fields originate from independent sources, the phases of the fields will fluctuate randomly over times that are large compared to the coherence times of the fields. Because of these fluctuations it will in general be impossible to predict the change of the phase of a field from one measurement to the next. Subsequent measurements will yield a random distribution of phases, i.e. $\Delta\Phi$ in equ. 2.3 will no longer be a constant; it will be a *random process* $\Delta\Phi(t)$ (see [83]). It changes with time, and its value is determined by some probability distribution $p(\Delta\Phi, t)$.

We will only be interested in the case where the probability distribution is independent of the origin of time, i.e.:

$$
\forall T > 0: \ p(\Delta\Phi, t) = p(\Delta\Phi, t + T).
\tag{2.4}
$$

Such random processes are called *stationary* (see fig. 2.1). Over measurement times that are long compared to the coherence time of the laser field the phase will take all possible values on the interval $[0, 2\pi]$. That means, if we divide this long measurement time into intervals on the order of the coherence time and if we record the phase for each of these intervals, the observed values will be equal to the ensemble of $\Delta\Phi$. In other words, if we average over the ensemble, the result will be equivalent to the time average. We will assume that this holds true as well for any function of $\Delta\Phi(t)$, i.e. for any function $F[\Delta\Phi(t)]$ we have:

$$
\langle F[\Delta\Phi(t)] \rangle_{av} = \langle F[\Delta\Phi(t)] \rangle ,
\tag{2.5}
$$

where

$$
\langle F[\Delta\Phi(t)] \rangle_{av} \equiv \int_0^{2\pi} d\Delta\Phi \, F[\Delta\Phi(t)] \, p(\Delta\Phi, t)
\tag{2.6}
$$

is the ensemble average, and

$$
\langle F[\Delta\Phi(t)] \rangle \equiv \lim_{T \to \infty} \frac{1}{T} \int_{t-T/2}^{t+T/2} dt' \, F[\Delta\Phi(t')]
\tag{2.7}
$$
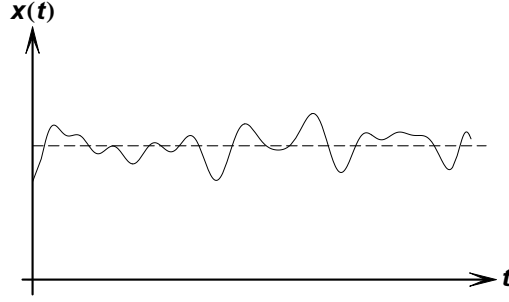
Figure 2.1.: Example of a stationary random process. The probability distribution governing such a process is independent of the origin of time. For this example we used a stationary Gaussian probability distribution, which is centered around the dashed line.

is the time average of F. Under these conditions the random process $\Delta\Phi(t)$ is called *ergodic*.

Equation 2.5 will hold true as well if we perform the time average over a finite time T if this time is long enough for $F[\Delta\Phi(t)]$ to take on enough random variables to carry all information about the ensemble. In other words, T has to be large compared to the coherence time of the field. We will denote an average over a finite time T as $\langle\rangle_T$.

2.1.3. Interference of plane waves with random relative phase

The phases of fields originating from independent sources vary independently of each other. If the observation time T, over which we integrate the intensity of the superposed fields, is much larger than the minimum of the coherence times of the two fields ($\min\left(\tau_{c1}, \tau_{c2}\right)$), the phase difference $\Delta\Phi$ will be completely random.

Because $\Delta\Phi(t)$ is a stationary ergodic process (see previous subsection) the intensity averaged over the observation time T will be equal to the ensemble average of equation 2.3 over $\Delta\Phi$:

$$\langle I\left(\mathbf{r}, t\right)\rangle_T = \langle I\left(\mathbf{r}, t\right)\rangle_{av} = E_0^2. \tag{2.8}$$

The interference term has been washed out because of the random distribution of the phases. That means if T is much longer than the (minimum of the two) coherence times, the observed intensity will be constant over time and space.

In order to observe second-order interference (see below) of classical fields from independent sources it is necessary for T to be *shorter* than (both of) the coherence times of the fields. Interference, which can only be observed under these conditions, is called *transient interference*.

2.1.4. Intensity correlations of fields from independent sources

Up to now we only investigated the modulation of intensity resulting from the superposition of various field amplitudes. The intensity is the *square* modulus of the field amplitude at a given point. That is why interference, which is apparent as a modulation of intensity, is called *second-order* interference.

While it is impossible to observe stable second-order interference patterns with light from independent sources, it is still possible to observe higher-order interference [1]. Specifically, the equal-time correlation between the intensities at points $\mathbf{r}_1$ and $\mathbf{r}_2$ depends on the distance $|\mathbf{r}_2 - \mathbf{r}_1|$.

All interference effects are correlations between fields at various space-time points. In the case of second-order interference these correlations are described using the cross-correlation function of the field $E(\mathbf{r}, t)$ at two space-time points $x_j = (\mathbf{r}_j, t_j)$ (see e.g. [83]):

$$\Gamma(x_1; x_2) = \langle E^*(x_1) E(x_2) \rangle_{av}. \tag{2.9}$$

Using this expression, the ensemble averaged intensity at a space-time point x_j is given by

$$\langle I(x_j) \rangle_{av} = \Gamma(x_j; x_j). \tag{2.10}$$

For stationary, ergodic fields we can use the time average instead of the ensemble average[2], and the cross-correlation function will (apart from the space coordinates) depend only on the time-difference between the space-time points, not on the absolute times:

$$\Gamma(\mathbf{r}_1, \mathbf{r}_2, \tau) = \langle E^*(\mathbf{r}_1, t) E(\mathbf{r}_2, t + \tau) \rangle = \lim_{T \to \infty} \frac{1}{2T} \int_{-T}^{T} dt \, E^*(\mathbf{r}, t) E(\mathbf{r}, t + \tau). \tag{2.11}$$

This we can normalize to get the *complex degree of coherence* between the field at the points $\mathbf{r}_1$ and $\mathbf{r}_2$ (see [83]):

$$\gamma(\mathbf{r}_1, \mathbf{r}_2, \tau) = \frac{\Gamma(\mathbf{r}_1, \mathbf{r}_2, \tau)}{\langle I(\mathbf{r}_1, t) \rangle^{\frac{1}{2}} \langle I(\mathbf{r}_2, t) \rangle^{\frac{1}{2}}}, \tag{2.12}$$

which is a powerful tool to describe second-order interference effects.

To describe higher-order interference effects the concept of the cross-correlation function has to be generalized. The correlation function of order (M, N) between the field at space-time points $x_1, x_2, \ldots, x_M$ and $y_1, y_2, \ldots, y_N$ is given by:

$$\Gamma^{(M,N)}(x_1, x_2, \ldots, x_M; y_1, y_2, \ldots, y_N) = \left\langle E^*(x_M) E^*(x_{M-1}) \ldots E^*(x_1) E(y_1) E(y_2) \ldots E(y_N) \right\rangle. \tag{2.13}$$

---

[1] We will describe a specific example in subsection 3.2

[2] In the following we will only use the time average because we average over the ensemble of random phases. These phases are stationary, ergodic random processes (see 2.1.2). If the fields should depend on additional random variables or if they should vary strongly during the observation times, more care will have to be taken. For an exact treatment of the points, which we cover here, see [83].
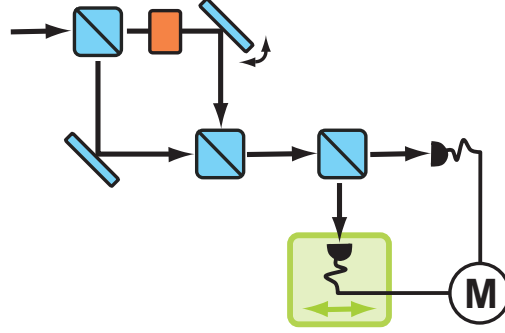
Figure 2.2.: Schematic setup to measure intensity correlations between two fields with random relative phase. The relative phase-shift χ in a Mach-Zehnder interferometer which is varied randomly. Tilting one of the mirrors allows to adjust the difference $\mathfrak{k}_2 - \mathfrak{k}_1$ (see equ. 2.3) between the wave vectors of the fields. The intensity correlations are measured after one more beam splitter. There the detector signals, which are assumed to be proportional to the field intensities, are multiplied and integrated over the varying phase-shift (this process is denoted by M). By translating one of the detectors after the last beam splitter the intensity correlations can be measured over a varying distance $\mathfrak{r}_2 - \mathfrak{r}_1$.

As has been mentioned above we are mainly interested in the correlation between the intensities at two space-time points. To investigate these correlations we use the fourth-order correlation function:

$$\begin{aligned}
G^{(2)}(\mathfrak{r}_1, \mathfrak{r}_2, \tau) &\equiv \Gamma^{(2,2)}(\mathfrak{r}_1, t, \mathfrak{r}_2, t+\tau; \mathfrak{r}_1, t, \mathfrak{r}_2, t+\tau) \\
&= \langle E^*(\mathfrak{r}_2, t+\tau) E^*(\mathfrak{r}_1, t) E(\mathfrak{r}_1, t) E(\mathfrak{r}_2, t+\tau) \rangle \\
&= \langle I(\mathfrak{r}_1, t) I(\mathfrak{r}_2, t+\tau) \rangle .
\end{aligned} \tag{2.14}$$

Let us now come back to our simple example of the superposition of two plane-wave fields. A possible experimental realization to superpose two plane-wave fields with randomly varying phase is shown in figure 2.2. This is the case where we expect the highest possible correlations for classical fields. Any other field can be described as a superposition of plane waves of varying frequencies and amplitudes. As long as the resulting field is stationary this will lead to a lower correlation visibility than for plane waves. If the field is not stationary, we will get unwanted correlations between the intensity envelopes of the fields (e.g. in the case of pulsed sources).

We can calculate the desired fourth-order correlations by using equ. 2.3 (see [94]):

$$G^{(2)}(\mathfrak{r}_1, \mathfrak{r}_2, 0) = 4 E_0^4 \left\{ 1 + \frac{1}{2} \cos\left[(\mathfrak{k}_2 - \mathfrak{k}_1)(\mathfrak{r}_2 - \mathfrak{r}_1) \right] \right\} . \tag{2.15}$$

Depending on the arguments of the cosine the correlations vary between a maximum value $I_{max} = \frac{3}{2}$ and a minimum value $I_{min} = \frac{1}{2}$. With these values the visibility of the interference

is given by:

$$V_M = \frac{I_{max} - I_{min}}{I_{max} + I_{min}}. \tag{2.16}$$

For the modulation of $G^{(2)}$ this results in 0.5, i.e. 50 %, visibility, the maximum achievable visibility for the interference of independent fields in classical electrodynamics.

We will refer to the visibility we have used above as *Michelson* visibility (thus the subscript M). This is the appropriate visibility to use if the signal in question varies (more or less) symmetrically around some average value. In general, visibility can be seen as the ratio of the signal modulation over the average signal. The average signal is given by:

$$\frac{I_{max} + I_{min}}{2}, \tag{2.17}$$

whereas the signal modulation is:

$$\frac{I_{max} - I_{min}}{2}. \tag{2.18}$$

Their ratio yields equ. 2.16.

Throughout the thesis we will encounter situations where the signal modulation is *not* symmetric but rather manifests itself as a dip with respect to a constant plateau. In this case equ. 2.18 yields only half of the actual signal modulation, and equ. 2.17 yields a far smaller value than the constant plateau.

To gain an appropriate expression for the visibility, one has to calculate the ratio of the signal modulation $I_{max} - I_{min}$, and the constant plateau I_{max}, i.e.:

$$V_D = \frac{I_{max} - I_{min}}{I_{max}}. \tag{2.19}$$

Here, we used the subscript D to indicate that this visibility applies for dip-like modulated signals. We will refer to this definition as *dip* visibility.

2.2. Interference of light from two spontaneously decaying atoms

A good example to compare classical and quantum interference is to measure intensity correlations in the field of two decaying atoms (see fig. 2.3). In contrast to the simple plane-wave examples, which we discussed earlier, this presents us with the possibility to examine the differences in the classical and quantum predictions in a realistic context. It also allows us to achieve maximum interference visibilities for both theoretical models. Apart from these points, the interference of light from two decaying atoms presented, to the author's best knowledge, the first discussion of two-photon interference, which has no classical counterpart [39, 82].
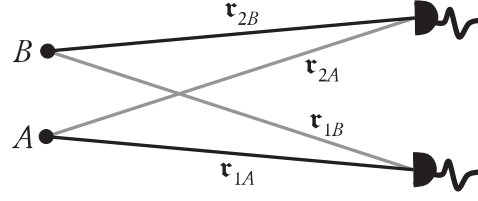
Figure 2.3.: Intensity correlations of light emitted by two Hertzian oscillators. We assume their dipole moments to be parallel to each other and perpendicular to the drawing plane. While there is no stable second-order interference because of the random phase difference between the two fields, the intensities at different positions are correlated.

We should point out that the following discussion of the classical description is, apart from hopefully clarifying abbreviations and adaptations, equivalent to the one in ref. [94]. The quantum mechanical description of the effect is based on [94], [70], and in large parts on [83].

2.2.1. Classical description

In classical terms we will have to deal with two Hertzian oscillators, A and B, emitting a field of exponentially decaying intensity. For simplicity we assume that the two dipoles have the same maximal oscillation amplitude and that they are oriented parallel to each other. Moreover, we will consider the field only in the plane perpendicular to the orientation of the dipoles.

The field amplitude in the far field of dipole j ($j = A, B$), which is located at position $\mathfrak{r}_j$, can be written as:

$$E_j(\mathfrak{r}, t) = f\left(\mathfrak{r} - \mathfrak{r}_j\right) a\left(t - \frac{\left|\mathfrak{r} - \mathfrak{r}_j\right|}{c}\right) e^{\iota \varphi_j}, \qquad (2.20)$$

where f describes the spatial distribution of the dipole radiation [94]:

$$f(\mathfrak{R}) = \frac{\omega^2 d_0}{4\pi\epsilon_0 c^2 |\mathfrak{R}|}. \qquad (2.21)$$

Here, ω is the frequency of the dipole, and φ_a is a randomly distributed phase. The dipole moment is $d(t) = d_0 a(t)$, where d_0 is the maximum amplitude of the dipole oscillation and

$$a(t) = \gamma(t)e^{-\iota\omega t}, \qquad (2.22)$$

where $\gamma(t) = \exp\left(-\frac{\Gamma}{2}t\right)$ describes the exponential decay of the dipole amplitude. It should be noted at this point that the fact that we use the same decay function $a(t)$ for both dipoles

includes the assumption that the dipoles start radiating at the same time $t = 0$. A deviation between these points of time would result in different intensities of the superposed fields and in reduced correlations between them [3].

Before we continue let us define the following shorthand notations (partly taken from ref. [94]):

$$\mathbf{r}_{ij} \equiv \mathbf{r}_i - \mathbf{r}_j, T_{ij} = t - \frac{\mathbf{r}_{ij}}{c}, f_{ij} \equiv f\left(\mathbf{r}_{ij}\right) \text{ and } a_{ij} \equiv a\left(T_{ij}\right), \tag{2.23}$$

where the index i stands for either one of the two positions, where the intensity of the field is measured ($i = 1, 2$). Using this notation, the instantaneous intensity of the superposed field of our two dipoles at a position r_i can be written as:

$$
\begin{aligned}
I\left(\mathbf{r}_i, t\right) &= \left|E_A\left(\mathbf{r}_i, t\right) + E_B\left(\mathbf{r}_i\right)\right|^2 \\
&= f_{iA}^2 |a_{iA}|^2 + f_{iB}^2 |a_{iB}|^2 + f_{iA} f_{iB}\left(a_{iA}^* a_{iB} e^{\iota \Delta \Phi} + a_{iA} a_{iB}^* e^{-\iota \Delta \Phi}\right).
\end{aligned} \tag{2.24}
$$

Here, we used $\Delta \Phi \equiv \varphi_B - \varphi_A$ in analogy to our plane-wave example (see section 2.1).

For independent oscillators the phase difference will be random, and the average intensity will just be the sum of the individual field intensities:

$$\langle I\left(\mathbf{r}, t\right)\rangle_{av} = I_A\left(\mathbf{r}, t\right) + I_B\left(\mathbf{r}, t\right). \tag{2.25}$$

Although there is no stable second-order interference there will be higher-order correlations between the field intensities at different space-time points. We will calculate these correlations for a situation, where the distance between the observation points, $|\mathbf{r}_2 - \mathbf{r}_1|$, and the distance between the dipoles, $\mathbf{r}_B - \mathbf{r}_A$ is small compared to the distance of the observation points from the dipoles. These assumptions lead to the following approximations (for all $i = 1, 2$ and $j = A, B$):

$$f \approx f_{ij}, \gamma \approx \gamma\left(T_{ij}\right). \tag{2.26}$$

That means we will neglect differences between the averaged intensities at the two points of observation.

With these assumptions equation 2.24 simplifies to

$$I\left(\mathbf{r}_j, t\right) = 2f^2\gamma^2(t)\left\{1 + \cos\left[\omega\left(T_{jA} - T_{jB} + \Delta\Phi\right)\right]\right\}. \tag{2.27}$$

It should be noted that this is equivalent to the expression in equation 2.3 apart from the time and position dependent global factors. Using this simplified relation the equal-time

---

[3]If one of the dipoles started radiating earlier than the other by a time difference $\Delta t > 0$, our conclusions would be largely the same, except that the visibility of the correlations (see equ. 2.28) would become $[1 + \cosh\left(\Gamma \Delta t\right)]^{-1}$.

correlations of the intensities at points $\mathbf{r}_1$ and $\mathbf{r}_2$ become:

$$
\begin{aligned}
G^{(2)}(\mathbf{r}_1, \mathbf{r}_2, 0) &= 4f^4\gamma^4(t) \\
&\quad \times \left\langle \{1 + \cos\left[\omega\left(T_{1A} - T_{1B} + \Delta\Phi\right)\right]\} \{1 + \cos\left[\omega\left(T_{2A} - T_{2B} + \Delta\Phi\right)\right]\} \right\rangle_{av} \\
&= 4f^4\gamma^4(t) \left\{ 1 + \frac{1}{2}\cos\left[\omega\left(T_{2A} - T_{2B} + T_{1B} - T_{1A}\right)\right] \right\} \\
&= 4f^4\gamma^4(t) \left\{ 1 + \frac{1}{2}\cos\left[k\left(\mathbf{r}_{2A} - \mathbf{r}_{2B} + \mathbf{r}_{1B} - \mathbf{r}_{1A}\right)\right] \right\},
\end{aligned}
\tag{2.28}
$$

where $k = \frac{\omega}{c}$ is the wave-number associated with the dipole oscillation.

Just like in the case of plane waves the visibility of the correlations (see equ. 2.16) is 50 %. This is the ideal value, which is only reached when the simplifying assumptions we made are close to accurate. If our assumptions do not hold, the amplitudes of the interfering fields will differ depending on the position and on the time needed for the field to reach that position. The visibility of the intensity correlations will be reduced in that case (see the remark and the corresponding footnote below equ. 2.22).

2.2.2. Quantum description

In the quantum mechanical description each of the two dipoles A and B corresponds to a two-level atomic system. We denote the excited and the ground state of an atom by $|e\rangle$ and $|g\rangle$, respectively. They correspond to energy eigenstates $E_0 \pm \frac{1}{2}\hbar\omega_0$ (see fig. 2.4). The corresponding raising and lowering operators at time $t = 0$ are:

$$
\hat{b} = |g\rangle\langle e| \quad \text{and} \quad \hat{b}^\dagger = |e\rangle\langle g|.
\tag{2.29}
$$

They fulfill the anti-commutation relations

$$
\{\hat{b}, \hat{b}\} = 0 = \{\hat{b}^\dagger, \hat{b}^\dagger\} \quad \text{and} \quad \{\hat{b}, \hat{b}^\dagger\} = 1,
\tag{2.30}
$$

where $\{\hat{A}, \hat{B}\} \equiv \hat{A}\hat{B} + \hat{B}\hat{A}$ denotes the anti-commutator. For later use we define the three spin operators [83]

$$
\hat{R}_1 = \frac{1}{2}\left(\hat{b}^\dagger + \hat{b}\right), \quad \hat{R}_2 = \frac{1}{2\imath}\left(\hat{b}^\dagger - \hat{b}\right) \quad \text{and} \quad \hat{R}_3 = \frac{1}{2}\left[\hat{b}^\dagger, \hat{b}\right],
\tag{2.31}
$$

where $\left[\hat{A}, \hat{B}\right] \equiv \hat{A}\hat{B} - \hat{B}\hat{A}$ denotes the commutator. Both basis states of the two-level system are eigenstates of the last of these operators:

$$
\hat{R}_3|e\rangle = \frac{1}{2}|e\rangle \quad \text{and} \quad \hat{R}_3|g\rangle = -\frac{1}{2}|g\rangle.
\tag{2.32}
$$

It is convenient to continue in the Heisenberg picture. There, in contrast to the Schrödinger picture, the time dependence lies in the operators and not in the states. To calculate the desired intensity correlations, we will only have to calculate the expectation value of the product of the time-dependent intensity operators in the initial (not time dependent) states.

Figure 2.4.: Energy structure of an atomic two-level system with energy eigenstates $|g\rangle$ and $|e\rangle$.

The time dependence of an operator $\hat{A}$ can be described by the Heisenberg equation of motion:

$$\frac{d}{dt}\hat{A}(t) = \frac{1}{\imath\hbar}\left[\hat{A}(t), \hat{H}\right],\qquad(2.33)$$

where $\hat{H}$ is the Hamiltonian of our system. It is given by

$$\hat{H} = \hat{H}_a + \hat{H}_f + \hat{H}_i.\qquad(2.34)$$

Here, we introduced $\hat{H}_a$, the Hamiltonian for the uncoupled atomic system, $\hat{H}_f$, the Hamiltonian for the free electromagnetic field, and $\hat{H}_i$, the Hamiltonian for the interaction between these two systems.

It is important to note that we do not take into account any interaction between the two atoms. Although the atoms are coupled to the same electromagnetic field this approximation should hold as long as the distance between the atoms is large compared to the wavelength of the emitted radiation.

The Hamiltonians in the equation above are given by (see [70] and [83]):

$$\begin{aligned}
\hat{H}_a &= E_0 + \hbar\omega_0 \hat{R}_3,\\
\hat{H}_f &= \hbar\omega\left(\sum_{\mathfrak{k}s}\hat{a}^\dagger_{\mathfrak{k}s}\hat{a}_{\mathfrak{k}s} + \frac{1}{2}\right),\\
\hat{H}_i &= -\dot{\hat{\mathfrak{d}}}_A(t)\cdot\hat{\mathfrak{A}}(\mathfrak{r}_A, t) - \dot{\hat{\mathfrak{d}}}_B(t)\cdot\hat{\mathfrak{A}}(\mathfrak{r}_B, t).
\end{aligned}\qquad(2.35)$$

The summation over $\mathfrak{k}$ and s corresponds to an integration over all wave vectors and a summation over both polarizations. We introduced the vector potential $\hat{\mathfrak{A}}$ and $\hat{\mathfrak{d}}_{A/B}(t) = \mathfrak{d}_0\hat{b}_{A/B}(t) + \mathfrak{d}^*_0\hat{b}^\dagger_{A/B}(t)$, the dipole moments of our two two-level system A and B, where $\mathfrak{d}_0$ defines the direction and amplitude of the dipole moment. For the time derivative of the dipole moment, which occurs in the interaction Hamiltonian, we use the following equation of motion:

$$\frac{d}{dt}\hat{\mathfrak{d}}_{A/B}(t) = \left[\hat{\mathfrak{d}}_{A/B}(t), \hat{H}_a\right] = -\imath\omega_0\left[\mathfrak{d}_0\hat{b}_{A/B}(t) + \mathfrak{d}^*_0\hat{b}^\dagger_{A/B}(t)\right].\qquad(2.36)$$

Inserting this into the interaction Hamiltonian yields:

$$\hat{H}_i = \imath\omega_0 \left[\mathfrak{d}_0 \hat{b}_A(t) + \mathfrak{d}_0^* \hat{b}_A^\dagger(t) \right] \cdot \hat{\mathfrak{A}}(\mathbf{r}_A, t) + \imath\omega_0 \left[\mathfrak{d}_0 \hat{b}_B(t) + \mathfrak{d}_0^* \hat{b}_B^\dagger(t) \right] \cdot \hat{\mathfrak{A}}(\mathbf{r}_B, t). \quad (2.37)$$

Now, if one takes into account that equal time atomic and field operators commute with each other (because there is no instantaneous interaction) as do the atomic operators for the dipoles A and B, one can calculate the Heisenberg equations of motion for the field operators, which are simply the Maxwell equations:

$$\begin{aligned}
\epsilon_{ijk} \frac{\partial}{\partial x_j} E_k(\hat{\mathbf{r}}, t) &= -\frac{\partial}{\partial t} \hat{B}_i(\mathbf{r}, t), \\
\epsilon_{ijk} \frac{\partial}{\partial x_j} B_k(\hat{\mathbf{r}}, t) &= \frac{1}{c^2} \frac{\partial}{\partial t} \hat{E}_i(\mathbf{r}, t) + \mu_0 \hat{j}_i(\mathbf{r}, t).
\end{aligned} \quad (2.38)$$

Here, ϵ_{ijk} is the permutation symbol, which is defined as [45]:

$$\epsilon_{ijk} = \begin{cases} +1, & ijk \text{ is } 123, 312 \text{ or } 231 \\ -1, & ijk \text{ is } 321, 132 \text{ or } 213 \\ 0, & \text{otherwise.} \end{cases} \quad (2.39)$$

The effective current density $\hat{\mathbf{j}}$ can be written as (see [83]):

$$\hat{\mathbf{j}}(\mathbf{r}, t) = -\imath\omega_0 \mathbf{g}(\mathbf{r} - \mathbf{r}_A) \hat{b}_A - \imath\omega_0 \mathbf{g}(\mathbf{r} - \mathbf{r}_B) \hat{b}_B + \text{c.c.}, \quad (2.40)$$

where we used

$$\mathbf{g}(\mathfrak{R}) = \frac{2}{3} \mathfrak{d}_0 \delta^3(\mathfrak{R}) - \frac{\mathfrak{d}_0}{4\pi |\mathfrak{R}|^3} + \frac{3 (\mathfrak{d}_0 \cdot \mathfrak{R}) \mathfrak{R}}{4\pi |\mathfrak{R}|^5}. \quad (2.41)$$

By inserting $\vec{\nabla} \times \hat{\mathfrak{B}} = \hat{\mathfrak{A}}$ in the Maxwell equations and solving the resulting wave equation for the vector potential the vector potential becomes:

$$\hat{\mathfrak{A}} = \frac{\mu_0}{4\pi} \int d^3 r' \frac{\hat{\mathbf{j}}(\mathbf{r}', t - |\mathbf{r} - \mathbf{r}'/c|)}{|\mathbf{r} - \mathbf{r}'|} \theta(|\mathbf{r} - \mathbf{r}'|), \quad (2.42)$$

where we neglected the free-field contribution as it will not contribute anything to the detection events, the correlations of which we are interested in. With this relation it is possible to calculate the electric field operator $\hat{\mathfrak{E}}$ by virtue of the relation $\hat{\mathfrak{E}} = -\partial_t \hat{\mathfrak{A}}$. The evaluation is simplified by using $\dot{\hat{b}}(t) = [\hat{b}(t), H_a]$ as an approximate equation of motion for $\hat{b}(t)$. In the far field of the two dipoles the result to the lowest order in $1/r$ and for $t > |\mathbf{r} - \mathbf{r}_{A/B}|$ is given by (see [83]):

$$\hat{\mathfrak{E}}(\mathbf{r}, t) = \mathfrak{f}(\mathbf{r} - \mathbf{r}_A) \hat{b}_B \left(t - \frac{\mathbf{r} - \mathbf{r}_A}{c} \right) + \mathfrak{f}(\mathbf{r} - \mathbf{r}_B) \hat{b}_B \left(t - \frac{\mathbf{r} - \mathbf{r}_B}{c} \right) + \text{c.c.}, \quad (2.43)$$

where $\mathfrak{f}(\mathfrak{R})$ is a function equivalent to the one encountered in the classical description of the dipole field (compare this to equ. 2.21). It is given by

$$\mathfrak{f}(\mathfrak{R}) = \frac{\omega_0^2}{4\pi\epsilon_0 c^2} \left[\frac{\mathfrak{d}_0}{|\mathfrak{R}|} - \frac{(\mathfrak{d}_0 \cdot \mathfrak{R})\mathfrak{R}}{|\mathfrak{R}|^3} \right]. \tag{2.44}$$

Just like in the classical description, we will consider the dipoles as well as our points of observation to lie in the plane defined by $\mathfrak{d}_0 \cdot \mathfrak{r} = 0$. If we choose our coordinate system such that its z-axis lies along $\mathfrak{d}_0$, the positive frequency part of equation 2.43 simplifies to:

$$\mathfrak{e}_z \hat{E}^{(+)}(\mathfrak{r}, t) = \mathfrak{e}_z f(\mathfrak{r} - \mathfrak{r}_A) \hat{b}_A(t - |\mathfrak{r} - \mathfrak{r}_A|/c) + \mathfrak{e}_z f(\mathfrak{r} - \mathfrak{r}_B) \hat{b}_B(t - |\mathfrak{r} - \mathfrak{r}_B|/c), \tag{2.45}$$

where we used $f(\mathfrak{R})$ as defined in equation 2.21.

Now, we are finally going to use these results to calculate the expectation values for the intensities and the intensity correlations in the field of our two atomic dipoles. Let us calculate the single-photon detection probability $P_s(\mathfrak{r}, t)$:

$$P_s(\mathfrak{r}, t) \propto \langle \psi | E^{(-)}(\mathfrak{r}, t) E^{(+)}(\mathfrak{r}, t) | \psi \rangle. \tag{2.46}$$

Here, $|\psi\rangle$ is the initial state the system, where both atoms are excited but the field is not:

$$|\psi\rangle = |\Omega\rangle |e\rangle_A |e\rangle_B. \tag{2.47}$$

To evaluate equ. 2.46 it is necessary to calculate expectation values of the form[4]:

$$\langle \psi | \hat{b}_i^\dagger(t_1) \hat{b}_i(t_2) | \psi \rangle = e^{-\frac{\Gamma}{2}(t_1 + t_2)} e^{-\imath(\omega_0 - \xi)(t_2 - t_1)}, \tag{2.48}$$

where $i = A, B$ and

$$\Gamma = \frac{|d_0|^2 \omega_0^3}{3\pi\epsilon_0 \hbar c^3} \tag{2.49}$$

is the decay constant, which we already encountered during the classical description of this effect. The shift of the dipole frequency,

$$\xi \approx \frac{\Gamma}{\pi} \ln\left(\frac{mc^2}{\hbar\omega_0}\right), \tag{2.50}$$

is known as Lamb shift (for details see [83]), and m is the electron mass. It is important to note that Γ and ξ are equal for both atoms because for each of them the two levels are assumed to be separated by the same energy.

---

[4]For the derivation of the expectation value in equ. 2.48 we refer to [70] and to chapter 15 of ref. [83].

By virtue of equ. 2.48 and because $\langle\psi|\hat{b}_{A/B}(t)|\psi\rangle = 0$ equ. 2.46 becomes:

$$
\begin{aligned}
P_s(\mathfrak{r}, t) \;\propto\; & \langle\psi|\hat{b}_A^\dagger(t - |\mathfrak{r} - \mathfrak{r}_A|/c)\hat{b}_A(t - |\mathfrak{r} - \mathfrak{r}_A|/c)|\psi\rangle + \\
& \langle\psi|\hat{b}_B^\dagger(t - |\mathfrak{r} - \mathfrak{r}_B|/c)\hat{b}_B(t - |\mathfrak{r} - \mathfrak{r}_B|/c)|\psi\rangle \\
=\; & |f(\mathfrak{r} - \mathfrak{r}_A)|^2\, e^{-\Gamma(t - |\mathfrak{r} - \mathfrak{r}_A|/c)} + |f(\mathfrak{r} - \mathfrak{r}_B)|^2\, e^{-\Gamma(t - |\mathfrak{r} - \mathfrak{r}_B|/c)}.
\end{aligned} \tag{2.51}
$$

As expected we see that there is no second-order interference. It should be noted that we did not have to introduce any phases $\varphi_{A/B}$ as we did in the classical description. The randomness of the phases is already contained in the description because the sources emit single-photon Fock states, and these states do not have defined phases. Transient interference, as we have encountered it in the case of classical interference, still occurs but in addition two-photon interference will take place, as we will see in the following.

Up to now the predictions of quantum electrodynamics have been equivalent to those of the classical description. Both predict that there can be no stable interference between fields emitted by independently oscillating dipoles. The difference between the classical and the quantum description will become apparent in the correlations between the intensities at two space-time points. In quantum theory the equal-time fourth-order correlation function is given by [83]

$$
G^{(2)}(\mathfrak{r}_1, \mathfrak{r}_2, 0) = \langle\psi|\hat{E}^{(-)}(\mathfrak{r}_1, t)\hat{E}^{(-)}(\mathfrak{r}_2, t)\hat{E}^{(+)}(\mathfrak{r}_2, t)\hat{E}^{(+)}(\mathfrak{r}_1, t)|\psi\rangle. \tag{2.52}
$$

In order to simplify our notation and the evaluation of the correlation function we will use the short-hand notations defined in equ. 2.23 like we did in the classical description. In addition we will again make the following (far-field) approximations[5] (for any $i, k = 1, 2$ and $j, m = A, B$):

$$
f \approx f_{ij} \approx f_{km}, \quad \gamma \approx e^{-\frac{1}{2}\Gamma T_{ij}} \approx e^{-\frac{1}{2}\Gamma T_{km}}. \tag{2.53}
$$

These notations and approximations allow us to write equ. 2.52 as:

$$
\begin{aligned}
G^{(2)}(\mathfrak{r}_1, \mathfrak{r}_2, 0) =\; & |f|^4 \langle\psi| \left[\hat{b}_A^\dagger(T_{1A}) + \hat{b}_B^\dagger(T_{1B}) \right] \left[\hat{b}_A^\dagger(T_{2A}) + \hat{b}_B^\dagger(T_{2B}) \right] \times \\
& \left[\hat{b}_A(T_{2A}) + \hat{b}_B(T_{2B}) \right] \left[\hat{b}_A(T_{1A}) + \hat{b}_B(T_{1B}) \right] |\psi\rangle \\
=\; & |f|^4 \Big[\langle\psi|\hat{b}_A^\dagger(T_{1A})\hat{b}_B^\dagger(T_{2B})\hat{b}_A(T_{2A})\hat{b}_B(T_{1B})|\psi\rangle + \\
& \langle\psi|\hat{b}_A^\dagger(T_{1A})\hat{b}_B^\dagger(T_{2B})\hat{b}_B(T_{2B})\hat{b}_A(T_{1A})|\psi\rangle + \\
& \langle\psi|\hat{b}_B^\dagger(T_{1B})\hat{b}_A^\dagger(T_{2A})\hat{b}_A(T_{2A})\hat{b}_B(T_{1B})|\psi\rangle + \\
& \langle\psi|\hat{b}_B^\dagger(T_{1B})\hat{b}_A^\dagger(T_{2A})\hat{b}_B(T_{2B})\hat{b}_A(T_{1A})|\psi\rangle \Big].
\end{aligned} \tag{2.54}
$$

In the last step we took into account only non-vanishing expectation values. If we employ equ. 2.48 to calculate the expectation values, we will get:

$$
G^{(2)}(\mathfrak{r}_1, \mathfrak{r}_2, 0) = 2|f|^4 \gamma^4 \left\{ 1 + \cos\left[(\omega_0 - \xi)(T_{2A} - T_{2B} + T_{1B} - T_{1A}) \right] \right\}. \tag{2.55}
$$

---

[5]They are equivalent to the approximations given in equ. 2.26.

In contrast to the classical correlation function (see equ. 2.28) quantum theory predicts correlations with 100 % visibility.

This surpasses any correlations, which one could expect from classical electrodynamics. In fact, if one photon is detected, there will be forbidden directions for the second photon to be detected in. This led Dicke to write [39]:

> *One might naively wonder with such a radiating system, initially in a state for which both atoms are excited, how the one atom would ever know about the existence of the other.*

2.3. Hong-Ou-Mandel interference

Hong-Ou-Mandel (HOM) interference [60] is a well known fourth-order quantum interference effect. It is closely related to the interference of photons originating from two decaying atoms, which we discussed in the previous section. In HOM interference the single modes of two photons [6] are overlapped at a 50 : 50 beam splitter (see fig. 2.5). If a photon detection event in any of the output ports does not even in principle allow to determine the origin of the detected photon, there will occur no coincidence detection events between the two detectors in the beam-splitter outputs.

HOM-type interference was introduced as a new method to measure optical-path differences with a sub-picosecond time resolution [60]. Its important role in quantum optics and quantum information processing experiments is mainly due to its usefulness in realizing Bell-state measurements (see subsection 2.3.5) and, in combination with post selection, probabilistic two-qubit gates (see e.g. [54, 71]).

2.3.1. The concept of HOM interference

Consider a symmetric 50:50 beam splitter (BS) with input modes a and b and output modes c and d. In each of the output modes we place a single-photon detector (D_c and D_d, see 2.5). Suppose one photon is emitted into each of the modes a and b. Then our initial state is:

$$|\psi_0\rangle = \hat{a}_a^\dagger \hat{a}_b^\dagger |\Omega\rangle, \tag{2.56}$$

where $|\Omega\rangle$ is the vacuum state and $\hat{a}_i^\dagger$ ($i = a, b$) are the creation operators for the input modes of the beam splitter. For the moment we neglect polarizations and frequencies of the photons.

Before we continue we have to describe the action of the beam splitter on our photon states. Assuming that it is loss-less, a beam splitter can be represented by a unitary transfor-

---

[6]In an experiment the photons will not exactly be in single modes. To achieve optimal interference visibility the mode overlap must be as good as possible. This can be achieved by guiding the interfering photons in single-mode fibers.

5cm
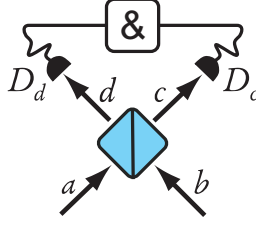
Figure 2.5.: HOM-type interference at a 50 : 50 beam splitter. Two-photon coincidences are measured between detectors D_c and D_d. None will occur if detection events due to a photon in mode a are indistinguishable from events due to a photon in mode b.

mation $\mathfrak{U}_{BS}$, which relates the annihilation operators of the input and output modes:

$$
\begin{pmatrix} \hat{a}_c \\ \hat{a}_d \end{pmatrix} = \mathfrak{U}_{BS} \begin{pmatrix} \hat{a}_a \\ \hat{a}_b \end{pmatrix}.
\tag{2.57}
$$

For a 50 : 50 beam splitter $\mathfrak{U}_{BS}$ will have to fulfill the following relations:

$$
\left| \langle \Omega | \hat{a}_c \left(\hat{a}_c^\dagger; 0 \right) \mathfrak{U}_{BS} \begin{pmatrix} \hat{a}_a \\ 0 \end{pmatrix} \hat{a}_c^\dagger | \Omega \rangle \right|^2 = \frac{1}{2} = \left| \langle \Omega | \hat{a}_d \left(0; \hat{a}_d^\dagger \right) \mathfrak{U}_{BS} \begin{pmatrix} 0 \\ \hat{a}_b \end{pmatrix} \hat{a}_d^\dagger | \Omega \rangle \right|^2.
\tag{2.58}
$$

In combination with the unitarity of $\mathfrak{U}_{BS}$ these relations allow us to write:

$$
\mathfrak{U}_{BS} = \frac{1}{\sqrt{2}} \begin{pmatrix} e^{\imath \phi_1} & e^{\imath \phi_2} \\ e^{\imath \phi_3} & e^{\imath \phi_4} \end{pmatrix},
\tag{2.59}
$$

where $(\phi_3 - \phi_1) + (\phi_2 - \phi_4) = (2n+1)\pi$, and $n \in \mathbb{Z}$. Our beam splitters are also symmetric, i.e. $\phi_3 - \phi_1 = \phi_2 - \phi_4$. We are free to set two of the phases to arbitrary values and to choose any Integer value for n. With the choice $\phi_1 = \phi_4 = n = 0$, we get:

$$
\mathfrak{U}_{BS} = \frac{1}{\sqrt{2}} \begin{pmatrix} 1 & \imath \\ \imath & 1 \end{pmatrix}.
\tag{2.60}
$$

We can summarize the action of the beam splitter in the following two relations:

$$
\begin{aligned}
\hat{a}_a &\rightarrow \frac{1}{\sqrt{2}} (\hat{a}_c + \imath \hat{a}_d) \\
\hat{a}_b &\rightarrow \frac{1}{\sqrt{2}} (\hat{a}_d + \imath \hat{a}_c).
\end{aligned}
\tag{2.61}
$$

Let us apply this to $|\psi_0\rangle$:

$$|\psi_0\rangle \rightarrow |\psi_1\rangle = \frac{1}{2}(\hat{a}_c^\dagger - \imath\hat{a}_d^\dagger)(\hat{a}_d^\dagger - \imath\hat{a}_c^\dagger)|\Omega\rangle = \frac{1}{2}(-\imath\hat{a}_c^{\dagger 2} - \imath\hat{a}_d^{\dagger 2} + [\hat{a}_c^\dagger, \hat{a}_d^\dagger])|\Omega\rangle. \qquad (2.62)$$

The commutator $[\hat{a}_c^\dagger, \hat{a}_d^\dagger]$ vanishes because these operators act on distinct modes, and we are left with:

$$|\psi_1\rangle = -\frac{\imath}{2}(\hat{a}_c^{\dagger 2} + \hat{a}_d^{\dagger 2}). \qquad (2.63)$$

There are no terms present, which could result in coincidence detection events in modes c and d. The reason is that $\hat{a}_c^\dagger \hat{a}_d^\dagger$ and $\hat{a}_d^\dagger \hat{a}_c^\dagger$ lead to indistinguishable two-photon detection events, the amplitudes of which interfere destructively.

2.3.2. Calculating the visibility of HOM-type interference

In our discussion of the concept of HOM-type interference in the previous subsection, the interfering photons had infinite coherence lengths and were indistinguishable in every respect. For physical states the indistinguishability of the photons and the detection events they trigger will not be guaranteed but will depend on various parameters. Prominent among them are the polarization of the photons, their coherence lengths and central wavelengths as well as optical path differences [7].

An important prerequisite for high-visibility HOM-type interference is that the number of photons in each of he input modes is well defined. More precisely, there must be exactly one photon in each input mode of the BS. The single-photon sources in our experiment were spontaneous parametric down conversion (SPDC) [28] crystals pumped by ultra-violet laser beams.

The two-photon-detection probability amplitude

Each photon of an SPDC pair has to pass through a polarization filter and a narrow bandwidth filter before it is coupled into a single-mode fiber (see fig. 2.6). In the mathematical treatment of the effect, we can neglect polarization because the polarizers are adequately adjusted to assure the indistinguishability of the interfering photons.

We will write the two-photon state for an SPDC pair, where one photon is coupled into mode 1 and one photon is coupled into mode 2 as (compare this to e.g. [105, 68]):

$$
\begin{aligned}
|\psi_{SPDC}\rangle &= \int d\omega_p \, g(\omega_p) e^{i\omega_p \tau_p} \int d\omega_s \int d\omega_i \, \delta(\omega_p - \omega_s - \omega_i) \hat{a}_1^\dagger(\omega_s) \hat{a}_2^\dagger(\omega_i)|\Omega\rangle \\
&= \int d\omega_s \int d\omega_i \, g(\omega_s + \omega_i) e^{i(\omega_s + \omega_i)\tau_p} \, \hat{a}_1^\dagger(\omega_s) \hat{a}_2^\dagger(\omega_i)|\Omega\rangle, \qquad (2.64)
\end{aligned}
$$

---

[7]We will not take into account differences between the spatial modes of the interfering photons.
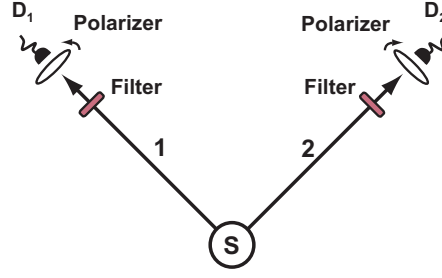
Figure 2.6.: Schematic of the measurement of an SPDC pair. The emission of an SPDC source (S) is coupled into two spatial single modes 1 and 2. In each of the modes a bandwidth filter and a polarizer are placed in front of the single-photon detector (D_1 and D_2).

where $g(\omega_p)$ is the frequency distribution of the pump laser and τ_p is the arrival time of the pump pulse in the SPDC crystal. The Dirac delta results from the integration over the interaction time between field and crystal. It should be noted that the SPDC state, as we have written it, is not normalizable because we omitted the function $\text{sinc}[L(k_{pz} - k_{iz} - k_{sz})]$, which should usually occur here (L is the length of the crystal, see [104]). To omit this function is equivalent to assuming that the bandwidths of our filters are narrower than the natural bandwidth of the SPDC photons (see also section 4.3.2). The group velocity mismatch due to the different wavelengths and polarizations is another effect, which we neglect here. It will be treated in section 5.2.

Because the frequency response of the detectors used is much broader than the transmission curve of the bandwidth filters, we can readily assume the bandwidth of the detectors to be infinite. That means, the frequency dependence of the photon-detection probabilities can be assumed to depend only on the filters and not on properties of the detectors. The probability amplitude for detector D_i (see fig. 2.6) to detect the photon in mode i at time t is given by [53, 52, 83]:

$$A^{(i)}(t) = \langle \Omega | E_i^{(+)}(t) | \psi \rangle, \qquad (2.65)$$

where $E_i^{(+)}(t)$ is the positive frequency part of the electromagnetic field operator at detector D_i. It is weighted by the transmission function of the bandwidth filter [8]:

$$E_i^{(+)}(t) = \int d\omega \, f_i(\omega) e^{-\iota \omega (t - T_i)} \hat{a}_i(\omega). \qquad (2.66)$$

where $f_i(\omega)$ is the frequency-response function of the bandwidth filter in mode i, $\hat{a}_i^\dagger$ is the annihilation operator for that mode, and T_i is the time, which light in mode i needs to travel from the SPDC crystal to the detector.

---

[8]For the moment we do not take into account the quantum efficiency of the detector.

In HOM-type interference our interest rests on coincidence detection events. The probability amplitude for a two-photon detection event, where one photon is detected by detector D_1 at time t_1 and one photon is detected by detector D_2 at time t_2 is given by (see e.g. [83]):

$$A_2^{(1,2)}(t_1, t_2) = \langle \Omega | E_1^{(+)}(t_1) E_2^{(+)}(t_2) | \psi_{SPDC} \rangle, \tag{2.67}$$

where we used the superscript $(1,2)$ to indicate the modes of the photons involved. For an analytical evaluation of this probability amplitude it is convenient to assume $f(\omega_p)$ and $f_i(\omega_i)$ to be Gaussian [9]:

$$g(\omega) = \frac{1}{\sqrt{2\pi}\sigma_p} e^{-\frac{(\omega-\omega_{p0})^2}{2\sigma_p^2}}, \; f_i(\omega) = f_{i0} e^{-\frac{(\omega-\omega_{f_i0})^2}{2\sigma_{f_i}^2}}, \tag{2.68}$$

where ω_{p0} is the center frequency of the pump-pulse frequency distribution, and ω_{f_i0} denotes the center frequency of filter i. We use a normalized pump-frequency distribution, while the frequency-response functions of the filters have bandwidth independent peak transmittivities f_{i0}^2. Throughout this thesis the Greek letter σ is associated with r.m.s. bandwidths.

Let us assume that $\omega_0 \equiv \omega_{f_i0} = \frac{1}{2}\omega_{p0}$ (for $i = 1,2$). To simplify the notation we define $\Delta T_i = t_i - T_i - \tau_p$. Then equation 2.67 becomes:

$$A_2^{(1,2)}(\Delta T_1, \Delta T_2) = \frac{\sqrt{2\pi} f_{10} f_{20} \sigma_{f_1} \sigma_{f_2}}{\sqrt{\sigma_{f_1}^2 + \sigma_{f_2}^2 + \sigma_p^2}} e^{-\frac{(\Delta T_1 - \Delta T_2)^2 \sigma_{f_1}^2 \sigma_{f_2}^2 + (\Delta T_1^2 \sigma_{f_1}^2 + \Delta T_2^2 \sigma_{f_2}^2)\sigma_p^2}{2(\sigma_{f_1}^2 + \sigma_{f_2}^2 + \sigma_p^2)} - i(\Delta T_1 + \Delta T_2)\omega_0}. \tag{2.69}$$

In contrast to equ. 2.67 we used ΔT_i instead of t_i as the arguments of the function.

HOM interference with one SPDC pair

In the original experiment by Hong, Ou and Mandel [60], the photons of an SPDC pair were overlapped at a beam splitter (see fig. 2.7). If a coincidence is detected behind the beam splitter, the detected photons can either have both been reflected or transmitted at the beam splitter. Because the relative phase between the corresponding amplitudes is π (see equ. 2.60) we can write the two-photon probability amplitude as (for the definition of the modes a, b, c and d see figure 2.7):

$$A_2(t_c, t_d, T, \Delta\tau) \equiv A_2^{(c,d)}(t_c - T, t_d - T - \Delta\tau) - A_2^{(d,c)}(t_d - T, t_c - T - \Delta\tau), \tag{2.70}$$

where we defined $T \equiv T_c$ and $\Delta\tau \equiv T_d - T$.

---

[9]To assume Gaussian shapes can only be an assumption, the validity of which will be tested by comparing the theoretical predictions with the experimental results. The transmittivity curves, especially of the broader filters (3 nm) is nearly flat at the top. Any deviations from a Gaussian shapes should lead to a HOM dip, which is not of an exactly Gaussian shape either. How well our approximation of Gaussian functions works can therefore be estimated from the χ^2 values of the Gaussian fits to our experimental data (see chapter 7).
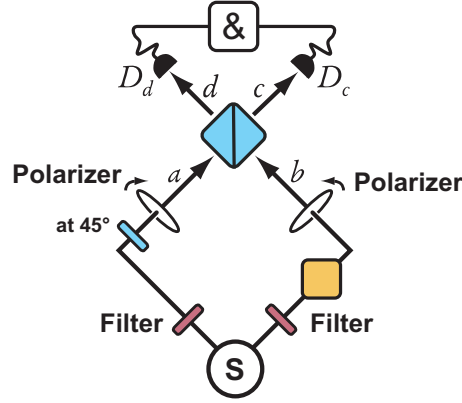
Figure 2.7.: HOM-type interference with one SPDC pair. Polarizers and a $\lambda/2$ plate assure that the two photons of the pair have identical polarizations. The two-photon coincidence rate behind the beam splitter is measured over a varying optical delay $\Delta\tau$.

The coincidence detection probability [10] *per pulse* is given by the time integral with respect to t_c and t_d over the square modulus of equ. 2.70:

$$P_2(\Delta\tau) = \frac{4\pi^2 f_0^4 \sigma_f^2}{\sqrt{2\sigma_f^2 \sigma_p^2 + \sigma_p^4}} \left(1 - e^{-\frac{1}{2}\Delta\tau^2 \sigma_f^2}\right). \tag{2.71}$$

Here, we assumed that $f_0 \equiv f_{10} = f_{20}$ and $\sigma_f \equiv \sigma_{f_1} = \sigma_{f_2}$.

P_2 approaches a constant value when $\Delta\tau$ becomes large compared to the coherence time of the interfering photons, which is σ_f^{-1}. For small $\Delta\tau$ the probability decreases, and it vanishes for $\Delta\tau = 0$. The interference pattern, which is obtained by varying $\Delta\tau$, has the form of constant plateau with a Gaussian dip. This modulation of the probability (or, equivalently, of the count rate) is known as *Hong-Ou-Mandel (HOM) dip*. It is the result of two-photon interference and has a maximum visibility of 100 %. Just like in the case of the light from two spontaneously decaying atoms, quantum predictions clearly exceed the maximal classical visibility of 50 % (see subsection 2.1.4).

The four-photon-detection probability amplitude

When we observe HOM-type interference with the photons of one SPDC pair, there is no need for us to worry about the timing between the photons, because the photons of a pair are created at the same time. If we want to observe HOM-type interference with photons

---

[10]To be precise, the quantities, which we denote as detection probabilities, are only proportional and not equal to the actual coincidence-detection probabilities per pulse. We will calculate the rates in 4.3.2.
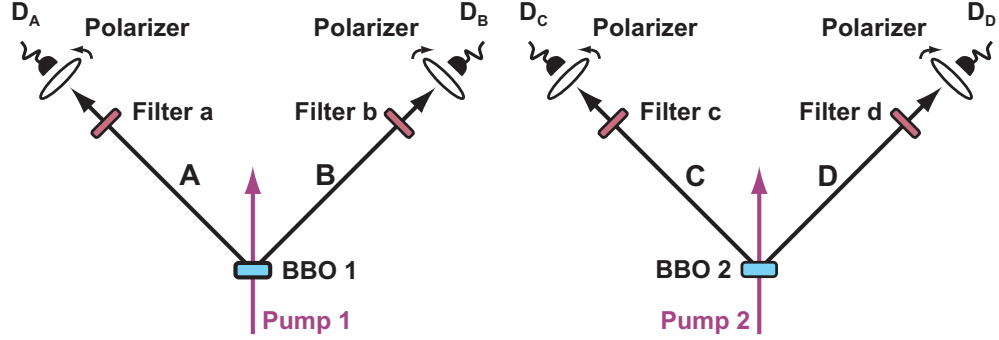
Figure 2.8.: Detection of two independently generated SPDC pairs. The probability amplitude for detecting the pair from source 1 with detectors D_A and D_B behind the filters a and b and the pair from source 2 with detectors D_C and D_D behind filters c and d at times t_A, t_B, t_C and t_D, respectively, is $A^{(a,b;A,B;c,d;C,D)}(t_1, t_2, t_3, t_4)$. All sub indices can take values from 1 to 4. In our case, each SPDC source consists of an ultra-violet pulsed laser beam pumping a β-Barium-Borate (BBO) crystal.

from independent SPDC sources, the situation is different. In our experiment we used pulsed SPDC sources. To guarantee the indistinguishability of the photons originating from independent pulsed sources, their emission times have to be synchronized (see also [141, 142]).

Because the presence of the interfering photons in this case is indicated by the trigger detection events of their partner photons, we effectively are observing four-fold-coincidence detection events (see fig. 2.9). The probability amplitudes for these four-fold events can be written as products of two-fold probability amplitudes because the emission processes in the two sources are independent of each other. In contrast to our earlier treatment it will be important to state not only the mode of each photon but also the filter, which it passes through, and the crystal, which it is created in. To describe the latter we will often talk of pulse 1 or 2, which is a short way to denote the pulse pumping crystal 1 or 2. To this end we will introduce a new notation for the two-photon-detection probability amplitudes. The amplitude for a photon pair created by the pump pulse $i = 1, 2$, where the photons in modes j and k pass through filters m and l, respectively, will be denoted as $A_2^{[i;j,k;m,l]}$. We also have to modify the notation for the electric-field operators at the detectors, e.g.:

$$E_{j,m}^{(+)}(t) \equiv \int d\omega \, f_m(\omega) e^{-\imath \omega (t - T_j)} \hat{a}_j(\omega). \tag{2.72}$$

With this new notation we can write the four-photon-detection probability amplitude as

(see fig. 2.8):

$$
\begin{aligned}
A_4^{(a,b;A,B;c,d;C,D)}(t_1,t_2,t_3,t_4) &= \langle\Omega|E_{A,a}^{(+)}(t_A)E_{B,b}^{(+)}(t_B)|\psi_{SPDC}^{(1)}\rangle\langle\Omega|E_{C,c}^{(+)}(t_C)E_{D,d}^{(+)}(t_D)|\psi_{SPDC}^{(2)}\rangle \\
&= A_2^{[1;A,B;a,b]}(t_A,t_B)A_2^{[2;C,D;c,d]}(t_C,t_D),
\end{aligned}
\tag{2.73}
$$

where the superscript $(a,b;A,B;c,d;C,D)$ indicates that the photons of the pair from pulse 1 (2) pass through filters a and b (c and d) and are detected by detectors D_A and D_B (D_C and D_D), respectively. The superscripts of the states indicate the source, which the corresponding pair originates from. This detailed notation is not strictly necessary for the problem discussed here because we will assume all filters to have equal center frequencies. The notation will be useful in cases where this assumption does not hold, and to employ it will become inevitable in the slightly different situation that we are going to discuss in appendix A.

Let us assume that $\sigma_S \equiv \sigma_{f_2} = \sigma_{f_3}$, $\sigma_T \equiv \sigma_{f_1} = \sigma_{f_4}$, $f_S \equiv f_{20} = f_{30}$, $f_T \equiv f_{10} = f_{40}$, $\sigma_p \equiv \sigma_{pi}$, and $\omega_0 \equiv \omega_{f_m 0} = 2\omega_{pi0}$ (for $m = 1,2,3,4$ and $i = 1,2$). Here, ω_{pi0} denotes the center frequencies and σ_{pi} denotes the bandwidths of the frequency distributions of the two pumps. τ_{pi} is the arrival time of the ith pump in the ith crystal. To simplify matters further, we will assume that the optical path lengths from crystals to detectors are the same for all of the four modes, i.e. we can choose $T_m = 0$ for all m, and we define $\Delta T_{im} \equiv t_m - \tau_{pi}$. Finally, we will only consider cases where the filters f_1 and f_4 are associated with the modes 1 and 4, respectively. That means we will only consider amplitudes of the form $A_4^{(1,b;1,B;c,4;C,4)}$. Employing all these assumptions we can write equ. 2.73 as ($b,c = 2,3$ and $B,C = 2,3$):

$$
A_4^{(1,b;1,B;c,4;C,4)}(t_1,t_2,t_3,t_4) = \frac{2\pi f_S^2 f_T^2 \sigma_S^2 \sigma_T^2}{\sigma_T^2 + \sigma_S^2 + \sigma_p^2} \, e^{-\frac{\left[(\Delta T_{11}-\Delta T_{1B})^2 + (\Delta T_{24}-\Delta T_{2C})^2\right]\sigma_S^2 \sigma_T^2}{2(\sigma_T^2+\sigma_S^2+\sigma_p^2)}}
$$

$$
\times \, e^{-\frac{\left[\left(\Delta T_{11}^2+\Delta T_{24}^2\right)\sigma_T^2 + \left(\Delta T_{1B}^2+\Delta T_{2C}^2\right)\sigma_S^2\right]\sigma_p^2}{2(\sigma_T^2+\sigma_S^2+\sigma_p^2)} - \imath(\Delta T_{11}+\Delta T_{1B}+\Delta T_{24}+\Delta T_{2C})\omega_0}.
\tag{2.74}
$$

HOM interference with two SPDC pairs

Like in our discussion of HOM-type interference with one SPDC pair, we have to add two four-fold amplitudes:

$$
A_4^{HOM}(t_1,t_2,t_3,t_4) = A_4^{(1,2;1,3;3,4;2,4)} - A_4^{(1,2;1,2;3,4;3,4)},
\tag{2.75}
$$

where the first term on the right-hand side corresponds to the case where both photons are transmitted, and the second term corresponds to the case where both photons are reflected (see fig. 2.9). The second term has a minus sign because each reflection contributes a relative phase $\imath$.

The four-fold-coincidence detection probability will be given by the square modulus of
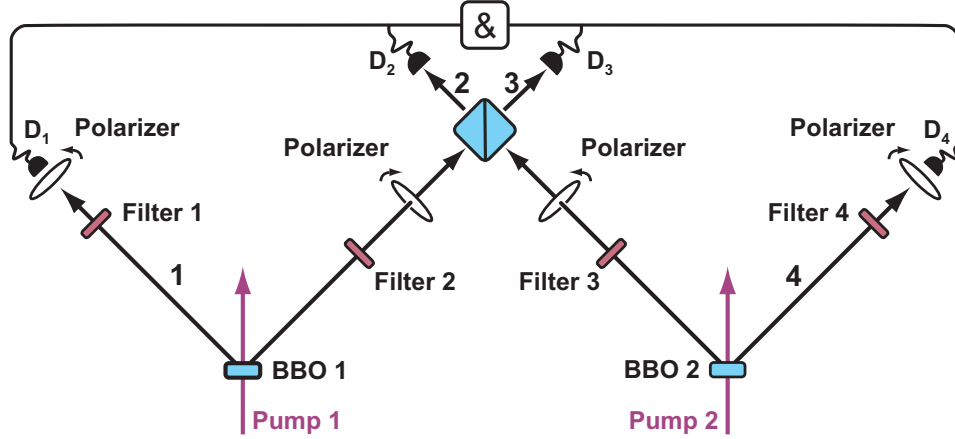
Figure 2.9.: HOM-type interference with two independently generated triggered single photons. Trigger events in the detectors D_1 and D_4 indicate the presence of photons in the input modes of the beam splitter. If the detection events in detectors D_2 and D_3 do not allow to determine the origin of the detected photons, there will be no four-fold coincidences. The rate of four-fold coincidences is measured over the relative time delay $\Delta\tau$ between the two laser pulses pumping the BBO crystals.

the probability amplitude integrated over [11] t_1, t_2, t_3 and t_4:

$$
\begin{aligned}
P_4(\Delta\tau) &= \int d^4t \left| A_4^{HOM}(t_1, t_2, t_3, t_4) \right|^2 \\
&= \frac{8\pi^4 f_S^4 f_T^4 \sigma_S^2 \sigma_T^2}{\sigma_p^2 (\sigma_p^2 + \sigma_S^2 + \sigma_T^2)} \left[1 - \sigma_p \sqrt{\frac{\sigma_p^2 + \sigma_S^2 + \sigma_T^2}{(\sigma_p^2 + \sigma_S^2)(\sigma_p^2 + \sigma_T^2)}} e^{-\frac{\Delta\tau^2 \sigma_p^2 \sigma_S^2}{2(\sigma_p^2 + \sigma_S^2)}} \right],
\end{aligned}
\tag{2.76}
$$

where we introduced $\Delta\tau \equiv \tau_{p2} - \tau_{p1}$. We see that, just like in the case of HOM interference with one SPDC pair, the asymptotically constant four-photon detection probability exhibits a HOM dip for small $\Delta\tau$.

From equation 2.76 we can calculate the visibility of the HOM-type interference with two independently generated triggered single photons to be:

$$
V^{HOM} = \frac{P(\Delta\tau \to \infty) - P(\Delta\tau \to 0)}{P\Delta\tau \to \infty} = \sigma_p \sqrt{\frac{\sigma_p^2 + \sigma_S^2 + \sigma_T^2}{(\sigma_p^2 + \sigma_S^2)(\sigma_p^2 + \sigma_T^2)}}.
\tag{2.77}
$$

---

[11]The integration over the detection times reflects the fact that the integration times are much longer than the time resolution of the detectors.

The r.m.s. width of the HOM dip is given by:

$$\sigma^{HOM} = \frac{\sigma_p^2 + \sigma_S^2}{\sigma_p^2 \sigma_S^2} = \sqrt{\sigma_p^{-2} + \sigma_S^{-2}}. \tag{2.78}$$

Prior to our work, M. Żukowski et al. [142] investigated the visibility of HOM-type interference with photons from SPDC sources pumped by pulsed lasers. They derived the following expression:

$$V_Z = \frac{\sigma_p}{\sqrt{\sigma_S^2 + \sigma_p^2}}. \tag{2.79}$$

In the limit $\sigma_T \to \infty$ our results are in agreement with theirs:

$$V_Z = \lim_{\sigma_T \to \infty} \left[\sigma_p \sqrt{\frac{\sigma_p^2 + \sigma_S^2 + \sigma_T^2}{(\sigma_p^2 + \sigma_S^2)(\sigma_p^2 + \sigma_T^2)}} \right] = \frac{\sigma_p}{\sqrt{\sigma_S^2 + \sigma_p^2}}. \tag{2.80}$$

2.3.3. Discussion of our results for the HOM-type interference visibility

In contrast to the two-photon case, the visibility of the interference (see equ. 2.77) depends not only on the bandwidths of the filters but also on the bandwidth of the pump pulses. Moreover, the width of the HOM dip does not only depend on the filter bandwidths but also on the pump bandwidth. To understand the physical meaning of this dependence let us investigate the extreme situations where we do not have filters in either the trigger or the signal modes, i.e. for the limits $\sigma_T \to \infty$ and $\sigma_S \to \infty$, respectively:

$$\lim_{\sigma_{T,S} \to \infty} V = \frac{\sigma_p}{2\sqrt{\sigma_p^2 + \sigma_{S,T}^2}}. \tag{2.81}$$

We can conclude that it is sufficient to have filters in either both of the trigger modes or in both of the signal modes. Yet, the bandwidths of the filters present (either σ_S or σ_T) must be small compared to σ_p in order to achieve high interference visibility. That means the coherence times of either the signal or the trigger photons must be longer than the length of the pump-pulse. Otherwise the origin of the detected photons could be determined either via the detection times themselves (in detectors D_2 and D_3) or via the detection times of the corresponding trigger photons (in detectors D_1 and D_4).

2.3.4. HOM-type interference with reduced visibility

Up to now we only considered HOM-type interference under perfect conditions. For example, we assume that the interfering photons are completely indistinguishable, that the

pump pulses are Fourier limited [12] and that there is exactly one photon in each of our spatial modes. Here, we are going to consider deviations from these perfect conditions and how these deviations reduce the interference visibility.

Including the effect of relative-timing jitter

Even if the laser pulses pumping the two SPDC processes are not originating from independent lasers, the timing of the two pulses is in general not perfectly stable. This is due to group-velocity dispersion in various optical components of the setup. A detailed description of causes of relative-timing jitter between the laser pulses and SPDC photons will be given in section 5.2.

We use the term "jitter" to describe random fluctuations of the timing between individual laser pulses. Let us assume we have two, possibly independent, pulse sequences. If the time interval T between two successive pulses in each sequence were constant, and if it were the same for both pulse sequences, the time delay between corresponding pulses of the two sequences, i.e. the time delay between the first pulses of every sequence, the second pulses of every sequence and so on, would also be constant. We shall denote this ideal, constant time delay as T_0. For example, in our treatment of HOM-type interference with two SPDC pairs (see above) we would have $T_0 = \tau_{p2} - \tau_{p1}$.

Now let us introduce relative-timing jitter. That means we will no longer assume the time interval between successive pulses to be constant but to randomly vary around its ideal value T. Let us use $\Delta\tau_\mu$ to denote the time delay between the μth pulses of the two pulse sequences. We can write $\Delta\tau_\mu = T_0 + J_\mu$, where we introduced the random variable J_μ, which corresponds to what we call "jitter".

In our theoretical treatment of HOM-type interference we always concentrated on single laser pulses out of sequences of pulses to pump the SPDC process. Therefore, we will drop the index μ and only consider a random variable J, which can take any value according to some probability distribution $D_J(J)$. We can assume this probability distribution to be Gaussian [13]:

$$D_J(J) = \frac{1}{\sqrt{2\pi}\sigma_J} e^{-\frac{J^2}{2\sigma_J^2}}. \tag{2.82}$$

The influence of timing jitter on the four-fold detection probability can be seen as a simple average of the four-fold probability over the relative time delay weighted by the jitter distri-

---

[12]Laser pulses are called Fourier limited if their duration is equal to the inverse of the spectral bandwidth of the laser output.

[13]Because the relative-timing jitter depends on many parameters (e.g. fluctuations of positions and orientations of optical components in the laser cavity) we can apply the central-limit theorem (see e.g. [83], page 30). This holds true as long as we can assume that the parameters, on which the jitter depends, fluctuate independently of each other. Long-time drifts are an example where this assumption of independent fluctuations fails (see subsection 7.1.2). These can, for example, be due to a change in the overall laboratory temperature.

bution. In other words, the modified four-fold-coincidence detection probability $P_4^{(J)}$ is the convolution of D_J and P_4:

$$
\begin{aligned}
P_4^{(J)} &= \int dJ P_4(\Delta\tau - J) D_J(J) \\
&= \frac{8\pi^4 f_S^4 f_T^4 \sigma_S^2 \sigma_T^2}{\sigma_p^2(\sigma_p^2 + \sigma_S^2 + \sigma_T^2)} \left[1 - \frac{\sigma_p \sqrt{\sigma_S^2 + \sigma_T^2 + \sigma_p^2}}{\sqrt{\sigma_T^2 + \sigma_p^2}\sqrt{\sigma_S^2 + \sigma_p^2 + \sigma_S^2 \sigma_p^2 \sigma_J^2}} e^{-\frac{\Delta\tau^2 \sigma_S^2 \sigma_p^2}{2(\sigma_S^2 + \sigma_p^2 + \sigma_S^2 \sigma_p^2 \sigma_J^2)}} \right].
\end{aligned} \tag{2.83}
$$

Here, it should be noted that the units in this and the following equations are correct. The unit of σ_J is time, the unit of σ_p, σ_S and σ_T is frequency. The HOM-dip visibility including relative-timing jitter is:

$$
V_J^{HOM} = \frac{\sigma_p \sqrt{\sigma_S^2 + \sigma_T^2 + \sigma_p^2}}{\sqrt{\sigma_T^2 + \sigma_p^2}\sqrt{\sigma_S^2 + \sigma_p^2 + \sigma_S^2 \sigma_p^2 \sigma_J^2}}, \tag{2.84}
$$

and the r.m.s. dip width is

$$
\sigma_J^{HOM} = \frac{\sigma_S^2 + \sigma_p^2 + \sigma_S^2 \sigma_p^2 \sigma_J^2}{\sigma_p^2 \sigma_S^2} = \sqrt{\sigma_S^{-2} + \sigma_p^{-2} + \sigma_J^2}. \tag{2.85}
$$

Partial distinguishability

In our treatment of HOM-type interference we did not take into account the polarization of the interfering photons. This is justified as long as we adjust the various polarizers in modes 1 to 4 (see fig. 2.9) adequately in order to guarantee the indistinguishability of the photons.

Suppose that we rotate the polarizers in the input modes of the BS relative to each other [14]. Let the polarization states prepared by the polarizers be denoted as $|\chi_1\rangle$ and $|\chi_2\rangle$. Because of the partial distinguishability of the states we get the following modified form of the four-photon detection probability:

$$
P_4^{(J)} = \frac{8\pi^4 f_S^4 f_T^4 \sigma_S^2 \sigma_T^2}{\sigma_p^2(\sigma_p^2 + \sigma_S^2 + \sigma_T^2)} \left[1 - |\langle\chi_1|\chi_2\rangle|^2 \frac{\sigma_p \sqrt{\sigma_S^2 + \sigma_T^2 + \sigma_p^2}}{\sqrt{\sigma_T^2 + \sigma_p^2}\sqrt{\sigma_S^2 + \sigma_p^2 + \sigma_S^2 \sigma_p^2 \sigma_J^2}} e^{-\frac{\Delta\tau^2 \sigma_S^2 \sigma_p^2}{2(\sigma_S^2 + \sigma_p^2 + \sigma_S^2 \sigma_p^2 \sigma_J^2)}} \right]. \tag{2.86}
$$

We see that if the two states are orthogonal to each other, the interference will vanish because the origin of the photons could with certainty be determined from their polarization. The dip visibility for partially distinguishable photons with respect to the visibility for indistinguishable photons is:

$$
V_{J,partial}^{HOM} = V_J^{HOM} |\langle\chi_1|\chi_2\rangle|^2. \tag{2.87}
$$

---

[14]If the pairs emitted by the SPDC source are entangled, the polarizers in modes 1 and 4 must be rotated accordingly in order to keep the pair rates constant.

Let us investigate what will happen if we remove all polarizers. Because we do not determine the polarization of the trigger photons, the reduced density matrix of each of the interfering photons will be completely mixed. We can write the two-photon density matrix as

$$\rho = \frac{1}{4}(|HH\rangle\langle HH| + |HV\rangle\langle HV| + |VH\rangle\langle VH| + |VV\rangle\langle VV|), \tag{2.88}$$

which can be interpreted as both photons having either equal or orthogonal polarizations with respect to each other. Both cases occur with equal probability.

To calculate the four-photon detection probability we take the mean value of $P_4^{(J)}$ for $|\langle\chi_1|\chi_2\rangle|^2 = 1$ and $|\langle\chi_1|\chi_2\rangle|^2 = 0$ (see equ. 2.86). The result is equivalent to the case, where $|\langle\chi_1|\chi_2\rangle|^2 = \frac{1}{2}$, and the visibility is:

$$V_{J,unpol}^{HOM} = \frac{1}{2}V_J^{HOM}. \tag{2.89}$$

For the special case where $V_J^{HOM} = 1$ the HOM-type interference visibility with unpolarized photons is $\frac{1}{2}$.

HOM-type interference without trigger photons

When we measure HOM-type interference with two SPDC pairs, the trigger events guarantee to high accuracy the presence of only one photon in each of the input modes of the beam splitter. If we disregard the trigger events, the number of photons in the interfering modes will be uncertain. The photon statistics will be equivalent to that of a thermal source (see below). That means by disregarding the trigger events we can simulate HOM interference with photons emitted by two independent thermal sources.

The probability $p(n)$ for an SPDC source to emit n photon pairs decreases exponentially with n. It can be written in the form:

$$p(n) = C\alpha^n. \tag{2.90}$$

Here, α is some constant depending on the efficiency of the SPDC source (for the sake of brevity we will denote it as the SPDC "efficiency") and C is a normalization factor. C can be determined from the normalization condition:

$$1 = \sum_{n=0}^{\infty} p(n) = C\sum_{n=0}^{\infty}\alpha^n = \frac{C}{1-\alpha}. \tag{2.91}$$

That means we have:

$$p(n) = (1-\alpha)\alpha^n. \tag{2.92}$$

This is similar to a thermal source, where the photon-number distribution is (see e.g. [83]):

$$p_{\text{th}}(n) = (1 - e^{-\beta})e^{-\beta n}. \tag{2.93}$$

Here, we used the usual dimensionless ratio $\beta = \hbar\omega/k_B T$ ($k_B \approx 1.38 \times 10^{-23} J/K$ is Boltzmann's constant).

By comparing $p(n)$ with $p_{th}(n)$ we see that they are equivalent if $\alpha = e^{-\beta}$. In other words: the statistics governing the pair emission of an SPDC source (with "efficiency" α) are equivalent to the photon statistics of a thermal source with $\beta = -\ln(\alpha)$. Although we couple only one spatial mode of the SPDC emission into the beam splitter the statistics of the photons in that mode will be equal to that of the emitted SPDC pairs because we neglect the trigger events.

To calculate the visibility of HOM interference in this case we will only take into account one- and double-pair emissions [15]. Suppose that p_1 and p_2 are the probabilities per pulse for source 1 and 2, respectively, to emit a photon pair. Photons detected in coincidence behind the beam splitter can either both originate from source 1, or both from source 2, or one from each source. Only in the latter case it is possible to observe HOM-type interference.

Under these conditions the overall two-fold probability is [16]:

$$P^{(J)}_{\text{untriggered}} \propto p_1^2 + p_2^2 + p_1 p_2 \left[1 - \frac{\sigma_p \sqrt{\sigma_S^2 + \sigma_T^2 + \sigma_p^2}}{\sqrt{\sigma_T^2 + \sigma_p^2} \sqrt{\sigma_S^2 + \sigma_p^2 + \sigma_S^2 \sigma_p^2 \sigma_J^2}} e^{-\frac{\Delta\tau^2 \sigma_S^2 \sigma_p^2}{2(\sigma_S^2 + \sigma_p^2 + \sigma_S^2 \sigma_p^2 \sigma_J^2)}} \right], \qquad (2.94)$$

which results in a dip visibility of

$$V^{HOM}_{\text{untriggered}} = \frac{p_1 p_2 V_J^{HOM}}{p_1 p_2 + p_1^2 + p_2^2}. \qquad (2.95)$$

For the special case, where $p_1 = p_2$ and $V_J^{HOM} = 1$, this yields $\frac{1}{3}$.

2.3.5. Realization of a Bell-state measurement using HOM-type interference

The projection on Bell-states (see equ. 1.58) is an important application of HOM-type interference. An implementation of a Bell-state measurement (BSM) with linear optics can perfectly distinguish between two out of the four Bell states [32] at the most. The first realization of a Bell-state measurement using HOM-type interference was used by Mattle et al. to demonstrate super-dense coding [86].

Here, we are going to discuss the principles of the most simple implementation of a Bell-state measurement with HOM-type interference, which allows to distinguish one out of four Bell states. For a more-efficient layout for a Bell-state measurement (like the one in [86]) see subsection 6.5.2.

---

[15]For our sources the SPDC efficiencies are small enough ($\sim 10^{-2}$) for this approximation to be very accurate.
[16]The probability for a double-pair emission will not be exactly $p_{1,2}^2$ but for low pair-production rates the error of this assumption is only on the order of one percent.

The principal layout is the same as for normal HOM-type interference (see fig. 2.5). The only difference is that we allow the interfering photons to have arbitrary states of polarization, which we represent by their density matrices ρ_a and ρ_b, respectively. Let $\rho_{ij}^{(a)}$ and $\rho_{km}^{(b)}$ denote the elements of their representations in the HV basis.

We can write the two-photon state before the beam splitter as (we sum over repeated indices):

$$\rho = \rho_{ij}^{(a)} \rho_{km}^{(b)} \hat{a}_{a,i}^\dagger \hat{a}_{b,k}^\dagger |\Omega\rangle\langle\Omega| \hat{a}_{b,m} \hat{a}_{a,j}, \qquad (2.96)$$

where $\hat{a}_{a,i}^\dagger$ denotes the creation operator for a photon of polarization $i = H, V$ in mode a. After the beam splitter, this becomes (see equ. 2.61):

$$
\begin{aligned}
\rho' \;=\; & \frac{1}{4} \rho_{ij}^{(a)} \rho_{km}^{(b)} \left[(\hat{a}_{c,i}^\dagger \hat{a}_{d,k}^\dagger - \hat{a}_{d,i}^\dagger \hat{a}_{c,k}^\dagger) + (\hat{a}_{c,i}^\dagger \hat{a}_{c,k}^\dagger - \hat{a}_{d,i}^\dagger \hat{a}_{d,k}^\dagger) \right] |\Omega\rangle\langle\Omega| \;\times \\
& \left[(\hat{a}_{d,m} \hat{a}_{c,j} - \hat{a}_{c,m} \hat{a}_{d,j}) + (\hat{a}_{d,m} \hat{a}_{d,j} - \hat{a}_{c,m} \hat{a}_{c,j}) \right].
\end{aligned}
\qquad (2.97)
$$

The coincidence probability P_c to detect both photons independent of their polarization is:

$$P_c = \mathrm{Tr}\left(\hat{a}_{c,r}^\dagger \hat{a}_{c,r} \hat{a}_{d,s}^\dagger \hat{a}_{d,s} \rho' \right) \qquad (2.98)$$

The trace is over all Fock states in modes c and d. Because we start with a two-photon state, the only contributions can come from states, where one photon is in each mode (there can be no more):

$$P_c = \langle\Omega| \hat{a}_{c,n_1} \hat{a}_{d,n_2} \left(\hat{a}_{c,r}^\dagger \hat{a}_{c,r} \hat{a}_{d,s}^\dagger \hat{a}_{d,s} \rho' \right) \hat{a}_{d,n_2}^\dagger \hat{a}_{c,n_1}^\dagger |\Omega\rangle. \qquad (2.99)$$

If we evaluate this by employing the commutation relations $[\hat{a}_{x,i}^\dagger, \hat{a}_{y,j}] = \delta_{xy}\delta_{ij}$ (all others vanish), we will get:

$$P_c = \frac{1}{4} \rho_{ij}^{(a)} \rho_{km}^{(b)} (\delta_{n_1 r} \delta_{ri} \delta_{n_2 s} \delta_{sk} - \delta_{n_1 r} \delta_{rk} \delta_{n_2 s} \delta_{si})(\delta_{mn_2} \delta_{jn_1} - \delta_{mn_1} \delta_{jn_2}). \qquad (2.100)$$

This can be reduced to:

$$P_c = \frac{1}{2} \rho_{ij}^{(a)} \rho_{km}^{(b)} (\delta_{mk}\delta_{ji} - \delta_{mi}\delta_{jk}) = \frac{1}{2} - \frac{1}{2} \rho_{ij}^{(a)} \rho_{ji}^{(b)}. \qquad (2.101)$$

The coincidence probability is $\frac{1}{2}$ if the photons are orthogonally polarized and $\frac{1}{4}$ if they are unpolarized.

To determine, which two-photon state we projected our photons on, let us divide equation 2.100 by $4P_c$ and rewrite it as[17]:

$$
\begin{aligned}
1 \;=\; & \langle n_1, n_2| \left[|r,s\rangle \frac{1}{4P_c} \rho_{ij}^{(a)} \rho_{km}^{(b)} (\delta_{ri}\delta_{sk} - \delta_{rk}\delta_{si})(\delta_{mk_2}\delta_{jk_1} - \delta_{mk_1}\delta_{jk_2}) \langle k_1, k_2| \right] |n_1, n_2\rangle \\
\;=\; & \langle n_1, n_2| \rho^{(p)} |n_1, n_2\rangle.
\end{aligned}
\qquad (2.102)
$$

---

[17] We regard n_1 and n_2 as indices. Because they appear repeatedly, we sum over them. Examples for this notation are $\langle k|k\rangle = \langle H|H\rangle + \langle V|V\rangle$ and $A_m|m\rangle = A_H|H\rangle + A_V|V\rangle$.

$\rho^{(p)}$ is the density matrix (in polarization space), which we will project the two photons on if they leave the BS via different output ports. Its representation in the HV basis is:

$$
\begin{aligned}
\rho^{(p)}_{l_1,l_2;k_1,k_2} &= \frac{1}{4P_c}\rho^{(a)}_{ij}\rho^{(b)}_{km}(\delta_{l_1 i}\delta_{l_2 k} - \delta_{l_1 k}\delta_{l_2 i})(\delta_{mk_2}\delta_{jk_1} - \delta_{mk_1}\delta_{jk_2}) \\
&= \frac{1}{4P_c}(\rho^{(a)}_{l_1 k_1}\rho^{(b)}_{l_2 k_2} - \rho^{(a)}_{l_2 k_1}\rho^{(b)}_{l_1 k_2} - \rho^{(a)}_{l_1 k_2}\rho^{(b)}_{l_2 k_1} + \rho^{(a)}_{l_2 k_2}\rho^{(b)}_{l_1 k_1}).
\end{aligned} \tag{2.103}
$$

We can see that this vanishes whenever $l_1 = l_2$ or $k_1 = k_2$. In all other cases it is equal to $\pm\frac{1}{2}$. Let us write it in matrix form:

$$
\rho^{(p)} = \begin{pmatrix} 0 & 0 & 0 & 0 \\ 0 & \frac{1}{2} & -\frac{1}{2} & 0 \\ 0 & -\frac{1}{2} & \frac{1}{2} & 0 \\ 0 & 0 & 0 & 0 \end{pmatrix}. \tag{2.104}
$$

This is indeed the density matrix of ψ^- in the HV basis.

We see that the knowledge that there is exactly one photon in each output mode of the beam splitter is enough to project the two-photon state on ψ^- independent of the original states of the photons.

3. Earlier Experiments

In the first experiment presented in this thesis we demonstrated HOM interference with photons originating from fully independent sources. To fully understand the implications of this experiment it is useful to see it in the historic context of previous related attempts. Specifically, we will discuss earlier ventures to demonstrate the interference of independent photons and related experiments, which could be viewed as their precursors [1]

I divided this review into three sections. The first one covers transient interference of independent classical sources, culminating in the experiments of Mandel and his colleagues. In the second section we discuss the seminal interference experiments by Hanbury Brown and Twiss. They observed higher-order classical interference of many independent but spatially-coherent sources. Finally, in the third section, we are going to review a number of two-photon experiments. For an overview of the works referred to in the third section see fig. 3.1.

3.1. Transient interference with independent classical fields

The experiments attempting to demonstrate interference with independent photons had several motivations. One of these was the quotation of Dirac that "each photon interferes only with itself" [40]. In the context of two-photon interference it has sometimes been concluded (see e.g. [94]) that Dirac's statement was erroneous. This is not true. On the one hand, Dirac referred to simple second-order interference only and, on the other hand, it can be argued that interference "between" photons does indeed never occur. What we observe is the interference due to the superposition of the probability amplitudes for indistinguishable detection events [99, 69].

Other motivations were the upcoming of the laser and later the availability of single photon sources, which offered up to then unknown possibilities to investigate the coherence properties of light.

3.1.1. Beating of light from independent sources

The earliest experiments that addressed the question at hand tried to demonstrate beating between light from independent sources. Beating results from the superposition of light

---

[1]The diploma thesis of B. Blauensteiner [17] contains an excellent overview over some of the earlier experiments, which we will discuss here.
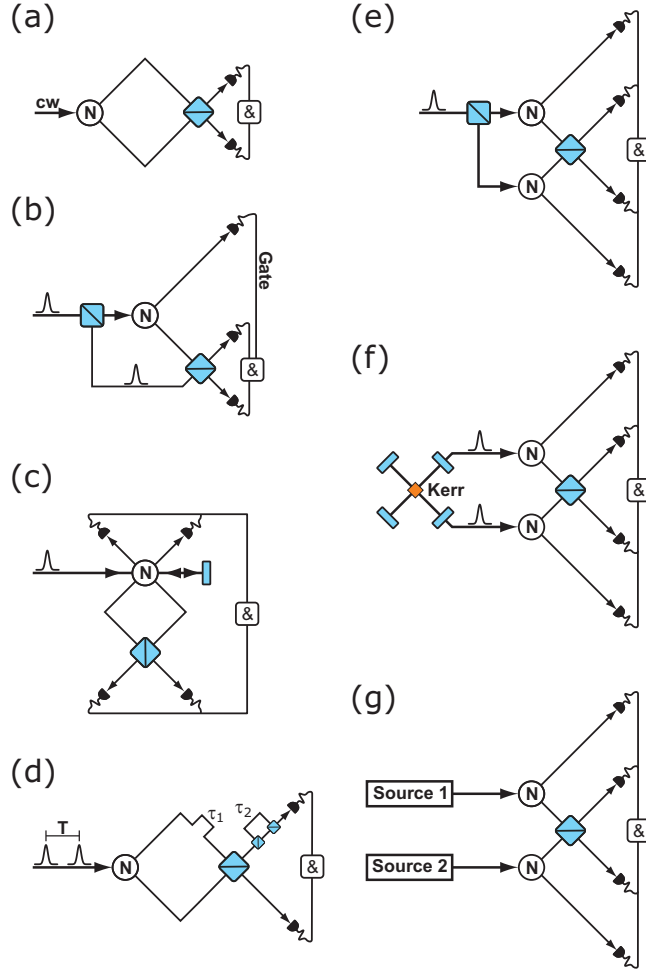
Figure 3.1.: Schematics of the various experiments on two-photon interference using SPDC. N denotes the nonlinear media used to create the photon pairs. In the illustrated cases these are SPDC crystals. **(a)** The two photons of one SPDC pair are overlapped at a beam splitter [60]. **(b)** An attenuated part of the pump beam is overlapped with a photon from an SPDC pair. The coincidences are gated on the detection of the second photon of the SPDC pair [101]. **(c)** Two SPDC pairs are created in a double-pass configuration. The interfering photons are heralded by the detection of their partner photons [24]. **(d)** Interference of two bi-photons generated by coherent pump pulses from the same laser [69]. **(e)** A beam splitter is used to pump two spatially separated SPDC crystals with one pump laser. Two-photon interference is observed with triggered single photons [37]. **(f)** Two intersecting laser cavities produce pulses, which are used to pump spatially separated SPDC crystals. Two-photon interference is utilized to demonstrate entanglement swapping [135]. **(g)** Two independent sources are used to pump spatially separated SPDC crystals. In our experiment [67] the two sources are pulsed and time synchronized. A recent experiment [59] makes use of continuous-wave sources and sub-coherence-time detection.

fields with neighboring frequencies. In the case of fields that have no stable phase relation, beating can only be observed if the integration time is shorter than the coherence times of the light fields (see subsection 2.1.3).

Beating of light from incoherent spectral lines

Forrester et al. [46] were the first to observe beating of incoherent light fields. They used light from two Zeeman components of the green line ($\lambda = 546.1$ nm) of Hg^{202}, which was contained in a discharge tube in the presence of a magnetic field of ~ 1000 Gauss. Let us denote the width of the lines as δ and their center frequencies as f_1 and f_2. The various frequency components of one line as well as the components from two lines are incoherent with respect to each other. Over time scales shorter than $\frac{1}{\delta}$, which is the coherence time of the light from one line, their relative phase can be approximated to be constant. A prerequisite to observe beating is that the frequency difference $\Delta = f_2 - f_1$ fulfills [2] $\Delta > 2\delta$. The two incoherent light fields were overlapped on a photo cathode. Its integration time was small compared to $\frac{1}{\delta}$ in order to have a phase relation stable enough not to wash out the beating signal. A resonant cavity tuned to Δ was used to detect the fluctuations of the photo current. With their ingenious setup they managed to reduce the background noise in their apparatus by four orders of magnitude and measured the beating signal. The presence of the beating signal proved the occurrence of transient interference between the incoherent light fields.

Beating of light from independent masers

The results of Javan, Ballik and Bond [62] also demonstrated beating of incoherent light fields. Instead of using one source to generate two incoherent light fields they did indeed use two spatially separate independent sources: two masers that were used as free-running oscillators, i.e. without frequency stabilization. In contrast to Forrester et al. [46] it was not their aim to demonstrate interference between independent sources. Rather they used the effect in order to measure the stability of the wavelengths of the light emitted by their masers.

3.1.2. Spatial interference of light from independent sources

While transient interference of light from independent sources had been demonstrated indirectly by the experiments described above, the question remained if it was possible to directly observe interference patterns. The intention of these experiments was already much closer to our own. They concerned themselves with the question if such interference were observable on the single-photon level and whether it would signify interference "between"

---

[2]Otherwise the phase would not be stable over a long enough period of time to observe a reasonable number of beats.

independent photons. As we will see the results could be explained in terms of classical interference, and it could not be interpreted as interference of independent photons.

Double-slit interference with independent masers

Magyar and Mandel [81] were the first to directly demonstrate spatial interference of light from independent sources. In their case, these sources were ruby masers. Their experiment is effectively the observation of a double-slit interference pattern, where each slit is illuminated by one of the independent masers. The integration time was on the order of 40 ns [3], which was short compared to the coherence time of the masers (~ 500 ns). They observed interference fringes of about 15 % visibility.

The authors specifically address the question whether they observed interference between independent photons. They conclude that their results are [81] "describable in completely classical terms", i.e. it is single-photon [4] and *not* two-photon interference.

Experiments with attenuated laser beams

The next important step in this line of experiments was performed by Pfleegor and Mandel [98] and later by Radloff [100]. They demonstrated interference between strongly attenuated independent laser beams. The attenuation was strong enough to necessitate single-photon detection.

In [98] attenuated laser beams were overlapped at a small angle θ relative to each other on the interference detector R (see fig. 3.2). R consisted of parallel glass plates. Their thickness corresponded to the expected distance between the interference fringes. These glass plates alternatingly guided the photons to either of the two photo multipliers (A or B). Because of the random phase between the two independent lasers the position of the interference fringes was unstable. Although it was impossible to predict whether A or B would register more counts, events in A and B had to be anti-correlated. For instance, if the maxima of the interference pattern coincided with the glass plates connected to A, the minima would have to coincide with the glass plates connected to B. As a result high count rates in A are correlated to low count rates in B. The nature of these correlations is the same as in the Hanbury-Brown-Twiss effect (see section 3.2).

By confirming these anti-correlations the experiment of Pfleegor and Mandel provided indirect evidence for the presence of a transient interference pattern. In order to optimize the signal-to-noise ratio the authors gated R on a beat signal between the two lasers. By activating R only when the frequency of the beat signal was below a threshold of of 50 KHz they assured that the frequencies of the lasers were sufficiently close to each other. This was

---

[3]The intensities of the output of the two masers was observed with photodetectors. These were connected to a coincidence unit. Each coincidence of intensity spikes was fed to a pulse generator that gated the image tube with pulses of 40 ns duration.

[4]The quantum-mechanical description of single-photon interference is equivalent to the interference of classical electromagnetic fields.
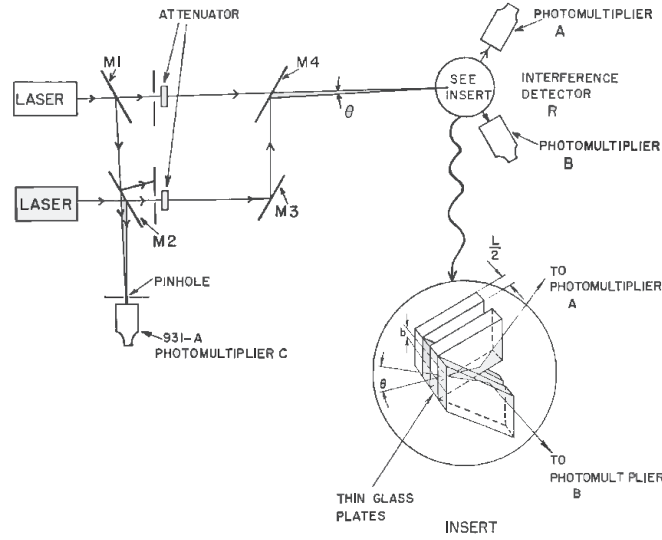
Figure 3.2.: Schematic of the interference experiment of Pfleegor and Mandel [98]. The illustration has been taken from their paper. Two independent and strongly attenuated laser beams are overlapped at a small angle θ. The unattenuated parts are overlapped at a photo multiplier. Its signal is used to produce a gate signal for the interference detector R.

necessary in order for the distance between the interference fringes to match the thickness of the glass plates.

Radloff [100] devised a similar experiment with attenuated laser beams, which allowed for a direct observation of the interference fringes. From each of the laser beams a strongly attenuated part was split off. The unattenuated parts were overlapped with each other as were the respective attenuated parts. Whenever the fringes of the transient interference pattern of the intense beams were at a predefined position, the attenuated beams were unblocked. In this way photons from the attenuated beams were detected only when their relative phase matched a predefined value. Integrating over these photons resulted in a well defined interference pattern.

Attenuating a laser beam does not change its photon statistics, i.e. the interfering beams were still describable as classical electromagnetic fields. If the prerequisites for the interference pattern to be visible are met, the possibility of identifying the source of an interfering photon will be impossible. Hence, the occurrence of interference is not due to interference of photons from independent sources. Rather it is due to interference of the two possible ways, via which each photon could have reached the detector, either coming from the one or from the other laser. As the authors of [98] put it: "...interference has been demonstrated under conditions where the effect cannot be readily described in terms of one photon from one source interfering with one from the other.".

3.2. Hanbury Brown and Twiss

Hanbury Brown and Twiss [5] (HBT) did not desire to demonstrate interference of photons from independent sources. They attempted to determine the angular diameter of a star from the coherence properties of the light it emitted [26, 27]. Nevertheless, these experiments involve the transient interference of (a great number of) incoherent light sources and the effect is closely related to later experiments (e.g. [98]).

Suppose we observe the light emerging from a star of diameter r_s at a distance R from Earth. Each point of the star's surface can be considered to be an *independent (point-like) light source*. Because we are only interested in the diameter of the star and not in the intensity distribution, we can treat the star as a flat disk with uniform intensity distribution.

If the star's light is filtered by a narrow bandwidth filter around the central wavelength $\overline{\lambda}$, the coherence area [6], A, of the light will be given by [83]:

$$A = \pi \left(\frac{0.16\overline{\lambda}}{2\alpha_s} \right)^2 , \tag{3.1}$$

where $\alpha_s = \frac{r_s}{R}$ is the angular diameter of the star. That means if we determined the coherence area of the light emitted by a star, the equation above would enable us to calculate the angular diameter of a star.

Michelson was the first to apply this principle to the determination of the diameters of satellites and the distances between double stars (see [89]). Either light from two portions of the objective of one telescope, or light from two telescopes, which are separated by a variable distance D, is overlapped to produce interference fringes. The visibility of these fringes is measured over an increasing distance D, and the distance d_0, where the first minimum of the visibility occurs, is determined [7]. This distance is related to the desired angular distance by (this is the first minimum of a Bessel function of the first kind and first order, see [83]):

$$d_0 = \frac{0.61\overline{\lambda}}{\alpha} . \tag{3.2}$$

This interferometric method has several disadvantages. The distance between the telescopes (or portions of the objective of one telescope) has to be interferometrically stable. This limits the accuracy of the method because the maximally achievable stable distance between the telescopes is limited. Another negative influence is atmospheric turbulence, which leads to fluctuations of the interference fringes.

---

[5]I want to note that these are two authors and not three, as is sometimes wrongly concluded from the name of R. Hanbury Brown.

[6]Over this area the light can be treated as approximately coherent.

[7]d_0 is larger than the radius of the coherence area. It is the distance where the spatial coherence becomes zero. To be exact we have to say: where the spatial coherence vanishes for the first time because it is proportional
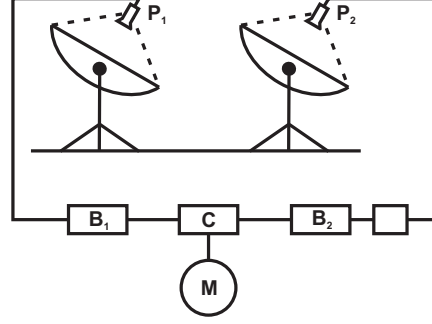
Figure 3.3.: Schematic of a stellar intensity interferometer after Hanbury Brown and Twiss (based on a schematic by Mandel and Wolf [83]). The intensity of the light emitted by a star is measured at two telescopes by two photo multipliers P_1 and P_2, respectively. Their signals are amplified (B_1 and B_2) and multiplied (C). The resulting signal is integrated (M) over time. In addition the signals of the photo multipliers could be passed through high-pass filters in order to eliminate DC currents because only fluctuations of the intensities are of interest. The delay, τ, between the signals can be adjusted in order to compensate for optical path delays.

Hanbury Brown and Twiss (HBT) developed a method, which overcomes these limitations. Their method is based on the observation of the correlations between the fluctuating current outputs of two photodetectors that measure the light from a star at two distant positions. Figure 3.3 shows a schematic of the HBT stellar intensity interferometer.

Because no interference between the light fields has to occur at the two detectors the optical path lengths do not have to be as stable as in the stellar Michelson interferometer. As a result there is no necessity for interferometric stability of the setup, and atmospheric turbulence has less influence on the result. Suppose, the signals of the photo multipliers are passed through high-pass filters. In that case, steady DC components are eliminated and only the product of the intensity fluctuations will be integrated. That signal is proportional to the square modulus of the "equal-time" complex degree of coherence γ (see equ. 2.12 on page 34 and [83]), i.e.:

$$C(d) = \frac{\langle \Delta J(\mathbf{r}_1, t) \Delta J(\mathbf{r}_2, t) \rangle}{\left\langle [\Delta J(\mathbf{r}_1, t)]^2 \right\rangle \left\langle [\Delta J(\mathbf{r}_2, t)]^2 \right\rangle} \propto |\gamma(\mathbf{r}_1, \mathbf{r}_2, 0)|^2, \tag{3.3}$$

where $\Delta J(\mathbf{r}_k, t) = J$ is the deviation of the photocurrent at time t from the average photocurrent of the photo multiplier at position $\mathbf{r}_k$, and $\langle \rangle$ denotes the average over time.

---

to a Bessel function of the first kind and first order. A function well known from the Fraunhofer diffraction at a circular aperture. It vanishes repeatedly. Between the zeros lie maxima and minima of decreasing amplitude.

A measurement of this product of photocurrent fluctuations over the varying distance $|\mathbf{r}_2 - \mathbf{r}_1|$ between the two telescopes allows to determine $|\gamma(\mathbf{r}_1, \mathbf{r}_2)|$. This is the same function that determines the spatial coherence in a stellar Michelson interferometer. Although the technique is very different from the Michelson interferometer the procedure to measure the angular diameter of a star is the same: the first minimum, d_0, of γ is determined and the relation 3.2 is used to calculate α_s.

To interpret the HBT effect in the historic context that we discuss here let us examine equation 3.3. It shows that the correlation between the fluctuating photodetector currents is simply the square modulus of the *second-order coherence function* γ. That means the HBT effect is due to simple second-order (or single-photon) interference.

Even if the HBT effect is observed on the single-photon level the observed correlations between single-photon detection events are due to correlated transient second-order interference at the positions of the detectors. No two-photon interference is involved. In other words: we observe interference not because independent photons interfere but because for each photon we cannot tell, which of the surface points it was emitted from. Like Dirac said [40]: "each photon interferes only with itself".

3.3. Experiments on two-photon interference

Two-photon interference surpasses the classical concept of interference. It cannot be explained via the superposition of electromagnetic field amplitudes but results from the superposition of probability amplitudes for indistinguishable two-photon detection events. Because the phase between these amplitudes is unrelated to the phase of the field amplitudes, two-photon interference is not subject to the limits of transient interference.

In all experiments, which we are going to describe (with one exception in the end), our description will make it evident that the photon sources utilized in these experiments are inseparable and not independent.

3.3.1. Hong, Ou and Mandel

The first experimental demonstration of two-photon interference was performed by Hong, Ou and Mandel [60]. A schematic of this experiment is shown in fig. 3.1(a). A detailed description can be found in section 2.3. The two photons photons originated from the same source and could hardly be called independent [8].

3.3.2. Interference of a single photon with an attenuated laser beam

Rarity, Tapster and Loudon [101] demonstrated HOM-type interference, where a photon from an SPDC triggered single-photon source (see section 4.3) and an attenuated laser pulse

---

[8]Actually, because they are both part of an SPDC pair, they not only originate from the same source but even from the same pump photon.

were overlapped at a beam splitter (see fig. 3.1(b)) . The logic gate that counted coincidence detection events after the beam splitter was gated on detections of the second SPDC photon. Because of the sub-Poissonian statistics of the triggered single-photon source high-visibility HOM-type interference could be observed in spite of the uncertainty of the photon number in the attenuated laser beam.

Although this is a progress in terms of the independence of the interfering photons, the experiment lacks full independence of the sources. The single photon is part of an SPDC pair, which is emitted by the interaction of the pump pulse with a non-linear crystal. The very same pulse is attenuated to give the second input to the beam splitter.

3.3.3. Interference with photons from two SPDC pairs

In [24] the authors use two SPDC pairs, which are created by two passes of the pump beam through one crystal, to demonstrate quantum state teleportation (see fig. 3.1(c)). The Bell-state measurement, which is needed for the implementation of the teleportation protocol (see subsection 1.6.1) was implemented using HOM interference (see subsection 2.3.5). Each of the interfering photons is part of one of the SPDC pairs and is triggered by its respective partner photon.

The progress compared to [101] is that HOM-type interference was observed with two single-photons instead of one single photon overlapped with an attenuated beam. Nevertheless, both photons are created by interaction of one pump pulse with one crystal. The phase relation between the two SPDC pairs is constant over a large number of subsequent pulses and probably even over the time between subsequent four-fold events. Over the duration of a complete scan the phase cannot be considered to be stable because no efforts were taken to stabilize the optical paths in the sub-wavelength regime (the same holds true for [101]). In an experiment with a similar setup it was demonstrated that the variations of the path lengths over the duration of a scan were larger than the pump wavelength [64].

3.3.4. Interference with photons created by two successive laser pulses

The photons in a later HOM-type interference experiment [69] again originate from two separate SPDC pairs. In contrast to earlier experiments these SPDC pairs are not created by the same pump pulse but rather by two out of a coherent sequence of laser pulses (see fig. 3.1(d)). This experiment clearly demonstrated that two-photon interference cannot be described as interference "between" two photons.

In a similar effort [107] two successive laser pulses are used to create single photons not via SPDC but by repeatedly exciting a single quantum dot.

Our conclusions are the same for both experiments. In both cases the two interfering photons originate from the same non-linear medium (SPDC in one case, a quantum dot in the other). The laser pulses used for excitation originate from the same mode-locked laser

and have a fixed relative phase [9].

3.3.5. Interference with photons from spatially separated nonlinear media

In [37] HOM-type interference was demonstrated with photons originating from spatially separated SPDC crystals (see fig. 3.1(e)). The optical paths cannot be assumed to have been stable enough for a fixed phase relation between the two SPDC pairs. Still, the two pairs did not originate from fully independent sources because the two crystals were pumped by the same laser [10]. Because of the common pump it would also be impracticable to separate the crystals by a distance much larger than the length of an optical table. A scheme requiring to distribute portions of one laser to multiple crystals is definitely not scalable as it should be for use in quantum networks.

In a more recent experiment [16] two atoms were trapped in two dipole traps separated by $\sim 6\,\mu$m. Both of them were excited by the same laser pulse and two-photon interference was observed. In contrast to the experiment of de Riedmatten et al. [37] the atoms, which represent the non-linear media in this case, were not separated far enough for the sources not to be pumped coherently. Apart from employing a different type of photon source this experiment does not add anything new to the line of experiments presented here.

3.3.6. Interference with passively synchronized single-photon sources

Later (in section 5.1), we will discuss in detail two common methods to synchronize femtosecond lasers. One of them is called *passive* laser synchronization. It synchronizes the output of two laser cavities by intersecting them and by overlapping the laser beams within the cavities in an intra-cavity Kerr medium. Because of the direct interaction of the laser beams the synchronization is very tight. For femtosecond lasers a timing jitter on the order of 1 fs or even less is possible [119]. *Active* laser synchronization, on the other hand, allows to synchronize an arbitrary number of independent and spatially separated lasers. Yet, it requires much greater efforts with this technique to achieve a timing jitter as small as with *passive* synchronization (see [114]).

In the experiment by Yang et al. [135] two SPDC sources are pumped by pulses emerging from passively-synchronized laser cavities (see fig 3.1(f)). They used HOM-type interference to realize a BSM in order to demonstrate entanglement swapping. Their synchronization scheme is not scalable to more than two lasers. The sources are not separable, and cannot be considered as fully independent because their synchronization relies on intra-cavity interaction. This interaction of the laser beams within the Kerr medium is strong enough to establish phase coherence between the beams [15].

---

[9]The coherence length of a passively mode-locked laser is in general much longer than the distance between two successive pulses.

[10]SPDC photons are generated by the interaction of a pump field with a nonlinear crystal. Both of these elements (field and nonlinear medium) compose the single-photon source.

3.3.7. Interference with photons from independent sources

In contrast to all previously described experiments ours is the first to utilize fully independent sources to demonstrate two-photon interference (see fig. 3.1(g) and [67]). These sources did not interact in any way and could, in principle, be separated by a large distance. Stable relative timing between the two sources was achieved by actively synchronizing the femtosecond lasers (see section 5.1) via electronic signals.

While writing this thesis, a new experiment was reported [59]. It is very closely related to our work. There, detectors were used, which had a time resolution better than the coherence times of the SPDC photons. To this end they employed very narrow bandwidth filters (0.01 nm, while our filters had a bandwidth of 1 nm in the first experiment and 0.4 nm in the second).

In comparison to our experiment, the visibilities and count rates achieved were quite poor. On the other hand, the sources in [59] do not need to be synchronized. Both techniques have their advantages and both are promising candidates for future applications in long distance quantum communication.

4. Elements and Principles of the Single-Photon Sources in the Setup

In reference to their synchronization (see chapter 5) we denote our sources as *master* and *slave*. Their layouts are nearly identical to each other. Only during our first experiment [1] there existed a noteworthy but not essential difference because the optical pumps of the femtosecond lasers were not the same on both sides (see 6.1.1).

Both sources can be subdivided into three parts: the femtosecond laser, second-harmonic generation and spontaneous parametric down-conversion. This chapter is a collection of theoretical concepts related to these parts of the setup. We will explain the working principles of the femtosecond lasers as far as they are relevant to understand the synchronization process. With respect to second-harmonic generation we will explain its principles and the tools needed to analyze and correct the profile of the ultra-violet laser beams.

We will conclude this chapter (after a very short review of spontaneous parametric down conversion) with a new result, which resolves a question, which has been bothering the experimenters in our group for several years: why is it that the coupling efficiencies in a setup with pulsed lasers is always poorer than in a setup with continuous-wave lasers.

4.1. The femtosecond lasers

Both our femtosecond lasers were passively modelocked with a Titan-Sapphire crystal as gain medium. The inversion of the gain medium is achieved by focusing an intense pump beam onto the crystal (for the specifications of the lasers see 6.1.1). Because the synchronization of our femtosecond lasers is an essential part of our work we will give a short overview of the principles of operation of these femtosecond lasers.

4.1.1. Passive mode locking

The output of a pulsed laser in general has a significantly larger bandwidth than continuous-wave (CW) laser beams. These contributions of different wavelengths are necessary to create the periodic laser output. Although we speak of bandwidth the contributing wavelengths are not spread continuously over the whole range because laser cavity modes have to fulfill

---

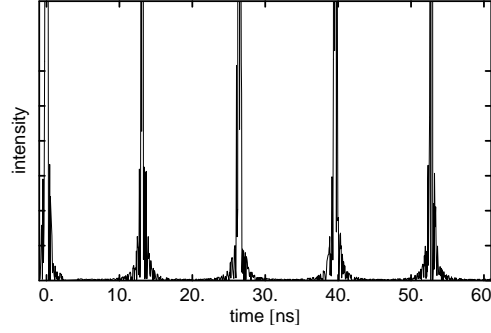[1]The experiment to demonstrate HOM-type interference (see 7.1).

Figure 4.1.: Simulation of mode-locked laser output. To gain this curve we superposed frequencies in regular intervals of $T^{-1} = \frac{c}{2L} \sim 76\,\text{MHz}$ over the wavelength range from 710 nm to 810 nm. These values correspond to the specifications of the lasers used in this experiment. We did not take into account the birefringent filter in the cavity, which reduces the bandwidth significantly. Another approximation is that we assumed equal intensities for all frequency contributions.

the boundary condition

$$\frac{2L\omega_n}{c} = n\pi, \tag{4.1}$$

where L is the cavity length. The round-trip time is $T = \frac{2L}{c}$. These "allowed" modes are called the longitudinal modes of the laser. They form a frequency comb with a line spacing of $\Delta\omega = \frac{\pi c}{L}$.

In order for these lines to contribute to the laser output they have to be amplified by the gain medium. For this reason the gain bandwidth of a pulsed laser must be significantly larger than in CW lasers. Titan-Sapphire crystals, for instance, have an emission range approximately from 680 nm to 1100 nm. In the case of our lasers this range is reduced to about 710 nm to 810 nm due to the cavity design and the cavity optics.

A stable pulse sequence can only be achieved if the longitudinal modes contributing to the laser output are in phase with each other. If this is achieved, the laser is said to be *mode locked* because the phases of the various modes are "locked" to each other. Suppose, the central frequency of the laser output is ω_0 and assume for simplicity that the amplification over the emission bandwidth is constant. Then the field amplitude is a superposition of the cavity modes within the emission bandwidth [2]:

$$E(t) \propto e^{\iota\omega_0 t} \sum_{q=-m}^{n} e^{\iota q \Delta\omega t}, \tag{4.2}$$

where n and m are defined such that $\omega_0 - m\Delta\omega$ is the lower limit and $\omega_0 + n\Delta\omega$ is the

---

[2]It should be noted that this relation holds only for mode-locked operation. Otherwise there would appear a mode dependent phase shift φ_q in the exponent.
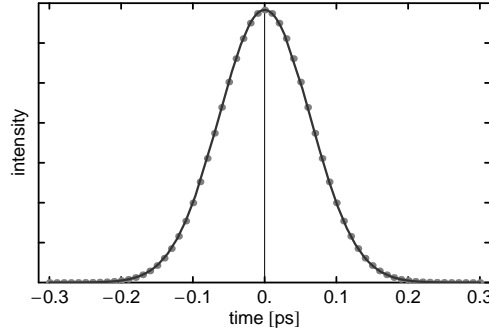
Figure 4.2.: Fourier-limited pulse for the experimental parameters of the *slave* laser. We generated data points for the intensity corresponding to the amplitude given in equ. 4.5 and fitted a Gaussian to these points.

upper limit of the emission bandwidth. Using the relation

$$\sum_{q=-m}^{n} x^q = \frac{1 - x^{-(m+1)}}{1 - x^{-1}} + \frac{x - x^{(n+1)}}{1 - x} \tag{4.3}$$

it is straight forward to show that $E(t)$ can be written as

$$E(t) \propto \frac{\imath e^{\imath \left[\omega_0 - \frac{(2m+1)\Delta\omega}{2}\right] t} \left\{1 - e^{[\imath(m+n+1)\Delta\omega t]}\right\}}{2 \sin\left(\frac{\Delta\omega t}{2}\right)} \propto \frac{\sin\left[(m+n+1)\Delta\omega t\right]}{\sin\left(\frac{\Delta\omega t}{2}\right)}. \tag{4.4}$$

Its modulus square is proportional to the laser output. Figure 4.1 depicts the first 60 ns of the resulting pulse train for a round-trip time of 13.2 ns and an emission range from 710 nm to 810 nm.

The range of amplified frequencies within the cavity is further narrowed by a birefringent filter within the cavity (see section 6.1 on page 105). We can include this additional filtering by introducing a Gaussian frequency response in equ. 4.2, i.e.:

$$E(t) \propto e^{\imath \omega_0 t} \sum_{q=-m}^{n} e^{\imath q \Delta\omega t} e^{-\frac{(q\Delta\omega)^2}{4\sigma_p^2}}. \tag{4.5}$$

A factor 4 (instead of 2) appears in the denominator of the exponent because σ_p^{-1} is the r.m.s. width of the intensity and not of the amplitude.

If we use the bandwidth of the *slave* laser, which was ~ 2.6 nm (see section 6.1), this amplitude distribution leads to Fourier-limited pulses with an r.m.s width of 64 fs (see fig. 4.2).

4.1.2. Laser noise

In [125] a theoretical description has been developed to characterize the noise of pulsed lasers. It is also useful for understanding the performance of laser synchronization. For

this reason we will present a short overview over the central points of [125]. The temporal intensity profile of the output of a mode-locked femtosecond laser in the absence of noise can be written as:

$$F_0(t) = \sum_\mu f(t + \mu T), \tag{4.6}$$

where $f(t)$ is the temporal intensity profile of the individual laser pulses. T is the time between two pulses and μ is an integer running from minus to plus infinity. The output of an imperfectly mode-locked laser can be written as:

$$F(t) = F_0(t) + \delta F(t), \tag{4.7}$$

where $\delta F(t)$ incorporates fluctuations that are small in comparison to $F_0(t)$. The power spectrum of the laser intensity is given by:

$$P_F(\omega) = \frac{1}{2\pi} \int_{-\infty}^{+\infty} dt\, G_F(t) e^{i\omega t}, \tag{4.8}$$

which is the Fourier transform of the intensity autocorrelation function

$$G_F(t) = \langle F(t+\tau)F(t) \rangle = \lim_{\Delta \to \infty} \int_{-\frac{\Delta}{2}}^{+\frac{\Delta}{2}} d\tau\, F(t+\tau)F(t). \tag{4.9}$$

For the purpose of this work it will be sufficient to examine noisy laser output where the shapes of the pulses do not change. Then the noisy laser intensity can be written as

$$F(t) = F_0(t) + F_0(t)A(t) + \dot{F}_0(t)\, TJ(t). \tag{4.10}$$

Here, the second term represents intensity fluctuations, which are characterized by the random function $A(t)$. It gives the relative deviation from the average pulse intensity. The third term is due to fluctuations of the repetition time, i.e. due to a temporal jitter of the pulses

$$\delta T = TJ(t). \tag{4.11}$$

Dots are used to indicate time derivatives. $J(t)$ is a random function of time representing the relative deviation from the average pulse repetition time T.

The power spectrum of the laser intensity becomes (see [125]):

$$P_F(\omega) = \frac{2\pi}{T} |\tilde{f}(\omega)|^2 \sum_\mu \left[\delta(\omega) + P_A(\omega_\mu) + (2\pi\mu)^2 P_J(\omega_\mu) \right], \tag{4.12}$$

where $\omega_\mu = (\omega - 2\pi\mu/T)$ and $\tilde{f}(\omega)$ is the Fourier transform of $f(t)$. This sum represents a series of frequency bands centered around the harmonics of the fundamental laser frequency. Each of these bands consists of three parts. The delta functions correspond to the

noise-free pulse train, P_A is the power spectrum of the intensity noise, and P_J is the power spectrum of the jitter distribution.

Because our work is centered around laser synchronization it is the term containing P_J, which should draw our attention. This contribution due to the temporal jitter is proportional to μ^2. That means it becomes significantly more pronounced for higher harmonics. We will see the importance of this effect in chapter 5. It explains why the electronics, which we use for synchronizing our femtosecond lasers, consists of two independent phase-locked loops (see section 5.1.1) and why the phase-locked loop, which operates at a higher harmonic, results in lower jitter than the phase-locked loop operating at the fundamental frequency.

4.2. Second-harmonic generation

The greatest hindrance for the scalability of optical implementations of quantum communication and quantum information processing schemes is the low efficiency of current photon sources and single-photon detectors. Especially in multi-photon experiments, which usually apply narrow bandwidth filters [142], it is paramount to optimize the photon sources and the detection process. For this reason it is common to produce single-photons in the near infrared (NIR) wavelength regime, because in this regime our detectors (silicon avalanche) are highly efficient and have low dark-count rates. To generate wavelength degenerate SPDC pairs at near infrared wavelength, the pump's wavelength has to be ultra-violet. Multi-photon experiments use pulsed, usually femtosecond, pumps [3] depending on the bandwidth of the filters employed [142]. Up to now no femtosecond lasers are available working in this wavelength regime. Instead, the light of pulsed infrared lasers is frequency doubled via second-harmonic generation (SHG).

4.2.1. The principles

SHG is a three-wave mixing effect. It is closely related to SPDC but is fully explainable in terms of classical optics. The pump field interacts nonlinearly with a non-isotropic medium producing secondary radiation proportional to the pump field's square. Let us assume the pump field to be given by a plane wave polarized along the y-axis (z shall be the direction of propagation):

$$\mathfrak{E}(z,t) = (Ae^{\imath(\omega t - kz)} + A^* e^{-\imath(\omega t - kz)})\mathfrak{e}_y. \tag{4.13}$$

---

[3]Recently a multi-photon experiment, which did not employ pulsed sources, was reported [59].

The components of the *dielectric polarization* vector $\mathfrak{P}$ of the nonlinear medium are related to the electric field via

$$
\begin{aligned}
P_i(z,t) &= \varkappa_0 E_i(z,t) + \chi^{(2)}_{ijk} E^j(z,t) E^k(z,t) + \dots \\
&= \varkappa_0 E_i(z,t) + 2\chi^{(2)}_{i22}|A|^2 \left[1 + \cos(2\omega t - 2kz)\right] + \dots
\end{aligned}
\tag{4.14}
$$

$\varkappa_0$ is the dielectric susceptibility in the absence of the electric field and $\chi^{(m)}$ are the nonlinear susceptibility coefficients (we stop the series at the second order, i.e. at $\chi^{(2)}$). As can be seen from equation (4.14), the polarizability oscillates with twice the frequency of the pump field. The secondary radiation emitted is proportional to $\mathfrak{P}$ and will also oscillate with the double frequency.

For our purposes SHG is of secondary interest because it is only a means to frequency convert the pump beam. Our only interest in SHG is

- how to increase the conversion efficiency

- how to ensure that the converted pump beam's properties are adequate for generating high-visibility entanglement and high-visibility HOM-type interference

Equation (4.14) shows that the intensity of the produced SHG light depends on the square of the nonlinearity of the crystal ($\chi^{(2)}$) and on the square of the intensity of the pump field. High conversion efficiencies can be achieved by focusing the beam, by using short pump pulses with high peak intensities, and by employing crystals with a high nonlinearity. Another possibility to optimize the conversion efficiency to increase the interaction time by using thicker crystals.

All these methods to increase the conversion efficiency have negative side effects on the suitability of the SHG light for further use in a multi-photon SPDC setup. The tighter the focus is the more astigmatic the converted beam will be, and the phase matching will suffer from the divergence of the pump beam. If we increase the bandwidth of the pump pulses, again the phase matching will be impeded as negative effects like group velocity mismatch (GVM) and dispersion of the pulses will increase. That results in additional timing jitter and lower interference visibilities in multi-photon experiments (see section 5.2). The same will occur for increased crystal thickness.

We are left with the task to find a tradeoff between preparing a frequency converted beam with high efficiency and being able to use this beam for our experiments. While in most earlier multi-photon experiments in our group Lithium Triborate (LBO or LiB_3O_5) was used for SHG, we decided to try a new approach for the presented experiment and used a β-Barium Borate (BBO or $\beta - BaB_2O_4$) crystal, which has a larger nonlinearity. After various measurements on the conversion efficiency and the pulse spread due to GVM [17], we chose a 2 mm thick BBO. An achromatic lens was employed to tightly focus the beam within the crystal. We achieved conversion efficiencies of ~ 50 %. While this efficiency was only slightly better than in the case of the SHG setup (using an LBO crystal) for the

other femtosecond laser in our setup, the BBO in contrast to the LBO did not suffer damage from the high pump powers. The BBO was pumped with up to 1.8 W at 789 nm focused to a waist of about 22 μm over periods up to 24 hours. When the LBO was pumped with comparably high power ($\sim$ 2 W) it suffered radiation damage within a few minutes. It should be mentioned that it could have been only the anti-reflection coating, which was damaged, and not the LBO itself.

In contrast to comparable setups in our group using pulsed sources, we were the first to use achromatic lenses to achieve tighter focusing of the (broadband) pump beam in the SHG crystal. As can be expected from tighter focusing and also from the higher nonlinearity of BBO, the astigmatism we encountered was larger than in comparable other experiments of our group. Additionally, the optical axis seems to have been not exactly orthogonal to the polarization of the pump beam. This error in adjustment led to a rotation of the UV beam profile. That it could probably have been corrected by simply rotating the crystal was, unfortunately, only noticed retrospectively. To correct this astigmatism of the UV beam is the topic of the following subsection.

4.2.2. General astigmatism and its correction

To optimize the efficiency of SPDC it is essential to prevent distortions of the wave front of the laser beam pumping the SPDC crystal. Otherwise only parts of the pump beam will fulfill the phase-matching conditions and contribute to the emission of SPDC photons. At the same time the beam profile should be circular in order to guarantee optimal mapping between the SPDC photons emitted and the single-mode fibers, which they are to be coupled into. For these reasons we thoroughly investigated the correction of the astigmatism of the UV beams generated via SHG.

We can divide astigmatism of two dimensional Gaussian beams (i.e. two dimensions x and y perpendicular to the direction of propagation z) into three sub categories:

1. the waists along the x and y axes are different but at the same position along the z axis (type 1)

2. the waists are different in size and position (type 2)

3. the orientation of the wavefront differs from that of the beam intensity (type 3).

The first case is easily compensated by cylindrical lenses, which are orthogonal to each other. They do not even have to be oriented exactly along the same axes as the beam profile. If a cylindrical lens is oriented at a small non-zero angle relative to the beam profile's axes, it can be approximated by a correctly oriented cylindrical lens with a different focal length [4].

---

[4] Suppose the axis of the cylindrical lens with focal length f_x is oriented along the y-axis and that the profile is rotated by a small angle α relative to the x-axis. Then the lens can be approximated to second order in α as a lens oriented along the axes of the beam profile with a focal length $f'_x = \cos^2(\alpha) f_x$. See also table 4.1.

Type 2 astigmatism can also be corrected with cylindrical lenses, which are oriented perpendicular to each other. Their orientation has to coincide exactly with axes of the beam profile, otherwise the beam will become astigmatic of type three.

To correct general astigmatism (type 3), cylindrical lenses of suitable focal lengths have to be employed at the correct positions at non-orthogonal angles relative to each other.

In order to understand the procedure we used to correct astigmatism (see subsection 6.2.2) it will be necessary to give a short introduction into the propagation of two-dimensional Gaussian beams.

Two-dimensional Gaussian beams

Our description of two-dimensional Gaussian beams is a combination of the results of [3], [72] and [2]. We can describe the spatial part of the electric field u of a freely propagating laser beam by a scalar wave equation (we do not take into account polarization)

$$\left(\nabla^2 + k^2\right) u\left(x, y, z\right) = 0. \tag{4.15}$$

For a Gaussian beam along the z axis we can write u as a product of a slowly varying complex function ψ and a plane wave $e^{-\imath k z}$ along the z axis (see [72]). The wave equation becomes

$$\left(\frac{\partial^2}{\partial x^2} + \frac{\partial^2}{\partial y^2} - 2\imath k \frac{\partial}{\partial z}\right) \psi = 0. \tag{4.16}$$

A solution of this equation is

$$\psi\left(x, y, z\right) = \frac{1}{\sqrt{q_1 q_2}} \exp\left[-\imath \frac{k}{2}\left(\frac{x^2}{q_1} + \frac{y^2}{q_2}\right)\right], \tag{4.17}$$

where q_1 and q_2 are complex Gaussian beam parameters for the xz and yz planes as known from one-dimensional Gaussian optics. They are functions of z depending on the Rayleigh length $z_{R1,2}$ of the Gaussian beam in the according plane and the position $t_{01,2}$ of the waist along the z axis:

$$q_{1,2}\left(z\right) = \imath z_{R1,2} - z_{01,2} + z. \tag{4.18}$$

Up to now our description does not include general astigmatism (type 3). Rather it describes a Gaussian beam with an elliptical profile oriented along the x and y axis. To get a more general description, we rotate the beam by an angle ϕ around the z axis [3]:

$$\begin{aligned}
\psi\left(x, y, z\right) &= \frac{1}{q_1 q_2} \exp\left\{-\imath \frac{k}{2}\left[\left(\frac{\cos^2 \phi}{q_1} + \frac{\sin^2 \phi}{q_2}\right) x^2 + \left(\frac{\sin^2 \phi}{q_1} + \frac{\cos^2 \phi}{q_2}\right) y^2 + \right.\right. \\
&\quad + \left.\left. \sin\left(2\phi\right)\left(\frac{1}{q_1} - \frac{1}{q_2}\right) xy\right]\right\}.
\end{aligned} \tag{4.19}$$

As long as ϕ is real, this will still describe an astigmatic Gaussian beam of type one or two. If ϕ is imaginary, the beam described by equ. 4.19 will be astigmatic of type 3.

Let us write $\phi = \alpha + \imath\beta$ where $\alpha, \beta \in \mathbb{R}$. The angle α corresponds to a normal rotation of the beam profile relative to axes x and y. We can always find a rotated coordinate system, such that $\alpha = 0$. To simplify our description, let us divide the exponent in ψ into an imaginary and a real part. The real part represents the intensity profile of the beam, the imaginary part represents the beam's wavefront. For $\alpha = 0$ the real part is given by:

$$x^2\left(\omega_2\sinh^2\beta - \omega_1\cosh^2\beta\right) + y^2\left(\omega_1\sinh^2\beta - \omega_2\cosh^2\beta\right) +$$
$$xy\left(\rho_2 - \rho_1\right)\sinh(2\beta). \tag{4.20}$$

If this is constant, it will describe an ellipsoidal or hyperbolic beam profile, which can be rotated relative to the xy coordinate system [5] by an angle depending on the position along the z axis. To find this angle let us perform an arbitrary rotation of the coordinate system:

$$x = \xi_\omega\cos\phi_\omega - \eta\omega\sin\phi_\omega$$
$$y = \xi_\omega\sin\phi_\omega + \eta\omega\cos\phi_\omega \tag{4.21}$$
$$. \tag{4.22}$$

We can determine the angle ϕ_ω of the beam profile by requiring that the off-diagonal coefficients of x and y in equation (4.20) vanish. This yields:

$$\tan(2\phi_\omega) = \frac{\rho_2 - \rho_1}{\omega_2 - \omega_1}\tanh(2\beta), \tag{4.23}$$

where

$$\rho_i(z) = \frac{z - z_{0i}}{\left(z - z_{0i}\right)^2 + z_{Ri}^2}$$
$$\omega_i(z) = \frac{z_{Ri}}{\left(z - z_{0i}\right)^2 + z_{Ri}^2}. \tag{4.24}$$

The wave front of the beam is also of an ellipsoidal or hyperbolic form. Its angle relative to the xy coordinate system can be retrieved in an similar fashion, where we use variables ξ_R and η_R for the new coordinates and ϕ_R for the angle. We get:

$$\tan(2\phi_R) = -\frac{\omega_2 - \omega_1}{\rho_2 - \rho_1}\tanh(2\beta). \tag{4.25}$$

From equations (4.23) and (4.24) we see that only if $\beta = 0$ or if the beam is circular ($\rho_1 = \rho_2$), the angle ϕ_ω will not depend on z. That means the profile of a generally astigmatic beam will rotate around the z axis even when freely propagating. We used this fact in our experiment to determine the correct angle of our cylindrical lenses (see 6.2.2).

---

[5]That is the coordinate system defined by $\alpha = 0$.

Optical elements in two-dimensional Gaussian optics

For one-dimensional Gaussian beams the complex beam parameter $q(z) = (z - z_0) + \imath z_R$ provides us with a complete description of the beam. z is the position along the direction of propagation, z_0 is the position of the beam waist and z_R is the beam's Rayleigh length. Linear optical elements can be represented by 2×2 transfer matrices:

$$\begin{pmatrix} A & B \\ C & D \end{pmatrix}. \tag{4.26}$$

Their effect on the beam is given by

$$q' = \frac{Aq + B}{Cq + D} \text{ or } q'^{-1} = \frac{Dq^{-1} + C}{Bq^{-1} + A}. \tag{4.27}$$

This is known as the "ABCD law", see e.g. [106].

In the case of two-dimensional Gaussian beams, the complex beam parameter q is replaced by a 2×2 matrix Q. The elements A, B, C and D of the transfer matrices are replaced by matrices as well, and the ABCD law (see equ. (4.27)) can be generalized to (see [2]):

$$Q' = (AQ + B)(CQ + D)^{-1} \tag{4.28}$$

or

$$Q' = (DQ^{-1} + C)(BQ^{-1} + A)^{-1}, \tag{4.29}$$

where the exponent -1 denotes the matrix inverse. The ABCD law applies only if these inverse matrices exist.

If a two-dimensional beam does not suffer from general astigmatism, the two axis of its profile will be independent of each other and can be described by separate complex beam parameters q_1 and q_2 (see equation (4.19)). The complex beam tensor Q describing such a beam will be diagonal in the coordinate system defined by the axis of the beam profile:

$$Q = \begin{pmatrix} q_1 & 0 \\ 0 & q_2 \end{pmatrix}. \tag{4.30}$$

If we want to describe a beam with a profile, which is rotated with respect to the laboratory coordinate system by an angle ϕ, the correct Q will be given by

$$Q = (R_1(\phi) Q_0 + R_2(\phi))(R_3(\phi) Q_0 + R_4(\phi)), \tag{4.31}$$

where $R_i(\phi)$ are 2×2 sub matrices of the rotation matrix

$$R(\phi) = \begin{pmatrix} R_1(\phi) & R_2(\phi) \\ R_3(\phi) & R_4(\phi) \end{pmatrix} = \begin{pmatrix} \cos(\phi) & \sin(\phi) & 0 & 0 \\ -\sin(\phi) & \cos(\phi) & 0 & 0 \\ 0 & 0 & \cos(\phi) & \sin(\phi) \\ 0 & 0 & -\sin(\phi) & \cos(\phi) \end{pmatrix} \tag{4.32}$$

free propagation over a distance L	$\begin{pmatrix} 1 & 0 & L & 0 \\ 0 & 1 & 0 & L \\ 0 & 0 & 1 & 0 \\ 0 & 0 & 0 & 1 \end{pmatrix}$
a thin lens with focal length f	$\begin{pmatrix} 1 & 0 & 0 & 0 \\ 0 & 1 & 0 & 0 \\ -\frac{1}{f} & 0 & 1 & 0 \\ 0 & -\frac{1}{f} & 0 & 1 \end{pmatrix}$
a thin cylindrical lens with a focal length f_x and with its axis along the y-axis	$\begin{pmatrix} 1 & 0 & 0 & 0 \\ 0 & 1 & 0 & 0 \\ -\frac{1}{f_x} & 0 & 1 & 0 \\ 0 & 0 & 0 & 1 \end{pmatrix}$

Table 4.1.: Transfer matrices for optical elements acting on two-dimensional Gaussian beams.

and Q_0 is the complex beam tensor in the beam profile's coordinate system. On the other hand, if we have an optical element, which is usually described by a transfer matrix M (see table 4.1) but which is rotated by an angle θ against the coordinate system of the beam, the transfer matrix in the beam's coordinate system will be given by

$$R(-\theta)MR(\theta). \tag{4.33}$$

Given these tools it is not too complicated to find optimization routines to compensate even general astigmatism. The only problem is to accurately characterize a general astigmatic beam by measuring the beam profile with a CCD camera. If the errors (especially regarding the angle of the profile) are too large, optimization routines will still be able to fit the data, yet the result's errors are usually too large to get useful results for the positions and angles of the cylindrical lenses intended to compensate the astigmatism. A prerequisite to accurately characterize a beam is to measure its profile at several positions over a distance, over which the beam diverges significantly.

4.3. Spontaneous parametric down conversion

Spontaneous parametric down-conversion (SPDC) has several properties, which make it a good choice for a single-photon source until deterministic single-photon sources become available. The simultaneity of the emission of the photons of an SPDC pair [28] allows using the detection of one of the photons as a trigger event for the presence of its partner photon. If the production rate of SPDC pairs is not too high, the probability for multiple pair emissions will be negligible and the trigger event assures with high probability the presence of one and only one partner photon [6]. We will only present a very short review of SPDC. For an excellent discussion see [139].

4.3.1. SPDC - a very short review

SPDC photons can only be emitted if the phase-matching conditions inside the non-linear medium (usually a non-isotropic crystal) are fulfilled [105, 139]:

$$\omega_p = \omega_1 + \omega_2 \tag{4.34}$$
$$\mathfrak{k}_p \simeq \mathfrak{k}_1 + \mathfrak{k}_2. \tag{4.35}$$

These relations correspond to energy and momentum conservation. Equation 4.35 would only be exact if the crystal were infinitely large. For the transverse dimensions of the crystal this is usually a very good approximation. Especially in the case of pulsed SPDC sources, for which it is essential to minimize dispersion effects, the thickness of the crystal is often too small to get an exact conservation of the z components of the momenta.

In our experiments we use type-II down conversion [74]. The crystal's axis is tilted such that pairs of photons with the same wavelength (frequency-degenerate down-conversion) are emitted on intersecting cones (see fig. 4.3). The photons emitted along the intersection lines are coupled into single-mode fibers. Compensation of the walk-off effects is achieved in the usual way (see e.g. [129]) with a combination of half-wave plates and crystals of the same type but half the thickness of the down-conversion crystal. The compensator crystals allow to adjust the phase of the entangled photon states produced by the source. In our case we chose the phase in order to produce ψ^- states (see equ. 1.58).

4.3.2. Coupling efficiencies in SPDC

It has long been a topic for discussion in our group why we never could achieve as good coupling efficiencies in pulsed setups as we did in CW setups. Our calculations in this subsection should finally present the answer to these discussions. At the same time our results

---

[6]In practice the collection efficiencies and the detection efficiencies are usually rather low, especially if narrow bandwidth filters are used (see subsections 4.3.2 and 6.3.1). Because of these limited efficiencies the occurrence of a trigger event does not tell us with certainty that we will couple and detect the other photon.
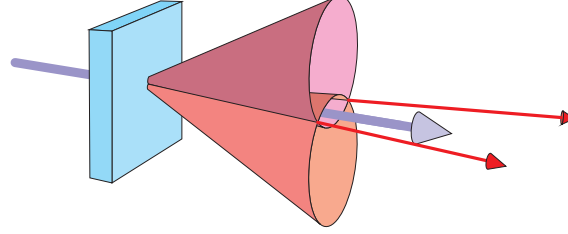
Figure 4.3.: Schematic of SPDC emission. We indicated the beam path of the photons on the intersection lines.

will show how narrow bandwidth filters lead to apparently lower coupling efficiencies in SPDC setups.

The overall efficiency (for coupling *and* detection of an SPDC photon) in a given mode can be calculated by evaluating the ratio of the coincidence count rate over the single-photon count rate in the other mode. That means, if we have a coupler for each of the modes 1 and 2, if N_c is the coincidence count rate between these two couplers, and if N_1 and N_2 are the single count rates, the overall efficiencies (sometimes called "heralding efficiencies") for the two modes are

$$\eta_1 = \frac{N_c}{N_2} \quad \text{and} \quad \eta_2 = \frac{N_c}{N_1}. \tag{4.36}$$

It is common in experiments to estimate the coupling efficiency for a mode by dividing these overall efficiencies by the respective quantum efficiencies η_D of the detectors. This estimation does neither take into account the frequency correlation between the SPDC photons nor the finite bandwidth of the pump. We will show in the following that this approach leads to increasingly wrong results for the coupling efficiencies the narrower the bandwidth filters in the modes are compared to the natural bandwidth of the SPDC photons. Another point where this estimation fails is that it does not take into account the difference between the bandwidths of the signal (extraordinary) and idler (ordinary) photon in a pulsed type-II SPDC setup [57]. These lead to different coupling efficiencies for horizontally and vertically polarized photons [7].

All of these reasons lead us to discuss coupling efficiencies for pulsed SPDC with narrow bandwidth filters in the following paragraphs.

---

[7]The transverse walk-off of the signal photons reduces the coupling efficiency of the signal photons relative to the coupling efficiency of the idler photons. This effect partially compensates the difference in the efficiencies, which we discuss here.

The state of the field generated in SPDC

We start out from the state of the field, which is generated by SPDC. For simplicity we will only consider states where either no pair or one pair is created, i.e. we will neglect double-pair emissions. In this case we can write the state in the following form [104, 68]:

$$|\psi\rangle = \left\{ C_1 + C_2 \int d\omega_s \int \text{sinc} \left[\frac{L}{2} \left(k_{pz} - k_{sz} - k_{iz} \right) \right] g(\omega_s + \omega_i) e^{\iota \tau_p(\omega_s + \omega_i)} \right\} |\Omega\rangle, \quad (4.37)$$

where C_1 and C_2 are normalization constants, and the rest is defined as in equ. 2.64.

Before we continue to calculate the normalization constants, we have to make some additional approximations. The sinc-function makes the expression above impossible to integrate analytically even if we approximate the z components of the wave vectors only to first order. Because we are interested in cases where the bandwidth of the interference filters is smaller than the natural bandwidth of the SPDC photons, we will approximate the sinc with a Gaussian function.

Following Keller and Rubin [68] the argument of the sinc function can be approximated by:

$$S(\omega_s, \omega_i) = -\frac{L}{2} \left[D_1(\omega_s + \omega_i - 2\omega_0) - \frac{D_2}{2}(\omega_i - \omega_s) \right], \quad (4.38)$$

where L is the thickness of the BBO crystal, and D_1 and D_2 are given by (for type-II SPDC):

$$D_1 = \frac{1}{2} \left[u_o^{-1}(\omega_0) + u_e^{-1}(\omega_0, \Psi_{OA}) \right] - u_e^{-1}(2\omega_0, \Psi_{OA}) \quad (4.39)$$

$$D_2 = u_e^{-1}(\omega_0, \Psi_{OA}) - u_o^{-1}(\omega_0). \quad (4.40)$$

Here, u_o and u_e denote the group velocities for ordinarily (idler) and extraordinarily polarized photons (signal and pump) of the indicated wavelengths. In the case of the extraordinary photons the angle Ψ_{OA} relative to the optical axis is approximated to be the same for both signal and pump photons.

The argument in equ. 4.38 will maximize the sinc function along a line, which is defined by $S(\omega_s, \omega_i) = 0$. A parallel line, which is defined by $S(\omega_s, \omega_i) = \pi$ consists of the points of the first minimum of the sinc function. The distance of these two lines is:

$$\Delta_1 = \frac{2\sqrt{2}\pi}{L\sqrt{4D_1^2 - D_2^2}}. \quad (4.41)$$

With this definition equ. 4.38 can be written as

$$\frac{\pi\gamma(\omega_i - \omega_0 - \alpha(\omega_s - \omega_0))}{\Delta_1}, \quad (4.42)$$

where we used the abbreviations

$$\alpha = \frac{D2 - 2D1}{2D1 + D2} \quad \text{and} \quad \gamma^{-2} = 1 + \alpha^2. \tag{4.43}$$

Let us define a Gaussian function with a FWHM equivalent to the FWHM of the first maximum of the sinc function. The corresponding r.m.s. width shall be denoted as σ_g. Our approximation can then be written as:

$$\text{sinc}\left[\frac{\pi\gamma(\omega_i - \omega_0 - \alpha(\omega_s - \omega_0))}{\Delta_1}\right] \sim \exp\left[-\frac{\gamma^2(\omega_i - \omega_0 - \alpha(\omega_s - \omega_0))^2}{2\sigma_g^2}\right]. \tag{4.44}$$

We can see that the natural bandwidths of signal and idler will be different unless $\alpha = 1$ (for our experiment $\alpha \sim -3.55$) [8]

With this approximation we can evaluate all necessary integrals, and the normalization condition for our SPDC state ψ becomes:

$$1 = \langle\psi|\psi\rangle = |C_1|^2 + \frac{|C_2|^2 \sigma_g}{2|1 + \alpha|\gamma\sigma_p}. \tag{4.45}$$

We need one more equation to be able to determine both normalization constants. A convenient choice is to use the rate N of SPDC pairs emitted per second as a reference:

$$N = \nu \int dt_1 \int dt_2 \left|\langle\Omega|\hat{E}_1^{(+)}(t_1)\hat{E}_2^{(+)}(t_2)|\psi\rangle\right|^2. \tag{4.46}$$

Here, we introduced ν, the repetition rate of the laser, and the free electric-field operators with only one photon per mode (there cannot be more photons because we ignore double-pair emission):

$$\hat{E}_m^{(+)}(t) = \frac{1}{\sqrt{2\pi}} \int d\omega \, e^{-\imath\omega t} \hat{a}_m^\dagger(\omega). \tag{4.47}$$

The expression for the rate N corresponds to the case where we detect both photons with perfect, frequency-independent detectors and without bandwidth filters.

If we evaluate equ. 4.46 together with the normalization condition, and if we do not care about the phases of the normalization constants, we will be able to write C_1 and C_2 as:

$$C_1 = \sqrt{1 - \frac{N}{\nu}} \quad \text{and} \quad C_2 = \sqrt{\frac{2N|1 + \alpha|\gamma\sigma_p}{\nu\sigma_k}}. \tag{4.48}$$

---

[8]The whole treatment breaks down if α get close to -1. In this case our approximations are wrong because the group velocities of ordinary and extraordinary beams are equal and we would have to take into account higher order terms in equ. 4.38 (compare the appendix on type-I down-conversion in [68]).

The single and coincidence count rates

The single-photon count rates N_m for mode $m = 1, 2$ are defined by

$$N_m = \nu \eta_D \int dt \, \langle \psi | \hat{E}_m^{(-)}(t) \hat{E}_m^{(+)}(t) | \psi \rangle, \tag{4.49}$$

where η_D is the quantum efficiency of the detectors (we assume it to be the same for both detectors), and the field operator now includes the bandwidth filtering, i.e.:

$$\hat{E}_m^{(+)}(t) = \frac{f_m}{\sqrt{2\pi}} \int d\omega \, \exp\left[-\frac{(\omega - \omega_0)^2}{2\sigma_m} - \imath \omega t \right] \hat{a}_m^\dagger(\omega). \tag{4.50}$$

The r.m.s. bandwidths of the filters are given by σ_m, there peak transmittivities are $|f_m|^2$. We will name our modes such that the signal photon is emitted in mode 1, and the idler photon is emitted in mode 2. If we evaluate the expression for the single rate, we get (see e.g. [83]) $N_m = N\eta_D f_m^2 H_m$, where

$$H_1 = \frac{|1+\alpha| \sigma_1}{\sqrt{\sigma_g^2(1+\alpha^2) + (1+\alpha)^2\sigma_1^2 + \sigma_p^2}}$$

$$H_2 = \frac{|1+\alpha| \sigma_2}{\sqrt{\sigma_g^2(1+\alpha^2) + (1+\alpha)^2\sigma_2^2 + \alpha^2\sigma_p^2}}. \tag{4.51}$$

The same field operators are employed in the definition of the coincidence count rate N_c between the detectors in modes 1 and 2:

$$N_c = \nu \eta_D^2 \int dt_1 \int dt_2 \left| \langle \Omega | \hat{E}_1^{(+)}(t_1) \hat{E}_2^{(+)}(t_2) | \psi \rangle \right|^2, \tag{4.52}$$

and we get $N_c = N\eta_D^2 f_1^2 f_2^2 H_c$, where

$$H_c = \frac{|1+\alpha| \sigma_1 \sigma_2}{\sqrt{\sigma_g^2(\sigma_1^2 + \sigma_2^2 + \sigma_p^2)(1+\alpha^2) + (1+\alpha)^2\sigma_1^2\sigma_2^2 + (\alpha^2\sigma_1^2 + \sigma_2^2)\sigma_p^2}}. \tag{4.53}$$

This expression depends on σ_1 as well as on σ_2 while H_m depends only on σ_m. From equation 4.36 we see that η_m is proportional to the ratio $\frac{H_c}{H_m}$. This leads to markedly lower coupling efficiencies for modes with narrower bandwidth filters. At the same time equation 4.51 shows that $H_2 < H_1$ for $|\alpha| > 1$ as it is in our experiment. That means that the overall coupling efficiency will be lower for idler photons than for signal photons.

On the other hand the dependence of H_c on σ_p results in significantly lower values for the overall efficiencies (see equ. 4.36) for pulsed sources in comparison to CW sources. As I

have indicated above this is the answer to the question why we never could achieve as good coupling efficiencies in pulsed setups as we did in CW setups.

In subsection 6.3.1 we will use the equations above to analyze the efficiencies of our SPDC sources, and we will compare the results of this theoretical approach with our experimental data.

5. Synchronization of Independent Sources

In order to be able to observe high-visibility HOM-type interference it is essential to assure the indistinguishability of the photon detection events behind the beam splitter (see section 2.3). Specifically, the time delay between the detection events must not exceed the coherence time of the interfering photons. In the case of independent sources the photon emission times of the two sources will in general be uncorrelated. If the coherence times of the photons is shorter than the time resolution of the detectors, no interference can occur [141, 142]. This problem can either be overcome by sufficiently narrow filtering and sub-coherence-time detection or by synchronizing the timing of the independent sources. Another future solution might be to use sources, which generate photons with sufficiently long coherence times (see e.g. [73]).

The filtering approach (i.e. sub-coherence-time detection) has the advantage of allowing for interference of photons from independent sources, which do not even share timing information. In a recent experiment [59] a configuration of this type was realized. The disadvantage of this method is that the count rates are rather low because of the narrow filters and because of all the continuously created photon pairs only those pairs are taken into account, which are produced at a fixed time delay relative to each other. In addition the interference visibility is significantly lower than it would be in pulsed setups with comparably narrow filters.

The approach we used is based upon the synchronization of pulsed pump lasers. Compared to [59] our scheme requires only moderate filtering in order to achieve high-visibility interference.

5.1. The synchronization method

There are two common methods to synchronize femtosecond lasers, called *active* and *passive* synchronization. The advantages and disadvantages of these methods shall be discussed in the following.

Passive laser synchronization synchronizes the output of two femtosecond laser cavities by means of a Kerr medium, which is shared by both cavities. The presence of a laser pulse from one cavity in the Kerr medium alters the length of the optical path for pulses in the second laser cavity. If the overlap of the two laser beams within the Kerr medium is large enough, this will automatically lead to the synchronization of the pulse trains. As

the two laser modes form a small angle ($\approx 3°$) within the Kerr medium, they will form an interference pattern with a diameter on the same order as the beam diameter [15]. For various lengths of the laser cavities this effect automatically leads to phase locking between the two laser outputs.

While passive synchronization is certainly an elegant way to produce two synchronized and independently tunable laser beams, it has several limitations, which make this method unsuitable for our purposes. On the one hand, the direct influence between the coherence properties of the two laser beams clearly renders these sources non-independent and inappropriate for the objective of the presented work. On the other hand, it is impossible to separate the sources and the method is hardly extensible to synchronize more than two sources. Therefore, passive synchronization is neither fit for future applications in long-distance quantum-communication schemes nor for quantum networking.

These limitations are overcome by *active* synchronization. In this scheme the rising edges of the intensity envelope of the output of a ("slave") laser are synchronized via electronic means to a reference or "master" oscillator. To this end, the *slave* laser is equipped with several piezo actuators attached to cavity mirrors. Adjusting the mirror positions allows to tune the length of the cavities in order to regulate the repetition frequency of the lasers. Because of these actuators the *slave* laser can be considered as a "voltage-controlled oscillator" (VCO), i.e. its frequency can be adjusted via the applied voltage. Using "phase-locked loops" (PLLs, see section 5.1.1) these VCOs can be synchronized to the *master* oscillator [1].

The fact that the synchronized lasers do not have to share any common optical elements guarantees the independence of the lasers and allows to separate the lasers over long distances. An additional feature, which makes active synchronization attractive for future applications, is that it allows an arbitrary number of sources to be synchronized.

In contrast to passive synchronization it is not trivial to achieve coherence between actively synchronized lasers [114]. Because we intended to work with truly independent sources, we did not have any inclination to achieve optical coherence between them.

5.1.1. Phase-locked loops

A Phase-locked loop (PLL) is a feedback system comprised of a phase comparator, a low-pass filter and an error amplifier in the forward signal path and a voltage-controlled oscillator (VCO) in the feedback path (see fig. 5.1). A VCO is an oscillator with a variable frequency, which can be adjusted by applying a control voltage. The purpose of a PLL is to lock the output of the VCO to a periodic input signal.

In the case of the presented experiment, the periodic input signal originates from a fast

---

[1]It is very important to note the different meanings of phase depending if we use it in the context of electronic circuits or optical interference. In both cases "phase" describes the offset of periodic signals. It denotes an offset between field or probability amplitudes in optics and an offset between electronic signals in the context of active synchronization. "Phase-locked" electronic signals do **not** imply a common optical phase between the synchronized laser beams because the electronic signals correspond to the intensity envelopes of the laser output and do not carry any (optical) phase information.
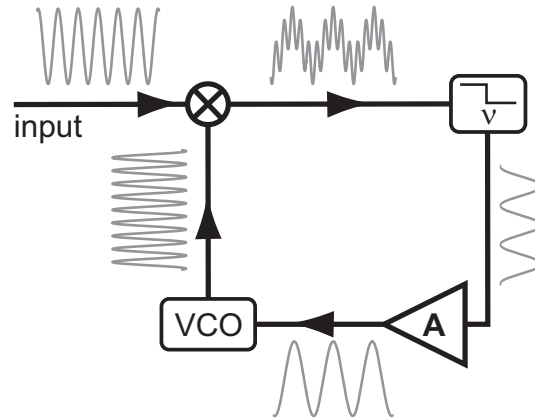
Figure 5.1.: Schematic of a phase-locked loop (PLL). A PLL produces a feedback signal, which synchronizes the frequency of a voltage-controlled oscillator (VCO) to the frequency of a given input signal. To this end the input signal is multiplied with the VCO signal. The resulting signal is passed through a low pass filter to get a signal, which oscillates with the frequency difference of input and VCO signal. After being amplified (A) the signal is fed back as control voltage to the VCO.

photo diode (2 GHz bandwidth), which monitors the intensity output of the *master* laser. The output of the VCO is the signal of another fast photo diode, which monitors the intensity of the *slave* laser. Its frequency can be controlled by applying voltage to piezo actuators in the *slave* laser's cavity (see subsection 6.1.2).

With no input signal present in the PLL, the VCO control voltage $V_d(t)$ will be zero, i.e. the VCO will operate at its "free-running" frequency ω_{vco}. As soon as an input signal is provided, the phase comparator will compare this input to the signal generated by the VCO and produce an error signal $V_e(t)$, which is in general a function of the frequency difference, the phase difference and the frequency sum of the two signals. After being filtered and amplified, this signal is fed back to the control terminal of the VCO. If the input frequency ω_i is sufficiently close to the frequency of the VCO signal (i.e. ω_i is within the "capture range" of the PLL), the feedback causes the VCO to lock with the input signal. The development of the feedback signal over time from the initiation of the feedback to the point where the loop locks is called a *capture transient* and is illustrated in figure 5.2. Figures 5.3 and 5.4 show the corresponding capture transients for the VCO's frequency and the VCO signal's phase, respectively. Once the loop is locked, the VCO and the input signal will have equal frequencies but also a finite phase shift between them. In the locked mode the VCO will also follow changes of the input signal, as long as they are with in a certain limited range called the *lock-range*.

In order to understand the working principle of a PLL we will present a simple example. We will assume that the phase comparator is a signal multiplier. The input signal

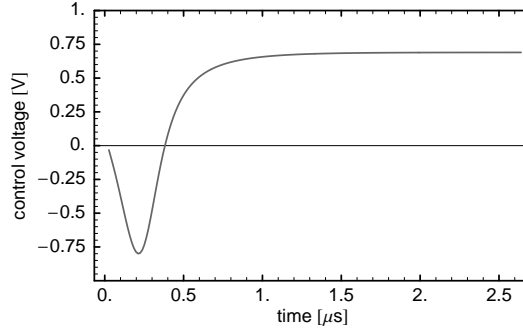$$V_i(t) = V_{i0} cos(\omega_i t) \tag{5.1}$$

Figure 5.2.: Example capture transient of a simple PLL. This curve corresponds to a very simple simulation of the locking process of a PLL. The frequencies of the oscillators were taken to be the repetition rates of our lasers. The response time of the PLL was taken to be equal to the delay between two successive pulses. Typical for capture transients is that their behavior in the beginning, i.e. before they start to converge, depends very strongly on the initial conditions.

and the VCO signal

$$V_o(t) = V_{o0} \cos\left(\omega_o t + \Theta_e\right) \tag{5.2}$$

are simple cosines with frequencies ω_i and ω_o, a phase shift or phase error Θ_e and with amplitudes V_{i0} and V_{o0}, respectively. The phase comparator will generate an error signal by multiplying these signals:

$$V_e(t) = K_1 V_{i0} V_{o0} \cos\left(\omega_i t\right) \cos\left(\omega_o t + \Theta_e\right) =$$
$$= \frac{1}{2} K_1 V_{i0} V_{o0} \left(\cos\left(\left(\omega_i - \omega_o\right) t + \Theta_e\right) \cos\left(\left(\omega_i + \omega_o\right) t + \Theta_e\right)\right), \tag{5.3}$$

where K_1 is a dimensional constant. The low-pass filter will remove the sum-frequency
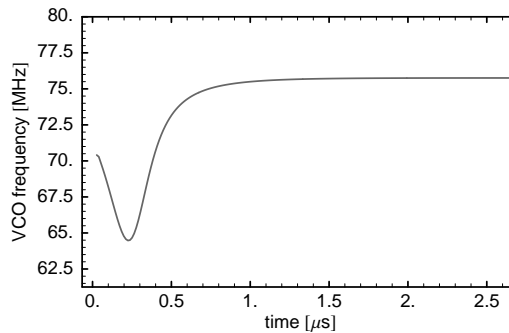

Figure 5.3.: Example capture transient of the VCO signal's frequency in a simple PLL. This curve corresponds to the same PLL as fig. 5.2.
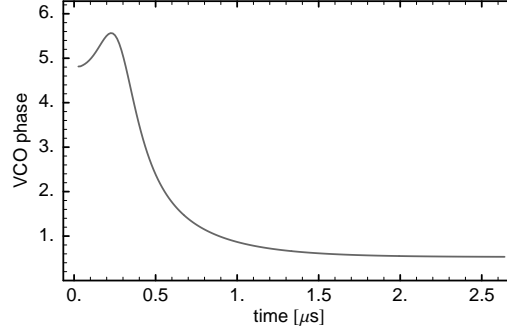
Figure 5.4.: Example capture transient of the VCO signal's phase in a simple PLL. This curve corresponds to the same PLL as fig. 5.2.

component, and the amplifier leaves us with

$$v_d(t) = AK_2 V_{i0} V_{o0} \cos\left((\omega_i - \omega_o) t + \Theta_e\right). \tag{5.4}$$

A is a factor, which depends on the gain of the amplifier, and K_2 is another dimensional constant. This signal is fed back to the VCO's control terminal. It will shift the VCO output frequency by some $\Delta\omega$. If the electronic circuits are appropriately engineered (i.e. the gains and filters are set correctly for the frequencies of the oscillators, no signal limiting or saturation occurs, etc.), the feedback signal will bring the frequency of the VCO eventually closer to ω_i (see fig. 5.3). That means this feedback will eventually lead to the locking of the loop.

Once the loop is locked, the frequency of VCO will be equal to the frequency of the input signal, i.e. $\omega_i = \omega_o$. This condition simplifies equ. 5.4 to:

$$v_d(t) = V_D = AK_2 V_{i0} V_{o0} \cos\left(\Theta_e\right). \tag{5.5}$$

We see that there is still a phase shift between the VCO and the input signal. To analyze this phase shift, let us suppose the free-running frequency of the VCO to be equal to the frequency of the input signal. The free-running frequency refers to the case where the control voltage is zero. That means in this special case the two oscillators are locked for zero control voltage, i.e. $V_D = 0$. It follows that $\Theta_e = \pm\frac{\pi}{2}$. Any drift in the input frequency will change this phase shift. In order to take this possibility into account let us redefine Θ_e as:

$$\Theta_e = \Theta_r \pm \Delta\theta. \tag{5.6}$$

$\Theta_r \equiv \pm\frac{\pi}{2}$ for our example, where the VCO's free-running frequency is equal to the input signal's frequency.

It is the departure $\Delta\theta$ of the phase shift from its reference value of Θ_r that makes the PLL lock. The PLL reaches the locked state by adjusting the frequencies to be the same and by introducing an appropriate phase shift between the signals to supply the VCO with the necessary control voltage to keep its frequency locked to the input signal.

The strength of PLLs lies in the fact that they work not only for such simple cases as the synchronization of two cosine signals. For example they can as well be used to synchronize a triangular wave to a rectangular one. To get a better impression of the wide range of applications of PLLs see e.g. [61].

5.1.2. Active laser synchronization

The oscillators in the PLLs used in the presented experiment are each comprised of a laser producing femtosecond pulses and of a fast photo diode, which monitors the laser's output. These photo diodes have a limited bandwidth (2 GHz in the setup used). The signal generated by the diodes will be the convolution of the actual laser signal and the frequency response function.

The active synchronization scheme used in the presented experiment utilizes two independent PLLs working at different operating frequencies. One operates at 76 MHz, which is the fundamental frequency of the femtosecond lasers. The second PLL operates at the 9th harmonic of this frequency, i.e. at 684 MHz. For tight synchronization the use of higher harmonics is essential. This can be seen by analyzing the noise of femtosecond lasers, because various kinds of noise in femtosecond lasers lead to different characteristics in the power spectrum of a laser (see subsection 4.1.2 on page 75). There we saw that the contribution of jitter to the power spectrum of a periodic signal increases quadratically with the number of the harmonic observed.

Which harmonic should be used for synchronization is a practical question and a trade off between several aspects. In high harmonics the contribution of jitter is higher. As a result the signal to noise ratio of the error signal in the synchronization electronics tends to improve for higher harmonics. On the other hand, the design of electronic circuits becomes more difficult and error-prone with increasing frequency, which leads to a reduction of the signal to noise ratio. In addition, if high harmonics are going to be used, the photo diodes need to have an increasingly broad frequency response. Using such high frequencies will also be problematic if it is intended to separate the synchronized lasers by large distances (see chapter 8).

In the commercially available Coherent Synchrolock, which we used in our experiments, the 9th harmonic is employed. This system is specified to reduce the jitter between the lasers to roughly 3 ps (according to communications with Coherent), when it is operated at the fundamental frequency of $\sim 76\,\mathrm{MHz}$, and to less than 250 fs $(0.02 - 160\,\mathrm{Hz})$, when it is operated at the 9th harmonic $(\sim 684\,\mathrm{MHz})$.

5.2. Sources of relative timing jitter

Apart from the obvious source of relative timing jitter, the imperfections of the laser synchronization, there are less obvious sources of jitter like dispersion of the pump pulses in the optical components and group-velocity mismatch (GVM) between infrared and ultraviolet
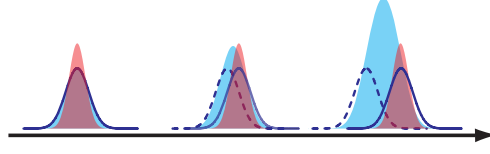
Figure 5.5.: Group-velocity mismatch in SHG. In our SHG crystals the ultraviolet light is slower than the infrared light. UV contributions, which are generated at the beginning of the crystal will lag behind the infrared pump pulse. The contributions at different positions along the crystal will add up incoherently to form the overall UV pulse, which will not be Fourier limited.

light in the SHG and SPDC crystals. We will only take into account the latter two effects and neglect the dispersion in other optical elements along the beam paths.

In most cases we will assume the relative jitter to be Gaussian, i.e. the probability distribution for the jitter will be of the form

$$D(J) = \frac{1}{\sqrt{2\pi}\sigma_J} e^{-\frac{J^2}{2\sigma_J^2}}. \tag{5.7}$$

The assumption of Gaussian distributions allows for analytical solutions in several calculations, which we will encounter, e.g. when we want to predict the visibility of HOM-type interference. Various Gaussian timing jitters of r.m.s. widths σ_{J_i} can easily be combined by convolution into an overall Gaussian distribution with an r.m.s. width of

$$\sigma_J = \sqrt{\sum_i \sigma_{J_i}^2}. \tag{5.8}$$

5.2.1. Second-harmonic generation

The output of the *master* laser is frequency doubled in a Lithium-Triborate (LBO) crystal, while output of the *slave* laser is frequency doubled in a β-Barium-Borate (BBO) crystal. We employed two different types of crystals because we used an already existing SHG setup on the *master* side of our setup. The *slave* side setup was built from scratch. This new setup offered the possibility to test various SHG crystals and to easily determine the properties of the UV beams (profiles and pulse lengths). In the setup on the *master* side we decided against introducing the necessary modifications, which would have been necessary in order to fully characterize the UV beam, because the setup had to be left unchanged for other experiments.

The GVM in SHG has its origin in the different refractive indices for the infrared pump beam and the frequency-doubled ultraviolet light. On its course through the SHG crystal the infrared light will generate ultraviolet light at each point along the crystal. Because of

the difference of the propagation velocities for the different wavelengths the ultraviolet light lags behind the infrared pump pulse. The overall UV pulse, which is created in SHG, will be an incoherent sum of contributions at various points of the SHG crystal (see fig. 5.5). It will not be Fourier limited.

A Fourier-limited Gaussian pulse can be written as the Fourier transform of a Gaussian spectral distribution:

$$E(t) = \frac{E_0}{\sqrt{2\pi}\sigma_p} \int d\omega\, e^{\iota \omega t} e^{-\frac{(\omega - \omega_{p0})^2}{2\sigma_p^2}} = E_0 e^{-\frac{t^2}{2\sigma_p^{-2}} + \iota t \omega_{p0}}, \qquad (5.9)$$

where E_0 is the pulse's peak intensity, σ_p is the spectral bandwidth of the laser pulse and ω_{p0} is its center wavelength. A pulse, which is not Fourier limited, can be described as the convolution of a Fourier-limited pulse with a jitter distribution. If the jitter distribution is Gaussian, and if its width is σ_J, the non-Fourier-limited pulse will be:

$$\begin{aligned}
E'(t) &= \frac{1}{\sqrt{2\pi}\sigma_J} \int d\tau E(t - \tau) \exp\left(-\frac{\tau^2}{2\sigma_J^2}\right) \\
&= \frac{E_0}{\sqrt{1 + \sigma_J^2 \sigma_p^2}} \exp\left[\frac{t^2 \sigma_p^2 - 2\iota t \omega_{p0} + \sigma_J^2 \omega_{p0}^2}{2(1 + \sigma_J^2 \sigma_p^2)}\right].
\end{aligned} \qquad (5.10)$$

By measuring the autocorrelation of the UV pulses we can determine σ_J. Our autocorrelator is based on frequency doubling a laser beam in a BBO crystal. For a UV beam this would generate light around a central wavelength of $\sim 197\,\text{nm}$, a regime in which BBO crystals are already very close to becoming opaque.

Solutions to this problem would be either to employ a different SHG crystal in the autocorrelator or to use SHG in a gas cell [87]. A third workaround, which is the one we used because everything necessary was at hand, is to use a BBO crystal but in the non-frequency-degenerate regime. In our case that meant to mix the UV beam (at 394.25 nm) with the original infrared beam (at 788.5 nm). To fulfill the phase-matching conditions in BBO the polarizations of both beams had to be rotated by 90°, such that the UV beam became ordinarily polarized and the IR beam became extraordinarily polarized with respect to the BBO crystal. This was achieved via a simple trick: we used the beam, which originated from SHG. It contained roughly 50 % UV light and 50 % IR light. The beam was passed through the cylindrical lenses such that both beams were not too divergent, and then it was folded (see fig. 5.6) to rotate the polarizations of the UV and the IR parts simultaneously. The resulting beam was directed into the autocorrelator, where we observed the cross correlation of the UV and IR pulses [2].

---

[2]The autocorrelator was a Pulsescope from APE Berlin. To use it for cross correlation not only the crystal has to be exchanged but also the photomultiplier and the bandwidth filter in front of the photomultiplier.
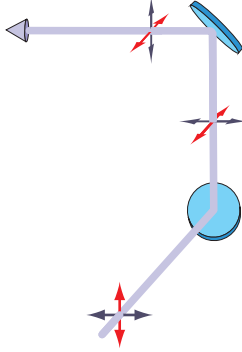
Figure 5.6.: Folding of a beam to rotate its polarization. A beam is reflected twice. First, it is reflected upwards, then at a right angle relative to the original direction back into the horizontal plane.

Because we knew the r.m.s. width of the IR pulse ($\sigma_{ir} = 69 \pm 2$ fs, see also subsection 6.1.1), the width of the UV pulse σ_{uv} could be calculated from the width of the cross correlation ($\sigma_{cc} = 123 \pm 2$ fs) via the relation:

$$\sigma_{uv} = \sqrt{\sigma_{cc}^2 - \sigma_{ir}^2}, \tag{5.11}$$

i.e. $\sigma_{uv} = 102 \pm 2$ fs. This measurement was performed before anything else was set up, i.e. long before any of the experiments were performed, which we present here. Once the rest of the setup had been built it would have been non-trivial to perform this measurement again because of the compact construction of the *slave* setup. For the estimation of the relative-timing jitter we will have to assume that our results were still approximately valid during later stages of the experiment. We used the value, which we measured here, as an estimate for the width of the UV pulses in both sources.

In order to determine the additional jitter due to GVM in the SHG crystals, we have to compare σ_{uv} with the width we would expect for a Fourier-limited pulse. The UV beam on the *slave* side had an r.m.s. bandwidth of ~ 0.92 nm (determined with a USB2000 spectrometer from Ocean Optics). If it was Fourier limited, the pulse width would be $\sigma_{fl} \sim 45$ fs. From these measurement results we can estimate the r.m.s. width of the jitter distribution for the *slave* side:

$$\sigma_J = \sqrt{\sigma_{uv}^2 - \sigma_{fl}^2} \sim 92 \text{ fs}. \tag{5.12}$$

Let us estimate the width of the jitter distribution for the *master* side with the same value. Then the overall jitter due to GVM in both of the SHG crystals will be the convolution of the contributions from the two crystals. Its width will be $\sqrt{2}\sigma_J \sim 130$ fs.

5.2.2. Spontaneous parametric down conversion

The additional timing jitter due to GVM in the SPDC crystals contributes significantly to the overall timing jitter between the interfering photons. Moreover, our discussion will show that its contribution depends on whether horizontally or vertically polarized photons are overlapped at the beam splitter to interfere. To the authors best knowledge this dependence on the polarization of the photons has not been investigated before.

We will estimate the jitter due to GVM in the SPDC crystals from the birefringent properties of the SPDC crystals. Essentially, the effect can be described as follows. In each of the two SPDC crystals the UV pump pulses can generate the observed SPDC pairs with equal probability at any point along their path. Assume that the position where the SPDC pair is created inside a crystal is described by a parameter x, which can take values between $-\frac{L}{2}$ and $+\frac{L}{2}$, where L is the length of the crystal. Depending on this parameter the photons of the SPDC pair will acquire the following time delay relative to the pump pulse:

$$
T_{e,o}(x) = \left(\frac{L}{2} - x \right) \left(\frac{1}{u_{e,o}} - \frac{1}{u_p} \right), \tag{5.13}
$$

where we used e and o to denote if we mean the extraordinarily polarized photon (signal) or the ordinarily polarized photon (idler). The quantity $u_{e,o}$ denotes the group velocities of these photons, and u_p denotes the group velocity of the pump photons. We will make the approximation that the angle of the signal photons and the pump photons relative to the optical axis are the same.

Suppose that $P(\Delta\tau)$ is the four-photon detection probability (see section 2.3), where $\Delta\tau$ is the delay in the optical paths of the interfering photons plus the time delay of the pump pulses. Depending if it is the signal or the idler photons, which we overlap at the beam splitter, the four-photon detection probability will be

$$
P\left[\Delta\tau - \left(T_{e,o}(x_1) - T_{e,o}(x_2) \right) \right], \tag{5.14}
$$

where $\Delta\tau$ is now only the time delay between the pulses, i.e. we assume that there is no difference in the paths for the photons from one crystal or the other to the detectors behind the beam splitter. x_1 and x_2 denote the positions where the SPDC pairs are created in crystal 1 and 2, respectively. Because this position can be anywhere inside the crystal, the overall probability must be written as:

$$
\overline{P}(\Delta\tau) = \frac{1}{L^2} \int_{-L/2}^{L/2} \int_{-L/2}^{L/2} d^2x \, P(\Delta\tau - T_{e,o}(x_1) + T_{e,o}(x_2)), \tag{5.15}
$$

or, if we include the (Gaussian) timing jitter between the two laser pulses (see also equ. 2.82):

$$\overline{P}(\Delta\tau) = \frac{1}{L^2\sqrt{2\pi}\sigma_J} \int dJ \int_{-L/2}^{L/2}\int_{-L/2}^{L/2} d^2x \; P(\Delta\tau + J - T_{e,o}(x_1) + T_{e,o}(x_2)) \exp\left[-\frac{J^2}{2\sigma_J^2}\right].$$
$$(5.16)$$

By substituting a new variable J this can be written as:

$$\overline{P} = \int dJ \; D_J(J - \Delta\tau) P(J), \qquad (5.17)$$

where we defined a new jitter distribution:

$$D_J(J) = \frac{1}{L^2\sqrt{2\pi}\sigma_J} \int_{-L/2}^{L/2}\int_{-L/2}^{L/2} d^2x \; \exp\left\{-\frac{\left[J + (T_{e,o}(x_1) - T_{e,o}(x_2))\right]^2}{2\sigma_J^2}\right\}. \qquad (5.18)$$

Let us calculate this distribution for the experimental parameters in our setup, i.e. for $L = 2$ mm, a UV wavelength of 394.25 nm, and an IR wavelength of 788.5 nm. Let σ_J for now only parametrize the jitter due to the imperfections of laser synchronization, i.e. $\sigma_J = 260 \pm 30$ fs for the first experiment and $\sigma_J = 240 \pm 20$ fs (see section 6.4), $J(\tau)$ for our second experiment. Then $J(\tau)$ can be approximated very accurately with a Gaussian. The width of this Gaussian can be calculated by numerically minimizing the overlap between a Gaussian of variable width and $J(\tau)$. The results for the width of $J(\tau)$ are given in table 5.1.

We see that the timing jitter due to GVM is more pronounced if signal photons are overlapped at the beam splitter. This should lead to noticeably higher dip visibilities if we used vertically aligned polarizers in front of the beam splitter input ports (see table 5.3). Because I discovered this difference in the predicted visibilities only while writing this thesis, it was not taken into account in our experiments. For scans of HOM dips we always used signal photons. Especially in our first experiment we could have achieved significantly higher visibilities (see table 5.3) by simply rotating all polarizers in our experiment by 90°, i.e. by using the signal photons as triggers and by overlapping the idler photons at the beam splitter. We hope that our results will help future experimenters to achieve higher interference visibilities.

5.3. Estimation of the overall relative timing jitter

We will now have to combine all the effects, which we have discussed in this chapter up to now. The effects of GVM in the SPDC crystals and the jitter due to imperfect laser synchronization have already been summarized in table 5.1. In order to gain an estimate for the width of the overall jitter distribution we only have to include the jitter of ~ 130 fs, which results from the GVM in the SHG crystals.

first experiment		second experiment	
idler	270 fs	idler	250 fs
signal	350 fs	signal	340 fs

Table 5.1.: Relative-timing jitter between interfering idler and between interfering signal photons in our two experiments. The timing jitter given here only includes the jitter due to imperfect laser synchronization and due to GVM in the SPDC crystals.

first experiment		second experiment	
idler	300 ± 30 fs	idler	280 ± 20 fs
signal	380 ± 30 fs	signal	360 ± 20 fs

Table 5.2.: Estimated overall relative-timing jitter between the interfering photons in our experiments. In the dip scans, which we are going to present in chapter 7, we always overlapped the signal photons at the beam splitter.

The results are given in table 5.2. If we substitute these values into equations 2.84 and 2.85, we can calculate the visibilities and the widths, which we would expect for HOM dips in our experiments. These estimations are given in tables 5.3 and 5.4. The errors, which we estimated for the visibilities and the widths, are calculated via error propagation. For the error propagation we used the errors of the measured values for the jitter due to imperfect laser synchronization, and we allowed for a 10 % error in all the other parameters, which our functions depend on (filter and laser bandwidths, jitter due to GVM in SHG and SPDC).

first experiment		second experiment	
idler	93 ± 2 %	idler	99.0 ± 0.2 %
signal	90 ± 2 %	signal	98.3 ± 0.4 %

Table 5.3.: Theoretically expected HOM-dip visibilities based on the jitter given in table 5.2. For the first experiment the predicted visibility of 80 ± 2 % is in excellent agreement with the experimentally observed visibility of 90 ± 2 %. In the second experiment the observed visibilities of 96 ± 1 % and 93 ± 3 % are both distinctively lower than our theoretical expectation. We will discuss this deviation in chapter 7.

first experiment		second experiment	
idler	$840 \pm 70\,\text{fs}$	idler	$2.0 \pm 0.2\,\text{ps}$
signal	$870 \pm 70\,\text{fs}$	signal	$2.0 \pm 0.2\,\text{ps}$

Table 5.4.: Theoretically expected r.m.s. widths of the HOM dips. These values are calculated for the jitter values given in table 5.2. In our first experiment we observed a dip width of $790 \pm 30\,\text{fs}$, which is in reasonable agreement with the prediction. In the second experiment the observed dip width was $1.8 \pm 0.1\,\text{ps}$ (see chapter 7), which also is in good agreement with the predicted value.

6. Experimental Setup

We are now going to discuss the details of our experimental setup. It was used to perform two experiments. First we aimed to demonstrate high-visibility HOM-type interference with single photons from independent time-synchronized sources. Our second experiment aimed to increase the visibility of the HOM-type interference even further in order to demonstrate entanglement swapping. In the latter case the visibility was intended to be high enough in order to violate a CHSH inequality with the swapped entangled pairs.

The setup was very nearly the same throughout both experiments. Its layout during the second experiment (apart from the synchronization electronics and the pumps of the femtosecond lasers) is shown in figure 6.1. A quick overview of the minor differences to the setup, which we used in the first experiment, is given in the figure caption.

6.1. Lasers

Here, we will give an overview of the specifications of the lasers, which we used in our experiments. For notes on the alignment of the femtosecond lasers see appendix B.1

6.1.1. Models and Specifications

During the first experiment, where we attempted to demonstrate two-photon interference with independent photons, the *master* laser was pumped with an Argon Ion laser, a Coherent Innova 400. Because of advanced stability requirements in the experiment on entanglement swapping and because of the degrading performance of the Innova we replaced this laser later on with a solid-state diode laser, a Coherent Verdi V10. Another Verdi was used from the beginning for pumping the *slave* laser. Both Verdis were operated at 10 W and at a wavelength of 532 nm. The Innova emitted 12 W at a wavelength of 514.5 nm.

We will not discuss the diode lasers any further but concentrate on the femtosecond lasers, both of which were Coherent MIRA 900F (see fig. 6.2). They were identical with respect to each other up to a modification in the cavity of the *slave* laser. This modification was necessary for active laser synchronization (see chapter 5 and also subsection 6.1.2).

Both lasers were tuned to a center wavelength of 788.5 nm. Their spectra were determined with a USB2000 spectrometer from Ocean Optics. In the first experiment the r.m.s. bandwidths of the *master* laser and the *slave* laser were 2.9±0.1 nm and 3.2±0.1 nm, respectively. The r.m.s. pulse widths of the lasers [1] were between 55 and 60 fs.

---

[1] It should be noted that it is important to use the smallest possible scan range on the autocorrelator for
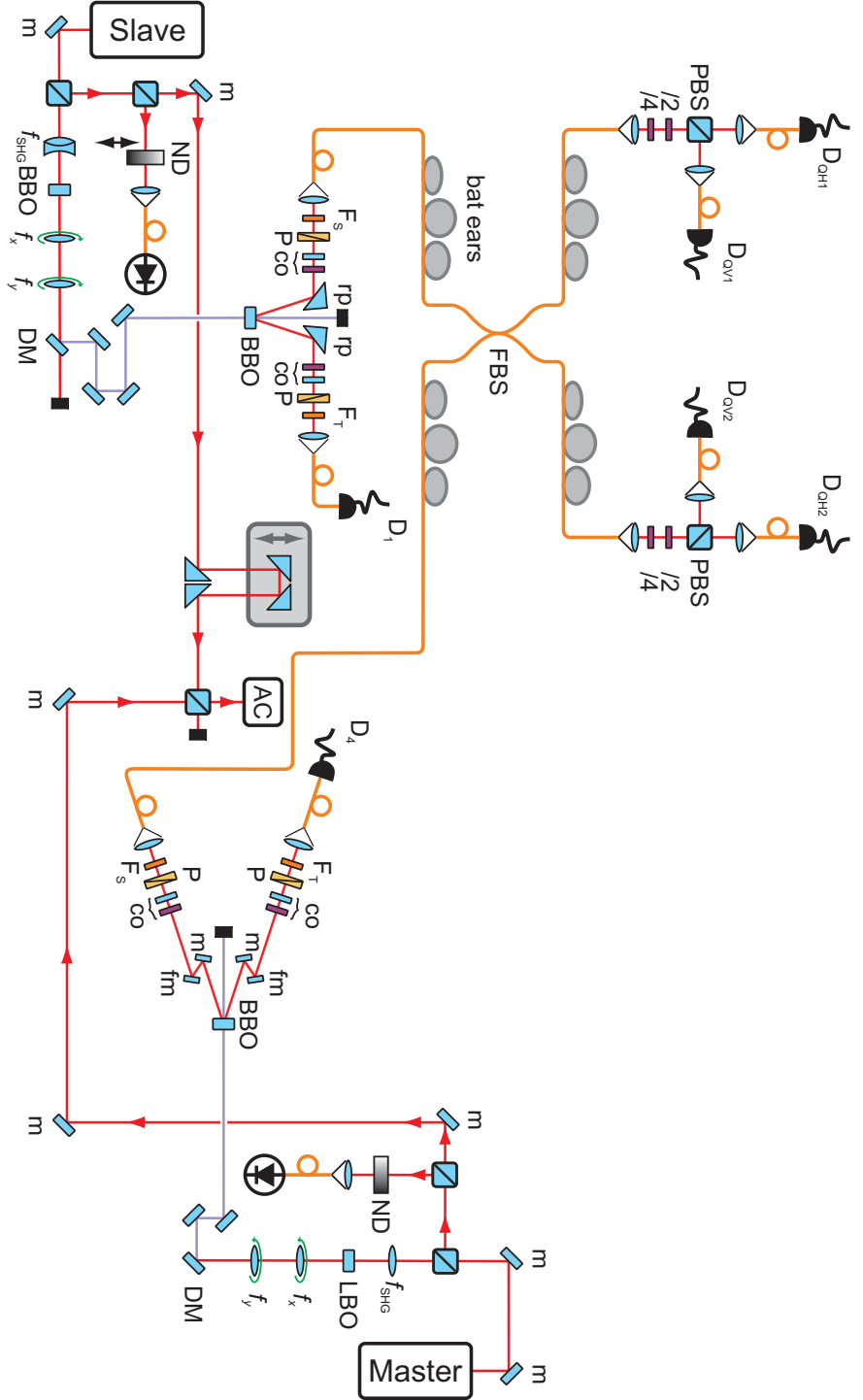
Figure 6.1.: The layout of the setup during the experiment on entanglement swapping with independent sources. With regard to the synchronization we only included the fast photo diodes. In the first experiment we did not implement a more-complete BSM, there were detectors directly after the fiber beam splitter (FBS). The bandwidth of the filters F_s in the modes leading to the FBS was 1 nm in the first experiment and 0.4 nm in the second experiment.
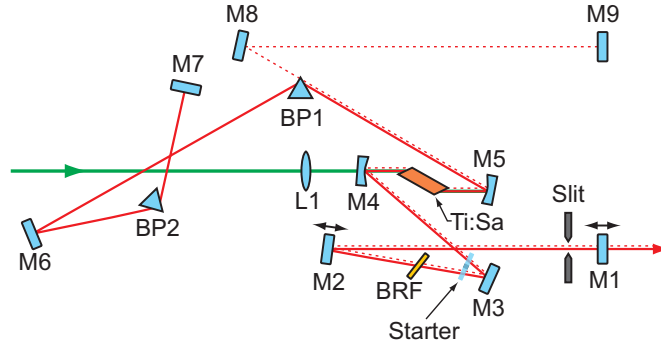
Figure 6.2.: Schematic of the cavity design of our femtosecond lasers (Coherent MIRA 900-F). The gain medium, a Titan-Sapphire crystal (Ti:Sa), is optically pumped. We used a dashed line to indicate the beam path in the auxiliary cavity and a full line to indicate the beam path in the main cavity. Via rotating a birefringent filter (BRF) the center wavelength of the laser can be tuned. The starter can be rotated to change the optical delay in the cavity. It is controlled by a feed-back signal from the MIRA control box to maintain the mode-locked operation of the laser. Piezo actuators allow to translate the cavity end mirror *M1* and the mirror *M2*.

During the second experiment the *master* laser's bandwidth was 2.6 ± 0.1 nm. Its pulse width (r.m.s.) was 67 ± 3 fs. The bandwidth of the *slave* laser has not been measured during the last stage of the experiment but its pulse width was 65 ± 3 fs, and because we know from earlier measurements that the *slave* laser's beam was nearly perfectly Fourier limited, the bandwidth of the laser can be estimated to ~ 2.6 nm. The errors of the pulse widths are calculated from the read-out errors of the autocorrelator. For a scan range of 1.5 ps on the autocorrelator, the read-out error is $\frac{1}{256} 1.5$ ps ~ 6 fs. To get the r.m.s. error, we divide this value by $\sqrt{\ln(256)}$ and round the result up to 3 fs.

6.1.2. The Synchrolock Extension

In order to actively synchronize the *slave* to the *master*, it is necessary to allow an electronic feedback signal to adjust the cavity length of the *slave* (see chapter 5). Because the synchronization scheme by Coherent Inc. uses two separate circuits for coarse and fine synchronization, the positions of two of the *slave's* cavity mirrors are adjustable via piezo actuators. These are the mirrors *M1* for coarse adjustment and *M2* for fine adjustment (see fig. 6.2).

---

measuring the autocorrelations of the pulses. The time resolution of the autocorrelator, a PulseScope from APE Berlin, can be calculated by dividing the scan range by 256. A large scan range leads to a low time resolution and in general results in values for the r.m.s. bandwidth that are smaller than the actual pulse widths.
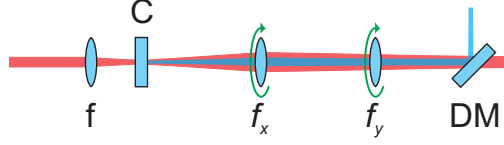
Figure 6.3.: Schematic of the setup for SHG. The principle layout is the same for the *master* and *slave* sources. A lens (f) focuses the infrared beam onto a non-linear crystal (C). Cylindrical lenses, f_x and f_y are used to correct the beam profile. They can be rotated around the beam axis.

6.2. Second harmonic generation

In order to get UV laser pulses, we had to frequency convert the infrared output of the femtosecond lasers. This is done via second harmonic generation (SHG) as described in 4.2. Here, we will elaborate on the experimental realization and optimization of SHG.

6.2.1. Experimental Realization of SHG

The setup for SHG differs slightly for the *master* and the *slave* sources. While the *master* source uses a 2 mm thick LBO (Lithium Triborate or LiB_3O_5) crystal, we chose a 2 mm thick BBO (β-Barium Borate or $\beta-BaB_2O_4$) crystal for the *slave* source. For details on this choice and the performance of various crystals for SHG, see [17].

A further difference is the use of an achromatic doublet instead of a single lens in the SHG on the *slave* side. Especially in the case of broad-band pumps achromatic lenses result in a better defined waist of the various constituent wavelengths (i.e. reduced chromatic aberration). Possible negative side effects are stronger dispersion due to the fact that achromatic lenses are thicker than single lenses and fluorescence in the glue between crown and flint of the achromatic doublet. The fact that the values, which we predict for the visibility and the width of the HOM dip in our first experiment, were in good agreement with the experimental results (see section 7.1) indicates that the dispersion in the achromatic lens can be neglected for our purposes. We did not experience any negative influence from fluorescence although it did trouble colleagues, who were working with a collinear SPDC setup.

Apart from these differences the SHG setups for both sources are identical and are illustrated in figure 6.3. The profiles of the ultra-violet beams were elliptic, and on the *slave* side the profile was also rotated noticeably with respect to the laboratory frame of reference. Cylindrical lenses, which could be rotated around the beam axis and translated along every coordinate axis, were used to correct the beam profile. How we realized the correction of this astigmatism (see 4.2.2) experimentally will be described in the following.

6.2.2. Measurement and correction of the beam profile

In subsection 4.2.2 we explained that the correction of the astigmatism of the UV beam generated via SHG is essential in order to achieve high SPDC efficiencies. It is not only important to prevent wave-front distortions but also to assure that the beam pumping the SPDC crystal is circular, i.e. that its waists [2] are of the same size and are located at the same position along the beam. There we also discussed how the astigmatism can be corrected by using two cylindrical lenses that are oriented orthogonal with respect to each other and that are oriented along the axis of the elliptical beam profile. To determine the positions where to place the cylindrical lenses it is necessary to determine the sizes and the positions of the waists of the UV beam.

To fully characterize the profile of a laser beam it is necessary to measure its profile with a CCD camera at multiple positions along the beam. The aim was to characterize a two-dimensional Gaussian beam, which would fit the recorded data best.

Because SHG is a second order effect the waist of the generated UV beam will be tighter than the waist of the IR beam pumping the process by a factor of about $\frac{1}{\sqrt{2}}$ [3]. The divergence of a (one-dimensional or circular) Gaussian beam is

$$\Theta = \frac{\lambda}{\pi w_0}, \tag{6.1}$$

where w_0 is the waist of the beam. Because the wavelength of the UV beam is half of the wavelength of the IR beam, the divergence for the UV beam will be smaller than that of the IR beam by a factor of about $\frac{1}{\sqrt{2}}$. Nevertheless, the emerging beam will diverge rapidly. As a result, the CCD has to be placed near enough to the SHG crystal to prevent the beam from becoming broader than the CCD chip. At the same time IR light has to be filtered out of the beam, especially since the CCD chip is much more sensitive in the IR regime. To prevent the CCD from being saturated the intensity of the remaining UV light has to be significantly reduced. This cannot be achieved by reducing the pump power. Due to the nonlinearity of the process this would change the UV beam profile, which we want to measure. We found the best solution to be a combination of two highly reflective IR mirrors and as many neutral density filters as necessary (see fig. 6.4). The huge advantage of IR mirrors in comparison to dichroic mirrors was that they filtered out the IR part much better than the dichroic mirrors, while they reflected a huge part of the UV light as well. Hence, they fulfilled two purposes simultaneously.

---

[2]That means the waist parallel to the optical table and the waist perpendicular to it, where the optical table could also be replaced by any plane rotated by a constant angle around the direction of propagation of the beam.

[3]Of course this is an approximation because the UV beam is astigmatic and has an elliptic and not a circular waist. Its intensity depends quadratically on the intensity of the IR pump. Because the IR intensity distribution is Gaussian, the UV intensity distribution will approximately be the square of this Gaussian distribution. The result will again be a Gaussian but with a width, which will be narrower by a factor of $\frac{1}{\sqrt{2}}$.
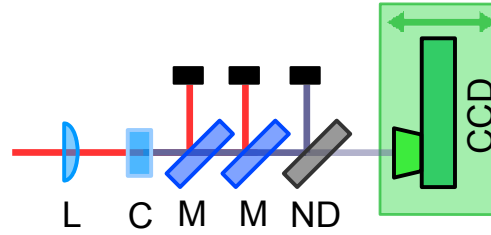
Figure 6.4.: Setup to record the profile of a UV beam generated via SHG. Highly reflective mirrors (M) are used to filter out all infrared light. Neutral-density filters (ND) have to be placed in front of the CCD camera to prevent saturation. The CCD itself is mounted on a translation stage in order to record the intensity profile at several positions along the beam.

The astigmatism of the UV beams encountered in the presented experiment turned out to be not general but rather of type 1 or 2 as defined in section 4.2.2. That means, they did not rotate around their own axis during free propagation but the profile was elliptic, i.e. it had two different waists along two orthogonal axes x and y, which are perpendicular to the direction of propagation z. These axes x and y had some constant angle relative to the laboratory reference frame. On the *master* side (SHG with an LBO) that angle was $\sim 0°$, while the rotation of the beam profile on the *slave* side (SHG with a BBO) was more pronounced. There, the profile was rotated by $\sim 10°$ relative to the optical table [4]. The angle of a profile can in principle be determined in two ways, which can be checked against each other:

- the CCD camera is mounted in correspondence with the coordinate axis of the laboratory reference frame. Then the angle of the beam profiles axis relative to the laboratory coordinate system can be measured directly with the CCD camera.

- a rotatable cylindrical lens is centered around the beam. If the lens's angle of rotation does not coincide with the angle of the beam's profile **and** if the two waists of the profile are not at the same position, the lens will introduce general astigmatism and the beam profile will rotate during propagation. This can be checked by moving the CCD camera along the beam (see fig. 6.5). By slightly rotating the cylindrical lens the general astigmatism can be minimized. If it vanishes, the angle of the lens will coincide with the angle of the beam profile.

In practice the second method has been used for fine adjustment after the angle was chosen approximately according to the angle observed with the CCD camera. This method was preferred as it does neither rely on the exact mounting of the CCD camera, nor does it rely on how well the cylindrical lenses have been glued to their rotation mounts. This method

---

[4]As has been mentioned earlier this angle could be easily explained if the normal vector to the plane defined by the optical axis of the BBO and the laser beam was not horizontal.

will only work if the two waists do not coincide in their position. Only in this case it is important to exactly determine the angle of the profile. For a beam, which is astigmatic of type 1, the more simple first method to determine a profile's angle is accurate enough.

Unfortunately, we only noticed this requirement when we tried to find the rotation angle of the profile of the beam emitted by the LBO on the *master* side. There, the second method failed utterly and we had to estimate the profile's angle via CCD. Subsequently the angles of the cylindrical lenses were fine tuned in order to optimize the circularity of the beam profile.

Interestingly enough, the second method worked fine for the *slave* side SHG, where we used a BBO crystal, but not for the *master* side SHG [5]. From these facts we can conclude that there must have been a difference between the waist positions in case of the BBO crystal. Nevertheless, we fitted a two-dimensional beam to the CCD data assuming the *slave* beam's waists to be at the same position within the BBO crystal. Our success in optimizing the circularity of the beam profile shows that it was legitimate to neglect the difference in the waist positions in our optimizing procedure once the cylindrical lenses had been adjusted to the profile's angle.

All fitting and correction procedures utilized in our experiment (see appendix C) were developed for their use in optimizing the *slave* side SHG. As has been described in the preceding paragraphs, the astigmatism encountered was more pronounced for the BBO than for the LBO crystal. Apart from the determination of the profile's angle the procedures for the correction of the beam profiles were equivalent for both SHG setups. In this section we will concentrate on the measurement and correction of the UV beam generated by the SHG on the *slave* side.

Because the angle of the beam profile relative to the laboratory coordinate frame was constant, the UV beam could be described relative to this rotated reference frame. The z-axis was defined by the laser beam's direction of propagation. x and y axis were those corresponding closest to horizontal and vertical, respectively. The two-dimensional Gaussian beam could thus be described by its waists in the x and y axis, and by the positions of these two waists along the z axis.

An additional simplification arose from the fact that it is a good approximation (see the discussion above) to assume that a UV beam generated by SHG has both of its waists at the same spot within the SHG crystal. This reduces the number of the parameters, which are necessary to describe the beam, to three: the position along the beam, and the sizes of its waists.

We used *Mathematica* to fit a two-dimensional Gaussian beam described by these three parameters to the profiles measured with the CCD camera (see fig. 6.6). For an exact description of the fitting procedure, see appendix C. In order for the fit to be accurate, the difference between the profiles recorded at the various positions must differ by more than the error in the profile measurements.

In our case the beam originating from the SHG crystal was diverging very rapidly limiting

---

[5]A plausible reason is the much tighter focusing of the beam in the *slave* side setup.
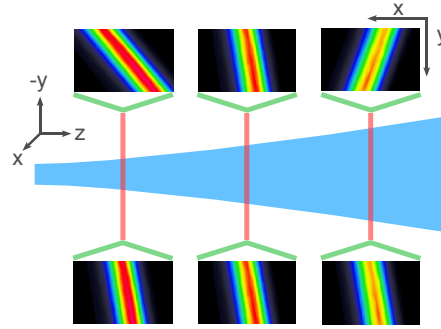
Figure 6.5.: Determining the angle of the beam profile relative to the laboratory coordinate system. The depicted beam profiles have been measured under conditions where the angle did not change. They have been rotated to illustrate this example. If a cylindrical lens is put in the beam path at an angle other than that of the profile, and if the beam already is astigmatic of type 2 (see 4.2.2 on page 79), the beam will become generally astigmatic, i.e. of type 3. Its profile will rotate around the axis of propagation (profiles sketched in the upper part, in contrast to the ones with constant angle below).

the distance coverable with the 1/4 inch-wide CCD area to about 15 to 20 cm from the crystal. Close to the outer limit of this distance we place a CCD camera on a translation stage with its axis along the beam. The translation stage had a travel range of 25 mm. Fitting a general astigmatic beam to the measurement results resulted in unrealistic results as the error of the measured profile angles over such a short distance was large enough to lead to largely varying fit results. In order to get good fit results we assumed the angle of the beam profile to be constant, i.e. no general astigmatism.

Once the beam profile is fully characterized, we will be able to correct its astigmatism. To this end we have to know where and how tight we want to focus the UV beam. In all pulsed
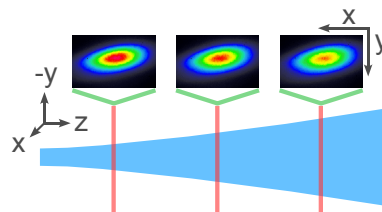

Figure 6.6.: Fitting of a Gaussian beam profile. The profile is measured at several positions with a CCD. Our *Mathematica* routines vary the parameters of a Gaussian beam to minimize the deviations of the measured and the calculated profile dimensions at these positions.

SPDC experiments in our group prior to this one the waist of the UV beam was chosen to be $\approx 150\ \mu$m (i.e. its diameter was $\approx 300\ \mu$m). This holds true for the *master* side of our setup as well.

Based upon observations made for the CW case [21], we chose a smaller waist of $\approx 80\ \mu$m for the *slave* side setup. Two cylindrical lenses of 10 and 15 cm focal lengths were employed for focusing the UV beam and for correcting its profile. These lenses allowed for a circular waist of about the desired size of 80 μm at a distance of about 65 cm from the SHG crystal. The exact results of our profile measurements and calculations are given in tables C.2 and C.3 in appendix C along with a detailed description how these results were obtained.

We employed the fit results to estimate the optimal positions of the cylindrical lenses in order to gain a maximally circular Gaussian beam. After placing these lenses at the calculated distances, their rotation angle around the beam was adjusted by the procedure described in the previous subsection. We maximized the beam's circularity by walking the positions of the two lenses.

The circularity[6] of the corrected beam was observed to be better than 0.98 at several positions over a distance of about 30 cm in the vicinity of the position of the UV-beam's waist. This presents a major improvement compared to other pulsed setups, where the cylindrical lenses were adjusted only to achieve circularity at the position of the SPDC crystal. Circularity at only one position is not sufficient to rule out distortion of the pump-beam's wave front within the down-conversion crystal. Such distortions will diminish the quality and the efficiency of the phase matching in the SPDC process.

To see that our method to optimize the circularity of the UV beam indeed proved useful in order to achieve higher SPDC efficiencies can best be seen by comparing the count rates achieved in our setup with the count rates in a comparable setup. In our case this comparison is easy because we used two SPDC setups, in one of which we corrected the UV beam as has been discussed above. In the first experiment (see tables 6.1 and 6.2) the number of coincidences on the *master* side at ~ 700 mW pump power was 67299 in 10 s (without polarizers). On the *slave* side they were 181652 in 10 s at ~ 800 mW pump power. Even if we take into account the difference between the pump powers (it gives a factor of $\frac{7}{8}$), the ratio between these rates will still be ~ 2.4. Here, we did not even take into account that the coupling efficiencies were significantly lower on the *slave* side. Similarly, we get a factor of ~ 2.6 for the second experiment (we compared the sum of all count rates, i.e. $HV + HH + VH + VV$, in table 6.5).

6.3. Spontaneous parametric down-conversion

Two independent SPDC sources had to be aligned. A new SPDC setup was built on the *slave* side (see fig. 6.8). On the *master* side a working setup was already in existence. Because this setup did not meet our needs regarding entanglement and filter bandwidths, we used flip mirrors to redirect the photons of this setup to additional couplers (see figures 6.7 and 6.9).

---

[6]Circularity is defined as the ratio of the minor to the major axis of an elliptical profile.
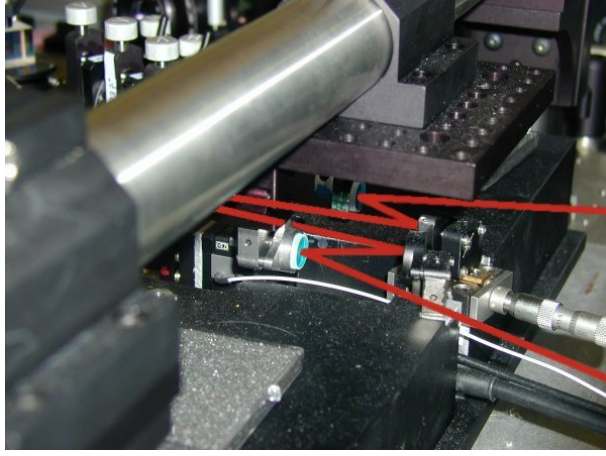
Figure 6.7.: Redirection of the SPDC photons in the *master* side SPDC setup (see fig. 6.9). The red lines illustrate how the flip mirrors redirect the SPDC photons.

We employed 2 mm thick BBO crystals, cut for type-II phase matching, as the nonlinear mediums in our SPDC sources. The pump beams traversed the crystals at angles $\Psi_{OA} = 43.5°$ relative to the optical axes. To compensate for longitudinal and transverse walk off (see [129]) we used a $\lambda/2$ plate and a 1 mm thick BBO crystal of the same type as the SPDC crystals in each of the modes of the emitted photons (see figures 6.8 and 6.9). The lenses of the single-mode fiber couplers had a focal length of 15.4 mm and a clear aperture of 5 mm. On the *slave* side the fiber tips were 25.0 ± 0.4 cm distant from the SPDC crystal. We chose this distance based on the results of a faulty simulation of the angular distribution of the SPDC emission. According to that simulation we would have expected optimal results by matching the single-mode fibers onto a waist of 40 μm at the crystal. A corrected and up-to-date version of this simulation will be presented in appendix D. The optimal distance [7] for a UV-waist of 80 μm and a crystal thickness of 2 mm would have been $\sim$ 98 cm. In the *master* side setup the distance between the fiber tips and the SPDC crystal was 80 ± 2 cm. The optimal distance for the *master* side for a waist of $\sim$ 150 μm and a crystal thickness of 2 mm would have been $\sim$ 140 cm.

6.3.1. Count rates and entanglement visibilities

In the following we will present the count rates, which we recorded in our experiments. They are used to estimate the coupling efficiencies of the single-mode fiber couplers and the efficiencies of the sources in general. We will show that the data is in good agreement with the predictions of our theoretical results from subsection 4.3.2. The contrast of the

---

[7]The optimum is where the mode of the single-mode fiber is matched with the illuminated volume of the crystal. The radius of this volume is the sum of the UV waist and half of the transverse walk-off of the UV beam.
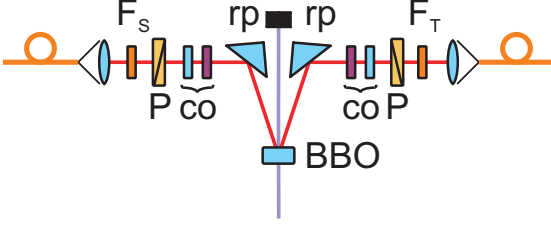
Figure 6.8.: Schematic of the SPDC setup on the *slave* side. The SPDC photons are emitted by a BBO crystal. They are redirected by reflection coated prisms (rp) before each of them passes through compensation optics (co), which consist of a $\lambda/2$-plate and a BBO half as thick as the SPDC crystal. After polarizers (P) and bandwidth filters (F_1 and F_2) the photons are collected into single-mode fibers.
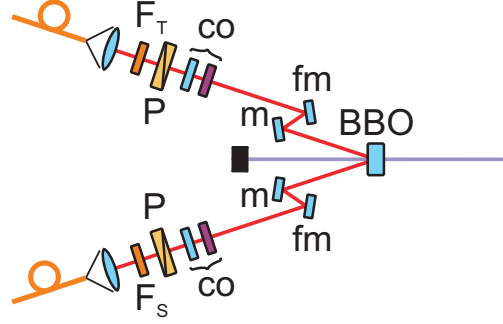
Figure 6.9.: Schematic of the SPDC setup on the *master* side. In contrast to the setup on the *slave* side the SPDC photons are reflected twice: first at mirrors (m) from the preexisting SPDC setup, then at flip mirrors (fm), which redirect the photons from the old setup to our two single-mode fiber couplers.

coincidences in the 45° basis is used as a measure for the visibility of the entanglement of the states generated by the sources.

The data

The count rates for the first experiment are given in tables 6.1 and 6.2 for the *master* and the *slave* source, respectively. Entanglement was unnecessary at this stage.

In the second experiment, we were mainly interested in optimizing the entanglement visibility to overcome the visibility threshold of $\frac{1}{\sqrt{2}}$ (see subsection 1.5.4) for the violation of the CHSH inequality in entanglement swapping. The visibilities and corresponding coincidence count rates are given in table 6.5 for both sources. In the tables 6.3 and 6.4 we present count rates in the HV basis, which were taken a few days before the optimization of the sources for high entanglement visibility. In the course of this optimization we reduced the UV pump powers to 510 mW on the *master* side and to 350 mW on the *slave* side (see also subsection 7.2.1).

Analysis of the data

The data given in the previous paragraph can be analyzed using the expressions for the coupling efficiencies, which we derived in 4.3.2. We will compare the ratios of single count

master source				
1 nm coupler		3 nm coupler		coincidences
H	311247	V	469730	33442
V	133301	H	946627	27377
	454421		1476725	67299

Table 6.1.: Single and Coincidences count rates in 10 s for the first experiment with 1 nm and 3 nm (FWHM) bandwidth filters. The count rates for the 1 nm coupler are the sum of the counts in the two outputs of the beam splitter, which the coupler was connected to. For those results, where polarizers were used in front of the couplers, we indicated the orientation of the polarizers left of the corresponding single count rates. The UV pump power was ~ 700 mW.

slave source				
1 nm coupler		3 nm coupler		coincidences
H	1630463	V	3182637	103839
V	895933	H	5558397	86321
	2544872		7790821	181652

Table 6.2.: Single and Coincidences count rates in 10 s for the *slave* source. The UV pump power was ~ 800 mW.

master source						
3 nm coupler		0.4 nm coupler				coincidences in sum
H	1175294	Q_{1V}	20683	Q_{2V}	23478	9016
		Q_{1H}	43110	Q_{2H}	36796	202
V	673273	Q_{1V}	20953	Q_{2V}	23506	91
		Q_{1H}	42940	Q_{2H}	36714	11118

Table 6.3.: Single and Coincidences count rates in 10 s for the *master* source in the second experiment with 0.4 nm and 3 nm (FWHM) bandwidth filters. The 0.4 nm couplers were connected to a more-complete Bell-state analyzer (BSA) (see fig. 6.19). We give the single count-rates for each of the outputs of the two PBS in the BSA. The coincidence count rates presented here are sums of coincidences, e.g. between the 3 nm coupler and Q_{1V} and Q_{2V}. These rates were measured at a UV-pump power of ~ 510 mW.

slave source						
3 nm coupler		0.4 nm coupler				coincidences in sum
H	5563351	Q_{1V}	123330	Q_{2V}	118397	30497
		Q_{1H}	252268	Q_{2H}	191996	3268
V	2451262	Q_{1V}	123579	Q_{2V}	118939	814
		Q_{1H}	252622	Q_{2H}	192606	32999

Table 6.4.: Single and Coincidences count rates in 10 s for the *slave* source in the second experiment with 0.4 nm and 3 nm (FWHM) bandwidth filters. The power of the UV pump was 700 mW.

master							*slave*						
settings		coinc.	settings		coinc.		settings		coinc.	settings		coinc.	
H	V	10610	+	-	9907		H	V	18086	+	-	17863	
H	H	293	+	+	313		H	H	689	+	+	611	
V	H	9185	-	+	10110		V	H	17261	-	+	17568	
V	V	197	-	-	212		V	V	257	-	-	615	
visibility: 95 %			visibility: 95 %				visibility: 95 %			visibility: 93 %			

Table 6.5.: Coincidence count rates over 10 s for the HV and the ± basis in the second experiment. The UV pump powers were 510 mW and 350 mW for *master* and *slave*, respectively. For each coincidence rate the left-hand measurement setting corresponds to the coupler with the 0.4 nm filter, the right-hand setting to the coupler with the 3 nm filter.

rates and coincidences to the theoretically expected ratios H_c/H_m ($m = 1, 2$). If we employ the definitions of H_c and H_m (see equations 4.53 and 4.51), we will get (η_D is the detection efficiency):

$$f_1^2 \eta_D = \frac{N_c/N_2}{H_c/H_2}$$

$$f_2^2 \eta_D = \frac{N_c/N_1}{H_c/H_1}. \tag{6.2}$$

That means, with these ratios we can estimate $\eta_D f_1^2$ and $\eta_D f_2^2$. Because we do not know the exact detection efficiencies (they are approx. 40 % but vary from detector to detector), we cannot extract the coupling efficiency. In our formal description we introduced f_1^2 and f_2^2 as the peak transmittivities of our filters. Effectively, they also contain information about the conditional coupling efficiency in the corresponding modes. We use the term "conditional coupling efficiency" to describe the probability to couple a photon into a single-mode fiber, when its partner photon has already been coupled and detected. If we know the actual peak transmittivities of the filters, we can calculate the products of these conditional coupling efficiencies with the detection efficiencies. Because the various detectors have roughly the same efficiencies these results will give us a coarse estimation of the coupling efficiencies.

From the data of the first experiment, we can conclude that $f^2 \eta_D$ for the 3 nm coupler in the *master* source is 0.34 for horizontally polarized (H) photons and 0.30 for vertically polarized (V) photons. For the 1 nm coupler in the *master* source we get 0.30 (H) and 0.26 (V). The smaller the difference between the values for horizontally and vertically polarized photons is, the closer we will be to the intersection lines of the SPDC cones. On the *slave* side we obtain 0.16 (H) and 0.18 (V) for the 3 nm coupler. For the 1 nm coupler we get 0.14 (H and V).

A similar analysis of the data for the second experiment yields 0.34 (H) and 0.38 (V) for the 3 nm coupler on the *master* side. For the 0.4 nm coupler on the *master* side we get 0.17 (H and V). On the *slave* side we obtain 0.21 (H) and 0.20 (V) for the 3 nm coupler. The data for the 0.4 nm coupler on the *slave* side yields 0.14 (H) and 0.12 (V).

The peak transmittivities for the 3 nm, the 1 nm and the 0.4 nm filters, respectively, were approximately 0.9, 0.8 and 0.7. With these values we can calculate the conditional coupling efficiencies times the detection efficiencies. The results are given in table 6.6. We see that the coupling efficiencies on the *master* side were always significantly better than on the *slave* side.

Our calculations in section 4.3.2 predict that the probability for detecting a signal photon will always be higher than the probability for detecting an idler photon. In our experimental data this should be reflected by higher single rates for horizontally than for vertically polarized photons.

The theoretical expectation of the ratio between signal and idler photons can be calculated with the expressions in section 4.3.2 to be 1.81, 1.91 and 1.92 for 3 nm, 1 nm and 0.4 nm filters, respectively. We calculated this ratio for all data, which we ever recorded during our

first experiment						second experiment						
master			*slave*			*master*			*slave*		
3 nm	H	0.38	3 nm	H	0.18	3 nm	H	0.38	3 nm	H	0.23
	V	0.33		V	0.20		V	0.42		V	0.22
1 nm	H	0.38	1 nm	H	0.18	0.4 nm	H	0.24	0.4 nm	H	0.20
	V	0.33		V	0.18		V	0.24		V	0.17

Table 6.6.: Estimated conditional coupling efficiencies of the couplers in our experiment. We use the values for f^2, which we calculated in the text, and divide them by the peak transmittivities of the filters (~ 0.9 for the 3 nm filters, ~ 0.8 for the 1 nm filters and ~ 0.7 for the 0.4 nm filters). In each case we distinguish between the coupling efficiencies for horizontally and vertically polarized photons.

experiment. In that data the ratio between H and V photons is 1.8 ± 0.2, 1.9 ± 0.3 and 1.71 ± 0.15 in the same order as the theoretical expectations are written above. Given the fact that the results depend very much if our couplers point along the intersection lines of the SPDC cones, these results are in reasonable agreement with the theoretical predictions.

6.4. Synchronization

As has been mentioned in chapter 5 we used the commercially available Synchrolock from Coherent Inc. for the active synchronization of our lasers. In this section we will discuss its operation, its performance and how we integrated it into our setup.

A schematic of Coherent's Synchrolock is given in fig. 6.10. In principle, the Synchrolock can be used to synchronize a *slave* laser to any periodic electronic signal, as long as that signal's stability is sufficiently high. The electronic signal we synchronized it to was the signal of a fast photo diode with 2 GHz bandwidth, which measured the intensity of the *master* laser. This signal represented the master oscillator in the PLLs (see 5.1.1). Another fast photo diode of the same type measured the intensity of the *slave* laser. We can say that the VCO (see 5.1) in our PLLs comprises three components:

- a *slave* laser

- a Synchrolock extension (see 6.1.2), which allows to control the oscillators frequency

- a fast photo diode to measure the intensity of the laser output. Its signal is the actual output of the VCO.

Coherent's Synchrolock uses two PLLs. One is working at the fundamental frequency 76 MHz of the lasers. We will refer to it as the "fundamental loop". The second operates at the 9th harmonic, i.e. 684 MHz, of that frequency. It will be referred to as the "9th-harmonic
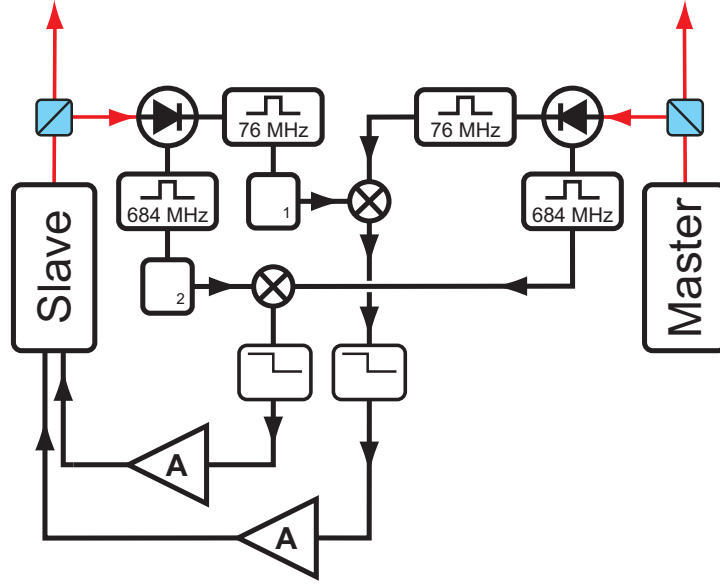
Figure 6.10.: Schematic of the Coherent Synchrolock. For each laser the reflection from a beam splitter with low reflectivity (plates of quartz glass in our setup) is redirected to a fast photo diode. The diode signals are passed through electronic bandwidth filters around the fundamental frequency and the 9th harmonic. For the fundamental as well as for the 9th harmonic loop it is possible to introduce electronic phase shifts (Φ_1 and Φ_2) between the signals to adjust the relative time delay of the laser pulses. The signals from both lasers are multiplied and then passed through low-pass filters. These filtered signals are amplified and fed back to the piezo motors within the *slave* laser's cavity.

loop". Each of these two PLLs controls the VCO via a corresponding piezo actuator in the Synchrolock extension (see 6.1.2).

The fundamental loop is used to achieve a first, coarse synchronization of the two lasers. Additionally, as soon as the fundamental loop is active the relative time delay of the two lasers can easily be adjusted by changing the (electronic) phase shift between the signals of the photo diodes. This adjustment can be done by using the Synchrolock control software, which allows to change the delay in 3 ps steps over a range of 15 ns (these 3 ps corresponds roughly to the resolution of the fundamental loop).

Once the delay between the lasers is adjusted to this degree of accuracy, the 9th-harmonic loop can be activated to replace the fundamental loop. According to the specifications of Coherent's Synchrolock the relative timing jitter between the two lasers should be on the order of (or even less than) 250 fs ($0.02 - 160$ Hz) as long as the 9th-harmonic loop is operating. Long-time drifts (longer than ~ 50 s) are not compensated for by the Synchrolock and have to be taken care of separately.
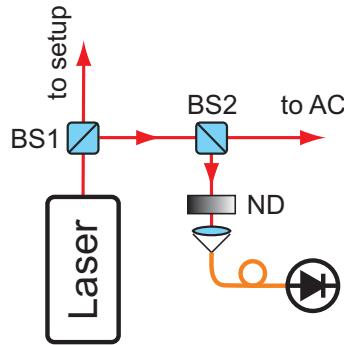
Figure 6.11.: Schematic of the setup to split off light from the lasers for the Synchrolock and the autocorrelator (AC). The reflex from a beam splitter (BS1) with low reflectivity (plates of quartz glass in our setup) is split once more by a symmetric 50 : 50 beam splitter (BS2). The reflected part is coupled into a multi-mode fiber, which leads to a fast photo diode in the Synchrolock. The transmitted part of the beam is redirected to the AC.

6.4.1. Photo diodes and their signals

The synchronization works with electronic signals only. But still we had to transfer part of the laser beams to the Synchrolock's control box because it contained the fast photo diodes to measure the lasers' intensities. That the photo diodes were packed into one huge black box with the Synchrolock electronics is one of the disadvantages of a corporate solution. If we had manufactured the electronic circuits ourselves, we could have separated the photo diodes from them. This way the distinction between the master oscillator, the VCO and the PLL electronics would have been clearer. In a long-distance synchronization experiment it would make more sense to measure the optical signals locally and to transmit electronic signals than to send parts of the laser beams over these distances to be detected afterwards (see chapter 8).

Figure 6.11 shows the assembly that we used to split off parts of the laser beams for the Synchrolock's photo diodes and for our autocorrelator (see below).

At some distance from the laser we placed a glass plate at an angle of 45° in the beam. The more distant face of the glass plate is anti-reflection coated for the laser's wavelength. Significant reflection only occurs for the front face of the plate. Because the IR laser beams are horizontally polarized, only about 0.85 % (assuming a refractive index of 1.5) of its intensity are reflected at the glass plate. For the *slave* laser, which had an output power of ∼ 1.7 W this amounted to about 15 mW.

The part of the beam that is reflected at *BS2* [8] (see fig. 6.11) is passed through a linearly graded neutral-density filter. Then it is coupled into a multi-mode fiber, which leads to the

---

[8]The beam splitter was designed for a 50 : 50 splitting ratio at a wavelength different from ours. As a result the transmission was noticeably stronger than the reflection.
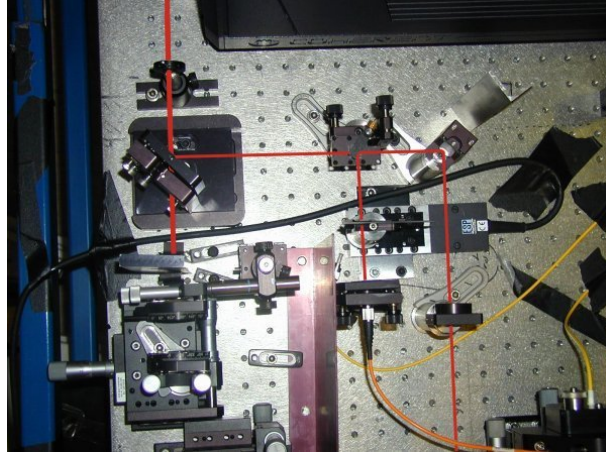
Figure 6.12.: Picture of the part of the setup on the *slave* side, which corresponds to fig. 6.11. The beam path is indicated by a red line. In this picture the beam path was blocked before entering the SHG setup. The translation stage for the linearly-graded neutral-density filter is clearly visible.

photo-diode in the Synchrolock control box. On the *slave* side the neutral-density filter was mounted on a translation stage. By moving the translation stage we could control the intensity of the light coupled into the multi-mode fiber, i.e. the intensity of the VCO's signal.

Changing the intensity of the coupled light does not negatively influence the relative-timing jitter as long as the intensity does not become too low (lower than $\approx 2.5\,\mathrm{V}$ on the *slave* photo diode). But a change in the coupled intensity leads to an additional phase shift between the *slave* diode's electronic signal and the *master* signal. We will explain the origin of this phase shift in the following subsection.

6.4.2. Shifting the electronic phase via the beam intensity

Let us reexamine the equations we employed in the simple example, which we presented in section 5.1.1 in order to elucidate the principle of operation of a PLL. While we keep the definition of the signal $V_i(t)$ of the master oscillator, we will introduce a slight modification to the signal of the VCO (see equ. 5.2 on page 94):

$$V_o(t) = V_{o0} cos \left(\omega_o(v_d) t + \Theta_e \right). \tag{6.3}$$

Actually, we only applied what a VCO is defined to be: its frequency depends on the control voltage, v_d. Let us assume the VCO to operate at frequency $\overline{\omega}_o$ for $v_d = 0$ and suppose that ω_o is a linear function of v_d, i.e.:

$$\omega_o(v_d) = \overline{\omega}_o + \Lambda v_d, \tag{6.4}$$

where Λ is some constant. To assume a linear response is justifiable for many analogue VCOs, as they are constructed for linear response. There are also VCOs with an exponential frequency response, but in our case, linear response is more interesting because our *slave* laser is a VCO with an approximately linear frequency response (apart from hysteresis and creep of the piezo actuators). The voltage applied to any of the piezo actuators in the *slave* laser's cavity changes the cavity length, which is linearly related to the laser's frequency (see subsection 4.1.1).

The feed-back voltage of the PLL will be:

$$v_d(t) = A K_2 V_{i0} V_{o0} \cos\left(\left(\omega_i - \omega_o(v_d(t))\right) t + \Theta_e\right). \tag{6.5}$$

As soon as the frequencies are locked, the time-dependence of this equation must vanish, i.e.:

$$\omega_i - \omega_o(v_d(t)) = 0, \tag{6.6}$$

or, if we use equation (6.4):

$$v_d(t) = \frac{\omega_i - \overline{\omega}_o}{\Lambda}. \tag{6.7}$$

Combining this result with equation (6.5), we get:

$$\cos\Theta_e = \frac{\omega_i - \overline{\omega}_o}{\Lambda A K_2 V_{i0} V_{o0}}. \tag{6.8}$$

As we can see, the phase shift Θ_e depends on the amplitudes of both oscillators. Although this relation will be different if the phase comparator is not implemented as we did it in our simple example, the phase shift must necessarily be a function of the signal amplitudes.

That Θ_e is symmetric with respect to the two amplitudes was of imminent importance during the last stage of our second experiment. Due to an unknown reason changing the signal amplitude of the VCO output stopped to result in a change in the relative time delay of the lasers from one moment to the next. Because we have been, to the best knowledge of the author, the only ones adjusting the laser delay via changing the signal amplitudes, Coherent could neither give possible reasons for the problem nor suggestions how to solve it.

As is stated above, the phase shift must necessarily depend on the signal amplitudes as long as they are not normalized. Therefore, the Synchrolock's malfunction can be expected to have its origin in the *slave* side photo diode.

We resolved the problem by exchanging the two oscillators, i.e. we connected the *slave* multi-mode fiber to the *master* photo diode and connected the *master* multi-mode fiber to the *slave* photo diode. Because the multiplication of the signals is commutative this exchange did not influence the synchronization process.
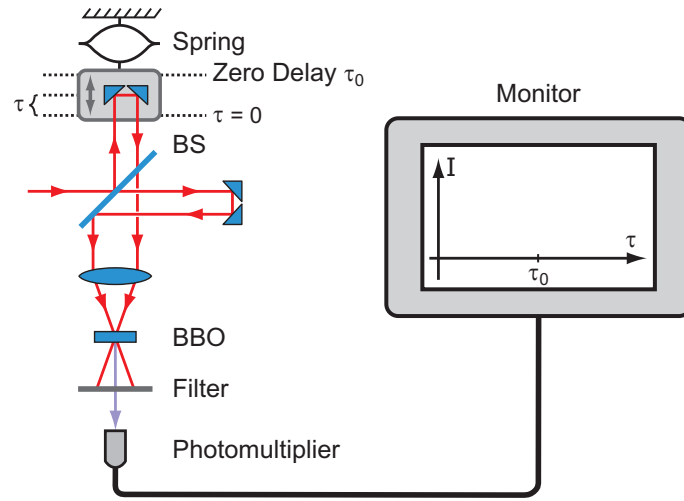
Figure 6.13.: Schematic of the autocorrelator used in our experiments. A beam splitter (BS) splits the input beam. The two parts are reflected at retroreflectors. One of them is attached to a spring. It is moved periodically over an adjustable scan range. The reflected parts are redirected to a lens and focused onto a BBO crystal for SHG. The original beams are filtered out by a low-pass filter and the intensity of the up-converted beam is measured by a photomultiplier. A monitor displays this intensity I over the relative time delay τ between the optical path lengths of the two beam parts.

6.4.3. Determining the time delay between the lasers

Before we are able to explain how we use the neutral-density filters to adjust the time delay between the lasers, we will have to describe how we measure that time delay.

On both sides of the setup those parts of the laser beams, which are transmitted by *BS2* (see figures 6.11 and 6.1) are routed to an autocorrelator (AC) (see fig. 6.13). There they are collinearly overlapped [9]. Because of the long beam paths from the lasers to the AC both beams had to be collimated (independent of each other) to improve the signal-to-noise ratio of their cross-correlation (CC). This was necessary because of the low intensities of the beams. A neutral density filter in the path of the beam originating from the *slave* side assured that the autocorrelations of the two beams had equal amplitudes. A thorough description of the autocorrelator we used and its application to determine the cross-correlation of pulses can be found in B. Blauensteiner's diploma thesis [17].

The *slave* beam was passed along a delay path (see fig. 6.14 and 6.15). This was necessary because there were two delays we had to compensate for:

- the delay between the independent single photons, which we want to interfere (HOM-

---

[9]To assure that they are collinear, we position a flip mirror in front of the autocorrelator. This mirror could be used to adjust both beams to pass collinearly through two pin holes, which were separated by more than two meters.
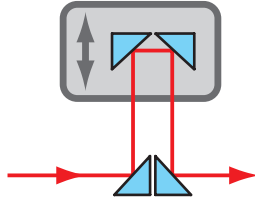
Figure 6.14.: Variable optical delay in the path of the *slave* beam to the autocorrelator. We used four prisms, which were coated for high reflectivity. Two of them were placed on a motorized translation stage, which we denote as $MT2$.
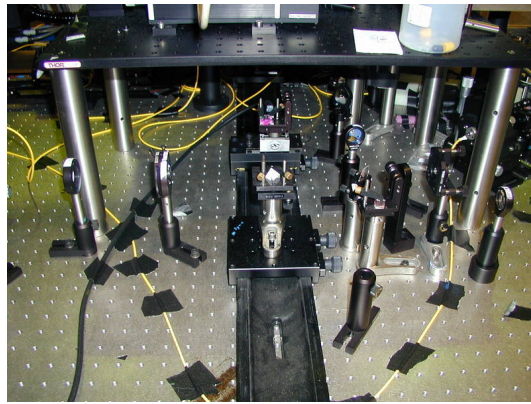

Figure 6.15.: Picture of the delay path (see fig. 6.14). The translation stage $MT2$ with two of the prisms was mounted on a sledge on a rail to allow for coarse manual translation.

    type interference, see 2.3)

- the delay between the pulses of the two lasers as they arrive at the autocorrelator

The autocorrelator could be controlled and its data could be read out via *GPIB* using a *LabView* program, which was written by B. Blauensteiner. We introduced some modifications later on (see appendix E).

6.4.4. Adjusting the relative time delay

Now, that we have explained the origin of the phase shift, we will discuss how we utilized this effect in our experiment. The intensity of the coupled light on the *slave* side can be adjusted by moving the motorized translation stage $MT1$, on which the linearly graded neutral-density filter is placed. The relation between the relative time delay of the lasers and the position of the neutral-density filter was linear to a good degree over a certain range. It was measured by B. Blauensteiner during her Diploma thesis (see Figure 3.3 on page 50
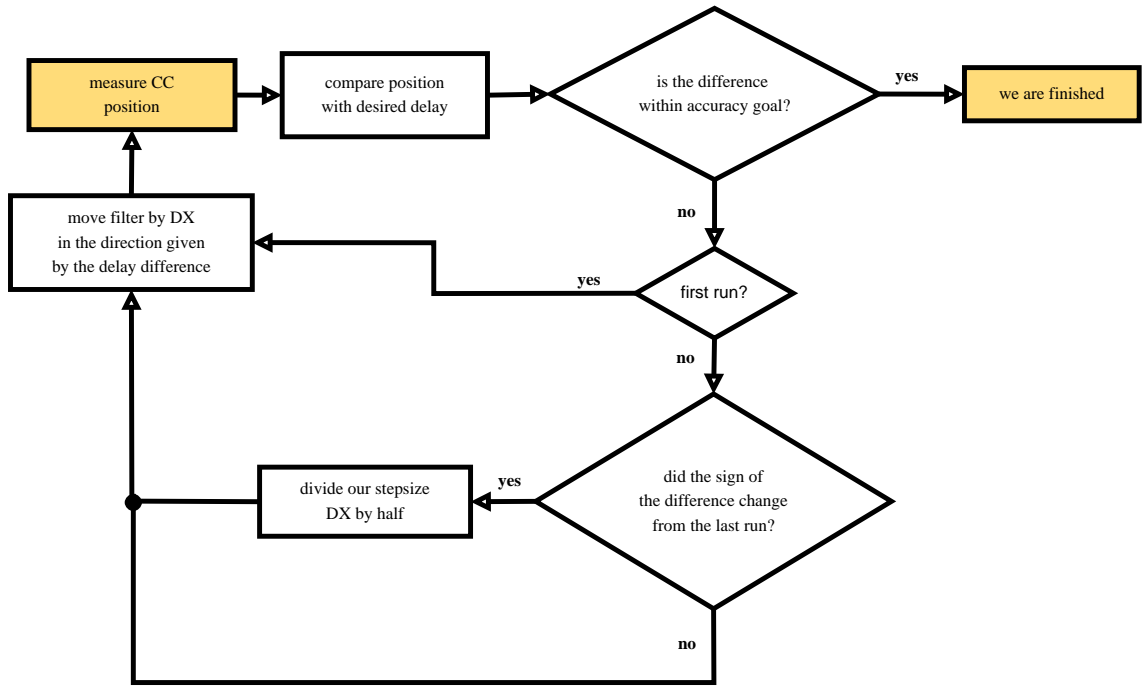
Figure 6.16.: Flow chart of the algorithm to adjust the relative time delay between the two lasers.

in [17]). The relation ceases to be linear as soon as the diode voltage falls beneath 5 V. In the range between 2.5 V and 5 V the rate, with which the delay changes, increases rapidly with decreasing voltage.

Due to the fact that the phase shift depends on the amplitudes of both oscillators and because the lasers and beam paths were often adjusted between series of scans, we would have had to record a calibration curve to relate the phase shift with changes in the oscillator's amplitude after each tuning of the lasers and after each change to the beam paths. In addition, the position of the neutral-density filter relative to the translation stage had to be adjusted before each series of scans. This was necessary in order to assure that we could change the relative time delay by translating the filter over as large a range as possible. It was the only automatable way of adjusting the time delay. The shorter its range the more often human intervention to adjust the delay would have been necessary. Due to all of these reasons it would not have made much sense to calibrate the relation between time delay and the position of $MT1$.

Rather, we used a simple algorithm, which controlled the position of $MT1$ and checked the delay of the lasers by observing the position of the CC of the laser beams (from now on shortly denoted as *CC position*). Its workflow is illustrated by the following list and in fig. 6.16:

1. measure current CC position

2. compare it with the desired CC position

3. if they coincide up to a given accuracy, leave the loop - we are finished

4. if this is not the first run, check if the sign of the difference between the current and the desired position has changed relative to the measurement in the last run

5. if the sign has changed, reduce our motor step size Δ by a factor of 2

6. move $MT1$ over a distance Δ to shift the delay in the correct direction (depending if the difference between the current and the desired delay is positive or negative)

7. continue again with step (1)

By using this algorithm it was possible to adjust the relative time delay of the lasers with an accuracy of at best 50 fs.

6.4.5. Measuring the relative-timing jitter

The CC signal is the convolution of the pulse envelopes. If we assume these envelopes to be Gaussian with equal peak amplitudes A, with r.m.s. widths σ_{p1} and σ_{p2} and a relative time delay T, the CC will be:

$$F_{cc}(t) = A^2 \int d\tau \, \exp\left[-\frac{(\tau - t_0)^2}{2\sigma_{p1}^2}\right] \exp\left[-\frac{(t + \tau - t_0 - T)^2}{2\sigma_{p2}^2}\right], \qquad (6.9)$$

where t_0 is some time offset. The evaluation of the integral yields:

$$F_{cc} = \frac{\sqrt{2\pi}A^2\sigma_{p1}\sigma_{p2}}{\sqrt{\sigma_{p1}^2 + \sigma_{p2}^2}} \exp\left[\frac{(t - T)^2}{2(\sigma_{p1}^2 + \sigma_{p2}^2)}\right]. \qquad (6.10)$$

If the relative-time delay of the lasers varies, and if the jitter varies randomly according to a Gaussian jitter distribution of width σ_J, the CC will become:

$$F_{cc} = \frac{2\pi A^2\sigma_{p1}\sigma_{p2}}{\sqrt{\sigma_{p1}^2 + \sigma_{p2}^2 + \sigma_J^2}} \exp\left[\frac{(t - T)^2}{2(\sigma_{p1}^2 + \sigma_{p2}^2 + \sigma_J^2)}\right]. \qquad (6.11)$$

This tells us that the width of the CC signal can be used to determine the r.m.s. relative-timing jitter σ_J if we know the pulse widths of the lasers. That is, if σ_{cc} denotes the width of the Gaussian CC signal, we will have:

$$\sigma_J = \sqrt{\sigma_{cc}^2 - \sigma_{p1}^2 - \sigma_{p2}^2}. \qquad (6.12)$$

Another method, which Coherent suggests to use in order to determine the performance of the Synchrolock, does not require knowledge of the pulse widths of the lasers. It states that the relative-timing jitter of two lasers can be estimated by the following relation:

$$\sigma_J = \frac{\Delta_{cc} \Delta V_{rms}}{V_0}. \tag{6.13}$$

Here, we introduced $\Delta_{cc} = \sqrt{8 \log 2} \sigma_{cc}$, i.e. the FWHM of the CC signal, and V_0, i.e. the maximum amplitude of the (averaged) CC signal. The quantity ΔV_{rms} denotes the fluctuation of the CC signal at the position $\Delta_{cc}/2$ relative to the CC signal's maximum (that corresponds to the position of the CC-signal's maximum slope).

Although this method is only an approximation, it is usually in good agreement with the results from the method described above. Let us give a simple derivation of this approximate expression. Assume that we adjust the delay between the pulses to $\Delta_{cc}/2$. We can approximate the derivative of the CC signal at this position with [10]:

$$\frac{V_0/2}{\Delta_{cc}/2} = \frac{V_0}{\Delta_{cc}}. \tag{6.14}$$

Let us denote the variation of the signal at position $\Delta_{cc}/2$ as ΔV_{rms}. This variation is due to the relative-timing jitter of the lasers and if we employ the simple approximation for the derivative above, we will be able to write it as:

$$\Delta V_{rms} = \frac{V_0}{\Delta_{cc}} \sigma_J. \tag{6.15}$$

This is equivalent to equation 6.13.

In the experiment we measured Δ_{cc} using the autocorrelator. The output of the autocorrelator could be connected via coaxial cables to an oscilloscope, where the height V_0 of the CC signal was measured. Then the relative time delay of the lasers was adjusted such that the voltage dropped to $V_0/2$. The fluctuations ΔV_{rms} of the voltage at this point were measured with a true-rms digital multimeter.

This method yielded a value of $260 \pm 30\,\text{fs}$ for the relative-timing jitter in the first experiment. For the second experiment we calculate the jitter with the first method. To this end we analyze the widths of the CC signals, which we recorded during the measurement of the data for the violation of the CHSH inequality in the second experiment. The average of the measured widths is $\Delta_{cc} = 600 \pm 40\,\text{fs}$. The r.m.s. pulse widths of the *master* and the *slave* laser were $67 \pm 3\,\text{fs}$ and $65 \pm 3\,\text{fs}$, respectively (see subsection 6.1.1). In combination with equation 6.12 this data yields a relative-timing jitter of $240 \pm 20\,\text{fs}$. For comparison, application of the approximate formula 6.13 leads to an estimation of $\sim 250\,\text{fs}$.

---

[10]This approximation would be exact if the CC signal were a triangular function.

6.5. Detection and measurement

We used silicon avalanche detectors for single-photon detection. Part of them were designed and built by Th. Jennewein [63] and G. Weihs [129], the rest were commercially available detectors from Perkin Elmer. The detection efficiency of the detectors was roughly 40 %.

6.5.1. Polarization compensation for Hong-Ou-Mandel interference

A schematic for our first experiment, the demonstration of high-visibility HOM-type interference with independent photons (see section 2.3.), was given earlier in figure 2.9. For the experiment we did not used a fiber beam splitter instead of the cube beam splitter that is indicated in the schematic. Both SPDC sources are used not to produce entangled pairs but to generate single photons (in the input modes of the beam splitter) heralded by trigger events (in modes 1 and 4 of the schematic). That means that all data points for the measurement of the HOM dip represent four-fold coincidence detection events (in modes 1 to 4 of the schematic).

In order to achieve high-visibility HOM-type interference these single photons have to be indistinguishable to a high degree (see section 2.3). Optimal mode overlap (and low coupling losses) are guaranteed by the fiber beam splitter. The narrow bandwidth filters in the input modes of the beam splitter assure that the coherence times of the photons are longer than the duration of the pump pulses (plus the relative-timing jitter). In the first experiment their bandwidth was 1 nm FWHM for the photons in the input modes of the beam splitter and 3 nm FWHM for the modes 1 and 4 (the trigger photons). To reduce background we placed polarization filters in all of the four spatial modes (see fig. 2.9). They were oriented for vertical polarization in the trigger modes (1 and 4) and for horizontal polarization in the input modes of the beam splitter.

In order to guarantee indistinguishability of the interfering photons with respect to their polarization we had to compensate for rotations of the polarization in the single-mode fibers and in the fiber beam splitter. We achieved that compensation via two polarization controllers. Both of them are needed because with our method the compensation is done independently for each input arm of the fiber beam splitter. We will describe it in the following.

Our procedure for polarization control is illustrated in figure 6.17. We coupled light from the *slave* laser into a single-mode fiber and connected it to one of the output ports of the fiber beam splitter. The light passed the fiber beam splitter and exited via the single-mode fiber couplers (one at the *master* side, one at the *slave* side). There it had to pass through polarizers. These polarizers were oriented the same (horizontal) at both couplers. From there the light was redirected onto photo-multipliers, where we measured the light's intensity in dependence of the alignment of the polarization controllers. Compensation of the rotation of the polarization in the fibers was reached as soon as the intensity measured by the photo-multipliers was at its minimum for both couplers. This ensured that horizontally (or vertically) polarized photons entering via the single-mode fiber couplers would reach the fiber beam splitter in a state of polarization, which was unknown but necessarily the same
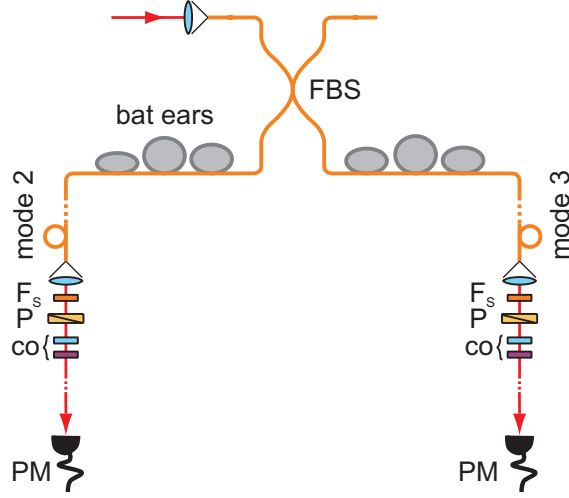
Figure 6.17.: Compensation of polarization rotation in the fibers for the first experiment. An alignment beam (part of the *slave* laser beam) is sent backwards into one of the fiber-beam-splitter (FBS) outputs. The bat ears are adjusted to get minimum intensity in both of the photo multipliers (PM) at the same setting of the polarizers (P) within the HV basis. We used dotted lines to indicate where we did not draw the full path (compare to fig. 6.1). The light, which passed back through the FBS was redirected to the PMs via mirrors, which were temporarily put into the beam paths.

for both input ports. The contrast in the HV basis in both input arms was about 96 %

6.5.2. More-complete Bell-state measurement (BSM)

If there are no polarizers in front of the single-mode fiber couplers in modes 2 and 3, a coincidence detection in modes a and b (see fig. 6.18) will be equivalent to a projection of the two-photon state of the photons in modes 2 and 3 on ψ^-. This is the most simple realization of a BSM. Only ψ^- can lead to a coincidence detection (see subsection 2.3.5).

In principle it is sufficient to use only this very simple BSM in order to demonstrate entanglement swapping. A four-fold coincidence between the detectors in the modes 1, a, b and 4 indicates that the photons measured in modes 1 and 4 must originally, i.e. before they were detected, have been projected onto a ψ^- state by the Bell-state measurement (see subsection 1.6.2).

In addition to detecting ψ^- states a more-complete BSM [86] allows to discern ψ^+ from $\phi^\pm$ states. The principle layout of a more-complete Bell-state measurement is simple (see fig. 6.19). If the two photons leave via the same output port of the BS, they will not be in the ψ^- state. They are led into a PBS, and if they are in the ψ^+ state, they will have orthogonal
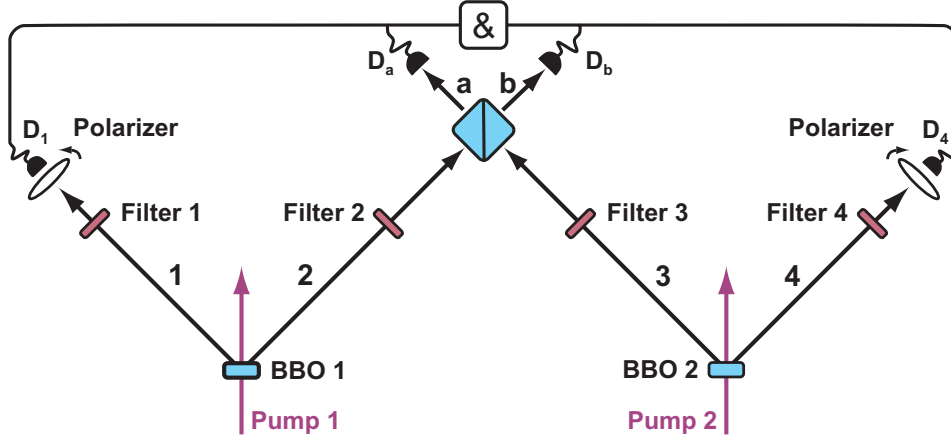
Figure 6.18.: Schematic of an experiment for entanglement swapping with a simple BSM, which can only discriminate ψ^-. The photons in modes 2 and 3 are overlapped at a beam splitter. Successful entanglement swapping is indicated by a four-fold coincidence between the detectors D_1 and D_4 in the trigger modes and detectors D_a and D_b behind the BS.

polarizations with respect to each other and will leave via opposite output ports of the PBS. The table accompanying figure 6.19 illustrates, which coincidence events correspond to a projection on ψ^- or ψ^+.

In a simple BSM ψ^+ and $\phi^\pm$ events cannot be distinguished and are discarded. Because it allows to distinguish ψ^+ events a more-complete BSM allows to salvage twice as many measurement results as a simple BSM. The outcome of the BSM determines the two-photon state ψ_{14} of the swapped entangled pair in modes 1 and 4 (see equ. 1.65). ψ_{14} will be the same as the outcome of the BSM, i.e. $\psi_{14} = \psi^-$ if the outcome is ψ^-, and $\psi_{14} = \psi^+$ if the outcome is ψ^+.

As we have discussed in subsection 1.5.4 we have to choose the CHSH inequality, which we want to maximally violate, depending on the state of the entangled pair. For a ψ^- state the optimal inequality is (see equ. 1.50)

$$S_{\psi^-} \equiv |E(\mathfrak{a}_1, \mathfrak{b}_1) - E(\mathfrak{a}_1, \mathfrak{b}_2) + E(\mathfrak{a}_2, \mathfrak{b}_1) + E(\mathfrak{a}_2, \mathfrak{b}_2)| \leq 2, \qquad (6.16)$$

where $E(\mathfrak{a}, \mathfrak{b})$ is the expectation value of the product of outcomes ± 1 of polarization measurements $\mathfrak{a}$ and $\mathfrak{b}$ on the two photons of each entangled pair (see subsections 1.5.3 and 1.5.4).

For ψ^+ the optimal CHSH inequality is

$$S_{\psi^+} \equiv \left| -E_{(}\mathfrak{a}_1, \mathfrak{b}_1) + E_{(}\mathfrak{a}_1, \mathfrak{b}_2) + E_{(}\mathfrak{a}_2, \mathfrak{b}_1) + E_{(}\mathfrak{a}_2, \mathfrak{b}_2) \right| \leq 2. \qquad (6.17)$$

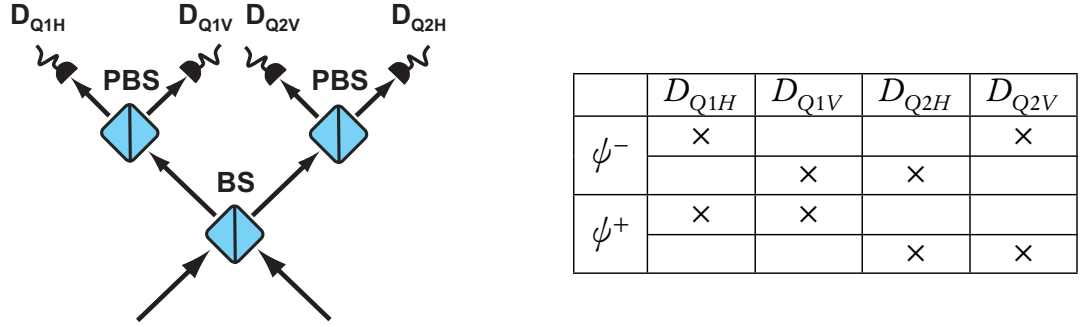|	D_{Q1H}	D_{Q1V}	D_{Q2H}	D_{Q2V}
ψ^-	×			×
		×	×	
ψ^+	×	×		
			×	×

Figure 6.19.: Schematic of a more-complete Bell-state measurement. This measurement is a simple extension of the scheme, which we discussed earlier (see subsection 2.3.5). A polarizing beam splitter (PBS) is added in every output port of the BS. The table on the right-hand side shows, which combinations of detection events (symbols ×) in a more-complete BSM indicate a projection on either ψ^- or ψ^+.

6.5.3. Polarization compensation for entanglement swapping

The implementation of a more-complete BSM for entanglement swapping posed more stringent demands on the polarization compensation. To fulfill these demands we used a novel method to completely compensate for any polarization rotation in all the arms of the fiber beam splitter (and the single-mode fibers connected to them).

We could not use the simple polarization compensation scheme, which we used in the case of the demonstration of HOM-type interference. For entanglement swapping it is important to assure that the two-fold coincidences between the PBS outputs really correspond to projections of the original state of the photons emitted into modes 2 and 3 on ψ^+ or ψ^-. Any phase-shift or polarization rotation between the two photons would result in the BSA projecting on a superposition of various Bell states [11].

Our new method for polarization compensation utilizes the fact that each of our polarization compensators can be adjusted to perform an arbitrary unitary transformation. The novelty of our scheme is how we adjusted the bat ears to achieve the unitary transformation desired: two of the bat ears were adjusted such that the unitary transformation corresponding to tilting of the third bat ear became approximately factorable with respect to the tilting angles of the other two bat ears.

Each of the bat ears contained one loop of the fiber and by tilting them around their common axis it was in principle possible to implement any unitary transformation of the polarization passing though the fiber. Due to the nature of the process, which is based

---

[11]We could also have swapped this superposition of Bell states. First we would have had to determine the exact states we project on. Then we would either have had to transform the swapped state back to $\psi^\pm$ or we would have had to use a variation of the CHSH inequalities adapted to our states.

on bending the fiber, the intended unitary transformation was achieved by a step-by-step adjustment of the tilting angles of the three ears. To fully compensate the polarization rotation in a fiber it is necessary to match two (non-identical) polarization bases. Here is a detailed step by step description of our method [12]:

1. prepare the input state to be horizontal

2. prepare the PBS at the output port to project in the HV basis

3. choose two ears and tilt them to match horizontal input to horizontal output

4. prepare the input state to be +45° (short: +)

5. prepare the PBS at the output port to project in the +/− basis

6. use the third ear to match + input to + output as good as possible

7. start again with step (1)

In most cases we chose the two ears for matching the HV basis to be the outer two and the ear in the middle was used to match the +/− basis. By repeating this method over and over again, the matching in the HV basis should gradually become independent of the tilting angle of the middle ear [13]. If that did not happen, and if the contrast in the HV basis always diminished when we tried to match the +/− basis, we would try the same method with a different combination of two out of three bat ears for the HV basis.

To achieve full compensation of the polarization rotations in the various arms of the fiber beam splitter we needed at least three polarization controllers, one in each input mode of the beam splitter and one in any of the two output modes. Let us assume that a polarization compensator is placed in the beam-splitter output mode leading to the PBS (Q2) in front of D_{QH2} and D_{QV2}. Then the two compensators in the input modes of the beam splitter were used to map the polarization of photons entering the single-mode fiber couplers onto the corresponding measurement bases of Q1 (the PBS in front of D_{QH1} and D_{QV1}). Afterwards the compensator in the output mode leading to Q2 would be adjusted.

Instead of these three necessary compensators we used four, i.e. one in each arm of the fiber beam splitter (see fig. 6.20). The additional compensator could be adjusted if necessary to help when adjusting one of the compensators in the input modes of the beam splitter.

By mapping the input polarizations to the basis of Q1 we assure two things. For one, we make sure that the polarization measured by Q1 will correspond to the original polarization of the input photons. Second, we ensure that two input photons, which are in state ψ^-, will also be in state ψ^- at the fiber beam splitter. By mapping the input states with basis of Q2,

---

[12]That this method should in general converge was intuitively clear to me but I did not find a mathematical proof for the convergence. The excellent contrasts (see table 6.7), which I achieved, should be proof enough.

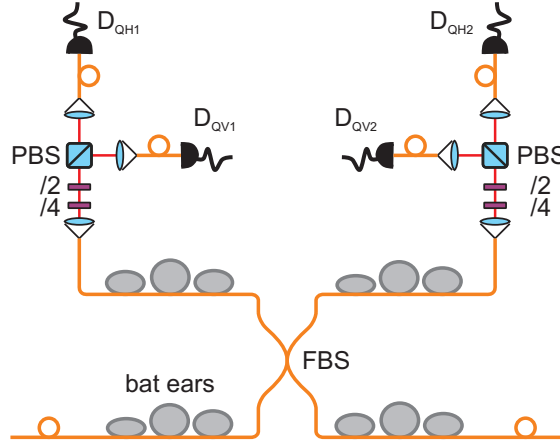[13]At least for tilt angles on the order of $\pm 10 - 20°$

Figure 6.20.: Compensation of polarization rotation for the more-complete Bell-state measurement. The basis, into which each polarizing beam splitter (PBS) projected, could be adjusted via a combination of a $\lambda/4$ and a $\lambda/2$ plate. To allow for compensation of polarization rotation in every basis (not only in the HV basis), we added two more "bat ear" assemblies. Compensation was achieved by sending triggered single photons of a well defined polarization into the FBS. The bat ears were adjusted to optimize (in two non-orthogonal bases) the ratio between the coincidences between the trigger and D_{QH1} and the coincidences between the trigger and D_{QV1}. The same was done for the second PBS. Finally, the bat ears in the second input of the FBS were adjusted to optimize the ratio of the *sums* of the coincidences in the horizontal and the vertical outputs of the two PBS.

we guarantee that a measurement result in $Q1$ will be equivalent to a measurement result in $Q2$. When the compensation has succeeded our more-complete BSM will work as indicated in figure 6.19.

We performed our procedure for polarization compensation using coincidence detection. We used our SPDC sources as triggered single-photon sources. For instance, to adjust the polarization controller in the *slave* input arm of the fiber beam splitter, we placed polarization filters in modes 1 and 2 (see fig. 6.18). These were oriented orthogonal to each other. That means, to match the HV basis, we rotated the polarizer in mode 2 to be horizontal and the polarizer in mode 1 to be vertical [14]. The polarization controller was used to minimize the coincidences between the detector in mode 1 and $Q1V$.

There are several advantages to using coincidence detection. We directly use the photons, which we will finally work with, instead of an alignment beam. There is nearly no background when coincidences are measured because of the narrow coincidence window

---

[14] Because the polarizations of the photons of an SPDC pair are always orthogonal to each other, this would not strictly be necessary, but it helps to reduce the background.

Basis	*slave* - Q1	*master* - Q1	*slave* - Q2	*master* - Q2
HV	820:1	510:1	360:1	512:1
+/−	1000:1	360:1	280:1	591:1

Table 6.7.: Contrast of polarization compensation for the various input and output arms. The two input arms are denoted by *slave* and *master* corresponding to which source they are connected to. Q1 and Q2 denote the two PBSs in the output arms of the fiber beam splitter. All contrasts are gained via coincidence measurements.

(3.12 ns). Due to the lack of background the achievable contrast is limited only by the quality of the polarization controllers and the PBSs. The contrasts of our polarization compensation before the final measurements for entanglement swapping are given in table 6.7.

7. The experiments and their results

This chapter contains the results of our two experiments. Section 7.1 will describe our attempt to achieve high-visibility HOM interference with photons originating from independent sources. In contrast to earlier experiments (see chapter 3) the independence of our photon sources is unconditional. Both of the sources can be operated independent of each other. Their relative timing is synchronized not via optical but via electronic means. They share no stable optical phase relation nor any optical correlation or interaction. Our experiment is the first to satisfy the prerequisites to experimentally test a prediction of quantum theory, about which Dicke said [39] (he refers to an equivalent experimental situation where the radiation originates from atoms, see chapter 2):

> *One might naively wonder with such a radiating system, initially in a state for which both atoms are excited, how the one atom would ever know about the existence of the other.*

Mandel said that "this prediction has no classical analogue, and its confirmation would represent an interesting test of the quantum theory of the electromagnetic field" [82].

In our second experiment we demonstrated entanglement swapping, and we used the swapped entanglement to violate CHSH inequalities. The results will be described in section 7.2. Our experiment realizes a central prerequisite for quantum repeaters: the swapping of entanglement with pairs originating from spatially separated, independent nodes. Compared to our first experiment we significantly improved the stability of the setup, we implemented a more-complete BSM (see subsection 6.5.2), and we used even narrower bandwidth filters.

7.1. Interference of independent photons

To confirm the prediction of quantum theory of high-visibility two-photon interference with independent photons we need to overcome the classical limit of 50 % interference visibility (see chapter 2). To surpass it is a direct contradiction to classical electromagnetism and a confirmation of the quantum theory of light. This was our main goal during the first experiment.

An additional aim of our experiment was to see whether we could also overcome the visibility threshold of $\frac{1}{\sqrt{2}}$ (see chapter 1). To do so clearly demonstrates the feasibility of utilizing HOM-type interference to achieve strong entanglement between independent photons, a prerequisite for our second experiment (see section 7.2).

7.1.1. Minimizing the delay between independent single photons

The indistinguishability of the photon detection times is one of the prerequisites for high-visibility HOM-type interference. Because of the independence of the lasers in our experiment, the time difference between those detection events can vary up to $\sim 6.5\,$ns, i.e. half the period between successive laser pulses. Synchronizing the lasers stabilizes this delay to some constant value. An important task in our experiment was to measure the difference between the detection times and to minimize it.

The best method to find the correct delay is to look for the HOM dip. To determine optical path delays with sub-picosecond time resolution was the application, which HOM-type interference was originally introduced for (see [60] and section 3.3.1). In these long-range scans we did not use polarizers in the photon modes because it was more useful to have high count rates and short scan times than to have high-visibility interference. Given the bandwidths of our filters (3 nm and 1 nm FWHM), and the relative-timing jitter of $380 \pm 30\,$fs (see section 5.3) we expect a dip visibility of $45 \pm 1\,\%$ for unpolarized photons (see section 2.3.2). The r.m.s. width of the HOM dip should be $870 \pm 70\,$fs.

To prevent missing the dip in our scans, the step size of our scans had to be smaller than the dip width. We chose a step size of 300 fs. It is not necessary to scan over the full $\sim 6.5\,$ns range, which could in principle separate our laser pulses. By investigating the times of occurrence of detection events for photons from the two sources (see below) it is possible to determine the correct delay to an accuracy of about $\pm 40\,$ps. Only this smaller range must be scanned for the HOM dip.

Electronic means to determine the relative time delay of single photons

The (triggered) single photons from the two sources arrive at the fiber beam splitter through different input ports (see figures 2.9 and 6.1). Let us denote the difference between their arrival times at any of the two detectors after the beam splitter as $\Delta \tau$. This delay comprises the relative time delay $\Delta \tau_p$ between the laser pulses, which generated the photons, and a time delay $\Delta \tau_g$, which depends on the geometry of our setup. In our setup it was easy to adjust $\Delta \tau_p$. We did not implement a possibility to adjust $\Delta \tau_g$.

Our aim was to adjust $\Delta \tau_p$ in order to minimize the difference between the detection times of the photons, i.e. to achieve $\Delta \tau = 0$. We used an SR620, i.e. a device from Stanford Research to measure and to analyze counts and time intervals, for that purpose. In our case we used this device to analyze the time intervals between detection events and a stable reference signal. The SR620 was fed two input signals. TTL pulses in one input channel triggered "start" events, TTL pulses in the second input channel triggered "stop" events. The time intervals between succeeding start and stop events were recorded. A predefined number of such time intervals (i.e. pairs of start and stop events) were measured. A histogram of the distribution of time intervals could be investigated in order to determine the average time delay between start and stop events.

We employed a fast photo diode, which monitored the output of the *master* laser, to

provide a stable periodic start signal. The stop signals were single-photon detection events. They were generated by one of the detectors after the fiber beam splitter. It was arbitrary, which one of the two detectors was chosen, because the relative time delay between the photons was the same in both output arms of the beam splitter. We will call the average time delays, which we measure with the SR620, i.e. the positions of the peaks in the histogram, t_s and t_m. Here, we used sub indices to indicate whether the photons under investigation originated from the *slave* or the *master* source, respectively. Their difference is $\Delta\tau = t_s - t_m$.

The two sources were adjusted to produce the same number of counts per second in the detector used (see the note on measuring time delays below). When we determined t_s we were only interested in detecting photons from the *slave* source. Photons from the *master* source were blocked before they could enter the single-mode fiber couplers. We did not simply block the pump beam because reflexes from the beam block sometimes had a negative influence on the performance of the Synchrolock. In an equivalent way to determine t_m the photons from the *slave* source were blocked.

> **Note on measuring time delays between single-photon detection events**
>
> The average time delay between detection events and a stable reference signal depends on the detector count rate. If they are varied, the delay will change by up to several nanoseconds. This behaviour has also been observed by several of my colleagues. Up to now we did not find a satisfactory explanation. In order to determine the time delay between single photons as we did it it is paramount to match the count rates as exactly as possible. Otherwise the results will rather reflect the properties of the detector than the time delays, which one is interested in.

Adjusting $\Delta\tau_p$ is an iterative process:

1. measure t_s and t_m

2. if the difference is small enough, we are finished. If not, continue.

3. measure the position of the cross-correlation signal (the "CC position", which we are going to denote as T_{cc}. See subsection 6.4.3).

4. change the relative time delay of the lasers via the Synchrolock software or by adjusting the intensity of the VCO signal. At the same time monitor the CC position.

5. adjust the delay path for the *slave* beam, which is sent to the AC such that the CC signal is once more at the reference position T_{cc}.

6. start over again with step 1.

To keep the CC signal at T_{cc} while minimizing $\Delta\tau_p$ is necessary in order to adjust the delay path. Before the delay path is adjusted we can write the time delay between the pulses at the AC as $\Delta\tau_{AC} = \Delta\tau'_g + \Delta\tau_p + T_{cc}$. We used the same notation as in the delay between the detection times. Our aim is to adjust the delay path such that $\Delta\tau'_g$ differs from $\Delta\tau_g$ only by a small time offset. If this time offset is chosen correctly, it will be possible to monitor the CC signal once $\Delta\tau_p$ has been correctly adjusted in order to observe HOM-type interference.

During the measurements of t_s and t_m and the adjustments of $\Delta\tau_p$ the lasers were synchronized in the fundamental loop (see subsection 5.1.2). Its accuracy ($\sim 3\,\text{ps}$) was high enough for our purpose, and only in the fundamental loop the time delay of the lasers can be adjusted over a large range ($\sim 15\,\text{ns}$) using the Synchrolock software [1]. In the 9th-harmonic loop the time delay could only be adjusted manually over short ranges on the Synchrolock control box or by changing the intensity of the VCO's signal (see subsection 6.4.2).

The accuracy of the delay, which we determined from the histograms measured with the SR620, was about $\pm 20\,\text{ps}$. This corresponds to the time resolution of the SR620. In addition the centers of the peaks in the histograms also varied by the about same amount because of readout errors. These effects add up to an error of up to $\pm 40\,\text{ps}$. This is the range, which we have to scan over to find the delay where HOM interference occurs.

Scanning for the HOM dip

The scan for the HOM dip was performed in $300\,\text{fs}$ steps with a measurement time of $100\,\text{s}$ per point. Because we had adjusted the optical delay between the beams overlapped in the autocorrelator we were able to monitor the CC signal during our scans. When the delay path is kept constant, i.e. when $\Delta\tau'_g$ is kept constant, any change to $\Delta\tau_p$ is reflected in a change to T_{cc}. That means we could use T_{cc} as a measure for the time delay of the interfering photons in our scans.

Sometimes we had to scan over ranges, which were larger than the scan range of the AC [2]. To keep T_{cc} within the scan range of the AC we had to adjust $\Delta\tau'_g$ by moving the motorized translation stage $MT2$. This was the stage, on which the prisms for retroreflection were mounted (see subsection 6.4.3).

We explained above that T_{cc} is equivalent to the time difference between the photon-detection events up to some constant. This constant is equal to the difference between $\Delta\tau_g$ and $\Delta\tau'_g$ (see above). In all our experiments we used T_{cc} as our time coordinate. For every change in the relative time delay of the pump pulses we recorded T_{cc} and the count

---

[1] With the new Synchrolock system, which was acquired after our experiments had been finished, it is possible to adjust the relative time delay while the Synchrolock is operating in the 9th-harmonic loop .

[2] The largest useful range is $50\,\text{ps}$. On the next larger scan range ($150\,\text{ps}$) the AC signal becomes unstable because the oscillatory motion of the spring in the AC (see fig. 6.13) became anharmonic. This resulted in strong modulations of the zero-intensity line on the AC monitor. Most of the time we used a scan range of $15\,\text{ps}$. The accuracy of position measurements in the $50\,\text{ps}$ scan range was only $\sim 200\,\text{fs}$ because for any scan range the AC records the signal in 256 intervals ($\frac{50}{256}\,\text{ps} \sim 50\,\text{fs}$).
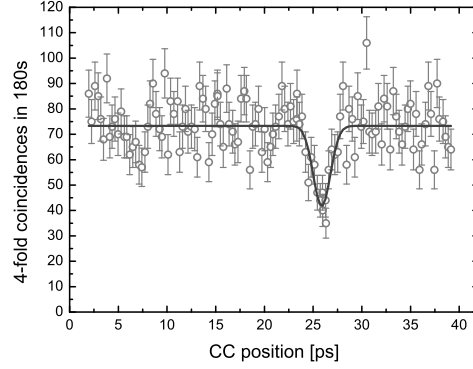
Figure 7.1.: The data of the scan to find the position of the HOM dip. In this scan the HOM dip with independent sources was observed for the first time. The data was taken without polarizers. The solid line is a Gaussian fit to the data (the reduced χ^2 is 1.21). Its visibility is $43 \pm 4\%$.

rates at that specific delay. The value of T_{cc} at the minimum of a HOM dip would then be equivalent to the constant time difference between T_{cc} and the delay between the photon-detection events. Nevertheless, we did not correct the values of T_{cc} in our scans but always plotted the data over T_{cc} itself. This way the data is presented in the way it was measured, and the plots do not depend on the position of a HOM dip, which is subject to measurement errors.

The data of the scan for the dip is given in figure 7.1. Because of the short measurement time per point the count-rates are quite low and the errors are relatively large. Nevertheless, the presence of a dip in the count rates is clear to see. Because we do not use polarizers, we expect a dip visibility of $45 \pm 1\%$. This is in good agreement with the experimental results, which yield a visibility of $43 \pm 4\%$.

7.1.2. Prerequisites for the high-visibility scans

The Gaussian fit to the HOM dip in figure 7.1 provides us with a good estimation of the constant time offset between T_{cc} and the time difference between the photon detection events. All follow-up scans, which were performed with smaller step sizes and longer scan times, centered around that position T_{cc} [3]. Before we continue, we will have to consider several effects, which might reduce the HOM-type interference visibility.

---

[3]The position of the minima of HOM dips in later scans might differ because we of adjustments to $\Delta\tau'_g$ or $\Delta\tau_g$. For example every adjustment on one of the SPDC single-mode fiber couplers results in a change to $\Delta\tau_g$
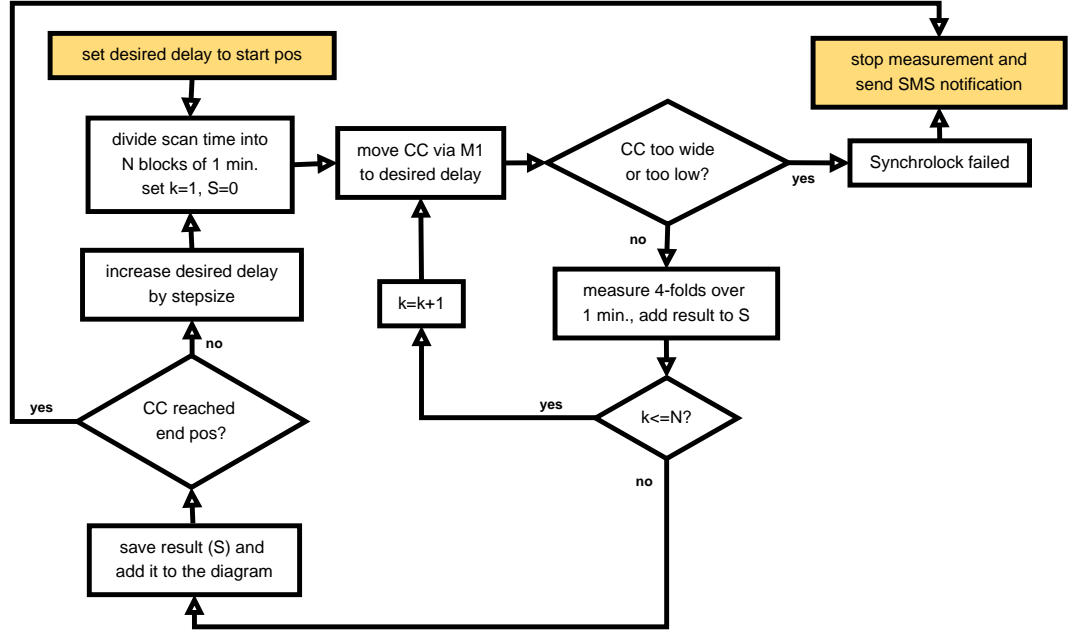
Figure 7.2.: Flow chart of the scanning procedure to measure high-visibility HOM-type interference with independent sources. The filled rectangles represent the start and end of the scan.

Long-time drifts

Coherent's Synchrolock does not compensate for drifts, which occur on time scales longer than $\sim 50\,\mathrm{s}$. Because our measurement times are longer than that, we will have to deal with long time-drifts. Monitoring of the CC position showed that these drifts were always less than $100\,\mathrm{fs}$ over one minute but increased with time. For our high-visibility scans we chose a measurement time of $15\,\mathrm{min}$ per point. Over these periods of time the long-time drifts could have had negative effects on our results.

To minimize any negative influences of the long-time drifts we took advantage of the Poissonian statistics of the four-fold coincidence rates. The probability of a four-fold event is independent of the origin of time [4]. Suppose we want to measure a four-fold rate over some period of time T. Due to the time independence of the four-fold detection probability this is equivalent to measuring the count rate over n intervals of Length t_n as long as $T = \sum_{k=1}^{n} t_n$. The time, which passes between these "partial" measurements, is irrelevant as long as the setup is stable on that time scale, i.e. as long as the count rates did not decrease on that time scale (see below).

We used this fact to divide the scan time of $15\,\mathrm{min}$ in 15 blocks of $1\,\mathrm{min}$ duration. Between these blocks the delay of the lasers was automatically readjusted (see 6.4.4) to compensate for

---

[4]This is true as long as the integration time is long compared to the delay between successive laser pulses.

any drifts, which might have occurred in the mean time. The count rates measured during each of these 15 blocks were finally summed to yield the overall count rate over 15 min. Figure 7.2 shows a flow chart of this procedure.

Normalization, count statistics and measurement errors

During our scans, which often ran over several hours or even days, there always was a deterioration of the alignment of the setup (mounts tilting under their own weight, detuning of laser cavities, etc.). The increasing misalignment resulted in a decrease of the number of detected photon-pairs. This decrease can be compensated for by adequate normalization of the recorded data. Our method of normalization will be described in the following.

Most of our measurement results are four-fold coincidences. Because we had two independent SPDC sources that spontaneously emitted photon pairs the statistics of the two-fold coincidences as well as the statistics of the four-fold coincidences were Poissonian [5]. If a measurement yields N events its error will be $\sqrt{N}$. How accurate this assumption is can be seen by comparing this error with experimental data. While scanning for the dip we collected huge amounts of data over delay ranges, where no interference did occur. We randomly chose one of these data sets [6]. It consists of 337 data points. The average four-fold count rate in this series was 70.0 ± 8.3. The standard deviation is in good agreement with the Poissonian error $\sqrt{70} \approx 8.4$. The same statistics hold true for two-fold coincidences and singles [7].

Apart from the four-folds we also recorded the two-fold coincidences for the photon pairs from *slave* and *master* source [8]. Suppose, the two-fold count rates at time t are given by $N_s(t)$ and $N_m(t)$ for *slave* and *master* source, respectively. T_c is the time between successive pulses, and the probability for a four-fold coincidence is proportional to $P(\Delta\tau)$, where $\Delta\tau$ is the time delay. The number, F, of detected four-fold coincidences at time t will be proportional to these quantities, i.e.:

$$F(t, \Delta\tau) \propto N_s(t) N_m(t) T_c P(\Delta\tau). \tag{7.1}$$

The time dependence (i.e. the decrease in the count rates due to detuning) can be eliminated to obtain what we call the "four-fold count rate normalized on the product of two-fold count

---

[5]This is an approximation because we neglect stimulated emission in the SPDC crystals.

[6]The corresponding measurement series consists of nine (futile) scans for the dip over a range of 95 ps from the 6th to the 8th of April, 2005. The measurement time was 180 s per point and was *not* divided in 1 min blocks. Because at that time we had not yet discovered the dependence of the mean delay of the detector signals on the count rate (see 7.1.1), we were scanning at a position several nanoseconds from the position of the HOM dip.

[7]For two-folds and singles the approximation of Poissonian statistics is not as good as in the case of four-folds. In the case of four-folds there have to be stimulated emissions in both crystals to modify the Poissonian statistics, in the case of two-folds and singles one stimulated emission is enough.

[8]Actually, we recorded the two-folds between the *slave* side trigger and one of the FBS outputs, and we record the two-folds between the *master* side trigger and one of the FBS outputs. We only need the ratio between the recorded two-folds at two different points in time. This ratio is the same as it would be for the overall two-folds, i.e. if we had recorded the sum of the two-folds for both FBS output ports.

rates":

$$\widetilde{F}(\Delta\tau) = \frac{N_s(0)\,N_m(0)}{N_s(t)\,N_m(t)}F(t,\Delta\tau).$$

(7.2)

Its error can be calculated to be:

$$\Delta\widetilde{F}(t,\Delta\tau) = \sqrt{\frac{F\,N_{s0}\,N_{m0}\left(N_s\,N_{s0}\,N_m\,N_{m0} + F\left(N_{s0}\,N_m(N_s+N_{m0}) + N_s\,N_{m0}(N_{s0}+N_m)\right)\right)}{N_s^3\,N_m^3}},$$

(7.3)

where we used the short-hand notations $N_s \equiv N_s(t)$, $N_m \equiv N_m(t)$, $N_{s0} \equiv N_s(0)$, $N_{m0} \equiv N_m(0)$ and $F \equiv F(t,\Delta\tau)$.

7.1.3. High-visibility HOM-type interference of independent photons

In order to illustrate the significance of the indistinguishability of the photons for high-visibility interference, we performed several scans to measure the HOM dip for varying degrees of indistinguishability:

1. high-visibility scan: the photons have parallel polarizations and are as indistinguishable as possible with any limitations mainly due to the relative-timing jitter of the sources.

2. perfect distinguishability: the polarizations of the photons entering the beam splitter were orthogonal to each other

3. partial distinguishability by polarization: a scan without polarizers.

4. HOM-type interference with photons from a source with thermal statistics

Case (1) is the main interest of this experiment. We expect (see 5.3) a HOM-dip with a visibility of $90 \pm 2\%$ and an r.m.s. width of $870 \pm 70\,\text{fs}$. The experimental results are shown in figures 7.3 and 7.4. They are in excellent agreement with the theoretical expectations.

Case (2) represents the direct opposite of case (1). The polarizer in mode 2 is oriented vertically and the polarizer in mode 3 is oriented horizontally. Due to the perpendicularity of the polarizations the photons in mode 2 and 3 are perfectly distinguishable. No interference, i.e. 0% HOM-dip visibility is expected in this case. From the data, which is shown in figures 7.5 and 7.6, it is apparent that there is indeed no interference for perfectly distinguishable photons.

Although the measurement times per point were the same in these scans as they were in the scans with parallel polarizers, there is a slight difference in the count rates even far from the dip. This has its origin in the fact that the coincidence count-rates of our sources are not completely symmetric with respect to the rotation of the polarizers (see 6.3.1).

For the scan in **case (3)** we removed the polarization filters from the setup. This scan is equivalent to the scans that were performed in order to find the position of the HOM dip (see fig. 7.1). Here, we used longer scan times in order to increase the signal-to-noise ratio of the scan.
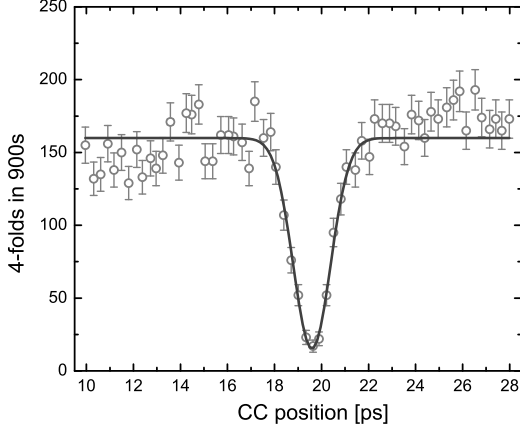
Figure 7.3.: Raw data for high-visibility HOM-type interference with independent photons. The solid line is a Gaussian fit to the data (red. $\chi^2 = 1.55$), it has a visibility of $90 \pm 2\%$ and an r.m.s. width of $790 \pm 30\,\text{fs}$.
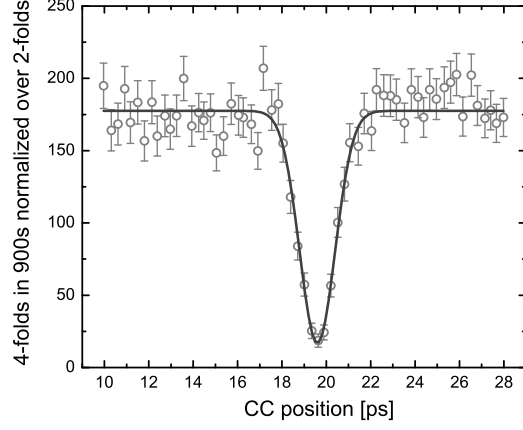
Figure 7.4.: Here, we normalized the data from fig. 7.3 over the product of coincidences of the *master* and *slave* sources. The solid line is a Gaussian fit to the data. Its reduced χ^2 is 0.89, the visibility is $90 \pm 2\%$, and its r.m.s. width is $800 \pm 30\,\text{fs}$.
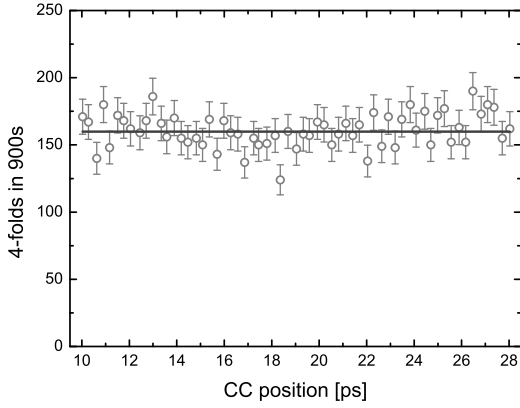

Figure 7.5.: Raw data for HOM-type interference with orthogonally polarized independent photons. The solid line is the fit of a horizontal line to the data (red. $\chi^2 = 1.00$).
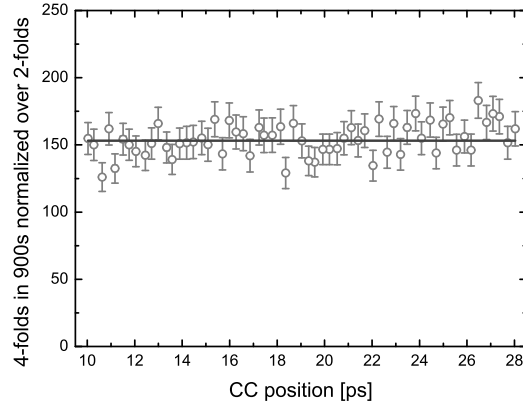
Figure 7.6.: Here, we normalized the data from fig. 7.5 over the product of coincidences of the *master* and *slave* sources. The reduced χ^2 for fit of the horizontal line is 0.98.
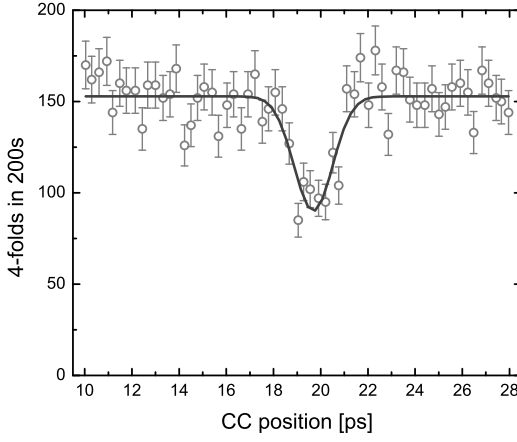
145

Figure 7.7.: Raw data for HOM-type interference with partially distinguishable independent photons. Both photons originate from triggered single-photon sources and are unpolarized. The solid line is a Gaussian fit to the data (red. $\chi^2 = 1.12$).
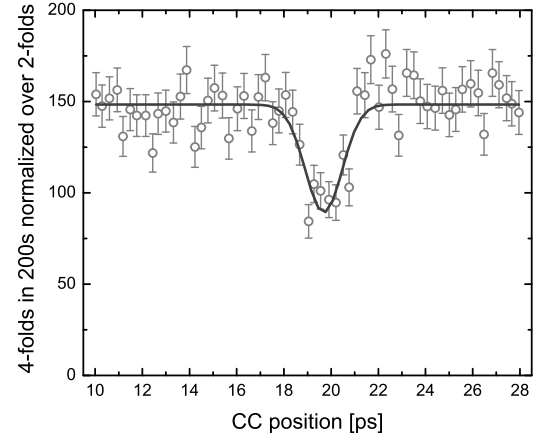
Figure 7.8.: Here, we normalized the data from fig. 7.7 over the product of coincidences of the *master* and *slave* sources. The solid line is a Gaussian fit to the data (red. $\chi^2 = 1.16$).

The results of this scan are given in figures 7.7 and 7.8. From the Gaussian fit to the raw data we calculate a visibility of $41 \pm 4\%$. For the normalized data we get a visibility of $40 \pm 4\%$. Both values are in reasonable agreement with the theoretically expected value of $45 \pm 1\%$.

In **case (4)** we ignore the trigger detection events in modes 1 and 4 (see fig. 2.9), i.e. we observed two-fold instead of four-fold coincidences. The trigger events are necessary in order to assure that exactly one photon enters via each of the input ports of the fiber beam splitter. If we ignore them, the interfering photons will not obey sub-Poissonian but thermal statistics (see subsection 2.3.4). Suppose that the probability for the creation of a photon pair is p for both sources. The probability $P(n_1, n_2)$ for having n_1 photons in one input mode of the fiber beam splitter and n_2 photons in the second input mode will be proportional to:

$$p^{n_1+n_2}. \tag{7.4}$$

It follows that $P(2,0) = P(1,1) = P(0,2)$. If a coincidence detection occurs behind the beam splitter, we will not be able to discern whether the two photons originated both from the *slave* source, both from the *master* source, or one photon from each of the sources. We expect a HOM-type interference visibility of $30.0 \pm 0.7\%$ (see subsection 2.3.4). Apart from a slight reduction due to the timing jitter of the interfering photons this is equivalent to the visibility we would expect from the interference of classical thermal sources.

Figure 7.9 shows the experimental results for HOM-type interference with these "thermal" photons. From the Gaussian fit we calculate a visibility of $25 \pm 3\%$. Because of the
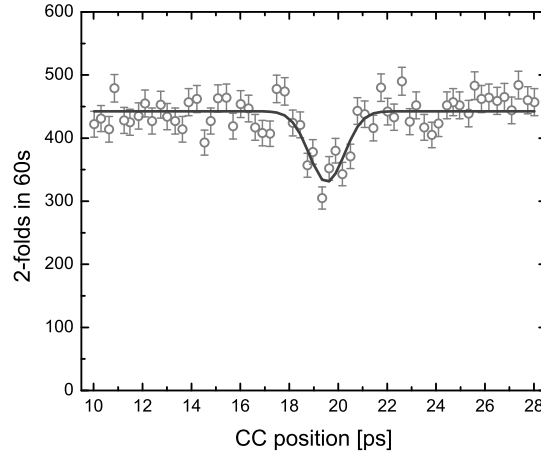
Figure 7.9.: Raw data for HOM-type interference with photons from SPDC sources without detection of the trigger photons. The solid line is a Gaussian fit to the data (red. $\chi^2 = 1.41$).

short measurement times per point we did not normalize the data [9].

We can see that there is a slight discrepancy between the visibility predicted and the visibility observed. It occurs because we did not take into account differences in the pair-production probabilities in the two sources [10], and because we did not consider stimulated double-pair emission in the crystals [11].

All of our results are in very good agreement with the predictions of quantum theory. They were published in [67]. It should be noted that the values for the visibilities given there were calculated using the *Michelson* and not the *dip* visibility, resulting in lower visibility values and in a different expression for the visibility in that paper's appendix.

7.2. Entanglement swapping

In our second experiment we realized entanglement swapping between entangled pairs of SPDC photons originating from spatially separate sources. Our implementation meets the requirements necessary for future quantum repeaters (see subsection 1.6.3): the sources of the entangled pairs are independent and spatially separable, and the swapped entanglement

---

[9] Normalization would have required a slightly different approach than in the other scans, where we recorded four-fold coincidences. Here, we would have had to normalized two-folds on single count rates.

[10] The pair-production rates of the two sources were approximately matched with each other by translating the 1 nm coupler on the *slave* side out of its optimal position.

[11] Stimulated emission leads to an increase in double-pair emission compared to the emission of one pair in each crystal. That means we would have $P(1,1) < P(2,0) = P(0,2)$.

is distillable (see subsection 1.6.3).

Compared to our first experiment we improved our setup to achieve even higher interference visibilities. We swapped the entangled states using a more-complete BSM (see subsection 6.5.2). The resulting swapped states could be used to violate a CHSH inequality (see subsection 1.5.4). That means the swapped entanglement was fit for immediate further use in quantum communication and quantum information processing protocols. The violation of a CHSH inequality is also a more than sufficient criterion for the distillability of a quantum state.

7.2.1. Preparing the setup for entanglement swapping

In the following we will give an estimate for the HOM interference visibility necessary in order to allow for a violation of an CHSH inequality with the swapped entangled pair. To this end we will assume that the original entangled states as well as the swapped state are Werner states (see equ. 1.54 in subsection 1.5.4).

Suppose that the visibilities of the original SPDC pairs (measured in the 45° basis) are V_m and V_s for the *master* and the *slave* source, respectively, and let us denote the HOM interference visibility as V_H. Then the entanglement visibility of the swapped pair will be:

$$V_{swap} \approx V_H \times V_m \times V_s. \tag{7.5}$$

For the swapped pair to violate a CHSH inequality we must have $V_{swap} > \frac{1}{\sqrt{2}}$. In the first experiment we had $V_H \sim 0.9$. With this visibility, and if we assumed $V_m = V_s$, the entanglement visibilities of the two sources would both have to be higher than 0.89 in order for V_{swap} to surpass $\frac{1}{\sqrt{2}}$. For a statistically relevant violation of a CHSH inequality, the limit 2 for LHV theories should be overcome by significantly more than one standard deviation. That means the entanglement visibilities either had to clearly surpass 0.89 or that V_H must surpass 0.9.

To increase the HOM interference visibility we exchanged the 1 nm filters, which we had used before, with 0.4 nm filters [12]. The entanglement visibility of the *slave* -SPDC source was always poorer than the visibility of the *master* source. We attempted to increase it by reducing the double-pair emissions. To this end we turned the UV-pump power down to 350 mW by translating the SHG crystal out of the focus of the IR beam. On the *master* side we reduced the UV-pump power to about 500 mW in order to prevent damages to the SHG crystal during long scans.

With these pump powers we achieved the entanglement visibilities (from 0.93 to 0.95), which are given in table 6.5 on page 117. If we assume the minimum (0.93) of these visibilities for both V_m and V_s and put them into equ. 7.5, we will see that we need to achieve a HOM-dip visibility higher than 0.82 in order for the swapped pair to violate a CHSH inequality.

---

[12]In the spatial modes of the trigger photons we kept using 3 nm filters. Reducing the bandwidth of the filters in the trigger modes would have significantly reduced the count rates while it would not have had much effect on the HOM interference visibility.

It must be noted at this point that, due to a misunderstanding, I always used the *Michelson* visibility during the experiments. Hence, I interpreted 0.82 as the minimum required value for the Michelson visibility. This posed significantly stricter requirements on the experiment than apparently necessary because, as we saw, we already achieved 90 % *dip* visibility in the first experiment. Given this value it might seem that we could have violated a CHSH inequality with the setup of the first experiment. That is misleading. Test runs, where we tried to observe teleportation with our independent sources, showed that the measured visibilities lay below the simple estimations given here. This in mind it is improbable that we could have clearly violated a CHSH inequality without improving the setup.

With the 0.4 nm filters and the jitter of 360 ± 20 (see table 5.2) we expect a HOM-dip visibility of $V_H = 0.983 \pm 0.004$ for signal photons and even 0.990 ± 0.002 for idler photons. The r.m.s. dip width is expected to be 2.0 ± 0.2 ps (see tables 5.3 and 5.4 on page 103). This should clearly suffice for violating a CHSH inequality. With these visibilities the value for S (see equations 6.16 and 6.16) should lie between 2.40 and 2.53. The smaller value was calculated using the relative-timing jitter for interfering signal photons (360 ± 20, see section 5.3) and an entanglement visibility of 0.93 for both sources. The higher value was obtained using the jitter for interfering idler photons (280 ± 20) and an entanglement visibility of 0.95 for both sources. These estimations of S should not be seen as strict boundaries because there are still effects that we did not take into account, which reduce the HOM interference visibility (see below).

Another change of the setup became necessary due to the increasingly poor synchronization of the femtosecond lasers, which would have rendered a continuation of the experiment impossible. Specifically, the position of the CC signal started to shift randomly up over a range of several picoseconds on a time scale of a second or less. The time scale of these fluctuations was too short to allow for a compensation by a feed back algorithm and too large to allow for high-visibility interference.

After a thorough investigation of all components of the setup we concluded that the reason for these random shifts must have been either one or a combination of the following:

- poor performance of the cooling circuit for the Ti:Sa crystal in the *master* laser

- instability of the pump laser on the *master* side, a Coherent Innova 400

All of these possible reasons were eliminated simultaneously. The Innova 400 was replaced with a Coherent Verdi V10 and the cooling circuit of the *master* femtosecond laser was repaired. Afterwards the performance of the laser synchronization was back to normal, i.e. the relative-timing jitter of the lasers was on the order of 250 fs.

7.2.2. Scan duration and long-time drifts

Because we used the 0.4 nm filters and reduced UV-pump powers the count rates were significantly lower than in our first experiment (see subsection 6.3.1 on page 114). Additional
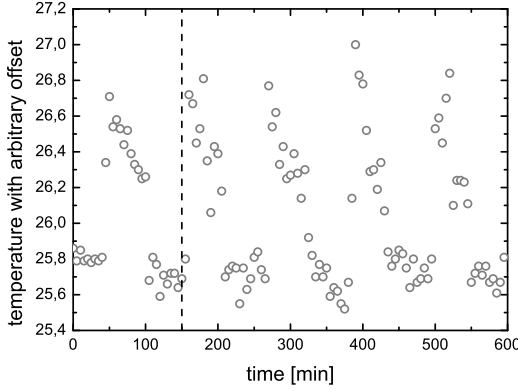
Figure 7.10.: Laboratory temperature (plus an unknown constant offset) over time. The period of the temperature modulation is ≈ 110 min. The dashed line indicates the time up to which the CC position has been recorded (see fig. 7.11).
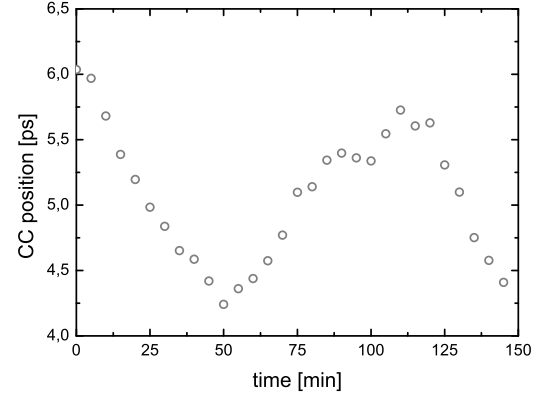
Figure 7.11.: CC position over time. Each data point corresponds to an average over 5 measurements, which were taken in immediate succession of each other. Although we let scans like this one run several times over night (to avoid disturbances) the Synchrolock always failed after a relatively short time. This is the best scan. A full period of the modulation can be seen. The failure of the Synchrolock during these measurements was due to damages to the coating of the SHG crystal on the *slave* side. As a result back reflections disturbed the modelocking of the *slave* laser.

coupling losses were encountered in the more-complete Bell-state analyzer because the photons had to be coupled out before passing the PBSs and had to be coupled in again afterwards. As a consequence of the lower count rates scan times were correspondingly longer than in the first experiment. There the scan-times were maximally 900 s. In the second experiment we had to deal with scan times up to 16000 s per data point. Over this time at least the delay between the lasers had to be stable. Otherwise we would have had to split the measurement time into smaller blocks of time as we did in our earlier experiments (see 7.1.2). This was not a feasible option as we will see below.

Let us assume we had split the measurement time in blocks of 1 min as we did before. For the BSM to work optimal the HOM-type interference visibility has to be maximal, i.e. the time delay between photons detected in the BSM must be minimal. We will refer to this situation as operating "at the minimum of the HOM dip". We attempted to position the CC signal within 50 fs of the delay corresponding to the minimum of the dip. On average

our algorithm (see subsection 6.4.4) took about 2 min to adjust the delay to that accuracy [13]. If we had to run the algorithm every minute, this would increase our scan time per data point by a factor of three. For the violation of the CHSH inequality we need 16 such data points. Instead of about three days the scans for the violation of the inequality would have taken about nine days. To keep two lasers and the synchronization running without significant loss of performance over three days is already an achievement. Nine days would have been close to inconceivable. It was inevitable to significantly improve the stability of the synchronization. We had to eliminate drifts of the lasers' relative time delay over times of the order of the measurement time per data point (16000 s). Between data points the delay was readjusted to compensate for any drifts during the measurement time.

In order to eliminate the lasers' relative time drift it is important to know whether these drifts are random or whether they follow a systematic pattern. If they were random, they could only be compensated by implementing an additional feed-back loop running in parallel to the measurements. We could not have used our standard algorithm (see subsection 6.4.4) to fine adjust time delays because it took too long and sometimes changed the laser delay unpredictably during its search for the correct delay. This way the visibility of the experiment would have become dependent on the performance of our algorithm. A solution would have been to implement an optical delay path to allow for fast and deterministic adjustments of the relative time delay of the laser pulses. If the drifts were systematic, it should be possible to find the reason for the drifts and maybe to eliminate it. It turned out (see below) that a great part of the long-time drifts were systematic and could be eliminated.

Measurements by R. Prevedel, which were unrelated to our experiment but which were performed in the same laboratory, showed periodic variations in the two-fold rates of the *master* source. He suspected that these periodic variations might be related to the cooling cycle of the air-conditioning system of the laboratory. We set out to investigate this phenomenon. The results of our long-time scans, which monitored the two-fold rates of the sources as well as the CC position and the laboratory temperature are shown in figures 7.10 to 7.13.

Apart from the coincidence count rate of the *master* source all these scans show the same periodicity of approx. 110 min [14]. The variation of the CC position over one modulation period was on the order of 2 ps. This is comparable to the expected width of the HOM dip in the second experiment, which was 2 ± 0.2 ps (see table 5.4 on page 103). Because these long-time drifts occurred on a time scale shorter than our measurement time per point they

---

[13]Two minutes is a good average.

[14]That the coincidences of the *master* source did not explicitly show the periodicity is surprising because our investigation of the temperature dependence of the laser delay started with R. Prevedel's observation of periodic variations of these coincidences. A possible explanation is that in contrast to R. Prevedel's observations our measurements were performed after the Innova 400 had been replaced with a Coherent Verdi V10. The *master* laser seems to not have been as susceptible to the temperature variations as the *slave* laser. That might have been due to the fact that Verdi and MIRA on the *master* side were cooled by separate chillers and were positioned under a flow box in contrast to the *slave* lasers. These were not placed under a flow box and were both connected in parallel to one chiller.
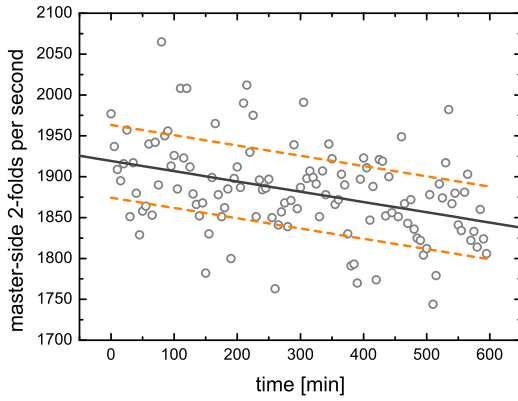
Figure 7.12.: Two-fold coincidence rate of the *master* source over time. The solid line corresponds to a linear fit to the data, which shows a decrease of the count rate due to increasing misalignment of the lasers and the setup over time. The dashed lines are parallels to the linear fit separated by the average Poissonian error of the count rates.

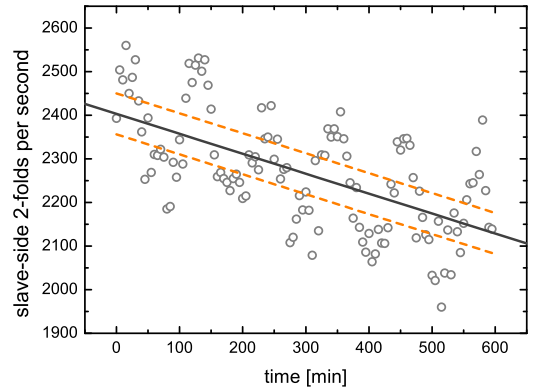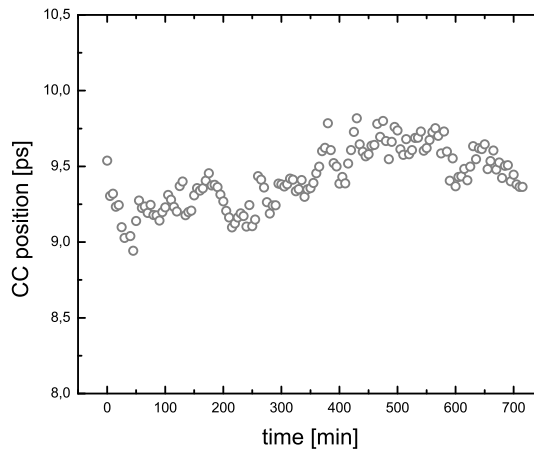**Figure 7.13.:** Two-fold coincidence rate of the *slave* source over time.

Figure 7.14.: Position of the cross-correlation signal over time after we had introduced constant cooling of the laboratory. There is still a noticeable long-time drift of the relative time delay of the lasers. Yet, there are no more periodic modulations and the delay changes on a much smaller scale than in figure 7.11.
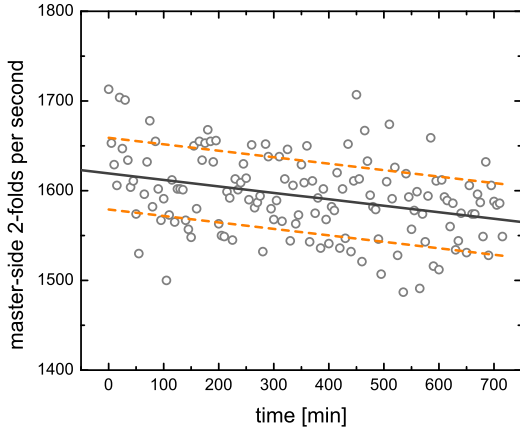
Figure 7.15.: Two-fold coincidence rate of the *master* source over time with constant cooling of the laboratory.
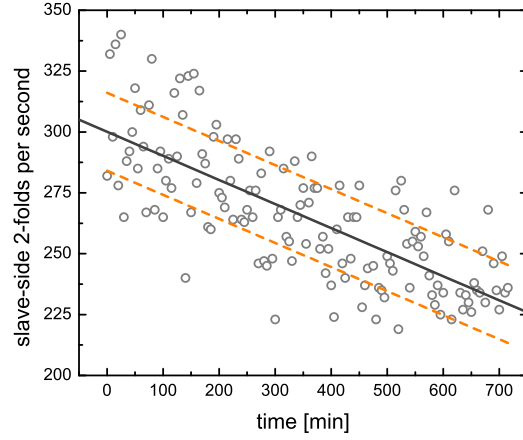
Figure 7.16.: Two-fold coincidence rate of the *slave* source over time with constant cooling of the laboratory.

would have significantly lowered the visibility of our interference experiments.

The origin of the periodic modulation of the laboratory temperature is easily explained by investigating the principle of operation of the air-conditioning system. The temperature of the laboratory is constantly measured and, as soon as it surpasses a variable limit, the air-conditioning system will automatically be switched on in order to cool the temperature below that limit. The period of the modulation depends on how fast the laboratory is heated by lab equipment and by the rate of heat exchange with the environment.

Thanks to discussions with M. Arndt we found a simple and elegant solution to overcome the resulting temperature variations. By lowering the temperature set for the air-conditioning system to a temperature it cannot reach. (we chose 14°C) the system is forced to constantly cool the laboratory. Depending on the cooling capacity of the air-conditioning system and on the heat emitted by the laboratory equipment and on heat entering the laboratory, the laboratory temperature will stabilize at some value above the intended but unreachable temperature. In our case the balance occurred at about 16°C to 18°C [15].

After the temperature had stabilized we repeated the long-time scans to test if we had eliminated the periodic drifts as expected. Figures 7.14 to 7.16 show the results of these scans. We did not record the temperature changes during these scans but the measurement results show, as expected, that the periodic modulations are gone.

The relative time delay of the lasers is stable over the whole scan period up to a few hundred femtoseconds. This stability was sufficient for our purposes and allowed us to abandon the method of dividing the measurement times into shorter blocks of time. Instead,

---

[15]There will still be temperature fluctuations because of changes in the outside temperature or in the heat emitted by the laboratory equipment.

we were now able to readjust the laser delay only in between measurement points.

Nevertheless, there will always be some drift in the relative time delay of the lasers as we can see in figure 7.14. This drift will reduce the interference visibility such that we cannot hope to fully achieve the predicted visibility of 98.3±0.4 % (see table 5.3 on page 102) because it does not take into account long-time drifts.

To measure the magnitude of the long-time drifts, we monitored the position of the CC signal in regular time intervals in parallel to our scans. These drifts have to be included into our estimate of the overall relative-timing jitter (see also table 5.2 on page 102). We will give these overall jitter estimates together with the scan data (see below).

7.2.3. Entanglement swapping with independent photon pairs

Before we attempted to violate the CHSH inequality with the swapped entangled pairs, we had to check the visibility of the HOM-type interference. This was done in perfect analogy with our first experiment, except that we did not split the measurement times in smaller blocks of 1 minute each.

HOM-type interference visibility

Figure 7.17 shows the raw data of a scan over the HOM dip before we implemented the more-complete BSM. Specifically, we measured four-fold coincidences between the trigger modes 1 and 4 and the output modes a and b of the fiber beam splitter (see fig. 6.18 on page 131). The Gaussian fit yields a visibility of 95 ± 1 %. Normalizing these results on the product of two-fold coincidences yields the data presented in figure 7.18. From the Gaussian fit to the normalized data we gain a visibility of 96 ± 1 % [16]. The r.m.s. width of the fitted Gaussian is 1.6 ± 0.1 ps.

The horizontal error bars of the data result from the measurements of the CC position in parallel to the scans (see above). These allows us to quantify the long-time drift during our scans to be 160 ± 40 fs over 9000 s. Combined with the jitter given in table 5.2 on page 102, we can estimate the jitter for each data point to be 400 ± 25 fs. We expect a dip visibility of 98.0 ± 0.5 % and an r.m.s. dip width of 2.0 ± 0.2 ps. That these values deviate from the fits to the data could be explained in various ways. One possibility is that the range over which we scanned was too narrow, and that the plateau would really be higher. Another possibility is that the number of data points at the minimum of the dip is too small to avoid that the visibility is reduced by some of the worse data points. Finally, it is possible that the bandwidth of the interference filters was broader than we anticipated. Due to the lack of a spectrometer with a sufficiently high resolution we could not check the transmission curves of the filters.

---

[16]To achieve reasonable errors for the visibilities of our dips, it is crucial to select an appropriate fit function. In our case, the optimal choice was the function $f(x) = A(1 - M \exp{-(x - x_0)^2/(2\sigma^2)})$. In this case, the visibility is equal to the parameter M; it cannot be influenced by the errors of the other fit parameters.
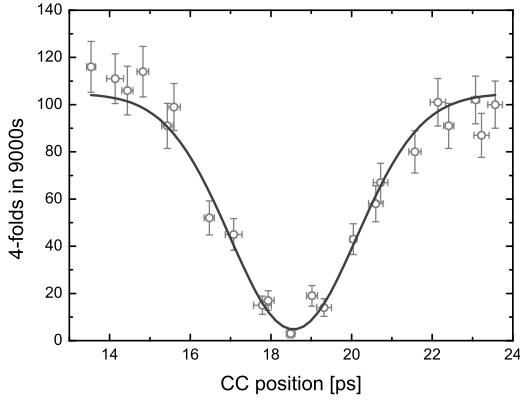
Figure 7.17.: Raw data for HOM-type interference before the implementation of the more-complete BSM. Both photons originate from triggered single-photon sources and are horizontally polarized. The solid line is a Gaussian fit to the data (red. $\chi^2 = 1.21$).
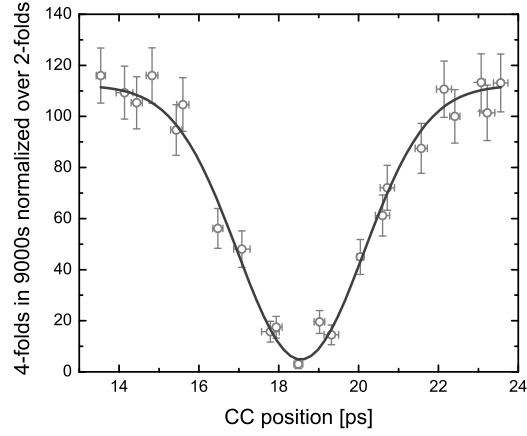
Figure 7.18.: Here, we normalized the data from fig. 7.17 over the product of coincidences of the *master* and *slave* sources. The solid line is a Gaussian fit to the data (red. $\chi^2 = 0.85$).

In the course of the implementation of the more-complete BSM we readjusted and further optimized both the lasers and the SPDC sources. After these procedures the dip width observed was slightly larger than in the scans, which we had performed before. This can be explained by the longer scan times [17]: because of the longer scan times the long-time drifts of the relative time delay of the lasers result in a larger effective jitter and a correspondingly broader dip. Similar to the earlier measurements, we monitored the CC position in parallel to the scans. Over 14000 s the drift of the position of the CC signal was 230 ± 60 fs. This increases the overall jitter per point to 430 ± 40 fs. We expect a dip visibility of $97.6 \pm 0.6\%$ and an r.m.s. dip width of 2.0 ± 0.2 ps.

The data of the dip scans after the implementation of the more-complete BSM is presented in figures 7.19 (raw data) and 7.20 (normalized on the product of two-fold coincidences). A Gaussian fit to the unnormalized data yields an interference visibility of $92.5 \pm 1.1\%$. For the normalized data we get a visibility of $93 \pm 2\%$. The width of the Gaussian fit in the normalized case is 1.8 ± 0.1 ps.

It is clear that there must have been some effect, which reduced the dip visibility but which we did not take into account. Despite very intensive investigations of every part of the setup the origin of the low visibility eluded our efforts to find it.

---

[17]In the earlier dip scan the measurement time was 9000 s per point. After implementing the more-complete BSM the measurement time per point had to be increased to 14000 s for the dip scan.
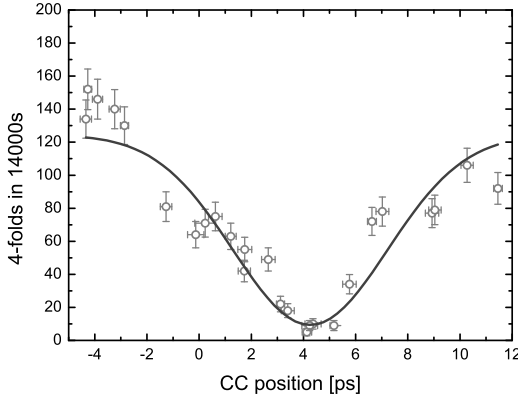
Figure 7.19.: Raw data for HOM-type interference after the implementation of the more-complete BSM. Horizontally oriented polarizers were placed in front of the inputs of the FBS. The drop in the signal at about −3 ps is due to a drop in laser power. The solid line is a Gaussian fit to the data (red. $\chi^2 = 4.26$).
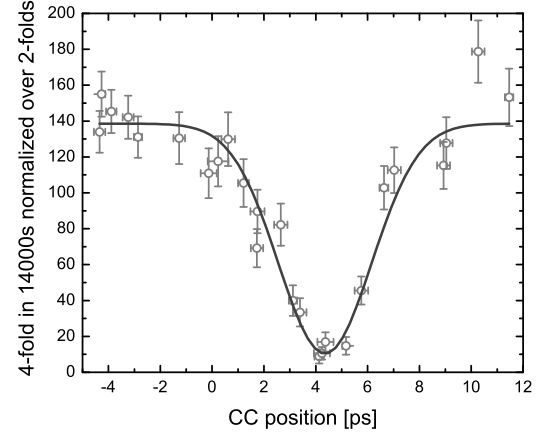
Figure 7.20.: Here, we normalized the data from fig. 7.19 over the product of coincidences of the *master* and *slave* sources. The solid line is a Gaussian fit to the data (red. $\chi^2 = 1.62$).

Violation of the CHSH inequality

The polarization measurements in the modes 1 and 4 (see 6.18 on page 131), which contained the swapped entangled pairs, were performed with polarization filters, not with polarizing beam splitters. To measure the expectation values for the violation of the CHSH inequality we had to perform 16 measurements.

The measurement time per each data point was 15000 s. We recorded the four-fold coincidences for both ψ^- and ψ^+ results of the BSM. The raw data is given in table 7.1, the normalized data (on the product of two-folds) is given in table 7.2. From these results we can calculate the expectation values. They are presented for the raw and the normalized results in the tables 7.3 and 7.4, respectively.

By inserting the expectation values in the inequalities for ψ^- and ψ^+ states (see equ. 1.50 and 1.53) we obtain:

$$S_{\psi^-} = 2.37 \pm 0.09 \tag{7.6}$$

and

$$S_{\psi^+} = 2.38 \pm 0.09 \tag{7.7}$$

for the raw data.

		Bob							
		22.5°		112.5°		67.5°		157.5°	
Alice	0°	44	52	121	126	185	176	46	32
	90°	132	109	36	42	20	22	126	122
	45°	30	141	126	23	41	138	134	31
	135°	136	26	22	129	131	40	39	118

Table 7.1.: Raw data for the Bell experiment with the swapped entangled pair. For every pair of settings, the left-hand value corresponds to ψ^- events, the right-hand value to ψ^+ events during 15000 s.

		Bob							
		22.5°		112.5°		67.5°		157.5°	
Alice	0°	44.0	52.0	113.9	118.6	147.7	140.5	40.1	27.9
	90°	149.7	123.6	36.6	42.7	18.5	20.4	129.0	124.9
	45°	30.5	143.3	128.3	23.4	37.4	125.8	133.4	30.9
	135°	143.4	27.4	22.0	128.9	120.9	36.9	38.7	117.2

Table 7.2.: Normalized data for the Bell experiment with the swapped entangled pair. For every pair of settings, the left-hand value corresponds to ψ^- events, the right-hand value to ψ^+ events during 15000 s.

The normalized data points result in

$$\widetilde{S}_{\psi^-} = 2.40 \pm 0.09 \tag{7.8}$$

and

$$\widetilde{S}_{\psi^+} = 2.38 \pm 0.09. \tag{7.9}$$

The CHSH inequality is clearly violated in all of these cases. Once more this rules out local realism as an explanation for experimental results. At the same time the experiment is in good agreement with quantum theory, which leads us to expect at best a value between 2.40 and 2.53. By violating the CHSH inequality we have shown that we succeeded in entangling particles that never have interacted and share no common past. The entanglement widely exceeds the minimum requirements for entanglement distillation. It is high enough for immediate further use for quantum information processing schemes.

BSM	$E(0°, 22.5°)$	$E(0°, 67.5°)$	$E(45°, 22.5°)$	$E(45°, 67.5°)$
ψ^-	-0.52 ± 0.05	0.65 ± 0.04	-0.67 ± 0.04	-0.54 ± 0.05
ψ^+	-0.43 ± 0.05	0.69 ± 0.04	0.69 ± 0.04	0.57 ± 0.05

Table 7.3.: Expectation values for the CHSH inequality calculated from the raw data.

BSM	$E(0°, 22.5°)$	$E(0°, 67.5°)$	$E(45°, 22.5°)$	$E(45°, 67.5°)$
ψ^-	-0.53 ± 0.05	0.65 ± 0.04	-0.68 ± 0.04	-0.54 ± 0.05
ψ^+	-0.44 ± 0.05	0.69 ± 0.04	0.69 ± 0.04	0.56 ± 0.05

Table 7.4.: Expectation values for the CHSH inequality calculated from the normalized data.

8. Conclusion and Outlook

In this thesis we demonstrated the interference of photons originating from independent time-synchronized sources, and we realized entanglement swapping to generate entanglement, which violated a CHSH inequality, between photons, which do not share a common past.

The results of our first experiments clearly confirm the predictions of quantum theory for various states of indistinguishability of the interfering photons. In contrast to earlier experiments (see chapter 3) our sources fulfill all requirements to be called independent. Although they are only separated by the length of the optical table ($\sim 4\,\mathrm{m}$) they could easily be separated by larger distances. Our sources did not share any optical interaction. Only the relative timing of their pulses was synchronized via electronic means, which do not influence the coherence properties of the lasers.

The positive results in our first experiment conclude an experimental challenge, which has been tried to meet in a series of experiments over the last decades (see chapter 3): to demonstrate non-classical interference of light from independent sources. Nevertheless, we find that Dirac was definitely right when he said that [40].

In our second experiment we realized a technique that will be essential for any optical full-scale implementation of a quantum repeater [25, 42]. These devices are based upon connecting entanglement over adjoining segments of a larger distance via entanglement swapping. In a real-world application the entanglement distributed over different segments must originate from independent nodes. Our experiment fulfills this requirement, and our results show that it is feasible to create distillable entanglement by swapping entangled states from independent nodes. Even more, our results violate a CHSH inequality in clear contradiction to local realism. The extend of the violation is in good agreement with quantum theory. It indicates strong entanglement of our swapped states, high enough for immediate further use, i.e. without distillation, in quantum information processing.

The demonstration of entanglement swapping in this configuration is a major step towards a working quantum repeater. We employed a technique to synchronize our pulsed sources that is not limited to two but can easily be extended to synchronize any number of sources. This makes it attractive for use in future optical realizations of quantum networks, where many communication parties communicate via the aid of sharing single photons or entangled pairs.

A novel method, which was reported recently [59], does not need synchronization but their count rates and HOM-interference visibilities were poor compared to our results. The question is whether the advantage of not needing synchronization really outweighs these obvious disadvantages. It should be noted that the synchronization of pulsed sources would

become undemanding, if we used as narrow filters as they did in [59]. In fact the HOM-dip visibility (see equ. 2.84 on page 55) would still be 99.9% if we only used the fundamental loop to synchronize our sources. Because of these reasons we think that our technique holds higher promise for future applications.

A huge future challenge for experimental quantum optics will be to realize entanglement swapping with pairs emitted by *distant sources*. This will be a large step towards real-world applications of quantum information processing techniques. The technique, which we employed is fit for that challenge. The synchronization depends only on electronic signals. These have a bandwidth that allows them to be easily transmitted with means that are available today, e.g. via microwave links. If we used narrower filters, the requirements on the electronic link would become even less demanding.

Another possibility, which will be worth exploring, is to use a configuration slightly different from ours. The technique we employed also allows both (or more) lasers to be synchronized not with each other but locally with atomic clocks. These atomic clocks can be synchronized with each other, e.g. with the network time protocol (NTP). It would be an interesting future experiment to test whether pulsed lasers can be synchronized well enough with this method to achieve high-visibility HOM interference with photons from distant sources. By using sufficiently narrow filters it should be no problem.

The development of deterministic single-photon sources would revolutionize these efforts because it would largely eliminate the scalability problems that are inherent in SPDC sources. Our synchronization technique applies to many promising candidates for deterministic single-photon sources, e.g. quantum dots, which are pumped by pulsed lasers (see e.g. [107]).

A central problem for long distance quantum communication will be to obtain high-visibility HOM interference. Not because of problems in the synchronization of the photon sources but because of fluctuations in the optical path lengths and because of low transmission rates. Moreover, our technique utilizes cross correlation of parts of the laser beams to monitor and control the delay between the interfering photons. This will not pose any restrictions for long distance experiments if HOM-type interference is intended. To observe such interference narrower filters have to be used (e.g. like those employed in [59]). But then the coherence lengths of the photons will be so large that it is enough (or close to) to determine the delay between the photons by investigating the detection signals (see subsection 7.1.1). No cross correlation will be necessary. Experiments will show, which techniques will prevail to finally realize real-world long-distance quantum communication. Our technique is definitely a very promising candidate.

We have only just begun to grasp the possibilities, which the concepts of quantum entanglement and its applications offer. The future remains wide open.

Part II.

Appendix

A. Fringes in HOM-type interference

In section 2.3.2 we introduced a very precise notation for the four-fold-coincidence probability amplitude in HOM-type interference in order to discriminate which filter the photons passed before being detected. The reason why we introduced this notation is that the four-fold probability shows qualitatively different properties depending whether the bandwidth filters are placed before or after the beam splitter (see fig A.1 and compare it to fig 2.9).

If the filters are placed before the beam splitter, the four-fold amplitude will be the one given in equation 2.75. If the filters are placed after the beam splitter, the amplitude will be:

$$A_4'(t_1, t_2, t_3, t_4) = A_4^{(1,3;1,3;2,4;2,4)} - A_4^{(1,2;1,2;3,4;3,4)}.$$

(A.1)

The difference occurs in the first addend.

We will calculate the four-photon probabilities for both filter configurations. This is also necessary in the case, where the filters are in front of the beam splitter, because we will introduce a slight change to the assumptions, which we made in order to obtain equ. 2.74. Specifically, we will assume that the center frequencies of the filters 2 and 3 are:

$$\omega_{f_2} = \omega_0 + \frac{1}{2}\Delta\omega \quad \text{and} \quad \omega_{f_3} = \omega_0 - \frac{1}{2}\Delta\omega,$$

(A.2)

respectively. $\Delta\omega$ is the difference of the center frequencies of the filters. It can be treated as an additional parameter.

In order for us to be able to directly compare the two cases let us first calculate the four-fold-coincidence detection probability for the case where the filters are *before* the beam splitter (see also equ. 2.76):

$$P_4(\Delta\tau, \Delta\omega) = \frac{8\pi^4 f_S^4 f_T^4 \sigma_S^2 \sigma_T^2}{\sigma_p^2(\sigma_p^2+\sigma_S^2+\sigma_T^2)} \left[e^{-\frac{\Delta\omega^2}{2(\sigma_p^2+\sigma_S^2+\sigma_T^2)}} \right] \left[1 - \sigma_p \sqrt{\frac{\sigma_p^2+\sigma_S^2+\sigma_T^2}{(\sigma_p^2+\sigma_S^2)(\sigma_p^2+\sigma_T^2)}} e^{-\frac{\Delta\tau^2\sigma_p^2\sigma_S^2}{2(\sigma_p^2+\sigma_S^2)} - \frac{\Delta\omega^2(\sigma_p^2+\sigma_T^2)}{2\sigma_S^2(\sigma_p^2+\sigma_S^2+\sigma_T^2)}} \right].$$

(A.3)

We can see that there is no qualitative difference compared to our earlier result (i.e. for $\Delta\omega = 0$). The difference in the center frequencies of the filters results only in a reduction of the four-fold rate and of the HOM-dip visibility.

If the filters are placed *after* the beam splitter, the four-fold-coincidence detection proba-
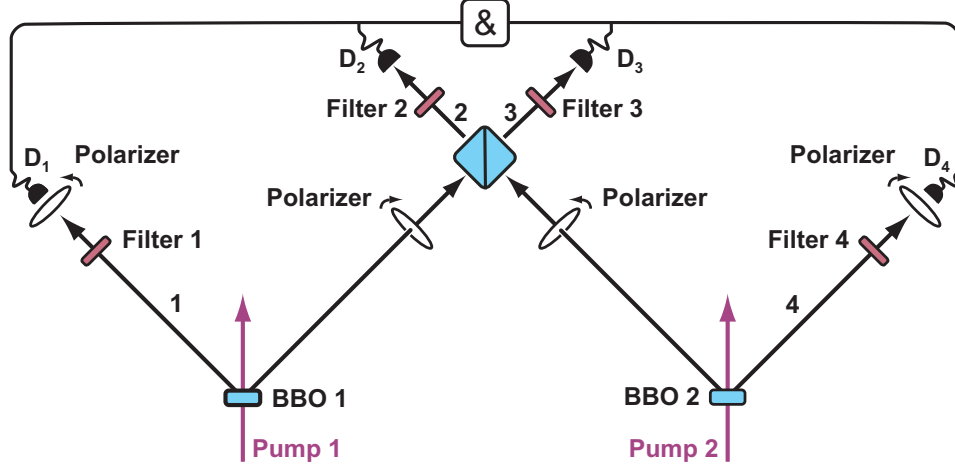
Figure A.1.: HOM-type interference with two independently generated triggered single photons, where the filters for interfering photons are placed after the beam splitter. If the center frequencies of these filters differ, fringes will occur in the interference pattern.

bility will become:

$$
P_4'(\Delta\tau) = \frac{8\pi^4 f_S^4 f_T^4 \sigma_S^2 \sigma_T^2}{\sigma_p^2(\sigma_p^2+\sigma_S^2+\sigma_T^2)} \left[e^{-\frac{\Delta\omega^2}{2(\sigma_p^2+\sigma_S^2+\sigma_T^2)}} \right]
$$

$$
\times \left\{ 1 - \sigma_p \sqrt{\frac{\sigma_p^2+\sigma_S^2+\sigma_T^2}{(\sigma_p^2+\sigma_S^2)(\sigma_p^2+\sigma_T^2)}} \left[e^{-\frac{\Delta\tau^2 \sigma_p^2 \sigma_S^2}{2(\sigma_p^2+\sigma_S^2)} - \frac{\Delta\omega^2 \sigma_T^2}{2(\sigma_p^2+\sigma_S^2)(\sigma_p^2+\sigma_S^2+\sigma_T^2)}} \right] \cos\left(\frac{\Delta\tau \Delta\omega \sigma_p^2}{\sigma_p^2+\sigma_S^2} \right) \right\} . \quad (A.4)
$$

In contrast to P_4 we get a cosine modulation of the four-fold rate. Its frequency is determined by the filter bandwidths and by $\Delta\omega$. This modulation is equivalent to an effect, which has been denoted as *quantum beat* [78]. There, photons with ultra-long coherence lengths were emitted by a strongly coupled atom-cavity system using a stimulated Raman process driving an adiabatic passage (STIRAP) [73] between two ground states of the atoms. Two such photons with slightly different wavelengths were created in succession. Both were overlapped at a beam splitter to observe two-photon interference. The coincidence count rate was modulated by a quantum beat.

To our best knowledge this effect has not yet been demonstrated with SPDC sources. One limiting factor in the case of SPDC sources is the jitter between the sources. To include the effect of relative-timing jitter we have to calculate the convolution of $P'(\Delta\tau - J)$ with the jitter distribution function $D_J(J)$ (see 2.3.4). Before we do so let us write equ. A.4 in a
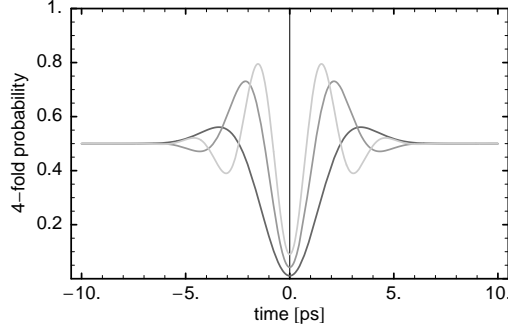
Figure A.2.: Fringes in HOM-type interference without jitter. Three curves are given for various differences between the center wavelengths of the filters. They represent four-fold coincidence probabilities, normalized such that the plateau lies at $\frac{1}{2}$. Apart from the differences in the center wavelengths all parameters were chosen in accordance to our second experiment. The gray level of the curves rises from dark to bright for 0.5 nm, 1.0 nm and 1.5 nm difference in center wavelength.

simpler form

$$P_4'(\Delta\tau) = A e^{-\frac{\Delta\omega^2}{2\sigma_1^2}} \left[1 - \frac{\sigma_p \sigma_1}{\sigma_2 \sigma_3} \cos\left(\frac{\Delta\tau\Delta\omega\sigma_p^2}{\sigma_2^2} \right) e^{-\frac{\Delta\tau^2\sigma_p^2\sigma_S^2}{2\sigma_2^2} - \frac{\Delta\omega^2\sigma_T^2}{2\sigma_1^2\sigma_2^2}} \right], \qquad (A.5)$$

where we introduced the abbreviatory notations:

$$\sigma_1^2 \equiv \sigma_p^2 + \sigma_S^2 + \sigma_T^2, \quad \sigma_2^2 \equiv \sigma_p^2 + \sigma_S^2, \quad \sigma_3^2 \equiv \sigma_p^2 + \sigma_T^2, \quad \sigma_4^2 \equiv \sigma_S^2 + \sigma_p^2(1 + \sigma_J^2\sigma_S^2) \qquad (A.6)$$

and

$$A = \frac{8\pi^4 f_S^4 f_T^4 \sigma_S^2 \sigma_T^2}{\sigma_p^2(\sigma_p^2 + \sigma_S^2 + \sigma_T^2)}. \qquad (A.7)$$

With this simpler notation we can write the convolution of the four-fold probability with the jitter distribution as

$$\begin{aligned}
P_4'^{(J)}(\Delta\tau) &= \int dJ \, P_4(\Delta\tau - J) D_J(J) \\
&= A e^{-\frac{\Delta\omega^2}{2\sigma_1^2}} \left[1 - \frac{\sigma_p \sigma_1}{\sigma_3 \sigma_4} \cos\left(\frac{\Delta\tau\Delta\omega\sigma_p^2}{\sigma_4^2} \right) e^{-\frac{\Delta\tau^2\sigma_p^2\sigma_S^2}{2\sigma_4^2} - \frac{\Delta\omega^2\sigma_2^2(\sigma_T^2 + \sigma_J^2\sigma_p^2\sigma_3^2)}{2\sigma_1^2\sigma_4^2}} \right]. \qquad (A.8)
\end{aligned}$$

The frequency of the quantum beat is proportional to the difference of the center wavelengths of the bandwidth filters in the beam-splitter output modes. It is interesting to note that the fringes are well visible even for wavelength differences larger than the bandwidth
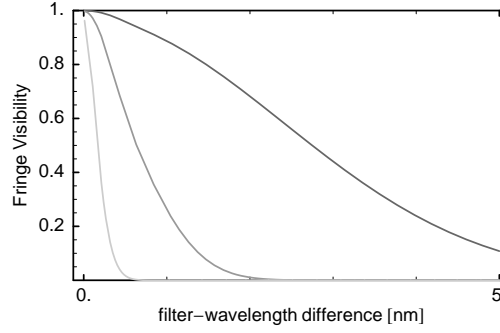
Figure A.3.: Visibility of HOM-type interference with fringes for various values of relative-timing jitter. All parameters were chosen like in our second experiment. The three curves can be distinguished by their gray level, which rises from dark to bright for 0 fs jitter, 100 fs jitter and 370 fs jitter (the estimated overall jitter for our second experiment, see table 5.2).

of the filters of the interfering photons (see fig. A.2), at least if there is no or only small relative-timing jitter. This is possible due to the broad wavelength distribution of the pump pulses. Figure A.3 shows the fringe-visibility over the wavelength difference of the filters for various values of relative-timing jitter. We use the *Michelson* visibility (see equation (2.16)) with the minimum (f_{min}) and maximum (f_{max}) of the fringes given by (see equ. A.8):

$$f_{max} = P'_4 \left(\Delta\tau = \frac{\pi\sigma_4^2}{\Delta\omega\sigma_p^2} \right), \tag{A.9}$$

and

$$f_{min} = P'_4(\Delta\tau = 0). \tag{A.10}$$

For low wavelength differences the visibility reduces to the visibility of the HOM dip. We see in figure A.3 that the visibility drops very rapidly for the relative-timing jitter in our experiment. This effect is even more pronounced for broader filters. To observe the fringes and not only the HOM-dip the wavelength difference has to be larger than the bandwidth of the filters behind the beam splitter. Otherwise the period of the cosine modulation becomes comparable or larger than the width of the HOM dip. On the other hand, for larger differences the visibility drops because the relative amplitude of the interference term decreases (see equ. A.8). That means, in an experiment a filter bandwidth has to be found, for which the fringe visibility is optimal.

To this end we have to redefine our visibility to exclude the visibility of the HOM-dip itself. Otherwise even in the absence of fringes we would get the Michelson visibility of the dip, which we are not interested in. The choice we make for the definition of the visibility is similar to the definition of the *dip* visibility (see equation (2.19)). Because only fringes lead to a modulation exceeding the signal plateau level, we will define the fringe visibility as the
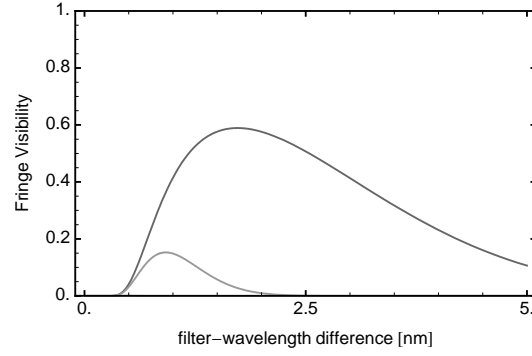
Figure A.4.: Redefined visibility for the fringes in HOM-type interference for various values of relative-timing jitter. The parameters are equal to the ones in fig. A.3. The visibility for the relative-timing jitter of 370 fs (the value estimated for our second experiment) is practically zero and not visible.

ratio of that positive modulation and the plateau, i.e.:

$$V_F \equiv \frac{I_{max} - I_{min}}{I_{min}}, \tag{A.11}$$

where I_{min} denotes the signal plateau. Plots of the redefined visibility for the same parameters as in fig. A.3 are given in figure A.4.

B. Notes on the alignment of the setup

In this chapter I will present some short notes on the alignment of parts of the setup. Although most of the alignment procedures described (or at least parts of them) are documented here or there I considered this appendix a good place to collect information on the alignment and to describe some not so well documented aspects that I encountered during my experiments. Examples are the alignment of the Brewster prisms in the femtosecond lasers and the determination of the correct orientation of the SPDC crystals.

B.1. Alignment of the femtosecond lasers

In general each enhancement in the adjustment of the femtosecond lasers improves the performance of the laser synchronization. Therefore, it has been paramount during the course of the experiment and its preparations to regularly adjust the laser cavities. Most of maladjustments that we at some time thought to disturb the synchronization have been ruled out as important sources of disturbance. Still, it is a good strategy to minimize every possible perturbation of the synchronization mechanism in order to achieve optimal experimental results.

B.1.1. Cavity alignment in general

Aligning and optimizing the femtosecond lasers (especially the *slave*) was a nearly daily procedure during our experiments. The workflow will be described in the following. In its essence it is a distilled form of the procedure, which is described in the handbook for the MIRA 900-F, with some additional personal notes. Details should be looked up in the handbook. For instance we did not depict the pump-fold mirrors $P1$-$P4$ in figure 6.2, but that figure can be used as a reference for all the other optical components of the laser, which we will refer to.

1. check whether the pump fold mirrors $P1$-$P4$ are clean. Even $P2$ and $P3$, which face downwards, tend to become exceedingly dirty. This results in unstable pulsing.

2. start the adjustment procedure by optimizing the auxiliary cavity according to the description in the MIRA handbook. Check the cleanliness of all the components involved and whether the infrared fluorescence and the infrared beam are centered on

all mirrors. This can be achieved by walking the corresponding components. Usually you have to walk the mirror that you want to center the beam on and the mirror with the succeeding number. For instance, to center the beam on $M2$ walk with $M2$ and $M3$. Optimize for output power by adjusting $P2$, $M5$ and $M1$. The output power of the auxiliary cavity is an upper bound for the maximum output power of the main cavity.

3. once the auxiliary cavity is well aligned you can switch to the main cavity. Now is the right moment for aligning the prism $BP1$ (see below). Although that should usually not be necessary it might be a good idea to do it if you intended to adjust $BP2$.

4. in order to align the main cavity refract part of the beam from the auxiliary cavity into the main cavity. Do so by translating $BO1$ into the beam such that the auxiliary cavity is still lasing. Center the refracted beam on $M7$ by walking with $M6$ and $M7$.

5. move $BP1$ completely into the beam path. If the main cavity does not lase, move *only* $M7$ until the cavity lases. Use *only* $M7$ to optimize the CW output power (otherwise you will misalign the auxiliary cavity)

6. one of the most important components for stable pulsing is the prism $BP2$. Its alignment should not be necessary in daily operation. Whether it must be optimized can be determined with the method that will be described in the following subsection. There we will also specify a method to align the prism.

7. the MIRA control box allows you to set a reference mark on the output power. It admits easy monitoring of changes to the laser output power. Set this mark now. It will help you to regain the achieved output power after you put the cover back on. For this realignment you should only employ $M7$ and $P2$.

8. once the cover is back in place, you can activate modelocking as described in the MIRA handbook. Of course you can also do it with the cover removed but then you should deactivate the flow box because the airflow will make it difficult for the laser to lock.

Always use a spectrometer or at least an oscilloscope, which monitors the laser signal via a fast photo diode, to assure correct pulsing. Best, use both methods. An oscilloscope makes it easy to distinguish between normal operation and double pulsing. A spectrometer, on the other hand, has the advantage that it allows to tell at one glance if there are any CW components in the laser output.
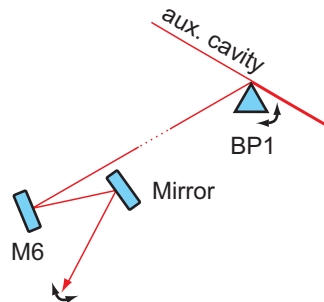
Figure B.1.: Alignment of the Brewster Prism *BP*1. The laser is adjusted to operate in the auxiliary cavity. The prism is translated to refract enough of the beam for alignment but little enough to not interrupt the lasing process. An additional mirror is placed close to *M*6 in order to project the beam over a greater distance to allow fine adjustment of the prism angle.

Note on laser operation: before you do anything else

- if the MIRA is not locking, first make sure that the chillers are operating. It might sound trivial but can result in quite nasty situations, where you misalign the laser although everything would actually work just fine. Even if the chillers seem to be running it is a good idea to check if water is actually pumped through the pipes. The flow of water through the MIRA cooling pipes should be ~ 0.8 liters per minute or more.

- if the Synchrolock does not lock, again check the chillers and whether there are any CW components in the laser output.

B.1.2. Prism Alignment

An alignment of the prisms should *not* be necessary under usual conditions. Whether it is advisable to adjust *BP*2 can be easily determined by a method given below. In that case the alignment of *BP*1 should be checked and optimized before adjusting *BP*2.

Aligning *BP*1

1. translate *BP*1 such that it refracts part of the CW laser beam from the auxiliary cavity into the main cavity. This part should be large enough to work with but small enough as not to disrupt the lasing in the auxiliary cavity.

2. place a mirror in front of $M6$ to redirect the beam coming from $M6$ out of the cavity onto a wall or similar (see fig. B.1). The greater the distance the more accurate will the adjustment of the angle of $BP1$ be.

3. carefully loosen the screw fastening $BP1$ and rotate the prism while observing the spot of the laser on the wall. If you move it in the correct direction, the spot should wander, then halt and then change the direction of its movement.

4. rotate the prism to the position where the movement of the spot changes direction. This is the point, where the deviation angle of the laser beam is at its minimum. The prism should be fastened at this point.

Aligning $BP2$

The alignment of $BP2$ is not straight forward, and the description in the MIRA handbook is ambiguous. How to do it correctly has been the subject of numerous discussions with laser technicians from Coherent Inc. - the following procedure has emerged. The first of these steps (up to and including step 5) can be followed to determine whether the $BP2$ prism needs alignment at all. It should be noted that Coherent technicians have mentioned in personal communication that in the case of High-Power MIRAs it is much more difficult to optimize the alignment of prism $BP2$. For these lasers the following procedure, which is employed to indicate the necessity of the alignment of $BP2$, will always indicate a slight misalignment.
Before you start adjusting $BP2$ you might want to check the alignment of $BP1$ (see above).

1. the main cavity should be well adjusted (see previous subsection) and should produce maximum CW output.

2. monitor the laser output with a broadband spectrometer (we used an Ocean Optics USB2000 with a range from 731 nm to 857 nm).

3. reduce the slit width to reduce the CW output power to $\sim 50\%$.

4. turn the BRF clockwise and watch he CW peak in the spectrometer. While you turn the prism the peak will move to shorter wavelengths, disappear and reemerge at a higher wavelength from where it will move to shorter wavelengths again. At some point the direction of the movement of the peak will reverse, i.e. it will move to higher wavelengths. The point where this change occurs indicates the desired position of the BRF.

5. rotate the horizontal screw of $M7$ clockwise and counter clockwise. If $BP2$ is misaligned, the CW peak in the spectrometer will move to shorter wavelengths for one of the directions you rotate $M7$ in. If $BP2$ is not misaligned, tilting of $M7$ will rapidly cause the cavity to stop lasing while the peak in the spectrometer moves to higher wavelengths no matter the direction of rotation of $M7$.

6. if *BP2* is misaligned, carefully loosen the screw on its platform such that the platform still offers a little resistance against rotations.

7. turn *M7* slightly in the direction where the peak moves to higher wavelengths.

8. the prism is rotated best by tapping with a screwdriver on the metal arm of the prism platform. Rotate the platform *very carefully* in the direction opposite to the one you just rotated *M7* in.

9. when the prism is rotated, the wavelength should change to shorter wavelengths. If at some point the change of the wavelength changes its direction, *BP2* will be correctly aligned. If this does not occur before the cavity stops lasing, repeat steps 5 to 9.

B.2. How to determine the correct orientation of a BBO for SPDC

The principal alignment of the optical axis of the crystal is done in the usual way by rotating it such that the polarization of horizontally or vertically polarized photons is not changed when they pass the crystal. But this method only tells us that the optical axis is either in a plane parallel to the optical table or perpendicular to it.

To distinguish between these two cases the crystal is placed at the position of the UV beam's waist. Then the crystal is rotated into four positions: the one, which has been determined above, and in 90° steps relative to that position. At each of these positions try to observe the down-converted light with the naked eye (i.e. naked apart from laser goggles). If SPDC occurs, it will be possible to make the following observation: keep an eye the on spot, where the UV beam passes through the SPDC crystal, and move your head sideways or upwards. The spot will appear to change its color depending on the angle of your eyes relative to the UV beam (mostly it will appear green but also red and yellow). Only when the optical axis is in a plane perpendicular to the optical table, the phase-matching conditions will allow for SPDC.

Even when the occurrence of SPDC is established we only know the plane, which the optical axis is in and not its exact orientation. Unless the angle Ψ_{OA} between the optical axis and the pump beam is $\pi/2$, there are two possible orientations left (see fig. B.2). They correspond to a flip of the optical axis with respect to the plane defined by the optical table. The idler and signal SPDC cones (see fig. 4.3) will be flipped as well, but that means that these two orientations of the optical axis can be discerned by observing the polarization of the SPDC light. For example, the polarization of the uppermost of the two cones will be vertical or horizontal depending on the orientation of the optical axis. As long as we are only interested in the photons on the intersection lines of the cones, this difference does not matter.
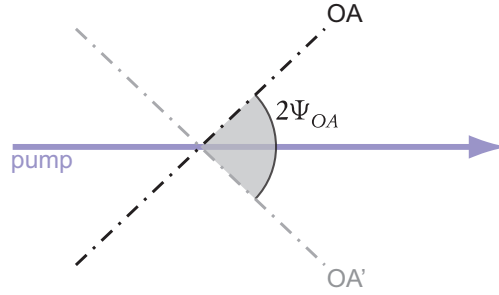
Figure B.2.: If $\Psi_{OA} \neq \pi/2$, the occurrence of SPDC only tells us that the optical axis is in one of the two indicated positions relative to the pump beam in a plane vertical to the optical table.

C. Beam profile measurement and correction

All profile data was recorded using a Coherent LaserCam II 1/2 (i.e. its sensor area has a diameter of 1/2 inch) in combination with Coherent's Analog BeamView Analyzer v2.4. For each profile two separate files were stored. One file contained all the recorded data in a BeamView specific format with the extension "ATS". A second file was exported from BeamView and contained all relevant data in text format. The content of these text files were not arranged in a straight forward way and it needed some processing before retrieving data from it. At the time I wrote the program to extract the profile data I was unaware of the advantages and possibilities of PERL. I used Visual Basic for Applications, which comes along with Microsoft's Excel. The code is given in the file "getCCDdata-modul1.bas" on the CD-ROM, which accompanies this thesis. To use the code the functions must be included in the module of an MS-Excel sheet. This sheet has to be placed in a parent folder of the CCD data (see below).

By inserting the correct paths and by adjusting the global variables the script can easily be adopted to deal with new data. It scans through all sub-directories and looks for data files exported by Coherent's BeamView Analyzer. These files are imported into Excel as spread sheets and the relevant data is extracted. The data obtained is stored in files called "shg_waist_math.txt" in the respective directories. An example content of that type of file is shown in table C.1.

These results were evaluated by a *Mathematica* notebook, which can also be found on the CD-ROM ("waistanalyse.m"). It varies the parameters of a two-dimensional Gaussian beam to optimally fit the recorded data. We will only discuss the optimization of the profile of the UV beam on the *slave* side. This beam was astigmatic of type 2 (see subsection 6.2.2 on page 109). Nevertheless, we assumed that the waists along the x and the y axes were at the same position within the SHG crystal. The two-dimensional Gaussian beam that we fitted to the data, was described by three parameters: the distance of the CCD-camera to the position of the waists, and the size of the two waists along the x and y axes. We measured the distance of the CCD-chip to the crystal up to a few millimeters of accuracy using a tape measure. This value could be used to check whether the results produced by the *Mathematica* routines were valid. Sometimes the routines got caught in local minima but usually that yielded unrealistic results for the distance of the CCD camera.

A call to the function EvalCCDData[] will scan through all sub-directories of the folder, which is defined by the variables in the beginning of the notebook. The function will try to fit a two-dimensional Gaussian beam to every "shg_waist_math.txt" data file found in these sub

w_x [mm]	σ_{w_x} [mm]	w_y [mm]	σ_{w_y} [mm]	Angle [rad]	CCD-Pos [mm]
4.07	0.005	1.721	0.003	0.0	0.0
4.132	0.013	1.753	0.011	0.0	5.0
4.2	0.005	1.8	0.002	0.0	10.0
4.248	0.005	1.825	0.002	0.0	15.0
4.287	0.006	1.845	0.003	0.0	20.0
4.338	0.009	1.888	0.007	0.0	25.0

Table C.1.: Example for an shg_waist_math.txt file. These files are used by our Visual Basic script to store collected data. $w_{x,y}$ denotes the waists along the x and y axis, $\sigma_{w_{x,y}}$ their respective r.m.s. errors. The angle was set to 0° on purpose because it was constant anyway and does not concern us here.

Scan	d_{CCD} [cm]	$\sigma_{d_{CCD}}$ [cm]	w_x [μm]	σ_{w_x} [μm]	w_y [μm]	σ_{w_y} [μm]
1	20.22	0.37	14.34	0.25	36.33	0.85
2	26.22	2.13	17.92	1.45	45.77	3.88
3	28.38	4.11	19.62	2.88	49.49	7.79
4	20.62	3.29	14.07	2.32	36.4	6.49
5	33.9	0.93	20.58	0.53	48.23	1.09
6	30.5	2.03	18.75	1.29	43.05	3.28

Table C.2.: Averages and standard deviations for the fits to data from multiple scans. d_{CCD} is the average of the calculated distances of the CCD chip from the waist of the UV beam, $\sigma_{d_{CCD}}$ is its error. $w_{x,y}$ are the averages of the calculated waists of the UV beam along the x and y axis, $\sigma_{w_{x,y}}$ are the corresponding standard deviations.

folders. For the data given in table C.1 the function EvalCCDData[] yielded (rounded to 6 digits):

Listing C.1: Example of a result of EvalCCDData

```
1  {0.360129, (* distance of CCD chip from waist *)
2   0.003929, 0.021449, (* Rayleigh lengths along x and y axis *)
3   0.000022, 0.000052, (* waists along x and y axis *)
4   23.922362, 5.304751*10^(-10) (* calculation time and precision *)}
```

This tells us that the CCD chip was supposed to be 36 cm distant from the waist of the UV beam. The beam itself was calculated to have a 22 μm waist along the x axis and a 52 μm waist along the y axis.

In order to obtain significant results fits had to be made to the data of multiple profile measurements. Table C.2 shows data recorded in 6 scans. For each scan we present the average and the standard deviation of the results of several profile measurements.

The measurements were performed under varying circumstances. During the scans 1 to 4 the CCD was moved in steps of 2 mm. Later we improved the setup (see fig. 6.4 on page 110)

in order to allow larger step sizes. In scans 5 and 6 the CCD could be moved in steps of 5 mm, i.e. the last two scans covered a greater distance and their results should be more accurate. Still, the errors are quite large (close to 10 % in the last run). Our goal was only to approximately calculate the positions of our cylindrical lenses in order to correct the beam profile as well as possible. For this purpose, the results were sufficiently accurate.

Listing C.2: Code to correct a beam profile with two cylindrical lenses.

```
1  (* first , we include several definitions necessary to deal with gaussian
2     beams , a Mathematica package we can use for displaying these beams with
3     function defined in gauss_propagation_defs *)
4  <<generalgaussdefs
5  <<Graphics 'SurfaceOfRevolution '
6  <<gausspropagationdefs
7
8  (* some constants *)
9  lam:=394.25 10^(-9)
10 meink:=2 \[Pi]/lam
11
12 (* additional definitions for gaussian optics *)
13 w0[zR_]:=Sqrt[zR lam/\[Pi]]
14 z0[waist_]:=waist^2 \[Pi]/lam
15 w[z_ ,zRay_]:=w0[zRay] Sqrt[1+(z/zRay)^2]
16
17 (* here , we turn off some annoying warnings *)
18 Off[FindMinimum::"precw"]
19 Off[FindMinimum::"cvmit"]
20 Off[FindMinimum::"reged"]
21 Off[FindMinimum::"lstol"]
22 Off[FindMinimum::"sdprec"]
23 Off[Part::"pspec"]
24 Off[General::"stop"]
25 Off[Dot::"dotsh"]
26 Off[FindMinimum::"sszero"]
27
28 (* this is the function , which takes a given gaussian beam ( described by the
29    complex matrix Q) and tries to correct it into beam , which has equally
30    sized waists at the same position , which should be between the minium
31    distance minD and the maximum distance maxD. The correction is performed
32    using two cylindrical lenses , one focussing in the x axis , the second
33    focussing in the y axis. Their focal lengths are given by fx and fy.*)
34 getItRound[fx_ ,fy_ ,Q_ ,minD_ ,maxD_ ,iterationen_ ,wprec_ ,maxits_]:=
35   Module[{gLi ,gLiti ,rnumsxx ,rnumsyx ,xx ,yx ,gLtime ,resTable ,resMin ,u ,minPos ,
36          tmpQ},
37     gLtime=TimeUsed[];
38     rnumsxx={};
39     rnumsyx={};
40     For[gLi=1,gLi ≤ iterationen ,gLi++,
41       rnumsxx=Append[rnumsxx , Random[]∗(maxD−minD)+minD];
42       rnumsyx=Append[rnumsyx , Random[]∗(maxD−minD)+minD];
43     ];
44     resTable=Table[
45       FindMinimum[
46         tmpQ=optics[Q, zylLenseX[xx,fx ,0.], zylLenseY[yx ,fy ,0.]];
47         Abs[Im[tmpQ[[1,1]]]−Im[tmpQ[[2,2]]]]^2 +
48         Abs[Re[tmpQ[[1,1]]]−Re[tmpQ[[2,2]]]]^2 ,
49         { {xx ,rnumsxx[[gLiti]],minD ,maxD},
50           {yx ,rnumsyx[[gLiti]],minD ,maxD}},
51         WorkingPrecision → wprec , MaxIterations → maxits
52       ],{gLiti ,1 ,iterationen}
53     ];
```

```
54        resMin=NMinimize[
55            {
56                resTable[[u,1]],
57                u\[Element]Integers&&1 ≤ u ≤ iterationen
58            },{u},Method → "DifferentialEvolution"
59        ];
60      minPos = resMin[[2,1,2]];
61      { resTable[[minPos]][[2,1,2]], resTable[[minPos]][[2,2,2]],
62        TimeUsed[]−gLtime,
63        resTable[[minPos]][[1]]
64      }
65    ]
66
67  (* the results gained in the various measurements for the waists are
68      collected into a matrix *):
69  measuredwaists = { {14.34,36.33},
70                     {17.92,45.77},
71                     {19.62,49.49},
72                     {14.07,36.4},
73                     {20.58,48.23},
74                     {18.75,43.05} }
75
76  (* for each of the results, a complex 2x2 matrix Q is defined to describe
77      the corresponding gaussian beam. These will then be used as parameter
78      Q in getItRound *)
79  SHGQs = Module[{i},
80      Table[
81          allQ[0.0,z0[measuredwaists[[i,1]]*10^(−6)],0.0,
82              z0[measuredwaists[[i,2]]*10^(−6)],0.0,0.0],{i,1,6}
83      ]
84  ]
```

The function $_{getItRound}$ of the notebook "profilecorrection.m" (see code listing C.2) can be used to optimize the positions of two cylindrical lenses to correct the UV-beam's profile. An example for the results (for the data of scan number 5) produced by $_{getItRound}$ is given in code listing C.3. It demonstrates the use of the function's parameters as well as the format of the result it generates. The return value is an array of four numbers, the first two of which are the calculated optimal distances of the two cylindrical lenses used to correct the beam profile. The third value represents the time needed for the calculation in seconds and the fourth value is the minimum value achieved for the function, which is minimized. That function is a sum of the absolute squares of the deviations of the waist sizes and positions along the x and y axes of the profile. An optimal result would yield a return value of 0 as the last value in the array. The optimization in the example is performed for two cylindrical lenses, one focusing in the x axis, the other in the y axis. The focal lengths are 10 cm and 15 cm, respectively, and positions of the lenses are bound to be between 10 cm and 120 cm after the SHG crystal. With the last three parameters of $_{getItRound}$ we can directly influence the optimization. We tell the function to generate 100 random initial positions for both cylindrical lenses, which *Mathematica's* $_{FindMinimum}$ optimization routine should start from. The last two parameters define the parameters $_{WorkingPrecision}$ and $_{MaxIterations}$ for $_{FindMinimum}$ to be 30 and 1000, respectively.

Listing C.3: Results of getItRound for the data of scan number 5.

```
1  (* the result from the 24th corresponds to the 5th entry in the list SHGQs *)
```

Scan	d_x [cm]	d_y [cm]	d_w [cm]	w [μm]
1	12.43	24.21	63.32	58.76
2	12.46	24.32	62.72	72.53
3	12.44	24.12	62.72	79.63
4	12.47	24.53	62.85	56.94
5	12.31	22.99	64.71	88.19
6	12.26	22.69	65.91	82.49

Table C.3.: Results of the optimization of the positions of two orthogonally oriented cylindrical lenses to correct the UV-beam's profile on the *slave* side. The calculation is based on the data given in table C.2. $d_{x,y}$ denotes the optimal positions of the cylindrical lenses for the x and y axes. All optimizations yielded a rotation-symmetric Gaussian profile with a waist w. With d_w we denote the distance of the waist from the SHG crystal.

```
2   getItRound[0.1,0.15,SHGQs[[5]],0.1,1.2,100,30,1000]
3
4   (* this function call yields the result *)
5   {0.12309177466096843688963148748 0,0.229915592819275591095688106349,49.8154,0}
```

The lens positions, which we obtained via getItRound for the data given in table C.2 are presented in table C.3. That table also contains the parameters, which define the Gaussian beams after passing trough the two cylindrical lenses.

From these results we can infer that the optimal position of the "x lens" is well defined with an uncertainty on the order of 2 mm. The uncertainty in the position of the y lens is higher due to its greater focal length. As we mentioned above, the results for the the last two scans are expected to be the most accurate. From these we can estimate that the the x lens should be placed about 12.3 cm and the y lens about 22.7 cm to 23 cm after the SHG crystal. The waist of the corrected UV beam was estimated to be slightly larger than 80 μm and to be located about 65 cm after the SHG crystal.

In the actual experiment we initially placed the cylindrical lenses at the calculated distances from the SHG crystal. Then we checked if the focus of the corrected beam was approximately at the expected position [1]. To optimize the circularity of the beam profile we set up the CCD camera in order to be able to observe the beam at two positions separated by about 30 cm. To assure the circularity of the UV beam we did not have to fully characterize it. We only had to optimize the circularity of the beam at those two distant positions. A high circularity at two distant spots that are not placed symmetrically around the waist assures the overall circularity of the beam profile. By walking the positions of the cylindrical lenses relative to another a circularity of more than 98 % could be achieved at both positions.

---

[1] It was.

D. Numerical analysis of SPDC emission

SPDC rapidly becomes inefficient for higher photon numbers because it is a spontaneous process, and because of limited coupling and detection efficiencies. Let us denote the probability for n pairs being emitted as p_n. The relation between p_n and p_1 is given by [1] p_1^n. The probability for coupling and detecting all of these photons can roughly be approximated by $(\eta_D \eta_c)^{2n}$ (see also subsection 4.3.2), where η_D denotes the detection efficiency and η_c the coupling efficiency. The overall probability

$$P \sim \left(p_1 \eta_D^2 \eta_c^2 \right)^n \tag{D.1}$$

for detecting n photon pairs decreases exponentially with n.

This puts a practical limit to the number of photons, which can be efficiently produced with an SPDC source. But even for low photon numbers (up to 4) it is important to optimize p, η_D and η_c, where possible, to reduce the scan times. This was paramount for the experiment at hand, where the relative time delay of the lasers was subject to long-term drifts (see subsection 7.1.2 on page 141).

To increase η_D it would be necessary to use better detectors. The only possibility to do that would have been to use highly-efficient super-conducting detectors. This step might be taken in the future.

Another way to increase the efficiency of our SPDC source is to increase the production probability p. The optimization of the UV pump has been discussed in earlier sections (see 6.2 and appendix C). A further possibility, which was not investigated in the course of this experiment, would be to use a different SPDC setup altogether (e.g. type I [75] or degenerate type-II SPDC [118]). We did not take this course because of our good experiences with type-II setups and because the purpose of the present work has not been to design a novel SPDC source.

The way we tried to go was to optimize the coupling efficiency. Our efforts in this direction during the design of our setup were futile because the optimization routines, which we will develop here, were still faulty at that time. While writing this thesis we managed to significantly improve these optimization routines. We are confident that, with a little further investigation, it will be possible to determine the optima of all parameters involved in the type of SPDC setup that we discuss here.

---

[1]This relation is only an approximation, see the paragraph on HOM interference without trigger photons in subsection 2.3.4.

The parameters to tune in order to achieve a high coupling efficiency are the waist size of the pump beam and the waist size of the modes coupled into the single-mode fibers. To this end we will simulate the SPDC emission in order to estimate the waist of the generated light. For that simulation we will solve the SPDC phase-matching conditions in the first section of this chapter. The simulation itself will be the content of the second section. In the third section will deal with the optimization of the UV beam waist and the thickness of the SPDC crystal.

D.1. Phase-matching in SPDC

In spontaneous parametric down-conversion the directions of emission are determined by the *phase-matching conditions*:

$$\mathfrak{k}_p \approx \mathfrak{k}_s + \mathfrak{k}_i \tag{D.2}$$

$$\omega_p = \omega_s + \omega_i. \tag{D.3}$$

$\mathfrak{k}_{p,s,i}$ are the wave vectors for the pump beam and the signal and idler photons, respectively. Similarly, $\omega_{p,s,i}$ denote the various angular frequencies. The first equation results from the superposition of the contributions of the various components of the pump field and the generated fields within the crystal:

$$\int_V d^3x \, e^{\iota(\mathfrak{k}_p - \mathfrak{k}_s - \mathfrak{k}_i)\cdot\mathfrak{r}}, \tag{D.4}$$

where V is the volume of the crystal. Equation (D.3) represents energy conservation during the conversion of a pump photon into the photon pair emitted.

In the beginning we will assume the crystal to be infinitely large, i.e. equation (D.2) will be exact. We will also assume that the pump is a CW beam with infinite waist and that our detectors register only the degenerate wavelength, i.e. $\omega \equiv \omega_s = \omega_i = \frac{1}{2}\omega_p$. Every deviation from these very strict assumptions will be taken into account later on.

D.1.1. Definitions and principles

Large parts of the work presented here are based on the work of G. Weihs [129]. All relevant code passages can be found on the accompanying CD-ROM (see appendix E). We will concentrate on the final *Scilab* version of our program (earlier versions were written in *Mathematica*).

Several coordinate systems are employed throughout the calculations. The original one is the coordinate system defined by the crystal faces. Its unit vectors shall be denoted by
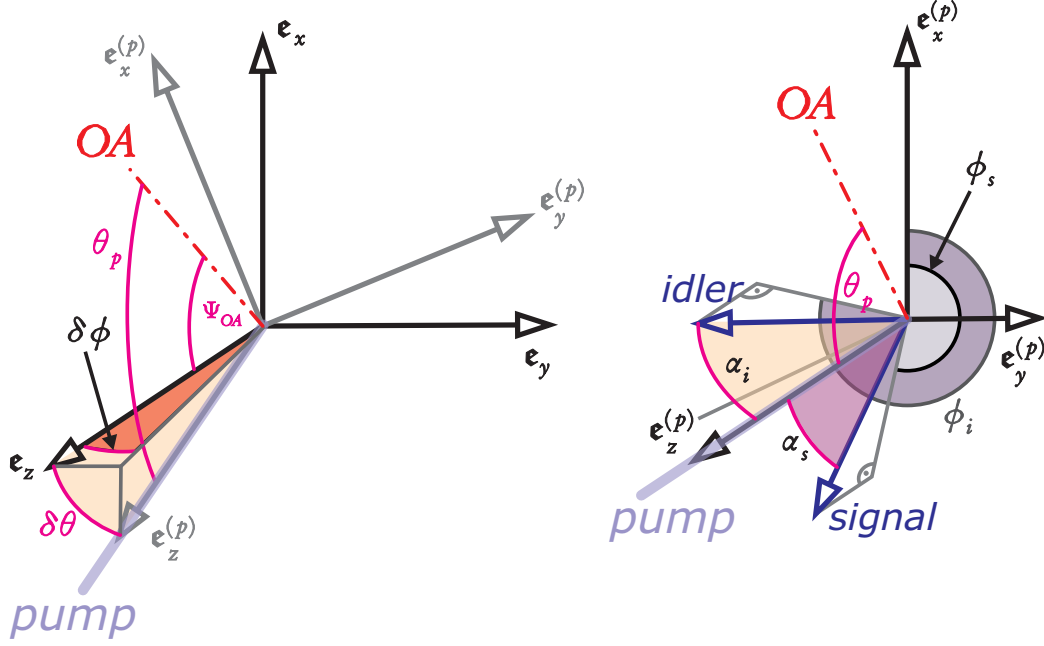
Figure D.1.: (left) Coordinate systems and their relative angles as they were used for phase matching. The pump coordinate system is rotated relative to the crystal's coordinate system by angles $\delta\theta$ and $\delta\phi$. We assumed the optical axis (*OA*) to be in the xz plane. Its cut angle is Ψ_{OA} and it forms an angle θ_p with the pump beam. **(right)** the directions of emission of the signal and the idler photons are each described by two angles. $\alpha_{s,i}$ denotes the angle between signal and pump and between idler and pump, respectively. $\phi_{s,i}$ is the angle between $\mathbf{e}_x^{(p)}$ and the projection of the wave vector of the signal (or idler) photon on the xy plane of the pump coordinate system.

$\mathbf{e}_{x,y,z}$. This system is needed to calculate the refraction of the signal and idler photons [2] at the crystal faces. The actual phase matching is done in two other coordinate systems. First, the system of the axis of the idler cone. Second, in a coordinate system defined by the pump beam. The unit vectors of the pump coordinate system are $\mathbf{e}^{(p)}_{x,y,z}$. For the definition of the pump coordinate system relative to the crystal coordinate system see the left part of figure D.1. This figure also points out the meaning of several angles, which we are going to use throughout this chapter: $\delta\phi$, $\delta\theta$, Ψ_{OA} and θ_p. On the right hand side of the same figure, the angles $\alpha_{i,s}$ and $\phi_{i,s}$ are illustrated. These will be employed to describe the orientation of the signal and idler photons relative to the pump coordinate system.

Now, we will describe the coordinate system that is defined by the axis of the idler cone. Suppose the direction of the axis of the cone is described by spherical coordinates θ and ϕ in the pump coordinate system. In the coordinate system, which we want to define, this axis serves as the z-axis. The transformation from the pump to the idler system can be decomposed in two rotations. First, a rotation by the angle ϕ around $\mathbf{e}^{(p)}_z$. Second, a rotation by the angle $-\theta$ around the new y-axis. The composition of these two rotations yields:

$$
R = \begin{pmatrix}
\cos\phi\cos\theta & \sin\phi\cos\theta & -\sin\theta \\
-\sin\phi & \cos\phi & 0 \\
\cos\phi\sin\theta & \sin\phi\sin\theta & \cos\theta
\end{pmatrix}.
\tag{D.5}
$$

Coordinates in the pump basis can be transformed into coordinates in the crystal basis by means of the transformation matrix:

$$
T = \begin{pmatrix}
\dfrac{\sin\Psi_{OA} - \cos\theta_p\cos\delta\phi\sin\delta\theta}{\sin\theta_p} & \dfrac{\sin\delta\phi\sin\delta\theta\cos\Psi_{OA}}{\sin\theta_p} & \cos\delta\phi\sin\delta\theta \\
-\dfrac{\cos\theta_p\sin\delta\phi\sin\delta\theta}{\sin\theta_p} & \dfrac{\sin\Psi_{OA}\cos\theta_p - \cos\delta\phi\sin\delta\theta}{\cos\Psi_{OA}\sin\theta_p} & \sin\delta\phi\sin\delta\theta \\
\dfrac{\cos\Psi_{OA} - \cos\theta_p\cos\delta\theta}{\sin\theta_p} & -\dfrac{\sin\delta\phi\sin\delta\theta\sin\Psi_{OA}}{\sin\theta_p} & \cos\delta\theta
\end{pmatrix}.
\tag{D.6}
$$

D.1.2. Parametrizing and solving the phase-matching conditions

Equation (D.2) represents a relation between wave vectors of photons, which have different wavelengths and polarizations. Their refractive indices within the SPDC crystal can be

---

[2]It is important to note that we use a different notation here than in the main part. There we used "idler" to denote the ordinarily polarized photons. Here, the role of signal and idler are exchanged. The naming convention is in general arbitrary, and this small inconsistency has not been motivation enough to correct the names of variables and functions in several thousand lines of code.

calculated by virtue of the Sellmeier equations for BBO crystals [41]:

$$n_o(\lambda) = \sqrt{2.7359 + \frac{0.01878}{\lambda^2 - 0.01822} - 0.01354\,\lambda^2} \tag{D.7}$$

$$n_e(\lambda) = \sqrt{2.3753 + \frac{0.01224}{\lambda^2 - 0.01667} - 0.01516\,\lambda^2} \tag{D.8}$$

$$n_e(\lambda, \theta) = \frac{n_e(\lambda)}{\sqrt{1 + \left(\left(\frac{n_e(\lambda)}{n_o(\lambda)}\right)^2 - 1\right)\mathrm{Cos}^2(\theta)}}, \tag{D.9}$$

where n_o is the ordinary, and n_e is the extraordinary refraction index. λ has to be entered in μm. θ is the angle between the wave vector of the extraordinarily polarized photon and the optical axis.

Now, we rewrite and square equ. (D.2) to give (see also [129]):

$$\Delta\Phi\left(\alpha_i, \phi_i\right) = 0, \tag{D.10}$$

where

$$\Delta\Phi\left(\alpha_i, \phi_i\right) \equiv k_p^2\left(\theta_p\right) + k_i^2\left(\theta_i\left(\alpha_i, \phi_i\right)\right) - k_s^2 - 2\,k_i\left(\theta_i\left(\alpha_i, \phi_i\right)\right)\,k_p\left(\theta_p\right)\cos\alpha_i. \tag{D.11}$$

The *phase-mismatch function* $\Delta\Phi$ will only be zero if the phase-matching condition is fulfilled. $k_{p,s,i}$ are the moduli of $\mathfrak{k}_{p,s,i}$. We denoted $\Delta\Phi$ as a function of α_i and ϕ_i because these are the only variables in the equation. θ_p and the various (implicitly involved) frequencies will be treated as constants. θ_i can be written as a function of α_i and ϕ_i, which is implicitly defined by the relation:

$$\cos\theta_i = \sin\theta_p\,\sin\alpha_i\,\cos\phi_i + \cos\theta_p\,\cos\alpha_i. \tag{D.12}$$

If the crystal is cut correctly, equation (D.10) will yield a unique solution for α_i for any $\phi_i \in [0, 2\pi]$, i.e. we can express α_i as a function of ϕ_i. The values of this function can be calculated numerically by solving equ. D.10. This is the purpose of the function loesungAX, see code listing D.1. The solutions are calculated in the coordinate system of the axis of the idler cone.

Listing D.1: *Scilab* code to calculate idler emission angles.

```
1  function [l,ax,axangles,coneangle,idthax]=loesungAX(li,lp,axphi,dtp,dpp,psiOA);
2  // calculates the "theta" angles of the idler in the idler axis' coord.
3  // system as a function of the "phi" angles axphi
4  costp=cosThetaP(dtp,dpp,psiOA);
5  tp=acos(costp);
6  sintp=sqrt(1-costp^2);
7  cosdtp=cos(dtp);
8  sindtp=sin(dtp);
9  cosdpp=cos(dpp);
```

```
10    sindpp=sin(dpp);
11    cospsiOA=cos(psiOA);
12    sinpsiOA=sin(psiOA);
13    kp0=2*pi*bboNet(lp,tp)/lp;
14
15    // searching start values
16    thi=(0:0.01:2*tp)';
17    mi=phaseMismatch(thi,li,lp,kp0,tp);
18    ind=find(diff(sign(mi)));
19
20    // procede only when two solutions have been found, i.e. if there is a cone
21    if max(size(ind))==2
22        // calculates two solutions on the x-axis
23        th=fzerof('phaseMismatch',thi(ind),thi(ind+1),1e-8,200,li,lp,kp0,psiOA);
24        // the mean of these two solutions defines the cone axis in pump coords
25        tho=mean(th);
26        alo=abs(tp-tho);
27        pho=pi*((tp-tho)>0);
28
29        // now we calculate the phase-matching solutions for all given values of
30        // axphi. That means, for each axphi we find the root of phaseMismatchAC
31        // by using G. Weihs' function fzerof, which uses the Regula Falsi
32        // this calculation is performed in the cone axis' coord. system
33        idthax=fzerof('phaseMismatchAC',zeros(axphi),...
34                      0.75*diff(th)*ones(axphi),...
35                      1e-6,200,axphi,li,lp,kp0,tp,alo,0);
36        ax=unitV(alo,0); // axis of idler cone in pump coords.
37        axangles=[alo, 0]; // angles of axis of idler cone in pump coords.
38        coneangle=th(1)-alo; // approximate opening angle of idler cone
39        l=1; // indicates that phasematching was achieved
40    else
41        disp('Kein Typ-II Phasematching moeglich!');
42        l=0; // indicates that no phasematching was achieved
43        ax=[0,0,0];
44        axangles=[0,0];
45        coneangle=0;
46        idthax=zeros(axphi);
47    end
48 endfunction;
```

Up to this point our work is largely equivalent to the *Matlab* simulation of G. Weihs [129]. Our first significant extension will be to take into account the spread of the SPDC photons due to finite crystal thickness. We base our method on the work of M. H. Rubin in [104]. He calculates the natural width of SPDC rings due to finite crystal length to be approximately given by:

$$\delta \mathfrak{k}_T = \frac{4\pi}{L \, |N|}, \tag{D.13}$$

where $\mathfrak{k}_T$ denotes the transverse component of the idler's wave vector and N is used to calculate the offset $|\overline{p}|$ of the SPDC rings from the pump beam. It is given by:

$$N = \frac{1}{2} n_e^2(\omega_i, \Psi_{OA}) \left(\frac{1}{n_o^2(\omega_i)} - \frac{1}{n_e^2(\omega_i)} \right) \sin\left(2\Psi_{OA}\right). \tag{D.14}$$

We include this additional broadening of the emission due to finite crystal thickness when we transform the solution for the idler photons to the pump coordinate system. This is

done by our function addImperfectPM. To this end we take the angle ϑ of the idler relative to the axis of the idler cone and add or subtract a variation $\delta\vartheta$. Addition and subtraction will yield two different solutions, which will be taken into account later on when we calculate the spread of the SPDC photons. The variation $\delta\vartheta$ is directly related to the natural width of the rings defined in equ. D.13. That equation is derived from the full width of the sinc^2 function (see [104]):

$$\operatorname{sinc}^2\left(x\,\frac{|N|\,L}{2}\right). \tag{D.15}$$

The r.m.s. width of the first maximum of this function is given by $\delta x = \frac{2\gamma}{L|N|}$, where $\gamma \sim$ 1.1939 is defined by sinc$^2\gamma = 1/\sqrt{e}$. We approximate the additional spread of the ring with:

$$\delta\vartheta = \frac{1}{2}\left[\arctan\left(\frac{k_x + \delta x}{2}\right) - \arctan\left(\frac{k_x - \delta x}{2}\right)\right], \tag{D.16}$$

where k_x is the x component of the idler photon's wave vector. After adding the effect of the finite crystal length, we change to the pump's coordinate system and use the phase-matching conditions for the transverse parts of the wave vectors to calculate the cone for the signal photons. In figure D.2 the results of these numerical calculations are used to draw the SPDC rings for the beam parameters in our experiment.

It is important to keep in mind that the presented method is based on perfect phase matching. For non-Fourier limited pulses or if the pump is focused to a degree, where it cannot be described as a Gaussian beam anymore, the method would have to be generalized. Because the pump pulses in our experiment were nearly perfectly Fourier limited and because the beam has not been focused too tightly, our approach should be accurate in this respect. Whether all our other approximations are sound, will have to be checked experimentally.

D.2. Simulating the spread of SPDC photons

In the previous section we used the phase-matching conditions to calculate and depict the emission angles of signal and idler photons. By repeating this procedure for different pump, crystal and idler parameters and by drawing the corresponding results it is possible to get an impression of the spread of the SPDC photons. An example for the change in the SPDC emission due to variations of the direction of the pump beam can be seen in figure D.3

The emission pattern of the SPDC photons will differ for each variation of the parameters. To simulate the spread of our SPDC photons we are going to apply all parameter variations in random combinations and record the various solutions. When all solutions have been calculated, we change into a coordinate system, where the z-axis lies in the center of all solutions for the idler photons. Then we calculate the minimum and maximum angles of the solutions with respect to that axis for all azimuth angles. The same we repeat for the solutions for the signal photons. In this way we get a distribution, which tightly envelopes
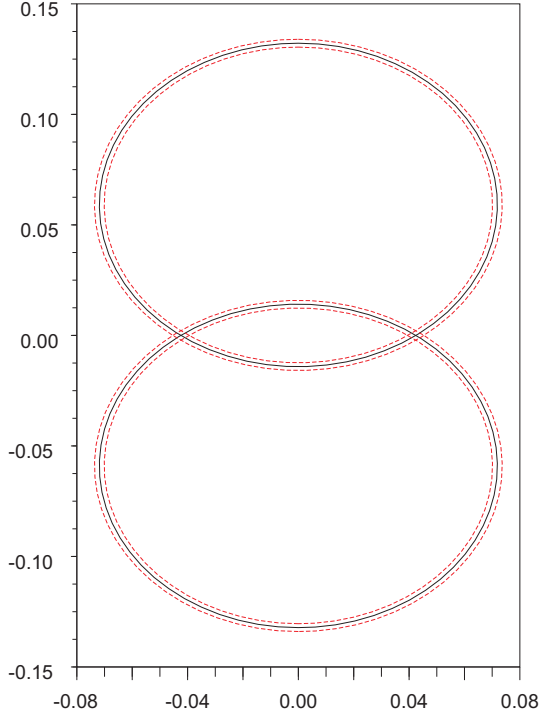
Figure D.2.: SPDC rings simulated by our *Scilab* routines. The black rings correspond to the signal and idler rings for a plane wave pumping an infinitely long crystal. The dashed red rings are corrections due to finite crystal thickness. In order to demonstrate this effect more clearly, we assumed only half the thickness, i.e. 1 mm, of the crystal used in our experiments.
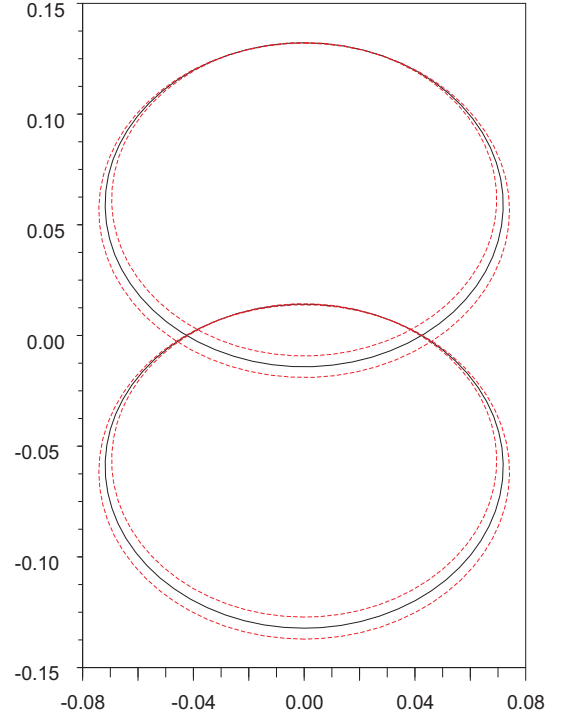
Figure D.3.: SPDC rings for three different directions of the pump beam. The black rings correspond to the standard configuration as in fig. D.2. The dashed red rings correspond to a plane-wave pump tilted vertically by ±0.09°. This demonstrates how we include focused pumping into our simulation. The tilting angles correspond to a pump that is vertically focused to a waist of 80 μm.
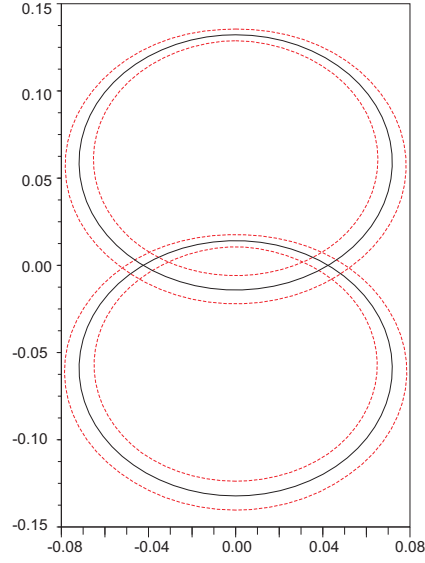
Figure D.4.: Envelope of all solutions for the various parameter variations. The cones for the unmodified parameters are drawn in a black, solid line. The inner and outer envelopes of the solutions for all possible combinations of parameter variations are drawn in red dashed lines. They signify the r.m.s. spread of the SPDC cones. We assumed a filter bandwidth of 3 nm FWHM.

all solutions, which we have calculated. This envelope describes the spread of the SPDC emission. It is calculated by the function calcConeSpread.

We are going to take into account the following parameters: the finite width of the detector response functions (defined by the narrow bandwidth filters), the bandwidth of the pump beam, the finite waist of the pump beam, and the finite length of the crystal. All these variations are applied in random combinations to the standard configuration (the black rings in figures D.2 and D.3). Each variation can either be not applied at all or it can be added or subtracted from the original beam parameter. There is one exception. Due to the finite waist of the pump beam the pump's wave vector is known only up to the divergence of the beam. We approximate this distribution by tilting the wave vector by the divergence angle and by rotating it around the original pump wave vector in discrete steps of $\frac{\pi}{4}$. There are 243 possible combinations of all these parameter variations. The envelope of all these solutions (see above) is depicted in figure D.4.
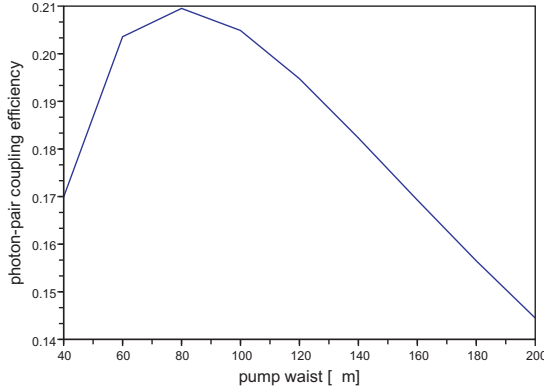
Figure D.5.: Efficiency for coupling an SPDC pair over varying UV-pump waist. The pump wavelength is 394.25 nm, the angle between pump and optical axis is 43.5°, the crystal thickness is 2 mm. In contrast to our experiments we assumed filters of 3 nm FWHM bandwidth for both photons.
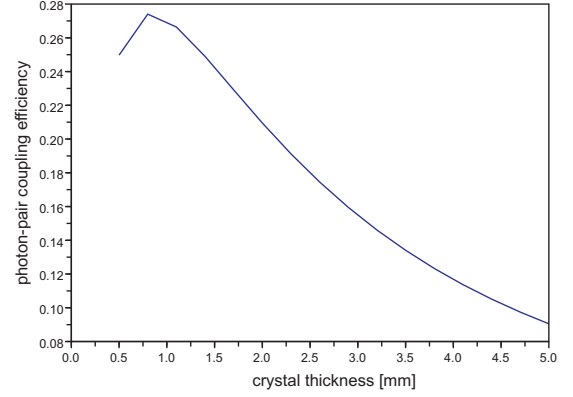
Figure D.6.: Efficiency for coupling an SPDC pair over varying thickness of the SPDC crystal. The pump wavelength is 394.25 nm, the angle between pump and optical axis is 43.5°, the pump waist is 80 μm. In contrast to our experiments we assumed filters of 3 nm FWHM bandwidth for both photons.

D.3. Optimizing the coupling of SPDC photons

The intersections of the envelope curves can be used to estimate the waists of the SPDC photons. A routine for optimizing the coupling efficiencies in an SPDC setup has to compare the waists of the coupling optics to the waists of the SPDC photons. It has to optimize the ratio between the coupled and the illuminated crystal volume, and it has to take into account that the overlap between signal and idler rings increases with the spread of the SPDC photons. Specifically, greater spread due to thinner crystals, can lead to higher photon fluxes [77]. On the other hand, the pair production probability scales with the square of the crystal thickness, while the relative-timing jitter due to GVM in the SPDC crystals (see section 5.2) increases with crystal thickness. The latter effect leads to low HOM-interference visibilities for thick crystals. The combination of all these effects should allow for calculating an optimal crystal length if the other parameters were kept fixed.

With our method it is possible estimate the maximum achievable coupling efficiencies over varying parameters (see figures D.5 and D.6). For these estimations we assumed that the optimal waist of the coupling optics should roughly be the waist of the UV pump plus half of the UV beam's transverse walk off within the crystal. By including the increased SPDC efficiency for thick crystals and by numerically calculating the overlap of the signal and idler SPDC cones we can give an estimate of the flux of coupled photon pairs for varying crystal thickness (see fig. D.7). These results should not be interpreted as being final. Specifically, the calculation of the overlap of the signal and idler SPDC rings, must still be optimized.
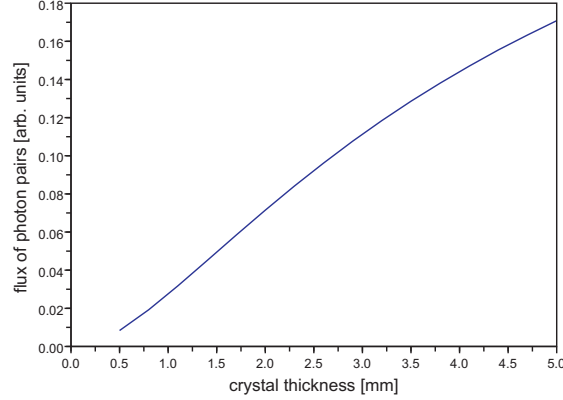
Figure D.7.: Estimation of the flux of photon pairs over varying thickness of the SPDC crystal. The plotted values are the product (1) of the overlap of the SPDC cones, (2) of the product of the overlap of the optimal coupling waist with the "circular SPDC waist", and (3) of the overlap of that "circular SPDC waist" with the actual waist of the SPDC photons. By "circular SPDC waist" we mean the waist of a rotation-symmetric two-dimensional Gaussian that is defined to have optimal overlap with one of the two intersection regions between signal and idler cones.

This could lead to slightly different results. It is also not sure that our assumption for the optimal coupling waist is correct. We set it equal to the radius of the illuminated crystal volume in order to couple as many photon pairs as possible.

Up to now, the numerical methods are rather slow, which makes it difficult to simultaneously optimize more than one parameter. We hope to improve the speed of the method in the future and to include an optimization routine for the entanglement visibility of the created SPDC pairs and the visibility in HOM-type interference.

E. Automation and control programs

In this chapter we will provide a short overview of the programs I included on the CD-ROM that accompanies this thesis. They can essentially be divided into four subcategories. The programs of these subcategories are stored on the CD-ROM in folders that correspond to the sections of this chapter.

E.1. LabView Programs

For both of our experiments I wrote a multitude of LabView programs to control the various devices involved and to read out measurement results. Derivatives of some of them are still in use by colleagues and many of them might prove useful for future experiments involving independent sources.

E.1.1. Interference of independent photons

Most of the programs that we present here are predecessors of the programs that we used in the second experiment. Yet, some of them are unique to this experiment because the scanning process was different and divided the scan times in blocks of shorter times to counterbalance long-time drifts. These programs can be found in the sub-folder *LabView HOMtypeInterference* on the CD-ROM.

The following programs have been written by me:

- **scan_dip_new.vi** - performs a dip scan over a predefined interval, i.e. it records four-fold coincidences over the relative time delay, which is varied in steps. This VI depends on all the other programs, which are described here.

- **count_in_stable_pieces.vi** - records detector events over a given time. This time is divided into shorter intervals. The result is the sum of all the counts recorded during the shorter intervals. Between the intervals the relative time delay of the lasers is adjusted to some predefined value.

- **find_delay.vi** - moves the linearly-graded neutral density filter in front of the Synchrolock fiber coupler on the *slave* side in order to adjust a predefined time delay between the lasers

- **fast_find_delay.vi** - in principle the same as "find_delay.vi" but this VI has its parameters predefined in order to allow for a fast adjustment of the time delay between the lasers

- **measure_CC.vi** - measures the FHWM and the position of the CC signal multiple times and returns the average and the standard deviation of the results. The time between the measurements can be adjusted.

- **getACsignal.vi** - communicates with the AC (autocorrelator). Used to retrieve the CC (cross correlation) signal.

- **average.vi** - calculates the average and the standard deviation of the entries of an array.

- **checkCC.vi** - calls "measure_CC.vi" to characterize the CC signal. If the signal does not meet certain criteria, this VI stops all scans running and sends an SMS notification.

- **check_bounds.vi** - checks whether a value is in between a given lower and higher bound. This is used to specify whether a motorized translation stage can be moved to a position without reaching its limit.

- **reinitAC.vi** - reinitializes the GPIB connection to the AC.

- **sendsms.pl** - a PERL script. It sends an SMS to one or more recipients. Uses the service "bulksms.net".

- **sendSMS.vi** - calls the PERL script "sendsms.pl" with appropriate parameters.

- **ACgpib.dll** - a DLL I wrote. It is used by all the VIs that need to communicate with the AC. It has been compiled from the source files **dllmain.c** and **dll.h**.

The following programs have not been written by me but have been included because my programs depend on them:

- **AC_display_average_and_fit.vi** - I modified this program such that it uses the *C++* libraries to read out the AC signal. Apart from these modifications this VI has been written by Bibiane Blauensteiner. It creates a graph of the AC signal and performs a Gaussian fit to the data.

- **Gaussian fits** - I included several VIs, which we use to fit Gaussians to the data gathered by the AC. These are "Gaussian Peak Fit.vi", "UtilityVIs.llb", "lvanlys.dll" and "Nonlinear Fit.llb".

- **ESP 300 library** - this VI library was written by Thomas Jennewein to control a Newport ESP300. Two of these motorized translation stages were used in our setup. One to move the linearly-graded neutral-density filter, the other to fine adjust the delay path for the *slave* beam on its way to the AC.

- **6602 library** - this VI library contains various functions connected to the PCI 6602 card from National Instruments. We used this card during our first experiment to record detector events. In my programs I only use one VI of this library: "Count 6602 with DIO".

E.1.2. Entanglement swapping

The main difference of the VIs presented here to the ones of the first experiment is that the four-folds are not measured over short time intervals. Because of the high stability of the synchronization during the second experiment, this was not necessary and the delay between the lasers did not have to be readjusted every minute but only after every measurement, which could take up to 16000 s. A minor difference is that I introduced some small changes to the $C++$ library that was used to communicate with the AC. Most of the VIs here are equivalent to the ones in the first experiment except that they use the new library. Their names indicate that because they have the same name as the old VIs but with an added extension "_new". The new library has the same extension to its name. I will not describe these VIs again but only VIs that we did not encounter during the first experiment. The VIs for the second experiment can be found in the sub-folder *LabView EntanglementSwapping* on the CD-ROM.

- **scan_dip_noblocks_new.vi** - scans all the specified counts over a stepwise varying relative time delay of the lasers. It is used for HOM-dip scans.

- **count_and_measure_CC_new.vi** - records the detector events over a specified time. At constant time intervals the CC position is measured in order to quantify the long-time drifts of the relative time delay of the lasers. It has been used for the dip scans as well as to record the data for the violation of the CHSH inequality. It is part of the VI library "counter_bibliothek_rk_08_06_2006.llb".

- **reloat_counter.vi** - resets the USB logic to its initial values. It is part of the VI library "counter_bibliothek_rk_08_06_2006.llb".

- **transform_coinc_pattern.vi** - the logic patterns, which define the coincidences to be recorded, are entered as two-dimensional Boolean arrays. This VI transforms them into one-dimensional integer (unsigned 32 bit) arrays before they are sent to the USB logic. It is part of the VI library "counter_bibliothek_rk_08_06_2006.llb".

- **Change Axis Parameters - changed by rainer.vi** - it is the same VI as in the "ESP 300 library" by Thomas Jennewein. I only added a connector for setting one of the parameters.

- **Detector.dll** and **Treiberinterface.dll** - the two .NET DLLs, which are needed to communicate with the USB logic. They must be imported into the Global Assembly Cache.

E.2. Programs to analyze and correct Gaussian beam profiles

In this section I present the programs I refer to in chapter C of the appendix. They can be found in the sub-folder *Gauss* on the CD-ROM.

- **getCCDdata-modul1.bas** - a Visual-Basic script, which must be inserted as a Macro module into an Excel file in order to operate correctly. It analyzes data exported by Coherent's BeamView and stores it in a format that can be read by our *Mathematica* routines.

- **generalgaussdefs** - this files contains a collection of definitions that are used by our *Mathematica* programs to deal with Gaussian beams in general.

- **gausspropagationdefs** - here, I have collected some useful definitions to calculate the propagation of Gaussian beams.

- **waistanalyse.m** - these functions can be employed to fit a two-dimensional Gaussian beam to data that has been recorded via CCD and prepared in an appropriate format by the Visual-Basic script.

- **profilecorrection.m** - given an astigmatic Gaussian beam, the functions that are defined here can be used to optimize the position of optical elements to make the profile rotation-symmetric.

E.3. *Scilab* code to simulate SPDC emission

The functions I refer to in chapter D of the appendix have all been written in *Scilab* and can be found in the file *SPDC loadfunctions.sci* on the CD-ROM.

E.4. Additional *Mathematica* programs

During my experiments and while writing this PhD thesis I wrote more than two hundred *Mathematica* programs. Many of them are outdated by now but some of them have been essential for parts of this thesis. I attached this selection of notebooks to render my results more easily traceable. Some of them might also be of use for others who work in this field. These additional notebooks can be found in the sub-folder *others* on the CD-ROM.

- **bellungleichungen.nb** - Here, I evaluate the data, which we collected in order to violate the CHSH inequality with the states resulting from entanglement swapping.

- **bellungleichung_fehlerrechnung.nb** - this notebook contains the functions, which I used to normalize our count rates, and it contains the functions necessary to calculate the errors of these normalized count rates. All of these functions are employed in "bellungleichungen.nb".

- **HOMinterference.nb** - This notebook contains all my analytical calculations that are used in section 2.3 and in chapter A. Here, I also calculate the jitter due to GVM in SPDC and combine it with the other jitters to calculate the expected visibilities and widths of the HOM dips in our experiments.

- **modelocking.nb** - in section 4.1 I gave a short overview over modelocking in a femtosecond laser. The figures in that section were generated by the code in this notebook.

- **PLL.nb** - in this notebook I simulate the process of a PLL locking a VCO to a given master signal. This simulation has been used to generate the capture transients in section 5.1.1.

- **pulsedcoupling.nb** - this notebook contains my analytical investigation of the coupling of SPDC photons. It builds the basis for the subsections 4.3.2 and 6.3.1

Bibliography

[1] G. Alber, T. Beth, M. Horodecki, P. Horodecki, R. Horodecki, M. Rötteler, H. Weinfurter, R. Werner, and A. Zeilinger. *Quantum Information*. Springer-Verlag, Berlin Heidelberg, 2001.

[2] J. Alda, S. Wang, and W. Bernabeu. Analytical expression for the complex radius of curvature tensor Q for generalized gaussian beams. *Opt. Comm.*, 80(5–6):350–352, 1991.

[3] J. A. Arnaud and H. Kogelnik. Gaussian Light Beams with General Astigmatism. *Appl. Opt.*, 8:1687–1693, 1969.

[4] A. Aspect, J. Dalibard, and G. Roger. Experimental Test of Bell's Inequalities Using Time-Varying Analyzers. *Phys. Rev. Lett.*, 49:1804–1807, 1982.

[5] A. Aspect, P. Grangier, and G. Roger. Experimental Tests of Realistic Local Theories via Bell's Theorem. *Phys. Rev. Lett.*, 47:460–463, 1981.

[6] A. Aspect, P. Grangier, and G. Roger. Experimental Realization of Einstein-Podolsky-Rosen-Bohm Gedankenexperiment: A New Violation of Bell's Inequalities. *Phys. Rev. Lett.*, 49:91–94, 1982.

[7] J. S. Bell. On the einstein-podolsky-rosen paradox. *Physics*, 1:195–200, 1964.

[8] J. S. Bell. On the Problem of Hidden Variables in Quantum Mechanics. *Rev. Mod. Phys.*, 38:447–452, 1966.

[9] J. S. Bell. Free Variables and Local Causality. *dialectica*, 39:103–106, 1985. Part of "An Exchange on Local Beables".

[10] C. H. Bennett, H. J. Bernstein, S. Popescu, and B. Schumacher. Concentrating partial entanglement by local operations. *Phys. Rev. A*, 53:5046–2052, 1996.

[11] C. H. Bennett and G. Brassard. Public Key Distribution and Coin Tossing. In *Proceedings of IEEE International Conference on Computers, Ssystems and Signal Processing*, pages 175–179, Bangalore, India, December 1984.

[12] C. H. Bennett, G. Brassard, C. Crépeau, R. Jozsa, A. Peres, and W. K. Wootters. Teleporting an unknown quantum state via dual classical and Einstein-Podolsky-Rosen channels. *Phys. Rev. Lett.*, 70:1895–1899, 1993.

[13] C. H. Bennett, G. Brassard, S. Popescu, B. Schumacher, J. A. Smolin, and W. K. Wootters. Purification of Noisy Entanglement and Faithful Teleportation via Noisy Channels. *Phys. Rev. Lett.*, 76:722–725, 1996.

[14] C. H. Bennett and S. J. Wiesner. Communication via one- and two-particle operators on Einstein-Podolsky-Rosen states. *Phys. Rev. Lett.*, 69:2881–2884, 1992.

[15] M. Betz, F. Sotier, F. Tauser, S. Trumm, A. Laubereau, and A. Leitenstorfer. All-optical phase locking of two femtosecond Ti:sapphire lasers: a passive coupling mechanism beyond the slowly varying amplitude approximation. *Opt. Lett.*, 29:629–631, 2004.

[16] J. Beugnon, M. P. A. Jones, J. Dingjan, B. Darquié, G. Messin, A. Browaeys, and P. Grangier. Quantum interference between two single photons emitted by independently trapped atoms. *Nature*, 440:779–782, 2006.

[17] B. Blauensteiner. A Single-Photon Spectrometer for Quantum Optics Experiments with Independent Sources. Master's thesis, Technische Universität Wien, 2005.

[18] B. B. Blinov, D. L. Moehring, L.-M. Duan, and C. Monroe. Observation of entanglement between a single trapped atom and a single photon. *Nature*, 428:153–157, 2004.

[19] D. Bohm. A Suggested Interpretation of the Quantum Theory in Terms of "Hidden" Variables. I. *Phys. Rev.*, 85:166–179, 1952.

[20] D. Bohm. A Suggested Interpretation of the Quantum Theory in Terms of "Hidden" Variables. II. *Phys. Rev.*, 85:180–193, 1952.

[21] H. R. Böhm. A Compact Source for Polarization Entangled Photon Pairs. Master's thesis, Atominstitut der österreichischen Universitäten, 2003.

[22] N. Bohr. Can Quantum-Mechanical Description of Physical Reality Be Considered Complete? *Phys. Rev.*, 48:696–702, 1935.

[23] D. Bouwmeester, A. Ekert, and A. Zeilinger. *The Physics of Quantum Information*. Springer, Berlin, 2000.

[24] D. Bouwmeester, J.-W. Pan, K. Mattle, M. Eibl, H. Weinfurter, and A. Zeilinger. Experimental quantum teleportation. *Nature*, 390:575–579, 1997.

[25] H.-J. Briegel, W. Dür, J. I. Cirac, and P. Zoller. Quantum repeaters: The role of imperfect local operations in quantum communication. *Phys. Rev. Lett.*, 81:5932–5935, 1998.

[26] R. Hanbury Brown and R. Q. Twiss. Correlation between photons in two coherent beams of light. *Nature*, 177:27–32, 1956.

[27] R. Hanbury Brown and R. Q. Twiss. A test of a new type of stellar interferometer on sirius. *Nature*, 178:1046–1048, 1956.

[28] D. C. Burnham and D. L. Weinberg. Observation of simultaneity in parametric production of optical photon pairs. *Phys. Rev. Lett.*, 25:84–87, 1970.

[29] C.-W-Chou, J. Laurat, H. Denkg, K. S. Choi, H. de Riedmatten, D. Felinto, and H. J. Kimble. Functional Quantum Nodes for Entanglement Distribution over Scalable Quantum Networks. Published online in Science Express, 5. April, 2007, doi: 10.1126/science.1140300, http://www.sciencemag.org/cgi/content/abstract/1140300, 2007.

[30] A. Cabello, Á. Feito, and A. Lamas-Linares. Bell's inequalities with realistic noise for polarization-entangled photons. *Phys. Rev. A*, 72:052112, 2005.

[31] A. R. Calderbank and P. W. Shor. Good quantum error-correcting codes exist. *Phys. Rev. A*, 54:1098–1105, 1996.

[32] J. Calsamiglia and N. Lütkenhaus. Maximum efficiency of a linear-optical bell-state analyzer. *Appl. Phys. B*, 72(1):67–71, 2001.

[33] G. De Chiara, Č. Brukner, R. Fazio, G. M. Palma, and V. Vedral. A scheme for entanglement extraction from a solid. quant-ph/0505107, 2005.

[34] J. F. Clauser. Experimental Investigation of a Polarization Correlation Anomaly. *Phys. Rev. Lett.*, 36:1223–1226, 1976.

[35] J. F. Clauser and M. A. Horne. Experimental consequences of objective local theories. *Phys. Rev. D*, 10(2):526–535, 1974.

[36] J. F. Clauser, M. A. Horne, A. Shimony, and R. A. Holt. Proposed Eexperiment to test Local Hidden-Variable Theories. *Phys. Rev. Lett.*, 23:880–884, 1969.

[37] H. de Riedmatten, I. Marcikic, W. Tittel, H. Zbinden, and N. Gisin. Quantum interference between photon pairs created in spatially separated sources. *Phys. Rev. A*, 67:022301, 2003.

[38] D. Deutsch, A. Ekert, R. Jozsa, C. Macchiavello, S. Popescu, and A. Sanpera. Quantum Privacy Amplification and the Security of Quantum Cryptography over Noisy Channels. *Phys. Rev. Lett.*, 77(13):2818–2821, 1996.

[39] R. H. Dicke. In P. Grivet and N. Bloembergen, editors, *Proceedings of the 3rd International Conference on Quantum Electronics*, page 35. Dunod, Paris, and Columbia University Press, New York, 1964.

[40] P. A. M. Dirac. *The Principles of Quantum Mechanics*, page 9. Oxford University Press, London, 4th edition, 1958.

[41] V. G. Dmitriev, G. G. Gurzadyan, and D. N. Nikogosyan. *Handbook of Nonlinear Optical Crystals*. Springer, Berlin, 1999.

[42] W. Dür, H.-J. Briegel, J. I. Cirac, and P. Zoller. Quantum repeaters based on entanglement purification. *Phys. Rev. A*, 59:169–181, 1999.

[43] A. Einstein, B. Podolsky, and N. Rosen. Can Quantum-Mechanical Description of Physical Reality Be Considered Complete? *Phys. Rev.*, 47:777–780, 1935.

[44] A. K. Ekert. Quantum cryptography based on Bell's theorem. *Phys. Rev. Lett.*, 67:661–663, 1991.

[45] A. A. Evett. Permutation Symbol Approach to Elementary Vector Analysis. *Am. J. Phys.*, 34:503–507, 1966.

[46] A. Th. Forrester, R. A. Gudmundsen, and Ph. O. Johnson. Photoelectric Mixing of Inchohernt Light. *Phys. Rev.*, 99:1691–1700, 1955.

[47] S. J. Freedman and J. F. Clauser. Experimental Test of Local Hidden-Variable Theories. *Phys. Rev. Lett.*, 28:938–941, 1972.

[48] E. S. Fry and R. C. Thompson. Experimental Test of Local Hidden-Variable Theories. *Phys. Rev. Lett.*, 37:465–468, 1976.

[49] S. Ghosh, T. F. Rosenbaum, G. Aeppli, and S. N. Coppersmith. Entangled quantum state of magnetic dipoles. *Nature*, 425:48–51, 2003.

[50] N. Gisin. Hidden quantum nonlocality revealed by local filters. *Phys. Lett. A*, 210(3):151–156, 1996.

[51] N. Gisin, G. Ribordy, W. Tittel, and H. Zbinden. Quantum cryptography. *Rev. Mod. Phys.*, 74:145–194, 2002.

[52] R. J. Glauber. Coherent and Incoherent States of the Radiation Field. *Phys. Rev.*, 131:2766–2788, 1963.

[53] R. J. Glauber. The Quantum Theory of Optical Coherence. *Phys. Rev.*, 130:2529–2539, 1963.

[54] D. Gottesmann and I. L. Chuang. Demonstrating the viability of universal quantum computation using teleportation and single-qubit operations. *Nature*, 402:390–393, 1999.

[55] D. Greenberger, M. Horne, and A. Zeilinger. A Bell Theorem Without Inequalities for Two Particles, Using Efficient Detectors. quant-ph/0510201, 2005.

[56] D. Greenberger, M. Horne, and A. Zeilinger. A Bell Theorem Without Inequalities for Two Particles, Using Inefficient Detectors. quant-ph/0510207, 2005.

[57] W. P. Grice and I. A. Walmsley. Spectral information and distinguishability in type-II down-conversion with a broadband pump. *Phys. Rev. A*, 56:1627–1634, 1997.

[58] S. Gröblacher, T. Paterek, R. Kaltenbaek anc Č. Brukner, M. Ż ukowski, M. Aspelmeyer, and A. Zeilinger. An experimental test of non-local realism. *Nature*, 446:871–875, 2007.

[59] M. Halder, A. Beveratos, N. Gisin, V. Scarani, C. Simon, and H. Zbinden. Entangling independent photons by time measurement. *Nature Physics*, 2007. published online: 19 August 2007; doi:10.1038/nphys700.

[60] C. K. Hong, Z. Y. Ou, and L. Mandel. Measurement of subpicosecond time intervals between two photons by interference. *Phys. Rev. Lett.*, 59:2044–2046, 1987.

[61] P. Horowitz and W. Hill. *The Art of Electronics*. Cambridge University Press, 2nd edition, 1989.

[62] A. Javan, E. A. Ballik, and W. L. Bond. Frequency characteristics of a continuous wave he-ne optical maser. *J. Opt. Soc. Am.*, 52:96–98, 1962.

[63] Th. Jennewein. *Quantum Communication and Teleportation Experiments using Entangled Photon Pairs*. PhD thesis, University of Vienna, 2002.

[64] Th. Jennewein, G. Weihs, J.-W. Pan, and A. Zeilinger. Experimental Nonlocality Proof of Quantum Teleportation and Entanglement Swapping. *Phys. Rev. Lett.*, 88:124–127, 2002.

[65] B. Julsgaard, J. Sherson, J. I. Cirac, J. Fiurášek, and E. S. Polzik. Experimental demonstration of quantum memory for light. *Nature*, 432:482–486, 2004.

[66] R. Kaltenbaek, M. Aspelmeyer, J. Jennewein, Č. Brukner, and A. Zeilinger. Proof-of-concept experiments for quantum physics in space. In *Quantum Communications and Quantum Imaging*, volume 5161, pages 252–268. Proceedings of SPIE, 2003.

[67] R. Kaltenbaek, B. Blauensteiner, M. Żukowski, M. Aspelmeyer, and A. Zeilinger. Experimental Interference of Independent Photons. *Phys. Rev. Lett.*, 96:240502, 2006.

[68] T. E. Keller and M. H. Rubin. Theory of two-photon entanglement for spontaneous parametric down-conversion driven by a narrow pump pulse. *Phys. Rev. A*, 56:1534–1541, 1997.

[69] T. E. Keller, M. H. Rubin, and Y. Shih. Two-photon interference from separate pulses. *Phys. Lett. A*, 244:507–551, 1998.

[70] H. J. Kimble and L. Mandel. Theory of resonance fluorescence. *Phys. Rev. A*, 13:2123–2144, 1976.

[71] E. Knill, R. Laflamme, and G. Milburn. A scheme for efficient quantum computation with linear optics. *Nature*, 409:46–52, 2001.

[72] H. Kogelnik and T. Li. Laser Beams and Resonators. *Appl. Opt.*, 5:1550–1567, 1966.

[73] A. Kuhn, M. Hennrich, and G. Rempe. Deterministic Single-Photon Source for Distributed Quantum Networking. *Phys. Rev. Lett.*, 89:067901, 2002.

[74] P. G. Kwiat, K. Mattle, H. Weinfurter, and A. Zeilinger. New High-Intensity Source of Polarization-Entangled Photon Pairs. *Phys. Rev. Lett.*, 75:4337–4341, 1995.

[75] P. J. Kwiat, E. Waks, A. G. White, I. Appelbaum, and P. H. Eberhard. Ultrabright source of polarization-entangled photons. *Phys. Rev. A*, 60:R773–R776, 1999.

[76] R. Laflamme, C. Miquel, J. P. Paz, and W. H. Zurek. Perfect Quantum Error Correcting Code. *Phys. Rev. Lett.*, 77:198–201, 1996.

[77] P. S. K. Lee, M. P. van Exter, and J. P. Woerdman. Increased polarization-entangled photon flux via thinner crystals. *Phys. Rev. A*, 26:043818, 2004.

[78] T. Legero, T. Wilk, M. Hennrich, G. Rempe, and A. Kuhn. Quantum Beat of Two Single Photons. *Phys. Rev. Lett.*, 93:070503, 2004.

[79] A. J. Leggett. Nonlocal hidden-variable theories and quantum mechanics: An incompatibility theorem. *Found. Phys.*, 33:1469–1493, 2003.

[80] D. A. Lidar, I. L. Chuang, and K. B. Whaley. Decoherence-Free Subspaces for Quantum Computation. *Phys. Rev. Lett.*, 81:2594–2597, 1998.

[81] G. Magyar and L. Mandel. Transient interference fringes between light from independent ruby lasers. *Nature*, 198:255–256, 1963.

[82] L. Mandel. Photon interference and correlation effects produced by independent quantum sources. *Phys. Rev. A*, 28:929–943, 1983.

[83] L. Mandel and E. Wolf. *Optical coherence and quantum optics*. Cambridge University Press, New York, 1995.

[84] I. Marcikic, H. de Riedmatten, W. Tittel, H. Zbinden, M. Legré, and N. Gisin. Distribution of Time-Bin Entangled Qubits over 50 km of Optical Fiber. *Phys. Rev. Lett.*, 93:180502, 2005.

[85] D. N. Matsukevich and A. Kuzmich. Quantum State Transfer Between Matter and Light. *Science*, 306:663–666, 2004.

[86] K. Mattle, H. Weinfurter, P. G. Kwiat, and A. Zeilinger. Dense Coding in Experimental Quantum Communication. *Phys. Rev. Lett.*, 76:4656–4659, 1996.

[87] G. Mayer. Rayonnement de l'harmonique pair d'une onde lumineuse par des molécules soumises à un champ élecrique statique. *C. R. Acad. Sc. Paris, Série B*, 267:54–57, 1968.

[88] N. D. Mermin. Is the moon there when nobody looks? Reality and the quantum theory. *Physics Today*, 26:38–47, April 1985.

[89] A. A. Michelson. On the application of interference methods to astronomical measurements. *Astrophys. J.*, 51:257–262, 1920.

[90] M. Nielsen and I. Chuang. *Quantum Computation and Quantum Information Theory*. Cambridge Univ. Press, Cambridge, 2000.

[91] A. Osterloh, L. Amico, G. Falci, and R. Fazio. Scaling of entanglement close to a quantum phase transition. *Nature*, 416:608–610, 2002.

[92] J.-W. Pan, D. Bouwmeester, H. Weinfurter, and A. Zeilinger. Experimental Entanglement Swapping: entangled photons that never interacted. *Phys. Rev. Lett.*, 80:3891–3894, 1998.

[93] J.-W. Pan, S. Gasparoni, R. Ursin, G. Weihs, and A. Zeilinger. Experimental entanglement purification of arbitrary unknown states. *Nature*, 423:417–422, 2003.

[94] H. Paul. Interference between independent photons. *Rev. Mod. Phys.*, 58:209–231, 1986.

[95] P. M. Pearle. Hidden-Variable Example Based upon Data Rejection. *Phys. Rev. D*, 2(8):1418–1425, 1970.

[96] A. Peres. Einstein, Podolsky, Rosen and Shannon. *Found. Phys.*, 35:511–514, 2005.

[97] A. Petersen. The philosophy of Niels Bohr. In A. P. French and P. I. Kennedy, editors, *A Centenary Volume*, page 299. Harvard University Press, Cambridge, MA, 1985.

[98] R. L. Pfleegor and L. Mandel. Interference of independent laser beams. *Phys. Rev.*, 159:1084–1088, 1967.

[99] T. B. Pittman, D. V. Strekalov, A. Migdall, M. H. Rubin, A. V. Sergienko, and Y. H. Shih. Can Two-Photon Interference be Considered the Interference of Two Photons. *Phys. Rev. Lett.*, 77(10):1917–1920, 1996.

[100] W. Radloff. Zur interferenz unabhängiger lichtstrahlen geringer intensität. *Ann. Phys. (Leipzig)*, 26:178–189, 1971.

[101] J. G. Rarity, P. R. Tapster, and R. Loudon. Non-classical interference between independent sources. In F. De Martini, G. Denardo, and Y. Shih, editors, *Quantum Interferometry*. VCH, Weinheim, 1996. eprint quant-ph/9702032 (1997).

[102] R. Raussendorf and H. J. Briegel. A One-Way Quantum Computer. *Phys. Rev. Lett.*, 86:5188–5191, 2001.

[103] M. A. Rowe, D. Kielpinski, V. Meyer, C. A. Sackett, W. M. Itano, C. Monroe, and D. J. Wineland. Experimental violation of a Bell's inequality with efficient detection. *Nature*, 409:791–794, 2001.

[104] M. H. Rubin. Transverse correlation in optical spontaneous parametric down-conversion. *Phys. Rev. A*, 54:5349–5360, 1996.

[105] M. H. Rubin, D. N. Klyshko, Y. H. Shih, and A. V. Sergienko. Theory of two-photon entanglement in type-ii optical parametric down-conversion. *Phys. Rev. A*, 50:5122–5133, 1997.

[106] B. E. A. Saleh and M. C. Teich. *Fundamentals of Photonics*. John Wiley & Sons, Inc., New York, 1991.

[107] C. Santori, D. Fattal, J. Vučković, G. S. Solomon, and Y. Yamamoto. Indistinguishable photons from a single-photon device. *Nature*, 419:594–597, 2002.

[108] E. Schrödinger. Die gegenwärtige Situation in der Quantenmechanik. *Die Naturwissenschaften*, 48:807–812, 1935.

[109] E. Schrödinger. Die gegenwärtige Situation in der Quantenmechanik. *Die Naturwissenschaften*, 49:823–828, 1935.

[110] E. Schrödinger. Die gegenwärtige Situation in der Quantenmechanik. *Die Naturwissenschaften*, 50:844–849, 1935.

[111] E. Schrödinger. Discussion of probability relations between separated systems. *Proc. Camb. Phil. Soc.*, 31:555–563, 1935.

[112] E. Schrödinger. Probability relations between separated systems. *Proc. Camb. Phil. Soc.*, 32:446–452, 1936.

[113] B. Schumacher. Quantum coding. *Phys. Rev. A*, 51(4):2738–2747, 1995.

[114] R. K. Shelton, L.-S. Ma, H. C. Kapteyn, M. M. Murnane, J. L. Hall, and J. Ye. Phase-Coherent Optical Pulse Synthesis from Separate Femtosecond Lasers. *Science*, 293:1286–1289, 2001.

[115] P. W. Shor. Scheme for reducing decoherence in quantum computer memory. *Phys. Rev. A*, 52:R2493–R2496, 1995.

[116] A. M. Steane. Error Correcting Codes in Quantum Theory. *Phys. Rev. Lett.*, 77:793–797, 1996.

[117] H. Takesue. Long-distance distribution of time-bin entanglement generated in a cooled fiber. *Optics Express*, 14:3453–3460, 2005.

[118] Shigeki Takeuchi. Beamlike twin-photon generation by use of type ii parametric downconversion. *Opt. Lett.*, 26:843–845, 2001.

[119] J. Tian, Z. Wei, P. Wang, H. Han, J. Zhang, L. Zhao, Z. Wang, J. Zhang, T. Yang, and J. Pan. Independently tunable 1.3 W femtosecond Ti:sapphire lasers passively synchronized with attosecond timing jitter and ultrahigh robustness. *Opt. Lett.*, 30:2161–2163, 2005.

[120] R. Ursin, F. Tiefenbacher, T. Schmitt-Manderbach, H. Weier, T. Scheidl, M. Lindenthal, B. Blauensteiner, T. Jennewein, J. Perdigues, P. Trojek, B. Ömer, M. Fürst, M. Meyenburg, J. Rarity, Z. Sodnik, C. Barbieri, H. Weinfurter, and A. Zeilinger. Entanglement-based quantum communication over 144 km. *Nature Physics*, 3:481–486, 2007.

[121] V. Vedral. Entanglement hits the big time. *Nature*, 425:28–29, 2003.

[122] V. Vedral. High-temperature macroscopic entanglement. *New Journal of Physics*, 6:102, 2004.

[123] V. Vedral, M. B. Plenio, M. A. Rippin, and P. L. Knight. Quantifying Entanglement. *Phys. Rev. Lett.*, 78(12):2275–2279, 1997.

[124] J. Volz, M. Weber, D. Schlenk, W. Rosenfeld, J. Vrana, K. Saucke, C. Kurtsiefer, and H. Weinfurter. Observation of Entanglement of a Single Photon with a Trapped Atom. *Phys. Rev. Lett.*, 96:030404, 2006.

[125] D. von der Linde. Characterization of the Noise in Continuously Operating Mode-Locked Lasers. *Appl. Phys. B*, 39:201–217, 1986.

[126] J. von Neumann. *Mathematische Grundlagen der Quantenmechanik*. Julius Springer, Berlin, 1932.

[127] E. Waks, A. Zeevi, and Y. Yamamoto. Security of quantum key distribution with entangled photons against individual attacks. *Phys. Rev. A*, 65:052310, 2002.

[128] P. Walther, K. Resch, Č. Brukner, A. M. Steinberg, J.-W. Pan, and A. Zeilinger. Quantum nonlocality obtained from local states by entanglement purification. *Phys. Rev. Lett.*, 94:040504, 2005.

[129] G. Weihs. *Ein Experiment zum Test der Bellschen Ungleichung unter Einsteinscher Lokalität*. PhD thesis, University of Vienna, 1999.

[130] G. Weihs, T. Jennewein, C. Simon, H. Weinfurter, and A. Zeilinger. Violation of Bell's Inequality under Strict Einstein Locality Conditions. *Phys. Rev. Lett.*, 81:5039–5043, 1998.

[131] R. F. Werner. Quantum states with Eeinstein-Podolsky-Rosen correlations admitting a hidden-variable model. *Phys. Rev. A*, 40:4277–4281, 1989.

[132] S. Wiesner. Conjugate coding. *SIGACT News*, 15:78–88, 1983.

[133] M. Wieśniak, V. Vedral, and Č. Brukner. Magnetic susceptibility as a macroscopic entanglement witness. *New Journal of Physics*, 7:258, 2005.

[134] W. K. Wootters and W. H. Zurek. A single quantum cannot be cloned. *Nature*, 299:802–803, 1982.

[135] T. Yang, Q. Zhang, T.-Y-Chen, S. Lu, J. Yin, J.-W Pan, Z.-Y. Wie, J.-R. Tian, and J. Zhang. Experimental Synchronization of Independent Entangled Photon Sources. *Phys. Rev. Lett.*, 96:110501, 2006.

[136] P. Zanardi and M. Rasetti. Noiseless Quantum Codes. *Phys. Rev. Lett.*, 79(17):3306–3309, Oct 1997.

[137] A. Zeilinger. Testing Bell's inequalities with periodic switching. *Phys. Lett. A*, 118(1):1–2, 1986.

[138] A. Zeilinger. A Foundational Principle for Quantum Mechanics. *Foundations of Physics*, 29:631–643, 1999.

[139] M. Żukowski. Mini-max theory of down conversion. Lecture notes: The physics of quantum information, 2002.

[140] M. Żukowski and Č. Brukner. Bell's Theorem for General N-Qubit States. *Phys. Rev. Lett.*, 88:210401, 2002.

[141] M. Żukowski, A. Zeilinger, M. A. Horne, and A. K. Ekert. "event-ready-detectors" Bell experiment via entanglement swapping. *Phys. Rev. Lett.*, 71:4287–4290, 1993.

[142] M. Żukowski, A. Zeilinger, and H. Weinfurter. Entangling independent pulsed photon sources. *Ann. N. Y. Acad. Sci.*, 755:91–102, 1995.

List of the Author's Publications

[1] M. Aspelmeyer, H. R. Böhm, T. Gyatso, T. Jennewein, R. Kaltenbaek, M. Linden-thal, G. Molina-Terriza, A. Poppe, K. J. Resch, M. Taraba, R. Ursin, P. Walther, and A. Zeilinger. Long-Distance Free-Space Distribution of Quantum Entanglement. *Science*, 301:621–623, 2003.

[2] M. Aspelmeyer, J. Jennewein, H. R. Böhm, Č. Brukner, R. Kaltenbaek, M. Linden-thal, G. Molina-Terriza, J. Petschinka, R. Ursin, P. Walther, A. Zeilinger, M. Pfennig-bauer, and W. Leeb. Quantum Communications in Space. Technical Report under Contract 16358/02, ESA, 2003.

[3] S. Gröblacher, T. Paterek, R. Kaltenbaek anc Č. Brukner, M. Żukowski, M. Aspelmeyer, and A. Zeilinger. An experimental test of non-local realism. *Nature*, 446:871–875, 2007. 8

[4] R. Kaltenbaek, M. Aspelmeyer, J. Jennewein, Č. Brukner, and A. Zeilinger. Proof-of-concept experiments for quantum physics in space. In *Quantum Communications and Quantum Imaging*, volume 5161, pages 252–268. Proceedings of SPIE, 2003. 21

[5] R. Kaltenbaek, B. Blauensteiner, M. Żukowski, M. Aspelmeyer, and A. Zeilinger. Experimental Interference of Independent Photons. *Phys. Rev. Lett.*, 96:240502, 2006. 62, 71, 147

[6] R. Kaltenbaek, R. Prevedel, M. Aspelmeyer, and A. Zeilinger. High-fidelity entangle-ment swapping with independent sources. to be published, 2008.

[7] R. Prevedel, P. Walther, F. Tiefenbacher, P. Böhi, R. Kaltenbaek, T. Jennewein, and A. Zeilinger. High-speed linear optics quantum computing using active feed-forward. *Nature*, 445:65–69, 2007.

[8] R. Ursin, T. Jennewein, M. Aspelmeyer, R. Kaltenbaek, M. Lindenthal, P. Walther, and A. Zeilinger. Quantum teleportation across the danube. *Nature*, 430:849, 2004.

Danksagung

Obgleich der Rest dieser Doktorarbeit in Englisch gehalten ist, möchte ich doch an dieser Stelle auf meine Muttersprache zurückgreifen, da die Danksagung keinen Anteil am fachlichen Inhalt dieser Arbeit hat, und da Dank in der am Besten ausdrückbaren und am Besten verständlichen Form gegeben werden sollte. Es gibt viele Menschen denen ich dankbar bin, und ich hoffe, dass ich zumindest ihrer Großteil hier erwähne. Wer sich nicht wiederfindet und sich doch meines Dankes gewiss denken kann, möchte mir bitte verzeihen.

Mein erster Dank geht an **Anton Zeilinger** und seine allem aufgeschlossene, stets den Horizont im Auge behaltende Gruppe - für die Möglichkeiten die sich durch die Zusammenarbeit eröffneten, für die Geduld, die meinem teilweise übertriebenen Perfektionismus entgegengebracht wurde, für die Freiheit, die mir in so vielen Dingen gewährt wurde, und für die Freude an der Forschung, die mir vom ersten Tag an vermittelt wurde.

Danken möchte ich auch jenen, die mich auf den Weg gebracht haben, der hierhin führte, gleich ob es ein Anstoß oder anhaltende Ermunterung und Betreuung waren. Hierunter fallen: **Martin Dangl**, ein besserer Physik- und Mathematiklehrer, als ihn sich die meisten Menschen vorstellen können. **Georg Oppitz**, der Wirbelwind, welcher mich hoffentlich auch in Zukunft wieder aus dem Alltag heben oder darin absetzen wird. **Markus Arndt** und **Gregor Weihs**, durch die ich überhaupt mal erfuhr und Interesse daran fand, was Quantenoptik ist. **Markus Aspelmeyer**, der mir eine Mischung aus all den Dingen bedeutet, die ich den anderen danke, und der mir ebenso Freund wie Betreuer war.

All meinen Kollegen ergeht Dank für Diskussionen, dafür, dass sie aus dem einen oder anderen Grund an mich glaubten, für ihre Hilfe in Experimenten oder bei der Ausarbeitung von Papers, für völlig unsachliche Freundschaft, für den einen oder anderen schönen Abend und vieles mehr. Darunter zähle ich **Andrea Aglibut**, **Marek Żukowski**, **Časlav Brukner**, **Simon Gröblacher**, **Rupert Ursin**, **Michael Taraba**, **Robert Prevedel**, **Thomas Jennewein**, **Bibiane Blauensteiner**, **Andreas Poppe**, **Philip Walther**, **Kevin Resch**, **Hannes Böhm**, **Michael Lindenthal**, **Lucia Hackermüller** und **Johannes Kofler**.

An meine **Mutter**, meinen **Vater**, meine **Schwester** und meinen **Bruder**, die ich alle kläglich vernachlässigte in der Zeit, die mich diese Arbeit kostete, dafür dass sie es mir nachsahen und sich freuten, wenn ich einen meiner kurzen unphysikalischen Momente dann doch mit ihnen verbrachte.

Ein großer Dank geht an all meine Freunde, denen ich, wie meiner Familie, ein Blatt im Wind war in dieser Zeit. Obwohl ich von ihnen sicher nicht alle nennen kann, möchte ich doch den Versuch tun, jene zu nennen, die am häufigsten von meiner Unabkömmlichkeit betroffen waren, ohne selbst unabkömmlich zu werden: **Thomas Bauer**, **Christoph**

Litschauer, Walter Scherer, Andreas Neumeister, Paul Dangl, Madeleine Kufner, Kathrin Kertesz, Elisabeth Lingg, Florian Kargl und Sabina Sanegre.

Curriculum Vitae

31.8.1979	Geboren in St. Pölten als Sohn von Walburga und Josef Kaltenbaek
1985-1989	Besuch der Volksschule Göpfritz/Wild, Waldviertel, Niederösterreich
1989-1997	Besuch des naturwissenschaftlichen Zweiges des Bundesrealgymnasiums Waidhofen/Thaya
1998	Erfüllung der Wehrpflicht beim Österreichischen Bundesheer im Lager Kaufholz
1998-2003	Physikstudium an der Universität Wien
2002-2003	Diplomarbeit über Active Switching in Long-Distance Quantum State Teleportation bei Prof. Anton Zeilinger, Institut für Experimentalphysik, Universität Wien
2003	Beginn der Dissertation bei Prof. Anton Zeilinger, Institut für Experimentalphysik, Universität Wien über Entanglement Swapping and Quantum Interference with Independent Sources
2007	Beginn einer Post-Doc Stelle bei Prof. Kevin Resch und Prof. Gregor Weihs am Institute for Quantum Computing, University of Waterloo, Canada